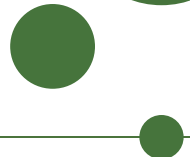


UNIVERSITY OF COPENHAGEN
FACULTY OF SCIENCE



PhD Dissertation

Michael. J. Larson

A Search for Tau Neutrino Appearance with IceCube-DeepCore

Advisor: Dr. D. Jason Koskinen

Handed in: March 14, 2018

Contents

1	Introduction	15
1.1	The History of the Neutrino	15
1.2	History of Cosmic Rays	16
1.3	Atmospheric Neutrinos	17
1.4	The Standard Model	18
1.5	Methods of Detection	22
2	Neutrino Oscillations	26
2.1	Oscillation Theory and the PMNS Matrix	26
2.2	Experimental Constraints on Neutrino Oscillations	29
2.3	Unitarity and Sterile Neutrinos	32
3	The IceCube Detector	38
3.1	The DOM: The Basic Unit of IceCube	38
3.2	The Geometry of the Detector	41
3.3	The Bulk Ice Model	46
3.4	The Hole Ice	47
4	Simulation of the IceCube-DeepCore Detector	49
4.1	Monte Carlo Generators	49
4.2	Propagation of the Particles and Light	53
4.3	Simulating the Detector Electronics	54
5	Updates to the Noise Simulation	57
5.1	A Summary of Previous Fits	57
5.2	Limitations and Disagreement with Previous Fits	58
5.3	Low-dt Noise from Vuvuzela	59
5.4	Updating the Fitting Code	60
5.5	Results of New Noise Fits	65
6	Low-Energy Muon Simulation	70
6.1	CORSIKA Generation In DeepCore	70
6.2	MuonGun for DeepCore	71
6.3	Simulation Efficiency with KDE Prescales	73
7	GRECO: An Event Selection at the Limits of DeepCore	76
7.1	Hit Cleaning	76
7.2	Level 1: The DeepCoreFilter	78
7.3	Low-En Level 3 Cuts	79
7.4	GRECO Level 4 Cuts	81
7.5	GRECO Level 5 Cuts	86

7.6	GRECO Level 6 Cuts	91
7.7	GRECO Level 7: Final Level	97
7.8	Calibration Discoveries with GRECO	100
7.9	The Properties of the GRECO Event Selection	112
8	A Search for Tau Neutrinos from Oscillations	114
8.1	Binning of the Appearance Analysis	114
8.2	Parametrizing the Tau Neutrino Appearance	117
8.3	Systematics Considerations	119
8.4	The Test Statistic for the Analysis	140
8.5	Expected Sensitivity to Appearance	145
8.6	Feldman-Cousins vs Wilk's Theorem	147
8.7	Impact of Systematics	150
8.8	Fitting Data	152
8.9	Results from the Search for Appearance	155
8.10	Complementary Measurements from This Analysis	160

List of Figures

1.1	The number of active neutrinos as measured by ALEPH, DELPHI, L3, and OPAL. The data from the four experiments strongly favors only three neutrinos coupling to the Z boson. Image taken from [9].	16
1.2	The cosmic ray spectrum covers many orders of magnitude and has been verified by many experiments to high precision. The various features are thought to be caused by multiple sources at different scales. Image taken from [17]	18
1.3	The expected neutrino flux at Kamioka mine, Japan (Super-Kamiokande, top left), Ino Peak, India (India-based Neutrino Observatory, top right), the South Pole (IceCube, bottom left), and Pyhasalmi mine, Finland (EMMA experiment, bottom right) as a function of energy. Note that the neutrino and anti-neutrino fluxes are characterized separately. The differences in the flux at each site is due to differences in the Earth's magnetic field and temperature profile. Figure taken from [18].	19
1.4	The expected flux of 3.2 GeV neutrinos at Kamioka mine, Japan; Ino Peak, India; the South Pole; and Pyhasalmi mine, Finland as a function of zenith angle. A value of $\cos \theta_Z = -1$ indicates neutrinos passing through the entire Earth and entering the detector from below while a value of $\cos \theta_Z = +1$ indicates neutrinos interacting in the atmosphere directly above the detector. The differences in the flux at each site is due to differences in the Earth's magnetic field and temperature profile. Figure taken from [18].	19
1.5	The Standard Model of particle physics is made up of charged and uncharged leptons, quarks, and the various bosons. Image taken from [19]	20
1.6	Feynman diagrams showing the interaction vertex of the neutrino with the W and Z boson.	20
1.7	The relative contributions to the cross section for ν (left) and $\bar{\nu}$ (right). The QE events dominate below 1 GeV while the DIS events dominate above 10 GeV. Note the different scales for the neutrino and antineutrinos. Images taken from [20]	21
1.8	A Feynman diagram showing an example of a CC neutrino DIS interaction. An incident muon neutrino interacts with a quark inside of a proton. The result is a hadronic shower as well as a charged muon. Diagram taken from [20]	22
1.9	An example of the energy loss ($\frac{-dE}{dx}$) calculated for muons incident on copper. Note the radiative losses due to bremsstrahlung, pair production, and photonuclear interactions above 1 TeV. Note also the labeled minimum demonstrating the energy of a minimum ionizing particle. Image taken from [17].	24

2.1	The first atmospheric neutrino oscillation measurements from the Super-K experiment. (a) The ν_e -like events show no shape in L/E, as expected from a lack of neutrino oscillations. The ν_μ -like interactions, however, show a clear drop, indicating the presence of oscillation effects. (b) Using the two neutrino approximation, Super-K produced contours of the best-fit oscillation parameters for $\nu_\mu \rightarrow \nu_\tau$ oscillations. Both figures from [56]	31
2.2	The global best-fit values for the three flavor neutrino oscillation fits as of November 2017. The first column shows results assuming the normal ordering while the second column shows the results for the inverted ordering. Image taken from [58]	32
2.3	Expectations (a) and results (b) of searches for sterile neutrinos in the neutral current interactions. (a) Effect of three hypothetical sterile neutrinos on the measurements of the MINOS detector [63]. "ND" and "FD" refer to the near and far detector of MINOS respectively. The sterile neutrinos have a small effect on the main oscillation minimum in the charged current channel, but up to 15% of the neutral current events are lost. (b) The results of the NO ν A search for sterile neutrinos using neutral current events. The limits are interpreted in terms of the 4x4 PMNS mixing elements in order to compare to searches with charged current interactions in Super-Kamiokande [65] and IceCube [66].	33
2.4	The results of the tests using 2.25 (solid) and 2.26 (dotted). A smaller value on the x-axis indicates a tighter constraint on observed unitarity of the 3x3 mixing matrix. Tests involving only muon or electron flavors show significantly tighter constraints than those including the tau flavor. Image taken from [68]	35
2.5	The constraints from a global fit to neutrino oscillation data[68] with an assumption of unitarity (black dotted) or no assumption of unitarity (red solid). The first two rows show little change from the unitarity assumption, indicating strong constraints from direct measurements. The elements of the third row, related to the ν_τ , show much larger changes, indicating that constraints are obtained from indirect oscillation measurements.	36
3.1	The IceCube DOM contains multiple components, including the PMT itself as well as various electronics necessary for semi-autonomous operation.	38
3.2	Afterpulsing calibration measurements performed in the lab. LEDs with known brightness were flashed to test for offtime response of the IceCube PMT. Clear dips, corresponding to detected charge, are visible. Drop (a) corresponds to the initial LED flash while (b), (c), and (d) show prominent afterpulsing peaks. Image taken from [69].	39
3.3	Examples of the ATWD (top) and FADC (bottom) waveforms output from an IceCube PMT. Taken from [37]	40
3.4	A histogram of the time between subsequent hits on DOM 15 of string 27. Hitspool data, specialized data collected with no trigger applied, is shown in blue. The "correlated" (non-Poissonian) and "uncorrelated" (Poissonian) features are shown in red and black respectively. The location of a large afterpulsing peak is shown in yellow. Note that the features included are not to scale. Image taken from [37].	41

3.5	The IceCube Neutrino Observatory. Three separate subdetectors are shown: IceTop, a cosmic ray air shower detector; IceCube, an array designed to search for astrophysical neutrinos; and DeepCore, a dense subarray optimized for atmospheric oscillation physics measurements. The detector was deployed over multiple years. Strings deployed in the same year are shown with identical colors at the surface.	42
3.6	A comparison of the standard IceCube string (right) to the DeepCore string (left). The IceCube string uses DOMs spaced 17 m apart while DeepCore divides the DOMs into a fiducial (bottom) and veto plug (top). The dust concentration is shown in red. The concentration of dust in the ice affects the scattering and absorption of the glacial ice.	43
3.7	Examples of event topologies above 1 TeV using the full IceCube array. Event views shown in (a) and (b) are from actual events discovered by the IceCube detector [77]. Images taken from [78]. (a) ν_e CC and ν NC show similar behavior from electromagnetic and hadronic interactions, which result in a shower of particles that quickly scatter in the ice. Cherenkov emission from these events appears roughly spherical in the detector. These events are known as "cascades". (b) ν_μ CC events begin with a hadronic interaction, then produce Cherenkov light from the outgoing muon. Above 1 TeV, the track of the outgoing muon becomes clearly visible. (c) Above 10 TeV, the tau lepton from a ν_τ CC may travel a significant distance before decaying. This results in two well-separated cascades in the detector, a tell-tale signature of ν_τ CC interactions.	44
3.8	The layout of the DeepCore detector. DeepCore is installed at the bottom of the IceCube detector in the clearest ice. A subset of DOMs were also deployed above DeepCore to improve muon identification of very-downgoing events.	45
3.9	A selection of 50 GeV simulated events in DeepCore taken from [78]. Unlike the event topologies at high energies, DeepCore events do not show distinct event types.	45
3.10	The data from the dust loggers deployed in various drill holes in IceCube during deployment. Data from individual holes has been offset in the y direction for clarity. Larger relative values of the "Optical Signal" represent more scattering in the ice while smaller values indicate clearer ice. The "dust layer" is visible in all drill holes around 2000 m. Deepcore DOMs are deployed below this layer. Image taken from [86].	46
3.11	The absorption and effective scattering properties of the ice as fit to flasher data. Two models are shown representing different generations of ice models used for simulation. The "Mie" model does not include anisotropy while the "Lea" model does. Figure from [87].	47
3.12	The effect of the anisotropy on the light output from a flasher on string 63. Measurements (points) are shown for receiving DOMs at three distances: at 125 m (red), at 217 m (blue), and at 250 m (green). A line is included to show the expected effect of anisotropy at each distance. The y-axis shows the ratio of a simulation of the same flasher without including anisotropy to data. A modulation is observed as a function of direction in the x-y plane. .	47

4.1	Average energy losses ($\frac{-dE}{dx}$) for a muon in ice. At very low energies, ionization losses dominate. Above approximately 1 TeV, pair production and photonuclear effects become more important. Image taken from [21]	53
4.2	Examples of the angular acceptance models used by IceCube. The relative sensitivity as a function of arrival direction is shown with $\cos(\eta)=-1$ indicating the back of the PMT and $\cos(\eta)=1$ the face. The variation of the acceptance model used for this search is shown using by varying two parameters in the model. The 'p' parameter primarily controls the acceptance at the side of the DOM while the 'p2' parameter controls the acceptance from the forward region. A second model, H2, is also shown.	55
4.3	The SPE template used in Monte Carlo simulation. The gaussian (red, dash-dot) and exponential (blue, dashed) parts of the full model (black) are shown. The SPE template is used as a sampling distribution for each incident photon in order to determine the observed charge. The SPE template is used for all DOMs.	56
5.1	Two examples of the original calibration work for the Vuvuzela model. The distribution of the time ("dt") between hits is shown. In black, untriggered detector data is shown. In red, a purely Poissonian noise model is shown. An afterpulsing peak is visible at 10^{-5} s. The Vuvuzela model is shown in blue. The Vuvuzela model shows improved agreement with data at all timescales.	58
5.2	The rates of events in DeepCore as a function of the number of hit DOMs in a cleaned hit series. The data, shown in black, consists of two components: the accidental triggers (red) and the atmospheric muons (blue). Accidental triggers produced using the Vuvuzela noise model reproduce most of the rate of events below 10 hit DOMs, although a rate disagreement remains. Image from [71].	59
5.3	The number of hit DOMs satisfying the (a) HLC and (b) SLC criteria described in Section 3.1.2. The distribution from 8 hours of data (black) is shown compared to a sample of CORSIKA muons at low-energy ($600 \text{ GeV} \leq E_{\text{primary}} \leq 100 \text{ TeV}$) and high energy ($100 \text{ TeV} \leq E_{\text{primary}} \leq 100 \text{ EeV}$). The addition of the low-dt extension to Vuvuzela improves the agreement between data and simulation in both HLC and SLC distributions.	60
5.4	The total amount of charge on DOMs satisfying the (a) HLC and (b) SLC criteria described in Section 3.1.2. The distribution from 8 hours of data (black) is shown compared to a sample of CORSIKA muons at low-energy ($600 \text{ GeV} \leq E_{\text{primary}} \leq 100 \text{ TeV}$) and high energy ($100 \text{ TeV} \leq E_{\text{primary}} \leq 100 \text{ EeV}$). Unlike in Figure 5.3, the charge distributions using the low-dt extension to Vuvuzela shows large disagreements with data. This is most visible in the SLC charge distribution.	61
5.5	The effect of changing the noise distribution parameters on the charge. Note the scale of the y-axis, which is scaled in order to emphasize the effect. Here, the gaussian mean is shifted from "5" (100 microseconds) to "3" (1 microsecond). All other parameters are held constant. By moving the correlated noise distribution to shorter timescales, more of distribution falls into one FADC bin, increasing the charge output for each launch.	61
5.6	A schematic diagram of the process used in the Vuvuzela V2 calibration fit.	62

5.7	Two examples of the new calibration fits for the Vuvuzela V2 model. The distribution of the time ("dt") between hits is shown on top. The distribution of charge is shown on the bottom. Note the y-axis of the charge distribution. In black, untriggered detector data is shown. The Vuvuzela V2 model is shown in blue. The new fits show good agreement in both time and charge distributions.	63
5.8	The distributions of each new fit parameter in the Vuvuzela V2 model. The colorbar scale shows the number of DOMs in each bin. The effects of fit bounds are visible in most distributions except for the thermal noise rate and the width of the log-normal distribution describing the non-Poissonian noise.	67
5.9	The distributions of each new fit parameter in the Vuvuzela V2 model as a function of the string and DOM number. Note that the top of the detector is at the bottom of this plot. No parameter appears to be correlated with depth. DOMs on string 25 are missing from the dataset. In addition, DOMs which are disabled due to malfunction are also unavailable.	68
5.10	The log-likelihood as a function of string and DOM number for the Vuvuzela V2 fits. Note that DOM 1 is at the top of the detector and DOM 60 at the bottom. The likelihood value was expected to be independent of depth, but shows some structure. These structures are correlated with both the ice model and the muon flux.	69
6.1	The distribution of CORSIKA muon energies at the MuonGun generation surface using GRECO Level 5 muon events. Very few events trigger are seen below 160 GeV and less than 5% of events occur beyond 500 GeV. These two energies set the bounds for the MuonGun generation. MuonGun simulation has also been produced and tested above 500 GeV, but no simulated events survived to final level in GRECO.	72
6.2	The generated spectrum from MuonGun in energy and zenith angle compared to the events reaching the final level of the GRECO event selection. Both distributions have been normalized to 1. The majority of events produced by MuonGun are downgoing and low energy. These events do not reach final level.	73
6.3	The generated spectrum from MuonGun in energy and azimuthal angle compared to the events reaching the final level of the GRECO event selection. Both distributions have been normalized to 1. Events in the final level sample are strongly biased in azimuth due to the geometry of the detector.	74
7.1	An illustration of the LC, SeededRT, and time window cleaning methods. (Left) All SLC pulses are removed while all HLC pulses are retained. (Middle) Pulses are removed based on time and distance from nearby HLC DOMs, allowing some SLC pulses to be accepted. (Right) Pulses are removed using the time relative to either the trigger (STW) or the maximum pulse density in time (DTW).	77
7.2	The distribution of effective particle speeds used by the DeepCoreFilter to identify and reject muons. Because muons interact first outside of DeepCore, a large peak is visible at speeds around 0.3 m/ns, the speed of light. Figure from [72].	79
7.3	The FirstHit Z position	82
7.4	Number of Hits Above Z=-200	82

7.5	QR6 and C2QR6	83
7.6	Tensor-of-Inertia Eigenvalue Ratio	83
7.7	The improvedLineFit Speed	84
7.8	The L4 BDT Score	85
7.9	Time to 75% Charge	87
7.10	A schematic diagram showing the regions of the VICH algorithm. VICH returns the number of hit DOMs in the shaded region, corresponding to the pulses that are both causally connected with the trigger and entering DeepCore.	87
7.11	Veto Identified Causal Hits	88
7.12	First Hit ρ Position	88
7.13	Quartile Distance	88
7.14	Quartile Z-Travel	89
7.15	SPE Reconstruction Zenith Angles	89
7.16	The L5 BDT Score	91
7.17	Fill-Ratio	93
7.18	The NChannel Distribution	94
7.19	CorridorCut Distribution	95
7.20	Example of Corridors into DeepCore	96
7.21	The FiniteReco Containment Cuts	96
7.22	Diagram Describing the FiniteReco Method	97
7.23	The FiniteReco containment cut applied at GRECO Level 6	98
7.24	The Pegleg containment cuts applied at Level 7	101
7.25	The 2D cuts applied to the time and energy variables at Level 7	102
7.26	The effect of the data SPE correction applied in 2015	103
7.27	A comparison if the old and new SPE templates for simulation	104
7.28	A comparison of the charge extraction in data and simulation at GRECO L7. Both the time and charge are shown for individual pulses on all DOMs. The time is measured relative to the largest pulse observed on each DOM during an event. The data and simulation histograms are independently normalized to 1.0. While the two show broad agreement, notable differences occur at low charge.	105
7.29	The reconstructed Z position plotted against the reconstructed distance from string 36. The L7 cuts from GRECO have been removed for this plot. The colorbars in both plots have been normalized to be identical. The data and simulation show reasonable agreement except for two points in the data, near $\rho_{36} = 75$ at depths of -310 and -490.	106
7.30	The reconstructed X position and Y position of events in the detector. The L7 cuts from GRECO have been removed for this plot. The colorbars in both plots have been normalized to be identical. Once again, reasonable agreement is observed in most regions, although data events have a clear excess near $x=110$ m, $y=-60$ m. This position corresponds to string 83.	107
7.31	The RMS of the charges showing the events with flaring DOMs	108
7.32	The reconstructed Z position using PegLeg. The GRECO L7 cuts have not been applied in order to show discrepancies below the detector. Noticeable disagreement is seen below the detector at a depth of -500 m. Additional disagreements are also visible at the top of DeepCore, a region dominated by atmospheric muons.	109
7.33	The NuGen and GENIE true energy spectra at final level	109

7.34	The NuGen and GENIE interaction depths at final level	110
7.35	The reconstructed azimuthal direction from Pegleg	111
7.36	The true neutrino energy and zenith of the GRECO sample at final level. The sample shows an asymmetry between upgoing ($\cos(\theta) < 0$) and downgoing ($\cos(\theta) > 0$) event rates in the neutrinos due to selection bias. The sample has a long tail of events at both high and low energies. Using the NuFit 2.2 oscillation parameters and the flux model from Honda, the ν_τ events are observed in the very upgoing region around $10^{1.4} = 25$ GeV.	112
7.37	The reconstructed energy and zenith of the GRECO sample at final level. Events in data reconstruct to both relatively high energies ($E_R > 100$ GeV) and very low energies ($E_R \approx 2$ GeV). Using the NuFit 2.2 oscillation parameters and the flux model from Honda, the ν_τ events are observed in the very upgoing region around $10^{1.4} = 25$ GeV.	113
8.1	Cumulative distributions of two PID variables in GRECO	115
8.2	Comparison of separating power between PID variables	116
8.3	Neutrino histograms for appearance analysis	123
8.4	Background and data histograms for appearance analysis	124
8.5	A tau neutrino event observed at OPERA	125
8.6	Signal and background in the Super-Kamiokande analysis	125
8.7	Effect of Δm_{31}^2 in the analysis histogram	126
8.8	Effect of θ_{23} in the analysis histogram	126
8.9	Effect of $\delta\gamma_\nu$ in the analysis histogram	127
8.10	Effect of N_{ν_e} in the analysis histogram	127
8.11	The neutrino flux shape uncertainties	128
8.12	Effect of $\nu/\bar{\nu}$ in the analysis histogram	128
8.13	Effect of Up/Horizontal in the analysis histogram	129
8.14	Effect of $\delta\gamma_{CR}$ in the analysis histogram	129
8.15	Effect of m_a^{QE} in the analysis histogram	130
8.16	Effect of m_a^{RES} in the analysis histogram	130
8.17	Effect of the neutrino DIS uncertainty in the analysis histogram	131
8.18	Effect of the neutrino DIS uncertainty in the analysis histogram	131
8.19	Effect of the neutral current normalization in the analysis histogram	132
8.20	Effect of the coincident events in the analysis histogram	136
8.21	Effect of the DOM efficiency in the analysis histogram	137
8.22	Effect of the absorption in the analysis histogram	138
8.23	Effect of the scattering in the analysis histogram	139
8.24	Effect of the hole ice parameter in the analysis histogram	139
8.25	Effect of the forward scattering parameter in the analysis histogram	140
8.26	The sensitivity of this analysis in the (a) NC+CC and (b) CC-only channel. The top plot shows the Asimov expectation (black dotted line) and the Brazilian flag (green, yellow bands). The significances assuming Wilk's theorem (gray horizontal lines) and Feldman-Cousins (red horizontal lines) are also shown. The bottom plot shows the expected 1σ and 90% ranges for Wilks theorem and Feldman-Cousins compared to the most recent results from the OPERA and Super-Kamiokande analyses.	146

8.27	The test statistic distributions for 11 points in N_{τ}^{True} in the NC+CC fit. The assumption of 1 degree of freedom from Wilk's theorem is tested by looking at the location of $(\Delta\chi^2_{FS})_{90\%}$ for each point. The distribution calculated from Monte Carlo trials is narrower than that predicted by Wilk's theorem, indicating that a more complete treatment with the Feldman- Cousins procedure is necessary.	149
8.28	The N+1 parameter tests	151
8.29	The N-1 redundancy tests	152
8.30	The goodness of fit in the appearance search	153
8.31	The "signed" χ^2_{FS} values for the CC-only fit	154
8.32	The "signed" χ^2_{FS} values for the NC+CC fit	154
8.33	The final result of the CC-only fit	155
8.34	The final result of the NC+CC fit	156
8.35	The best fit value of each systematic with priors	156
8.36	The CC-only posterior distributions expected compared to final fit values .	157
8.37	The NC+CC posterior distributions expected compared to final fit values .	158
8.38	The results of a disappearance fit with GRECO	161
8.39	Neutrino mass ordering measurement with GRECO	161

List of Tables

1.1	The branching ratios for the decay of tau leptons. Two-thirds of the time, the tau lepton decays hadronically.	23
6.1	The simulation requirements needed for the production of the standard CORSIKA sets in IceCube. The number of events reaching final level of the appearance search (Section 7.6.3) are shown. CORSIKA simulations are computationally intensive, but inadequate for low energy analyses in IceCube.	71
6.2	The simulation requirements needed for the production of MuonGun simulation for DeepCore. The MuonGun simulation is nearly two orders of magnitude more efficient at producing statistics at final level in the appearance analysis.	72
6.3	The simulation requirements and number of events for each muon generation scheme. The use of the KDE prescale improves the simulation efficiency by a factor of 50x compared to the DeepCore MuonGun simulation method described in Section 6.1.	75
7.1	The event rates after the Level 3 cuts in GRECO. The total simulated rate is calculated using CORSIKA events and ignoring MuonGun. The data rate is estimated from a burn sample of 10 runs at Level 3. Rates are given in mHz.	81
7.2	The event rates after the Level 4 cuts in GRECO. The total simulated rate is calculated using CORSIKA events and ignoring MuonGun. The data rate is estimated from a burn sample of 30 runs at Level 4. Rates are given in mHz.	86
7.3	The event rates after the Level 5 cuts in GRECO. The total simulated rate is calculated using CORSIKA events and ignoring MuonGun. The data rate is estimated from a burn sample of 30 runs at Level 5. Rates are given in mHz.	92
7.4	The event rates after the Level 6 cuts in GRECO. The total simulated rate is calculated using CORSIKA events and ignoring MuonGun. The data rate is estimated from a burn sample of 100 runs at Level 6. Rates are given in mHz.	97
7.5	The event rates at each cut level in the GRECO selection. Note that the MuonGun events are included in this table, but do not contribute to the total Monte Carlo expectation to prevent double-counting of muon events from the CORSIKA sample. All rates are given in millihertz.	112
8.1	The rates expected for each of the neutrino types in the Super-Kamiokande search for tau neutrino appearance	119
8.2	Total χ^2 impact of each of the oscillation parameters	120
8.3	Available systematics simulation sets for GENIE	133
8.4	Available systematics sets for MuonGun	134
8.5	Priors and allowed ranges for each systematic included in this analysis.	144
8.6	The numerical values of the systematics parameters	159

Introduction

Measurements of atmospheric neutrino oscillations, such as those performed in this thesis, require a background of understanding of both atmospheric neutrinos as well as neutrino oscillations. A history of neutrinos (Section 1) is used to explain the discovery of the three known flavors of neutrinos as well as the difficulties inherent in the study of these elusive particles. A discussion of the history of cosmic rays (Section 1.1) explains the source of both the neutrinos (Section 1.2) used as signal in this thesis as well as the muons, which form one of the primary backgrounds in the search for atmospheric oscillations.

The detection of neutrinos is described in two parts. A discussion of the neutrino interactions (Section 1.4), explains the interactions of neutrinos with matter. The detection of these interactions through electromagnetic emission is then covered (Section 1.4.1).

1.1 The History of the Neutrino

In 1896, Henri Becquerel discovered radioactivity in uranium [1]. Measurements over the following decades showed various types of nuclear decays based on the penetration depth of the ionizing emissions. Measurements of one type of radioactivity, the beta decays, over the following 30 years showed that the production of two observed particles from one parent nucleus: a daughter nucleus and an outgoing electron. A single body decay of this type produces a known spectrum due to conservation of energy and momentum. The energy of the daughter nucleus and the electron are completely determined by these two conditions, leading to a narrow line emission spectrum.

Contrary to expectations, however, the measurement of energies of the two resulting particles showed wide, continuous spectra [2]. The spectrum provided a major puzzle for physicists due to the contradiction with the simple theoretical expectations. A conundrum for many years, one possible solution was suggested in 1930 by Wolfgang Pauli. In his letter, Pauli suggested that the conservation of energy and momentum could be saved if "... there could exist in the nuclei electrically neutral particles... which have spin 1/2 and obey the exclusion principle, and additionally different from light quanta in that they do not travel with the velocity of light" [3]. The solution to the beta decay puzzle was, then, that this additional "neutron" particle was emitted simultaneously with the observed daughter particles. This newly proposed particle would be electrically neutral and, therefore, unable to be seen through traditional methods. The resulting spectrum of the observed particles could then be continuous, as verified experimentally.

Pauli's suggestion provided a way to save the beloved conservation laws in physics, but at the expense of the assumption of a new particle. The particle, called the "neutron" in Pauli's letter and later renamed the "neutrino" by Fermi, was proposed to be electrically neutral and, therefore, completely undetectable at the time. Later work proposed that the neutrinos interact only via the weak nuclear force, with an interaction strength many orders of magnitude smaller than electromagnetic and strong nuclear forces. Experimental measurements, sensitive only to electromagnetic forces, therefore cannot be used to study neutrinos directly in the same way that other particles may be measured.

It was not until nearly 20 years later, in 1956, that this mystery particle was first detected [4]. In a groundbreaking work, Cowen and Reines presented an experiment at the Savannah River Plant, a nuclear power plant, demonstrating detection of the neutrino. The experiment, made up of layers of scintillation detectors around polyethelene boxes,

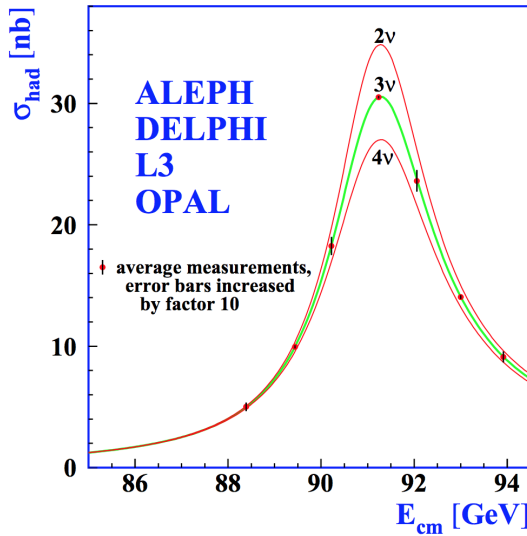


Figure 1.1 – The number of active neutrinos as measured by ALEPH, DELPHI, L3, and OPAL. The data from the four experiments strongly favors only three neutrinos coupling to the Z boson. Image taken from [9].

yielded a signal-to-background rate of about 3 to 1 with a rate of 2.88 ± 0.22 counts/hour with a total livetime of 1371 hours, including time during which the nearby nuclear reactor was offline. For the discovery of the first neutrinos, Frederick Reines was granted a shared Nobel Prize in Physics for the year 1995 [5].

Since the neutrino was first observed, additional measurements have discovered two new flavors of neutrinos: the muon neutrino [6] and the tau neutrino [7, 8].

Searches for additional neutrinos beyond the discovered three have been performed by investigating the decays of the Z boson. The Z boson, a particle of 91 GeV [pdg], couples both to the neutrinos and to more easily observed hadrons and charged leptons making it a useful probe of neutrino interactions. The width of the Z decay to hadrons, for instance, is affected by the number of active, light neutrino species [9]. Additional flavors of neutrinos coupling to the Z boson would lead to a smaller decay rate to hadrons observed in accelerator searches for hadrons as shown in Figure ???. The number of neutrinos may be calculated by comparing the best-fit ratio of "invisible" decays of the Z boson (ie, those involving two neutrinos) to the measured width expected from charged leptons in the standard model.

$$R_{inv} \equiv \frac{\Gamma_{inv}}{\Gamma_{ll}} = N_\nu \left(\frac{\Gamma_{\nu\nu}}{\Gamma_{ll}} \right)_{SM} \quad (1.1)$$

Here the number of neutrinos is extracted by assuming that all active neutrinos have the same coupling to the Z boson, result which has been verified experimentally. A precision measurement of the Z resonance completed at the LEP collider found the best fit value of $N_\nu = 2.9840 \pm 0.0082$, in good agreement with only three active neutrinos.

1.2 History of Cosmic Rays

In the early years of the 20th century, scientists began investigating previously-unknown ionizing radiation in the atmosphere. Scientists using electroscopes, early instruments designed to measure electric charge and radiation, discovered low levels of radiation

in the air. This new radiation was observed to be reduced when the electroscope was shielded by metal free of radioactivity, indicating that the signal was not an artifact of the detector itself and was, instead, coming from an external source.

Following just a few decades after the discovery of radioactivity by Becquerel, many scientists believed that the electroscope was picking up radiation from the Earth itself. The rate would be expected to decrease with increasing altitude above sea level and, to increase with increasing depth in the sea. Early measurements by Domenico Pacini in 1910 showed that the radiation rate decreased by 20% at a depth of 3 meters underwater compared to the rate at the surface [10], implying an origin independent of the Earth's crust. Measurements were performed with electroscopes by Victor Franz Hess in 1912 of the rate of ionizing radiation up to an altitude of 5 km [11].

Hess showed that the observed rate decreased until an altitude of around 1 km, but at a slower rate than expected from theory. Above 1400 meters, however, the rate of ionizing radiation increased again, rising substantially up to the maximum altitude reached at 5300 meters [12]. Hess's work, later confirmed by Henri Millikan, showed definitively that there exists a source of radiation of extraterrestrial origin, earning him the Nobel Prize in Physics for 1936 [13]. This radiation was later dubbed "cosmic rays" by Millikan in reference to their extraterrestrial origin.

Work on cosmic rays has lead to numerous discoveries. In 1937, the first *hadronic showers* were observed [14]. Hadronic showers of particles created by interactions of cosmic rays were shown to produce large numbers of particles [15, 11], with many producing from 5×10^6 to over 10^9 particles [16]. These showers begin with a cosmic ray primary particle, often a single proton accelerated to high energies, which interacts with particles of the Earth's atmosphere. The interaction leads to the creation of various daughters, including neutrinos, muons, pions, kaons, and other hadrons.

Modern measurements have shown that the cosmic ray spectrum primarily consists of protons with a small contribution from helium and heavier elements [17]. These ions are accelerated in unknown astrophysical sources up to extremely high energies. The cosmic ray spectrum extends over many orders of magnitude, with the highest energy observations reaching 10^{20} electronvolts - far higher than any Earth-based accelerator. The spectrum, shown in Figure 1.2, has multiple features that are believed to arise from different accelerator sources at different scales, each of which has been verified by multiple experiments.

1.3 Atmospheric Neutrinos

Air showers from cosmic rays provide a useful natural source of neutrinos in the GeV energy range and above that may be used for fundamental physics research. The hadronic shower produces pions and kaons which, in turn, decay to produce neutrinos

$$\pi^+ \rightarrow \mu^+ \nu_\mu \rightarrow e^+ \nu_e \bar{\nu}_\mu \nu_\mu \quad (1.2)$$

from the pions and from the kaons

$$K^+ \rightarrow \pi^+ \nu_\mu \rightarrow e^+ \nu_e \bar{\nu}_\mu \nu_\mu \nu_\mu \quad (1.3)$$

The neutrino flux depends on a number of parameters, including the Earth's magnetic field and temperature profile, the cosmic ray flux, and the details of hadronic interactions in air showers [18]. The calculation of the neutrino flux predictions requires significant, dedicated simulation work, producing fluxes as both a function of energy (Figure 1.3) and direction (Figure 1.4).

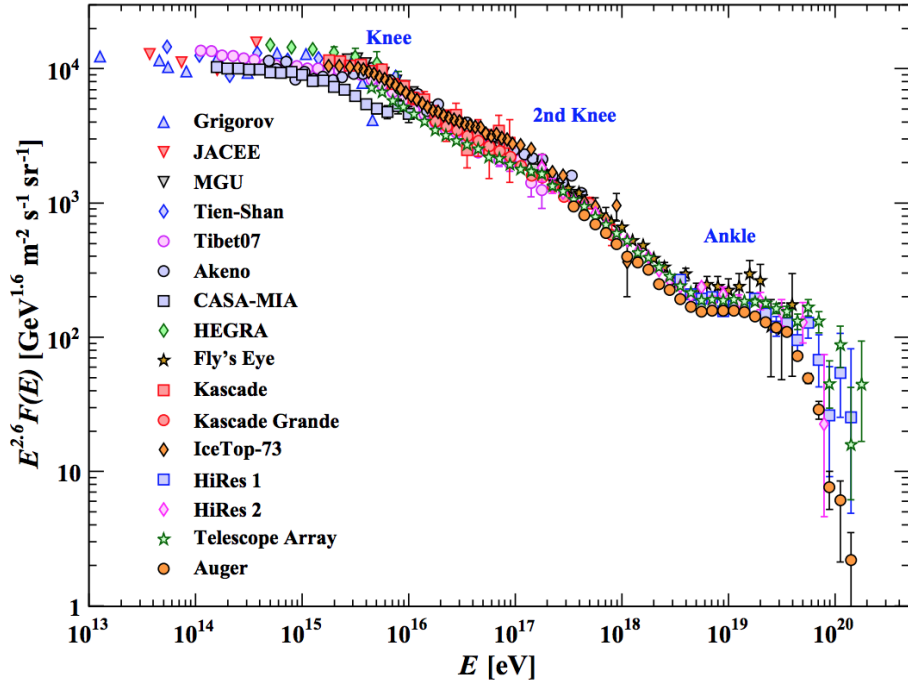


Figure 1.2 – The cosmic ray spectrum covers many orders of magnitude and has been verified by many experiments to high precision. The various features are thought to be caused by multiple sources at different scales. Image taken from [17]

1.4 The Standard Model

Muons and neutrinos form just a small part of the Standard Model of particle physics. The Standard Model, with fundamental particle types and properties shown in Figure 1.5, consists of six quarks (up, down, strange, charm bottom, and top), three charged leptons (electron, muon, tau), three uncharged leptons (electron neutrino, muon neutrino, and tau neutrino), and the five bosons related to interactions (photon, Z, W, gluon, and Higgs). Combinations of the quarks lead to various hadrons, particles which interact with and are formed via the strong force, with different combinations of quarks and anti-quarks producing a wide variety of particles. The Standard Model, developed over the last half century, elegantly encapsulates the range of phenomena known to occur in particle physics and has been verified repeatedly over decades by many experiments. Predictions of the Standard Model have been carefully verified by accelerator experiments, yielding precise checks on a wide range of parameters.

The three charged leptons and neutrinos form three "families" or "flavors". Each charged lepton possesses a coupled neutrino which shares a lepton number conserved in interactions. The electron, the lightest of the charged leptons at 511 keV [17], is a key ingredient of the atoms that make up the world, forming the basis for all of chemistry and is the only stable charged lepton. The muon, with a mass of 105.7 MeV, is the middle of the three charged leptons, often appearing in particle interactions accompanied by the muon neutrino. The muon has a relatively long lifetime of 2.197 microseconds, far longer than many unstable hadrons. The tau lepton is the heaviest of the leptons, and with a mass of 1.777 GeV, it is heavier than the proton and appears only in relatively high energy interactions. The tau has an extremely short lifetime, at 290.6 femtoseconds, and a rich

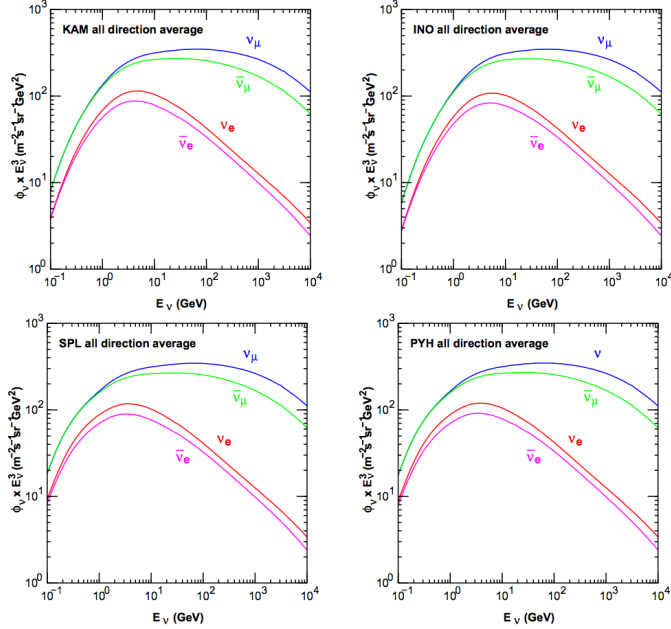


Figure 1.3 – The expected neutrino flux at Kamioka mine, Japan (Super-Kamiokande, top left), Ino Peak, India (India-based Neutrino Observatory, top right), the South Pole (IceCube, bottom left), and Pyhasalmi mine, Finland (EMMA experiment, bottom right) as a function of energy. Note that the neutrino and anti-neutrino fluxes are characterized separately. The differences in the flux at each site is due to differences in the Earth’s magnetic field and temperature profile. Figure taken from [18].

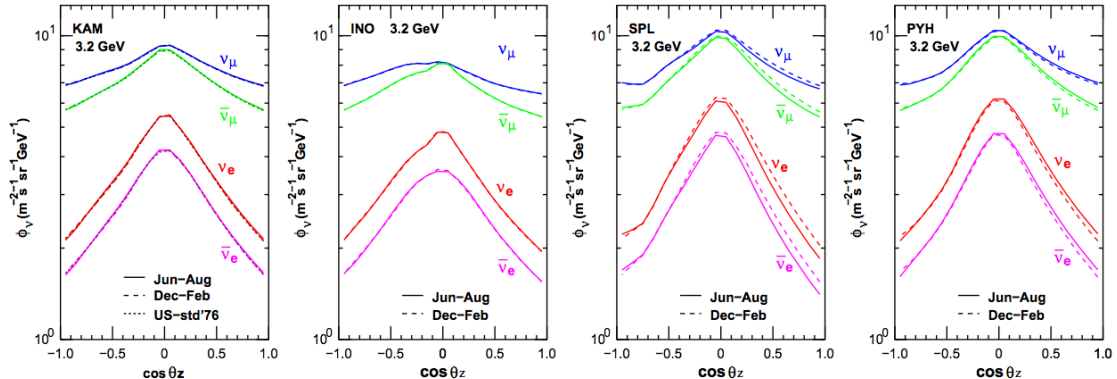


Figure 1.4 – The expected flux of 3.2 GeV neutrinos at Kamioka mine, Japan; Ino Peak, India; the South Pole; and Pyhasalmi mine, Finland as a function of zenith angle. A value of $\cos \theta_Z = -1$ indicates neutrinos passing through the entire Earth and entering the detector from below while a value of $\cos \theta_Z = +1$ indicates neutrinos interacting in the atmosphere directly above the detector. The differences in the flux at each site is due to differences in the Earth’s magnetic field and temperature profile. Figure taken from [18].

variety of decay products. This extremely short lifetime and high mass make the tau difficult to produce and study.

For the purposes of this work, the most significant parts of the Standard model are the neutrinos, which will be defined to be signal events; the up and down quarks, which will make up the protons and neutrons upon which the neutrinos will interact; the W and Z

Standard Model of Elementary Particles

three generations of matter (fermions)					
	I	II	III		
mass	$\approx 2.4 \text{ MeV}/c^2$	$\approx 1.275 \text{ GeV}/c^2$	$\approx 172.44 \text{ GeV}/c^2$	0	$\approx 125.09 \text{ GeV}/c^2$
charge	2/3	2/3	2/3	0	0
spin	1/2	1/2	1/2	1	0
	u	c	t	g	H
	up	charm	top	gluon	Higgs
QUARKS	d	s	b	γ	
	down	strange	bottom	photon	
LEPTONS	e	μ	τ	Z	
	electron	muon	tau	Z boson	
	ν_e	ν_μ	ν_τ	W	
	electron neutrino	muon neutrino	tau neutrino	W boson	
	$<2.2 \text{ eV}/c^2$	$<1.7 \text{ MeV}/c^2$	$<15.5 \text{ MeV}/c^2$	$>80.39 \text{ GeV}/c^2$	
	0	0	0	0	
	1/2	1/2	1/2	1/2	
					GAUGE BOSONS
					SCALAR BOSONS

Figure 1.5 – The Standard Model of particle physics is made up of charged and uncharged leptons, quarks, and the various bosons. Image taken from [19]

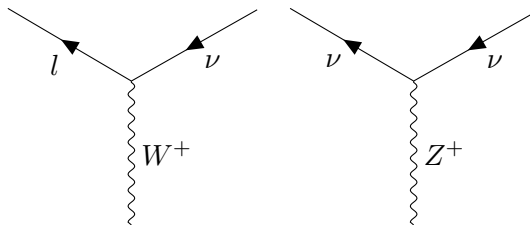


Figure 1.6 – Feynman diagrams showing the interaction vertex of the neutrino with the W and Z boson.

bosons, which mediate the weak interactions via which the neutrinos may be observed; and the photon, which gives a method of observation of the interactions.

1.4.1 Neutrino Interactions

In the Standard Model, neutrinos are assumed to be massless, left-handed spin-1/2 leptons which interact solely via the weak force. Neutrinos, therefore, are only visible via indirect effects, such as scattering or production of charged particles that may, in turn, give off their own visible signature. An understanding of the methods by which neutrinos are detected therefore forms an important basis for the study of these elusive particles. Two basic Feynman diagrams, shown in Figure 1.6, may be used to represent the interaction vertices available for neutrinos.

These two vertices describe the interactions relevant for the work presented in this thesis. During so-called *charged-current (CC)* interactions, a W^\pm boson is exchanged between a neutrino and target particle, in the process converting the uncharged neutrino to the corresponding charged lepton. The *neutral-current (NC)* interactions are those in which

the uncharged Z boson is exchanged with the target and the neutrino, although losing a fraction of the initial energy, does not get converted to a charged lepton.

Detectors used to study particle properties rely on electromagnetic interactions and photons in order to detect particles. Because the neutrino itself does not interact via the electromagnetic force, charged leptons and hadrons must be used to indirectly study the properties of the incident neutrinos. Outgoing charged leptons in charged-current interactions may be detected, although the direction will not necessarily correspond to that of the incident neutrino. The average angle between the incident neutrino and outgoing lepton may be approximated following Equation 1.4.

$$\bar{\theta}_{\nu l} \approx \frac{1.5^\circ}{\sqrt{E_\nu [TeV]}} \quad (1.4)$$

There exist three further classifications of neutral-current and charged-current neutrino interactions in the energy range used in this work: the quasi-elastic, resonant, and deep inelastic interactions [20]. A fourth type, coherent neutrino scattering, may also occur, although the energies involved are too low to impact this work. The three types of interactions contribute to the total cross-section with peaks at different energies, as shown in Figure 1.7.

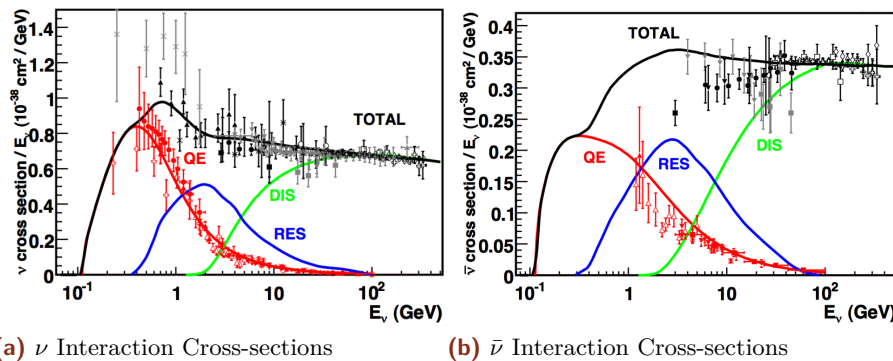


Figure 1.7 – The relative contributions to the cross section for ν (left) and $\bar{\nu}$ (right). The QE events dominate below 1 GeV while the DIS events dominate above 10 GeV. Note the different scales for the neutrino and antineutrinos. Images taken from [20]

lofsubfigure\numberline(a)\nu Interaction
Cross-sections
lofsubfigure\numberline(b)\mathaccen{V}{\bar{0}}16\nu Interaction
Cross-sections

Quasi-Elastic and Resonant Interactions

At low energies of approximately 100 MeV to around 2 GeV, the neutrinos interact via *quasi-elastic scattering (QE)* interactions. In the QE interaction, the neutrino scatters off an entire nucleon instead of the individual quarks. In a charged current QE neutrino (anti-neutrino) interaction, the target neutron (proton) is converted to a proton (neutron) while the neutrino is converted to a charged lepton.

The cross section for QE interactions depends on various nuclear form factors that must be fit to experimental data. Many of these form factors may be fit to electron scattering

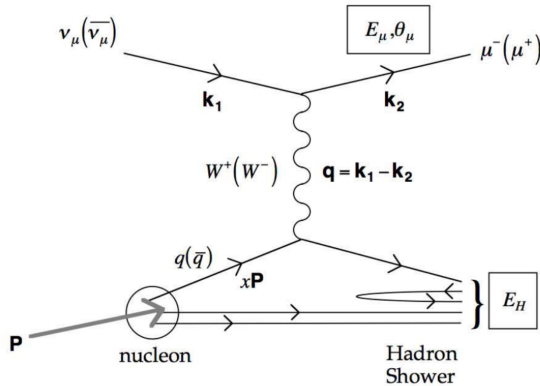


Figure 1.8 – A Feynman diagram showing an example of a CC neutrino DIS interaction. An incident muon neutrino interacts with a quark inside of a proton. The result is a hadronic shower as well as a charged muon. Diagram taken from [20]

data, leaving only the axial vector nuclear form factors to be measured in the neutrino sector [20]. This form factor is normally assumed to have the dipole form

$$F_A(Q^2) = \frac{g_A}{\left(1 + \frac{Q^2}{M_A^2}\right)^2} \quad (1.5)$$

where g_A is a constant fit to experimental data, Q^2 is the 4-momentum transferred in the interaction, and M_A is the "axial mass". This last term is fit to experimental data with a value of $M_A = 0.999 \pm 0.011$ GeV [20].

Resonant scattering interactions (*RES*), which result in the excitation of a nucleon followed by decay via emission of (typically) pions, occur for neutrinos of slightly higher energies of around 500 MeV to 10 GeV. Resonant interactions are modeled in a similar way as the quasi-elastic interactions, with an associated axial mass term used to describe nuclear uncertainties.

Deep Inelastic Interactions

Above a few GeV, the neutrino cross section rises approximately linearly with energy and is dominated by *deep inelastic scattering (DIS)* interactions. An example of a DIS interaction is shown in Figure 1.8. In DIS events, the exchange of the Z or W boson probes the internal structure of the nucleons, leading to a scattering off of the individual quarks of the nucleus. This results in disruption of the nucleon and the larger nucleus and a collection of daughter particles forming a *hadronic shower*.

As seen in Figure 1.7, the DIS events dominate the neutrino cross section above 10 GeV and form the only significant interaction above 100 GeV [20]. Experiments with high statistics samples of DIS events have been used to measure the charged current cross section to the few-percent level.

1.5 Methods of Detection

Neutrinos may be detected through the QE, RES, and DIS interaction channels, with each possessing a distinct signature. The interaction of neutrinos at the GeV energy ranges relevant for this thesis lead to the emission of hadrons in a hadronic shower. The lower energy QE and RES interactions typically yield only one pion which may decay into

Decay	Branching Ratio	Background
$\tau \rightarrow e^- \nu_e \nu_\tau$	$17.83 \pm 0.04 \%$	ν_e CC
$\tau \rightarrow \mu^- \nu_\mu \nu_\tau$	$17.41 \pm 0.04 \%$	ν_μ CC
$\tau \rightarrow \text{hadrons}$	Otherwise	ν NC

Table 1.1 – The branching ratios for the decay of tau leptons. Two-thirds of the time, the tau lepton decays hadronically.

a pair of photons (π^0) or into further charged hadrons and leptons (π^\pm). DIS interactions produce larger hadronic showers containing many charged particles that may be detected. In addition to the hadronic shower, charged-current interactions result in an outgoing charged lepton, the result of which depends on the flavor of the incident neutrino. Outgoing electrons quickly scatter in interactions with the surrounding media, ionizing atoms and producing a secondary *electromagnetic shower* of particles. Muons, on the other hand, travel longer distances before scattering or decaying in the medium, leading to an extended track.

The signature of a tau neutrino charged current interaction varies depending on the specific decay channel of those presented in 1.1. Because the tau lepton has a very short lifetime, outgoing taus tend to decay immediately, producing daughter particles. Each of the three decay modes mimic interactions of the electron and muon neutrinos. The secondary electromagnetic or hadronic cascade is theoretically distinguishable from the primary hadronic cascade produced by a tau neutrino charged current interaction, although the distance traveled by the tau lepton at the energies relevant for this work is on the order of millimeters, far below the reconstruction precision possible with the IceCube detector.

In each case, the charged particles deposit energy into the interaction medium during travel through a series of stochastic and continuous emissions. It is through the detection of these stochastic and continuous losses that daughter particles may be identified in the study of neutrinos.

1.5.1 Stochastic Emission Mechanisms

A total of five major stochastic emission mechanisms are important for the energy losses in neutrino experiments [21]. One such mechanism is the decay of the particle, a process which splits the energy of the parent into multiple, lower energy daughters. Decays of daughter leptons can often be important in the identification of the neutrino flavor, particularly for tau neutrino candidates occurring above 10 TeV when the primary and secondary hadronic interactions become well-separated.

Ionization losses occur when the charged lepton interacts with electrons in the medium, transferring enough energy to liberate the electrons from bound states. At energies below 1 TeV, these losses are the most significant form of energy loss for charged particles, producing a significant source of additional electrons. Ionization losses occur roughly independently of the energy of the charged lepton.

Above energies of a few hundred GeV, radiative processes dominate the energy losses for muons in matter [17]. Bremsstrahlung, photon emission from charged particles accelerating in a magnetic field, pair production, in which a particle and antiparticle (typically electron and positron) are created, and hadronic interactions of photons all dominate the energy losses of muons above 1 TeV.

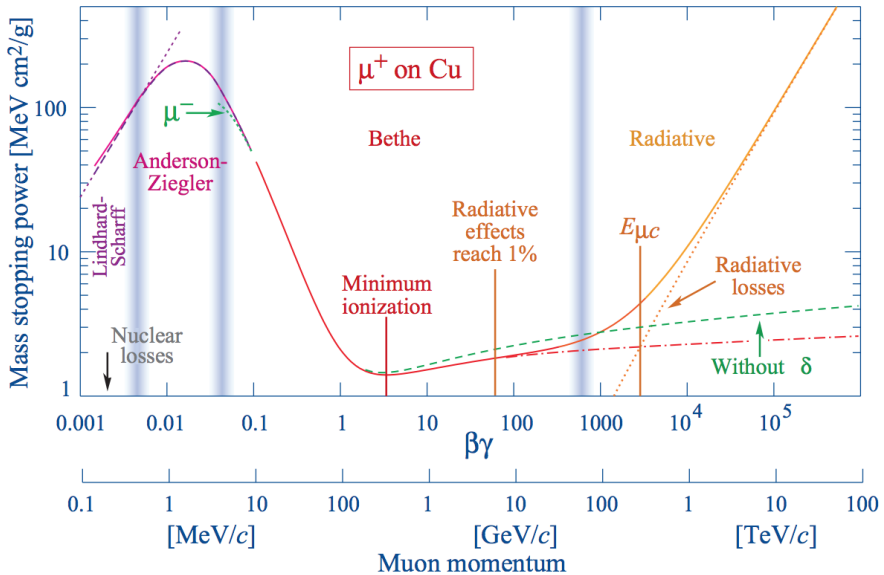


Figure 1.9 – An example of the energy loss ($-\frac{dE}{dx}$) calculated for muons incident on copper. Note the radiative losses due to bremsstrahlung, pair production, and photonuclear interactions above 1 TeV. Note also the labeled minimum demonstrating the energy of a minimum ionizing particle. Image taken from [17].

There exists a minimum in the energy loss rates. Particles emitting near this minimum rate are known as *minimum-ionizing* particles [17].

Stochastic emissions result in additional particles in the detector, leading to improved light yield. In addition, some detectors use photosensitive emulsions [22, 7], scintillators [23, 24, 25, 26], or time projection chambers [27] in order to track ionization losses. These emulsions yield precise characterization of particle decays, allowing experimentalists to uniquely determine the flavor state of the interacting neutrino.

1.5.2 Cherenkov Emission

When a charged particle passes through a dielectric medium with a speed larger than the local phase velocity of light, it will emit *Cherenkov radiation* [28]. The effect, first reported by Pavel Cherenkov in 1934 [29] remained unexplained theoretically until work done by Ilya Frank and Igor Tamm in 1937 [30].

For a dielectric medium, the electric field of the charged particle will polarize atoms by inducing a small dipole moment due to electromagnetic effects in nuclei of atoms in the medium [31]. The resulting disturbance of the medium propagates with the phase velocity of light, given by the speed of light, c , and the index of refraction as a function of the frequency of light, $n(\omega)$. If the charged particle is traveling faster than the local phase velocity, the electromagnetic disturbance propagates with constructive interference, resulting in a planar wavefront of emission known as *Cherenkov emission*. The angle of the wavefront relative to the propagation direction is given by the ratio of the distance traveled by the particle and photons in a given time.

$$\cos(\theta_C) = \frac{\frac{c}{n(\omega)}t}{vt} = \frac{c}{n(\omega)v}, \quad (1.6)$$

The energy threshold for Cherenkov emission is set by a combination of the particle mass and the local phase velocity for light, $\frac{c}{n}$. Using the relativistic kinetic energy [32],

$$E_C \geq \frac{mc^2}{\sqrt{1 - \left(\frac{c/n}{c}\right)^2}} \quad (1.7)$$

$$E_C \geq mc^2 \sqrt{\frac{n^2}{n^2 - 1}} \quad (1.8)$$

For ice with a index of fraction of 1.32 at 400 nanometers [33], this works out to a minimum energy of 270 keV for electrons and 56.2 MeV for muons. The number of photons emitted increases with energy, with approximately 50% more photos produced in blue visible light than in red[32] The full emission spectrum, first worked out by Ilya Frank and Igor Tamm in 1937 [30], depends on a number of parameters, including the energy and charge of the emitting particle as well as the properties of the medium. In the case of a particle traveling a distance L much larger than the photon frequency of interest, λ , the number of emitted photons may be approximated by

$$\frac{dN}{d\lambda} = \frac{2\pi\alpha}{\lambda^2} L \sin^2\theta_C \quad L \gg \lambda \quad (1.9)$$

Cherenkov emission is not limited to a single charged lepton. All charged particles emit Cherenkov radiation, including any hadrons and charged daughter particles, resulting in measurable signals. While the total amount of energy lost via Cherenkov emission is small relative to losses due to stochastic processes, this emission type is both continuous and results directly in photons which may be observed by photodetectors. This technique is used by multiple experiments, including SNO [34], Super-Kamiokande [35], ANTARES [36], and IceCube [37].

Neutrino Oscillations

The search for oscillation events requires an explanation of neutrino oscillations. The theory of neutrino oscillations is included here with broad descriptions of oscillations in vacuum (Section 2.1.1) and in matter (Section 2.1.2). Experimental evidence for the neutrino oscillations and current constraints on the oscillation parameters is presented in Section 2.1.3. Finally, a description of unitarity in the PMNS mixing matrix is given in Section 2.2.3 with particular emphasis placed on the search for additional neutrino flavors (Section 2.3). The motivation for this thesis as well as the purpose behind joint fits between appearance and disappearance data is discussed in Section 2.3.2.

2.1 Oscillation Theory and the PMNS Matrix

In 1968, Bruno Pontecorvo suggested a process, known as *neutrino oscillation*, by which neutrinos could change flavors [38]. The theory of neutrino oscillations was further developed for the neutrino sector by Ziro Maki, Masami Nakagawa and Shoichi Sakata in 1962 [39].

2.1.1 The PMNS Mixing Matrix

We now understand there to be three distinct flavors of neutrinos. Neutrinos are created via the weak force as pure flavor eigenstates. These states are coherent superpositions of mass eigenstates. Specifically, there exist three weak eigenstates of the left-handed neutrino fields that are related to three known neutrino mass eigenstates via the Pontecorvo-Maki-Nakagawa-Sakata (*PMNS*) lepton mixing matrix.

$$\begin{pmatrix} \nu_e \\ \nu_\mu \\ \nu_\tau \end{pmatrix} = U_{PMNS} \begin{pmatrix} \nu_e \\ \nu_\mu \\ \nu_\tau \end{pmatrix} = \begin{pmatrix} U_{e1} & U_{e2} & U_{e3} \\ U_{\mu 1} & U_{\mu 2} & U_{\mu 3} \\ U_{\tau 1} & U_{\tau 2} & U_{\tau 3} \end{pmatrix} \begin{pmatrix} \nu_1 \\ \nu_2 \\ \nu_3 \end{pmatrix} \quad (2.1)$$

The flavor eigenstates $(\nu_e, \nu_\mu, \nu_\tau)$ describe the fields of the left-handed neutrinos coupling via the weak charge to the electron, muon, and tau respectively. The three mass states (ν_1, ν_2, ν_3) represent the mass eigenstates. The mixing between the two types of states is given by the unitary matrix, U_{PMNS} . The mixing may be written in a shortened form

$$\nu_\alpha(x) = \sum_i U_{\alpha i} \nu_i(x) \quad (2.2)$$

where $\alpha = e, \mu, \tau$ and $i = 1, 2, 3$.

Neutrinos interact via the weak force and are created in flavor states e, μ, τ . The neutrino produced in flavor state ν_α exists in a superposition of the three mass eigenstates.

where δ_{ij} and $\delta_{\alpha\beta}$ are Kronecker delta functions. As a 3×3 unitary matrix, the PMNS matrix may be parametrized in terms of three mixing angles and six phases. Of these phases, five may be removed by rephasing the lepton fields with no change to the underlying physics, leaving one physical phase related to CP violation.

The PMNS may be written in terms of the product of three smaller unitary matrices using these mixing angles.

$$U_{PMNS} = \begin{pmatrix} 1 & 0 & 0 \\ 0 & c_{23} & s_{23} \\ 0 & -s_{23} & c_{23} \end{pmatrix} \begin{pmatrix} c_{13} & 0 & s_{13}e^{-i\delta_{CP}} \\ 0 & 1 & 0 \\ -s_{13}e^{i\delta_{CP}} & 0 & c_{13} \end{pmatrix} \begin{pmatrix} c_{12} & s_{12} & 0 \\ -s_{12} & c_{12} & 0 \\ 0 & 0 & 1 \end{pmatrix} \quad (2.3)$$

where the notation c_{ij} idenotes $\cos(\theta_{ij})$ and s_{ij} denotes for $\sin(\theta_{ij})$.

Note that if neutrinos are Majorana fermions, the additional phases may not be removed without making the masses complex. The Majorana terms form additional diagonal terms in Equation 2.3. While Majorana mass terms are beyond the scope of this work, further information may be found in [40, 41].

The three submatrices of Equation 2.3 have historically been studied by different types of experiments. This history has lead to the proliferation of alternative names for the matrices and of the mixing angles.

$$U_{PMNS} = U_{Atmospheric} U_{Reactor} U_{Solar} \quad (2.4)$$

This leads to the alternative names of the mixing angles, with θ_{23} , θ_{13} , and θ_{12} being referred to as the atmospheric mixing angle, the reactor mixing angle, and the solar mixing angle respectively.

2.1.2 Neutrino Mixing in Vacuum

Propagation of neutrinos requires the use of the Hamiltonian. However, the flavor states are not eigenstates of the Hamiltonian. For propagation of the neutrino, the mass eigenstates must instead be used.

$$|\nu(t=0)\rangle = |\nu_\alpha\rangle = \sum_i U_{\alpha i}^* |\nu_i\rangle \quad (2.5)$$

The propagation leads to a neutrino state at time $t \neq 0$ which is no longer a pure flavor state.

$$|\nu(t)\rangle = \sum_i U_{\alpha i}^* e^{-iE_i t} |\nu_i\rangle \quad (2.6)$$

where $E_i = \sqrt{p^2 + m_i^2}$ is the total energy of the i th mass eigenstate. If the neutrino state interacts, the flavor eigenstate must again be used to calculate the probabilities of interacting as each of the three known flavors.

$$P(\nu_\alpha \rightarrow \nu_\beta) = |\langle \nu_\beta | \nu(t) \rangle|^2 = \left| \sum_i U_{\beta i} U_{\alpha i}^* e^{-iE_i t} \right|^2 \quad (2.7)$$

Proper calculations from this point can be performed by treating each neutrino as a quantum mechanical wave packet [42]. This allows for the full description of neutrino oscillation in the context of decoherence of the mass states during propagation, allowing each mass state to possess separate momenta.

In practice, the description of neutrino oscillations necessary for this work is adequately described by making a few simplifying assumptions. In particular, this work assumes that all mass eigenstates propagate as plane waves possessing identical, well-defined momenta [40]. Neutrinos are further assumed to be extremely relativistic at the energies of interest, an assumption well-justified by cosmological fits to the sum of the three

neutrino masses, which give an upper limit of around 0.2 eV [17]. The total neutrino energy is also assumed to be unchanged during propagation. The resulting calculation of the oscillation probabilities is identical in both the simplified version and the full derivation.

To begin, equation 2.7 is expanded by explicitly including the complex conjugate,

$$P(\nu_\alpha \rightarrow \nu_\beta) = \sum_i^3 U_{\beta i}^* U_{\alpha i} \sum_j U_{\beta j} U_{\alpha j}^* e^{i(E_i - E_j)t} \quad \alpha, \beta = e, \mu, \tau. \quad (2.8)$$

In the highly relativistic limit, $E \gg m_i$, and $t \approx L$ where L is the distance traveled during propagation. Using these two approximations, the exponential term in Equation 2.7 may be rewritten using Euler's formula

$$e^{i(E_i - E_j)t} = 1 - 2 \sin^2 \left(\frac{m_{ij}^2 L}{4E} \right) + i \sin \left(\frac{m_{ji}^2 L}{2E} \right) \quad (2.9)$$

Note that a new shorthand has been defined, $\Delta m_{ji}^2 = m_j^2 - m_i^2$, giving a fundamental parameter of neutrino oscillations. The PMNS terms of equation 2.8 may be expanded further, yielding

$$\left| \sum_j U_{\beta j} U_{\alpha j}^* \right|^2 = \delta_{\alpha\beta} + 2 \sum_{i < j} \sum_i U_{\beta i}^* U_{\alpha i} U_{\beta j} U_{\alpha j}^* \quad (2.10)$$

where the factor of two arises due to the symmetry $i \leftrightarrow j$. Putting the terms together, the final oscillation probability formula is

$$P(\nu_\alpha \rightarrow \nu_\beta) = \delta_{\alpha\beta} - 4 \sum_{i < j} \operatorname{Re} \left[\sum_i U_{\beta i}^* U_{\alpha i} U_{\beta j} U_{\alpha j}^* \right] \sin^2 \left(\frac{m_{ij}^2 L}{4E} \right) + 2 \sum_{i < j} \operatorname{Im} \left[\sum_i U_{\beta i}^* U_{\alpha i} U_{\beta j} U_{\alpha j}^* \right] \sin \left(\frac{m_{ji}^2 L}{2E} \right). \quad (2.11)$$

This calculation has been derived for neutrinos. To calculate the probabilities for anti-neutrinos, the calculation changes by replacing $U \rightarrow U^*$, resulting in a change in sign of the last term of Equation 2.11.

From Equation 2.11, the general form of the oscillation probabilities becomes clear. The PMNS matrix elements yield the amplitude of oscillations, while the phase of the oscillations is related to three quantities: the squared difference in the masses, Δm_{ji}^2 ; the baseline, or distance traveled, L ; and the energy of the neutrinos. Only one of these three is a fundamental physics parameter. The choices of energy sensitivity and baseline are used to define characteristics of detectors used for measurements of the various mass splitting parameters and oscillation mixing angles.

Note that the oscillation probability is insensitive to the sign of the mass splitting parameter.

2.1.3 Matter Effects in Oscillation

Calculations up to this point have assumed neutrinos oscillating in vacuum. Modifications required for a description of matter effects begin with a modification of the Hamiltonian

with a potential, V , due to coherent forward scattering of neutrino on electrons and nucleons in the medium [43].

$$H = H_0 + V \quad (2.12)$$

The value of H_0 is the value of vacuum Hamiltonian. In the two-flavor case, the Hamiltonian can be shown [40, 44] to be

$$H_0 = \frac{\Delta m^2}{4E} \begin{pmatrix} -2\cos 2\theta & \sin 2\theta \\ \sin 2\theta & 0 \end{pmatrix}. \quad (2.13)$$

where θ is the mixing angle associated with the 2x2 PMNS matrix. If this effect leaves the neutrino momentum unchanged, the resulting additional terms in the Hamiltonian may interfere with the propagation of the unscattered neutrinos. The potential includes contributions from both charged current and neutral current interactions, although the charged current interactions arise solely from the electron neutrinos. The potential, expressed in the flavor basis, is then

$$V_{CC,\alpha} = \begin{cases} \sqrt{2} \pm G_F n_e(x) & \alpha = e \\ 0 & \alpha = \mu, \tau \end{cases} \quad V_{NC,\alpha} = -\frac{G_F}{\sqrt{2}} n_e(x) \quad \alpha = e, \mu, \tau \quad (2.14)$$

where a + is used for neutrinos and a - is used for antineutrinos, n_e is the density of electrons in the medium, and G_F is the Fermi coupling constant. Note that the angle included here is that of the PMNS matrix in two dimensions. A full description of three flavor neutrino oscillation in the presence of a matter potential is beyond the scope of this work. Further information and explicit forms may be found in [40, 44]. The full three-flavor oscillation calculation is used for this thesis using the Prob3++ code [45, 46], which includes an implementation of matter effects. The electron densities are calculated from the Preliminary Reference Earth Model (PREM) [47].

2.2 Experimental Constraints on Neutrino Oscillations

2.2.1 Solar Neutrinos: A Hint of Multiple Flavors

Early searches for neutrinos focused primarily on the Sun. The first major experiment, proposed by Ray Davis and John Bahcall, was designed to verify that fusion was the primary energy source of the Sun [48, 49]. While the core of the sun is not directly visible to telescopes, neutrinos produced via nuclear fusion could escape the sun relatively unchanged and be observed at Earth.

The Homestake experiment, named for Homestake mine in South Dakota, used 615 tons of perchloroethylene to measure neutrinos via the inverse beta decay reaction



The production rate was well-measured, with a rate of 0.48 counts per day and a background of 0.09 counts per day due to interactions from cosmic ray induced muons [50]. In the typical units of the solar neutrino experiments, this worked out to

$$(\sigma\phi) = 2.56 \pm 0.16 \pm 0.16 \text{ SNU} \quad (2.16)$$

where $1 \text{ SNU} = 10^{-36}$ captures/nucleus/second. The expected rate of neutrino interactions from the sun, however, was predicted to be 8.00 ± 0.97 SNU given the solar models at

the time. The Homestake experiment, therefore, was only observing approximately 30% of the predicted interaction rate. New measurements from other experiments, such as SAGE [51], GALLEX [52], and GNO [53] confirmed the results, although with a reduction of around 50% instead of 70% compared to theoretical expectations.

The disagreement between the number of neutrinos expected and the number predicted was not definitively solved until the Sudbury Neutrino Observatory (SNO) experiment. SNO was a detector located 2 km underground in Sudbury mine in Canada [34]. The detector consisted of a large tank filled with heavy water surrounded by photo-multiplier tubes for the detection of Cherenkov emission. By introducing heavy water, SNO was sensitive to not only the charged current interactions of previous experiments, but also to neutral current interactions invisible to the inverse beta decay experiments.

SNO detected the neutral current and charged current interactions via two distinct channels. The charged-current interactions caused a deuterium atom to break down into two separate protons while also transforming the neutrino into an electron. The electron would be produced with an energy high enough to emit Cherenkov radiation and could, therefore, be observed directly, with the energy of the electron used to constrain the incident neutrino spectrum. The primary charged current interaction at SNO was only sensitive to electron flavor neutrino interactions.

The neutral current interactions, with a threshold energy of 2.22 MeV, were able to separate the deuterium in the heavy water, leading to a free neutron in the detector. The detection of the free neutron posed initial challenges for the same fundamental reason that neutrino detection is difficult: neutrons are not charged and therefore do not emit electromagnetic radiation. Instead, early detections of these neutrons relied on the emission of a high energy gamma ray when the neutron was captured on a deuterium atom. The gamma ray could then, in turn, be absorbed on an electron, accelerating the charged particle and producing Cherenkov radiation.

Measurements at SNO were divided between these two measurement channels in order to investigate one possible solution to the missing solar neutrinos: neutrino oscillations [54]. Because the three known neutrino states all have the same neutral current interaction cross section, the neutral current rate is expected to be constant in the presence of oscillations. The charged current rate is, however, expected to change due to the different couplings of each neutrino flavor to the W^\pm boson. Measuring both the neutral current and charged current rates therefore provided a direct test of neutrino oscillations, allowing researchers to identify the effect independent of the solar model.

SNO expected a rate of neutral current interactions from solar neutrinos of $5.05 \times 10^6 \text{ cm}^{-2} \text{ s}^{-1}$ and observed

$$\phi_{NC}(\nu \text{ active}) = 5.25 \pm 0.16(\text{stat})^{+0.11}_{-0.13} \times 10^6 \text{ cm}^{-2} \text{ s}^{-1} \quad (2.17)$$

a result consistent with expectations. The charged current interaction was measured to be

$$\phi_{CC}(\nu_e) = (0.301 \pm 0.033) \phi_{NC}(\nu \text{ active}) \quad (2.18)$$

clearly indicating that the number of electron neutrinos was well below expectations. The combination of these two results gave the first clear indication of neutrino oscillations, a result which earned the SNO collaboration a Nobel Prize in 2015 [55].

2.2.2 Super-Kamiokande and Atmospheric Neutrinos

While the SNO experiment was working to identify the source of the solar neutrino deficit, the Kamioka Nucleon Decay Experiment (KamiokaNDE) and its successor, Super-Kamiokande (Super-K), were using a similar water Cherenkov detector to search for proton decay. The primary background for this rare process is neutrino interactions. Unlike SNO, however, Super-Kamiokande was sensitive to both MeV solar neutrinos and higher energy GeV neutrinos produced in the atmospheric showers from cosmic ray interactions.

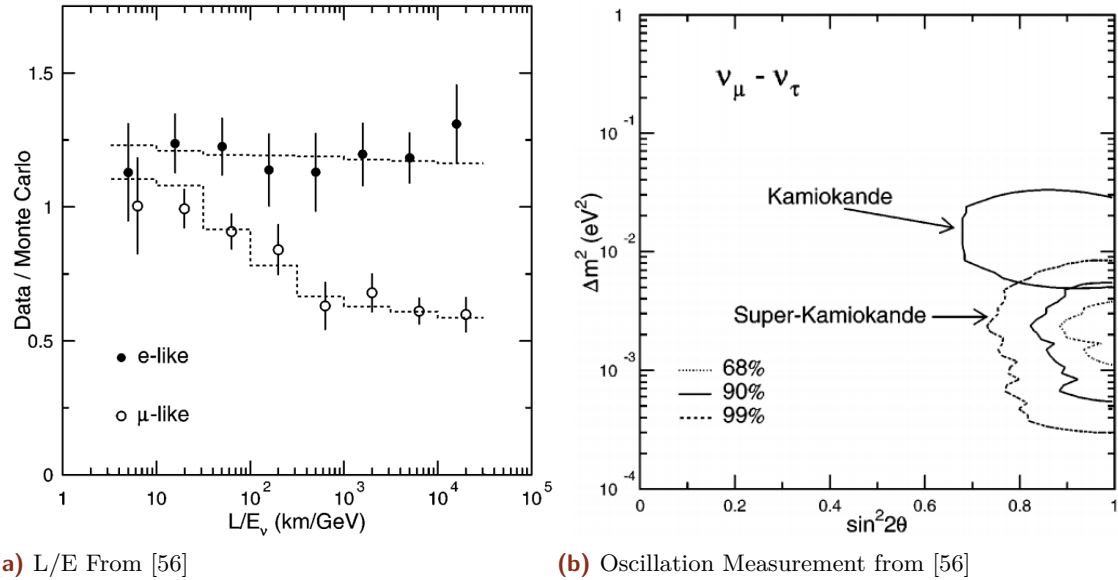


Figure 2.1 – The first atmospheric neutrino oscillation measurements from the Super-K experiment. (a) The ν_e -like events show no shape in L/E, as expected from a lack of neutrino oscillations. The ν_μ -like interactions, however, show a clear drop, indicating the presence of oscillation effects. (b) Using the two neutrino approximation, Super-K produced contours of the best-fit oscillation parameters for $\nu_\mu \rightarrow \nu_\tau$ oscillations. Both figures from [56]

lofsubfigure\newline(a)L/E From [56]lofsubfigure\newline(b)Oscillation Measurement from [56]

While investigating backgrounds, Super-Kamiokande observed an interesting deficit in the atmospheric neutrino signal. Unlike the case in the solar neutrinos, the deficit observed by Super-K was observed solely in the muon neutrino events with no effect seen in the electron neutrinos [56]. Using the reconstructed energy and direction of events, Super-K was able to show that the number of fully contained events of ν_μ -like interactions changed as a function of L/E - a clear signature of neutrino oscillations in the atmospheric neutrinos. The figure, reproduced in Figure 2.1a, was used, in part, with a 2x2 approximation to the PMNS matrix to produce the first measurements, shown in Figure 2.1b, of the atmospheric oscillation parameters. For the discovery of atmospheric neutrino oscillations at the same time as SNO's discovery of solar neutrino oscillations, the Super-K collaboration was jointly awarded the 2015 Nobel Prize [55].

Add a plot of the oscillation probabilities here

2.2.3 Global Fits to Oscillations

Since the initial discoveries of SNO and Super-K, many experiments have measured neutrino oscillations. Global fits are performed and updated regularly [57, 58].

The most recent results are shown in Figure 2.2 and include information from solar, reactor, and atmospheric oscillation experiments. The results explicitly assume unitarity and three neutrino species.

	NuFIT 3.2 (2018)			
	Normal Ordering (best fit)		Inverted Ordering ($\Delta\chi^2 = 4.14$)	Any Ordering
	bfp $\pm 1\sigma$	3σ range	bfp $\pm 1\sigma$	3σ range
$\sin^2 \theta_{12}$	$0.307^{+0.013}_{-0.012}$	$0.272 \rightarrow 0.346$	$0.307^{+0.013}_{-0.012}$	$0.272 \rightarrow 0.346$
$\theta_{12}/^\circ$	$33.62^{+0.78}_{-0.76}$	$31.42 \rightarrow 36.05$	$33.62^{+0.78}_{-0.76}$	$31.43 \rightarrow 36.06$
$\sin^2 \theta_{23}$	$0.538^{+0.033}_{-0.069}$	$0.418 \rightarrow 0.613$	$0.554^{+0.023}_{-0.033}$	$0.435 \rightarrow 0.616$
$\theta_{23}/^\circ$	$47.2^{+1.9}_{-3.9}$	$40.3 \rightarrow 51.5$	$48.1^{+1.4}_{-1.9}$	$41.3 \rightarrow 51.7$
$\sin^2 \theta_{13}$	$0.02206^{+0.00075}_{-0.00075}$	$0.01981 \rightarrow 0.02436$	$0.02227^{+0.00074}_{-0.00074}$	$0.02006 \rightarrow 0.02452$
$\theta_{13}/^\circ$	$8.54^{+0.15}_{-0.15}$	$8.09 \rightarrow 8.98$	$8.58^{+0.14}_{-0.14}$	$8.14 \rightarrow 9.01$
$\delta_{CP}/^\circ$	234^{+43}_{-31}	$144 \rightarrow 374$	278^{+26}_{-29}	$192 \rightarrow 354$
$\frac{\Delta m_{21}^2}{10^{-5} \text{ eV}^2}$	$7.40^{+0.21}_{-0.20}$	$6.80 \rightarrow 8.02$	$7.40^{+0.21}_{-0.20}$	$6.80 \rightarrow 8.02$
$\frac{\Delta m_{3\ell}^2}{10^{-3} \text{ eV}^2}$	$+2.494^{+0.033}_{-0.031}$	$+2.399 \rightarrow +2.593$	$-2.465^{+0.032}_{-0.031}$	$-2.562 \rightarrow -2.369$
				$\begin{bmatrix} +2.399 \rightarrow +2.593 \\ -2.536 \rightarrow -2.395 \end{bmatrix}$

Figure 2.2 – The global best-fit values for the three flavor neutrino oscillation fits as of November 2017. The first column shows results assuming the normal ordering while the second column shows the results for the inverted ordering. Image taken from [58]

2.3 Unitarity and Sterile Neutrinos

While global fits assume three flavors of neutrinos, additional neutrino flavors are theoretically possible. The number of active neutrino flavors is limited to the three known flavors from the measurements of ALEPH (see the discussion of Section 1), although such measurements implicitly only measure the number of species with a coupling to the Z boson [9]. Additional flavors with no or very small couplings to the Z boson may be allowed [59]. New neutrino flavors introduced with these properties are known as *sterile neutrinos*.

2.3.1 Sterile Neutrinos

Models of sterile neutrinos assume that no weak interactions are available to the new species, leaving only interactions with the world via oscillations. In this model, neutrinos oscillate using a 4x4 (or larger NxN) PMNS matrix [40, 60, 61, 59].

$$\begin{pmatrix} \nu_e(x) \\ \nu_\mu(x) \\ \nu_\tau(x) \\ \nu_s(x) \end{pmatrix} = U_{4 \times 4} \begin{pmatrix} \nu_e(x) \\ \nu_\mu(x) \\ \nu_\tau(x) \\ \nu_s(x) \end{pmatrix} = \begin{pmatrix} U_{e1} & U_{e2} & U_{e3} & U_{e4} \\ U_{\mu 1} & U_{\mu 2} & U_{\mu 3} & U_{\tau 4} \\ U_{\tau 1} & U_{\tau 2} & U_{\tau 3} & U_{\tau 4} \\ U_{s1} & U_{s2} & U_{s3} & U_{s4} \end{pmatrix} \begin{pmatrix} \nu_1(x) \\ \nu_2(x) \\ \nu_3(x) \\ \nu_4(x) \end{pmatrix} \quad (2.19)$$

The additional terms in U_{4x4} lead to new mixing angles, θ_{14} , θ_{24} , and θ_{34} . The new terms may be used in the standard oscillation framework introduced in Section 2.1.1 extended with a fourth flavor state, ν_s , and mass state, ν_4 .

$$P(\nu_\alpha \rightarrow \nu_\beta) = \sum_i^4 U_{\beta i}^* U_{\alpha i} \sum_j U_{\beta j} U_{\alpha j}^* e^{i(E_i - E_j)t} \quad \alpha, \beta = e, \mu\tau, s \quad (2.20)$$

Unlike the three active neutrinos, sterile neutrinos cannot interact with matter, leading to a deficit in the neutrino rates from oscillations of the form $P(\nu_\alpha \rightarrow \nu_s)$. The location and size of the deficit is determined by the oscillation parameters associated with the ν_s and ν_4 states. Sterile neutrinos may be indirectly observed through this deficit by studying the active neutrinos with either charged current or neutral current interactions.

2.3.2 Direct Searches for Steriles

While oscillation of the three active neutrinos preserves the total neutral current rate, sterile neutrinos do not. This provides a unique experimental signature for sterile neutrinos. Dedicated searches for this disappearance have been performed by MINOS [62, 63] and NO ν A [64] with assumptions on the new terms of the mixing matrix. The effect of three sterile hypotheses on the MINOS data is shown in Figure 2.3a. Around 15% of the neutral current events disappear in the three hypotheses tested by MINOS. The results of the NO ν A search are shown in Figure 2.3b.

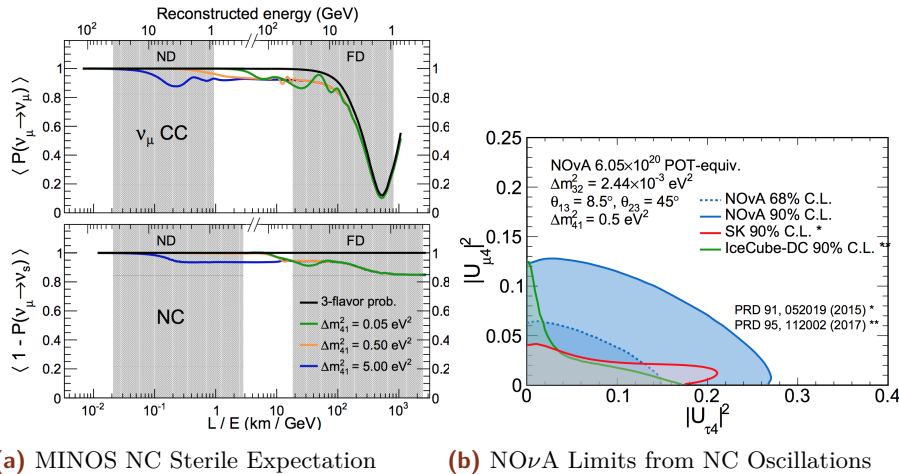


Figure 2.3 – Expectations (a) and results (b) of searches for sterile neutrinos in the neutral current interactions. (a) Effect of three hypothetical sterile neutrinos on the measurements of the MINOS detector [63]. "ND" and "FD" refer to the near and far detector of MINOS respectively. The sterile neutrinos have a small effect on the main oscillation minimum in the charged current channel, but up to 15% of the neutral current events are lost. (b) The results of the NO ν A search for sterile neutrinos using neutral current events. The limits are interpreted in terms of the 4x4 PMNS mixing elements in order to compare to searches with charged current interactions in Super-Kamiokande [65] and IceCube [66].

lofsubfigure\numberline(a)MINOS NC Sterile
Expectationlofsubfigure\numberline(b)NO ν A Limits from NC Oscillations

Most experiments attempt to investigate one of the additional terms only, assuming the remainder to be negligible [65, 66, 67]. The results rule out large mixing between a

hypothetical sterile neutrino and the three active flavors, although small mixing angles are still allowed by experiments [61, 59].

2.3.3 Indirect Searches for Steriles Using Unitarity

Experiments need not search for direct evidence of new mixing terms, however. The addition of a fourth generation of neutrino would have consequences for neutrino oscillation measurements performed in the 3x3 PMNS framework. Standard 3-flavor oscillation measurements may therefore be used to place limits on sterile neutrinos.

The PMNS matrix gives the change in basis and is assumed to be unitary. The unitary condition imposes summation rules for both the rows and columns of the matrix.

$$\sum_i U_{\alpha i} U_{\beta i}^* = \delta_{\alpha\beta} \quad \alpha, \beta = e, \mu, \tau \quad (2.21)$$

$$\sum_i U_{\alpha i} U_{\alpha j}^* = \delta_{ij} \quad i, j = 1, 2, 3 \quad (2.22)$$

If the neutrino mixing matrix consists of more than the three known active neutrinos, however, these unitary relations would only hold in higher dimensions. When projected down to the observed 3x3 PMNS matrix, non-unitarity would be observed.

Neutrino oscillation measurements are performed with the assumption of 3x3 unitarity imposed, allowing the PMNS matrix to be rewritten in terms of three mixing angles and a single phase. The appearance and disappearance probabilities in oscillation measurements are typically written in terms of these mixing angles. Using these mixing angles, the disappearance probability for atmospheric oscillations of $\nu_\mu \rightarrow \nu_\tau$ is given by

$$\begin{aligned} P(\nu_\mu \rightarrow \nu_\mu) &= 1 - \left| \sum_i U_{\mu i}^* U_{\mu i} e^{-im_i^2 L/2E} \right|^2 \\ &= 1 - \left(\cos^2 \theta_{13} \sin^2 2\theta_{23} + \sin^4 \theta_{23} \sin^2 2\theta_{13} \right) \sin^2 \left(\frac{\Delta m_{31}^2 L}{4E} \right) \quad (2.23) \\ &\approx 1 - \sin^2 2\theta_{23} \sin^2 \left(\frac{\Delta m_{31}^2 L}{4E} \right). \end{aligned}$$

where the final approximation has been made due to the small value of θ_{13} . The atmospheric appearance probability, $\nu_\mu \rightarrow \nu_\mu$, is given by

$$\begin{aligned} P(\nu_\mu \rightarrow \nu_\tau) &= \left| \sum_i U_{\mu i}^* U_{\tau i} e^{-im_i^2 L/2E} \right|^2 \\ &= \left(\cos^2 \theta_{13} \sin^2 2\theta_{23} \right) \sin^2 \left(\frac{\Delta m_{31}^2 L}{4E} \right) \quad (2.24) \\ &\approx \sin^2 2\theta_{23} \sin^2 \left(\frac{\Delta m_{31}^2 L}{4E} \right). \end{aligned}$$

The form of the oscillation probabilities for appearance and disappearance are very similar when written in terms of the mixing angles. However, the appearance and appearance probabilities in neutrino oscillation measurements depend on different elements of PMNS mixing matrix. Because of the difference in the elements probed, appearance and disappearance measurements may be interpreted to give limits on the fundamental elements of the mixing matrix without imposing unitary.

This method of searching for sterile neutrinos may be applied to global fits, reinterpreting standard oscillation measurements to place limits on the size of any non-unitarity. Using the unitarity conditions of Equation 2.21 and 2.22, limits on the size of non-unitarity have been calculated[68]. Experimental constraints from a number of experiments (see reference 26 of [68]) were used to evaluate the best-fit mixing matrix. The unitarity constraints were tested by looking at the potential deviation of each row or column

$$\Delta U_\alpha = 1 - \left(|U_{\alpha 1}|^2 + |U_{\alpha 2}|^2 + |U_{\alpha 3}|^2 \right) \quad \alpha = e, \mu, \tau \quad (2.25)$$

or

$$\Delta U_i = 1 - \left(|U_{\alpha i}|^2 + |U_{\beta i}|^2 + |U_{\delta i}|^2 \right) \quad i = 1, 2, 3 \quad (2.26)$$

The results are shown in 2.4. The constraints on unitarity of the 3x3 mixing matrix are strongest in the muon and electron sector, with constraints nearly an order of magnitude stronger than that observed in the tau sector. This is a result of limited measurements directly involving ν_τ oscillations.

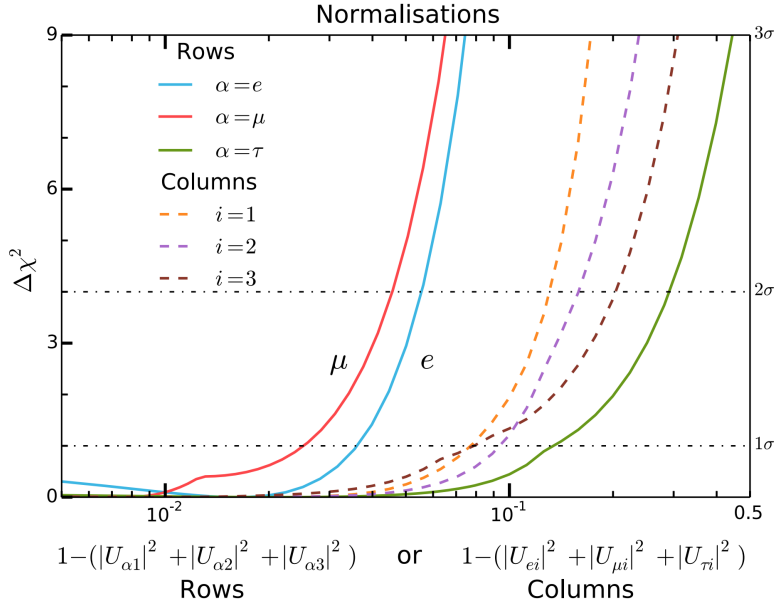


Figure 2.4 – The results of the tests using 2.25 (solid) and 2.26 (dotted). A smaller value on the x-axis indicates a tighter constraint on observed unitarity of the 3x3 mixing matrix. Tests involving only muon or electron flavors show significantly tighter constraints than those including the tau flavor. Image taken from [68]

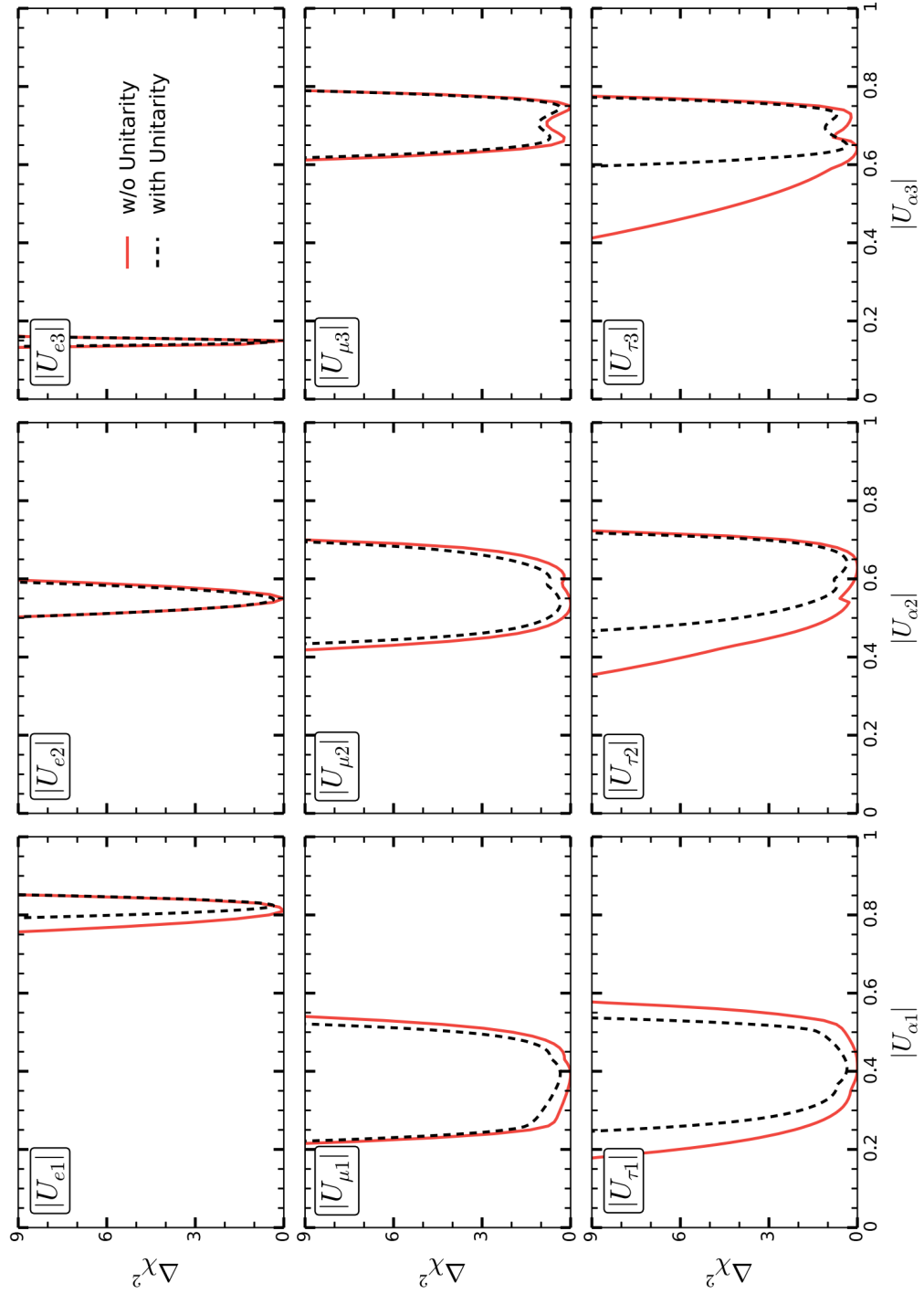


Figure 2.5 – The constraints from a global fit to neutrino oscillation data[68] with an assumption of unitarity (black dotted) or no assumption of unitarity (red solid). The first two rows show little change from the unitarity assumption, indicating strong constraints from direct measurements. The elements of the third row, related to the ν_τ , show much larger changes, indicating that constraints are obtained from indirect oscillation measurements.

When the individual limits for each element of the 3x3 PMNS matrix are checked, it is the tau sector that shows the largest uncertainties. Measurements of ν_τ oscillations therefore can provide valuable information on unitarity in the neutrino sector, leading to indirect constraints on sterile neutrino hypotheses.

The IceCube Detector

The low cross section of neutrinos is a challenge for experimentalists. There exist two avenues for the measurement of neutrinos. The precise measurements of individual events, used most notably in the OPERA [22] and DONUT [7] to identify individual events, gives unique constraining power with low backgrounds. More common, however, is the use of large experimental volumes to collect high-statistics neutrino samples. For the study of atmospheric neutrinos, volumes on the order of a kiloton are required.

The IceCube Neutrino Observatory is currently the largest neutrino detector in the world, encompassing a volume of 1 km^3 of glacial ice at the geographic south pole. The design of the IceCube detector is also presented in this chapter, beginning with a description of the DOMs that make up the primary detectors within the IceCube observatory (Section 3). The overall geometry of the detector is discussed in Section 3.1.6 with a focus on the differences between the larger IceCube detector and the DeepCore subarray used for oscillation searches.

3.1 The DOM: The Basic Unit of IceCube

3.1.1 The Photomultiplier Tube

The basic unit of the IceCube detector is the *digital optical module*, often referred to simply as the *DOM* [37]. The DOM is designed around a downward-facing 10 inch R7081-02 photomultiplier tube (*PMT*) from Hamamatsu Photonics [69, 70] and includes onboard electronics for standard operation as shown in Figure 3.1. Circuit boards are included for data acquisition, control, calibration, communications and power conversion as well as for high voltage input from the surface. The electronics of the DOM are encased in a spherical glass housing designed to withstand the high pressures associated with operation in the glacier of Antarctica. The PMT is optically coupled to the glass housing in order to minimize distortion of incoming light.

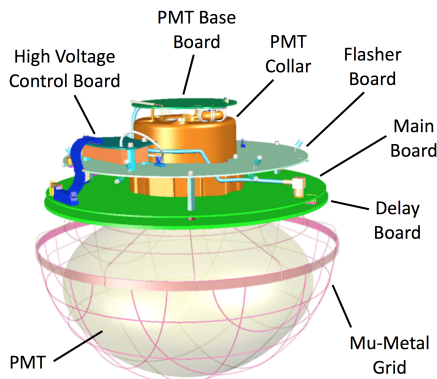


Figure 3.1 – The IceCube DOM contains multiple components, including the PMT itself as well as various electronics necessary for semi-autonomous operation.

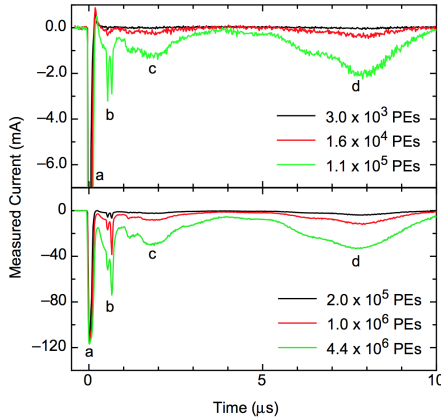


Figure 3.2 – Afterpulsing calibration measurements performed in the lab. LEDs with known brightness were flashed to test for offtime response of the IceCube PMT. Clear dips, corresponding to detected charge, are visible. Drop (a) corresponds to the initial LED flash while (b), (c), and (d) show prominent afterpulsing peaks. Image taken from [69].

Pre-, Late-, and Afterpulsing

Measurement with the IceCube photomultiplier tubes introduces known effects in the recorded charge. These effects are divided into *pre-pulses*, *late-pulses*, and *afterpulses*. The pre-pulses, arriving within a few dozens of nanoseconds prior to the main signal, are thought to arise from the small probability of an electron bypassing one of the dynodes. Late-pulses are likewise thought to be produced by electrons which return to a previous dynode, inducing a signal a few dozens of nanoseconds immediately following the main signal. These signals tend to be small and inconsequential for physics measurements. After-pulses, which arise from ionization of residual gases in the PMT, are a more significant concern for calibration work as addressed in Section 5.1. The ionized atoms tend to travel significantly more slowly than electrons, resulting in a delay between the main signal and the subsequent afterpulses that may be as large as 10 microseconds.

3.1.2 The Discriminator Used for DOM Triggering

A discriminator onboard the DOM is used to identify signals from the PMT with a voltage threshold corresponding to 0.25 photoelectrons (*PE*). Each discriminator crossing begins a *DOM launch*, the lowest level signal available in the IceCube detector containing a representation of the raw PMT output in the form of a *waveform*. Launches are stored in DOM memory while awaiting a decision from the triggering system.

3.1.3 Local Coincidence

If any of the notified DOMs also record a launch within a configurable 1 microsecond window, both launches are said to form a *hard local coincidence (HLC)* pair. Nearby DOMs, here defined to be either of the two DOMs above or below the current DOM, are notified of the launch via a signal sent using the *local coincidence* wiring. Launches which fail to satisfy the local coincidence conditions are referred to as *soft local coincidence (SLC)* hits. Launches recorded as part of an HLC pair receive a flag. This flag may be used to later identify only those launches which satisfy the local coincident conditions, providing a simple, default method of identifying hits likely to be caused by particle interactions in the detector.

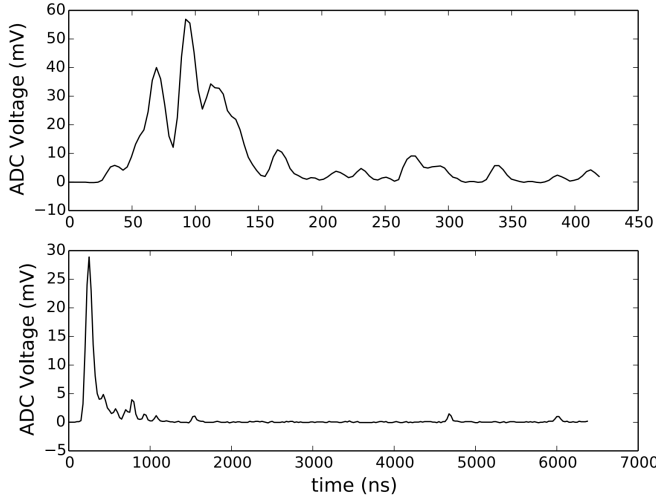


Figure 3.3 – Examples of the ATWD (top) and FADC (bottom) waveforms output from an IceCube PMT. Taken from [37]

3.1.4 Digitization

While awaiting a local coincidence decision, the waveform of a launching DOM is passed to the two onboard digitizers. Information from the PMT is digitized using the fast analog-to-digital converter (*fADC*), which provides binned information at 40×10^6 samples/second for the 6.4 microseconds following the initial DOM launch [37]. Simultaneously, the *Analog to Digital Waveform Digitizer*, or *ATWD*, will digitize the waveform using 322 bins with 3.3 nanoseconds per bin.

If a launch satisfies the HLC conditions, the DOM will request the full digitization of the waveforms from both the ATWD and FADC, providing a complete record of the launch. Examples of digitized waveforms from the ATWD and fADC are shown in Figure 3.3.

When digitizing a signal, the ATWD experiences up to 29 microseconds of deadtime [37]. During this time, the secondary ATWD is available to record further pulses, resulting in a total average fractional deadtime per DOM of 2.2×10^{-5} seconds/second. In addition, each of the two ATWDs possesses three channels with separate gains. This provides the ability to accurately measure the waveform, even in cases of saturation. The unsaturated ATWD with the highest gain provides a record for the launch.

If the launch is instead given the SLC label, the information in the ATWD is lost and the FADC instead digitizes only the three bins associated with the largest peak of the waveform. While this limits the information available for these launches, the lack of associated nearby launching DOMs provides strong evidence that the launch is due to random detector noise.

3.1.5 Noise in IceCube DOMS

Dedicated measurements using IceCube DOMs have shown multiple components to the detector noise[71]. A large fraction of the detector noise displays non-Poissonian behavior in time [37]. The model used in IceCube, shown in Figure 3.4, splits the detector noise into *Poissonian* and *non-Poissonian(time-correlated)* noise.

The Poissonian noise consists of thermal noise and radioactive decays in the glass of the PMT and DOM. Studies of these radioactive components are ongoing, with some evidence that Potassium-40 and Uranium-238 may be responsible for at least some of the observed decays. Once a decay occurs, a rapid series of pulses occurs in the PMT,

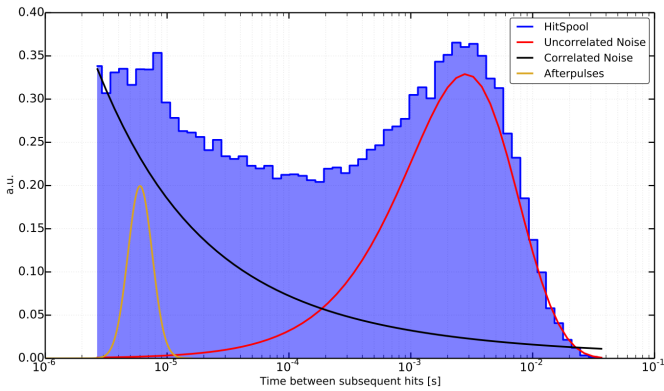


Figure 3.4 – A histogram of the time between subsequent hits on DOM 15 of string 27. HitSpool data, specialized data collected with no trigger applied, is shown in blue. The "correlated" (non-Poissonian) and "uncorrelated" (Poissonian) features are shown in red and black respectively. The location of a large afterpulsing peak is shown in yellow. Note that the features included are not to scale. Image taken from [37].

leading to a "burst" of noise that continues for up to a few milliseconds [71]. These hits are believed to be due to a scintillation or luminescence process.

The typical averaged noise rate is 560 Hz for standard IceCube DOMs and 780 Hz for high quantum efficiency DOMs. Poissonian noise makes up approximately 250 Hz of this rate with the remainder due to non-Poissonian processes.

3.1.6 Triggering in IceCube

Digitized versions of the waveforms are transmitted from the DOM to the IceCube physics data acquisition system (*pDAQ*) for use in trigger and event building. The most common type of trigger used in IceCube analyses is the *Simple Majority Trigger* or *SMT*. This trigger is designed to look for coincidences between DOMs using HLC launches. Each of the SMTs is defined by three fundamental configurations: a DOMSet, which lists the DOMs available for use in the trigger conditions; a threshold number of HLC launches before the trigger fires; and a time window length in which the HLC are required to coexist.

Once all triggers are identified, a *global trigger* is defined. This consists of the superset of all triggers occurring within 10 microseconds of one another. All detector readout enclosed within the global trigger as well as additional information within an additional 10 microseconds both before and after the trigger is combined into a single *event*.

3.2 The Geometry of the Detector

The IceCube detector is located at the geographic south pole in Antarctica. The Antarctic glacier forms a 3 km deep surface of clear ice over the bedrock. IceCube uses the Antarctic glacier as both a support structure and as a detection medium for Cherenkov radiation. The IceCube observatory consists of three distinct subarrays, shown in Figure 3.6, each optimized for separate physics measurements. A total of 5160 DOMs make up the IceCube in-ice array with an additional 324 DOMs used at the surface in the IceTop air shower array [37]. IceCube DOMs are deployed at depths between 1450 m and 2450 m below the surface to shield the detector from atmospheric background muons. The DOMs are deployed in a hexagonal grid in a series of 86 *strings*, each of which provides connections and support for 60 DOMs. Strings are spaced approximately 125 m apart

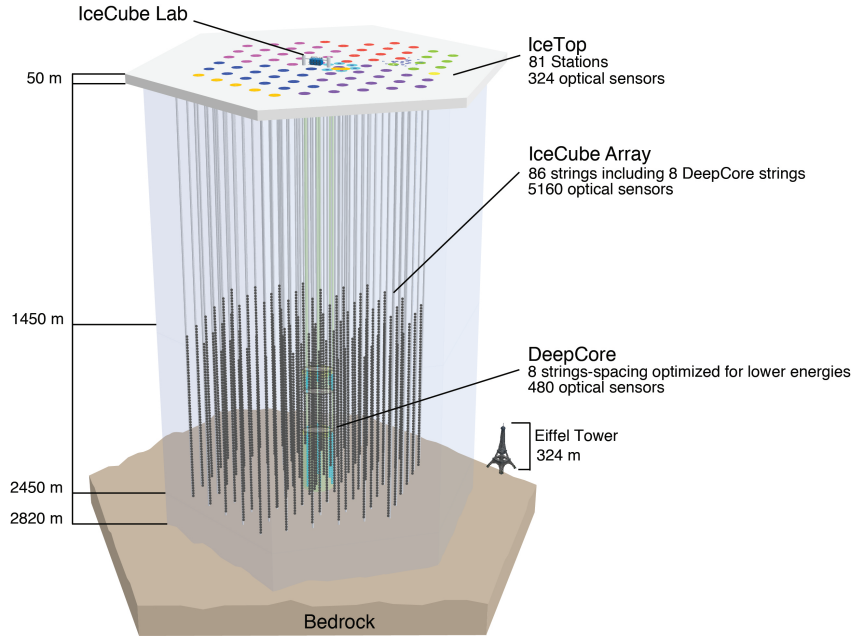


Figure 3.5 – The IceCube Neutrino Observatory. Three separate subdetectors are shown: IceTop, a cosmic ray air shower detector; IceCube, an array designed to search for astrophysical neutrinos; and DeepCore, a dense subarray optimized for atmospheric oscillation physics measurements. The detector was deployed over multiple years. Strings deployed in the same year are shown with identical colors at the surface.

with DOMs space 17 m apart on each string. Each DOM in the IceCube detector is assigned a unique string number (1-86) and DOM number (1-60).

Additional strings were installed in the glacier annually from 2004 until 2010 with partial detector data collected during construction. During the final years of construction, a denser section of the detector was built, known as DeepCore [72]. The DeepCore subarray consists of 8 strings equipped with high quantum efficiency PMTs 35% more sensitive than the standard IceCube DOM [69]. The DeepCore strings are split between a *fiducial* volume, in which 50 DOMs are spaced 7 m apart on a string, and a *veto plug* of 10 DOMs 10 m apart as shown in Figure 3.6. The DOMs in the DeepCore fiducial volume are located in the clearest ice of the detector at depths between 2100 m and 2450 m below the surface [73]. The veto cap, installed between 1750 and 1850 m below the surface, is used to identify background muons for DeepCore.

3.2.1 IceCube: A Detector for TeV Neutrinos

The IceCube detector is a regularly spaced hexagonal grid buried in the glacier with the proposed purpose of measuring astrophysical neutrino candidate events and identify the source of cosmic rays. The IceCube array has an energy threshold of around 50-100 GeV with an optimal response above 1 TeV[72, 37].

In the standard IceCube detector, an SMT using all DOMs with a threshold of 8 HLC launches within 5 microseconds is typically used [37]. This trigger, known as *SMT8* after the number of required hits, is designed for high signal efficiency at energies above 100 GeV with a minimum number of accidental triggers due to random detector noise. The IceCube detector records an SMT8 rate of around 2100 Hz with less than 1 Hz expected from neutrino interactions.

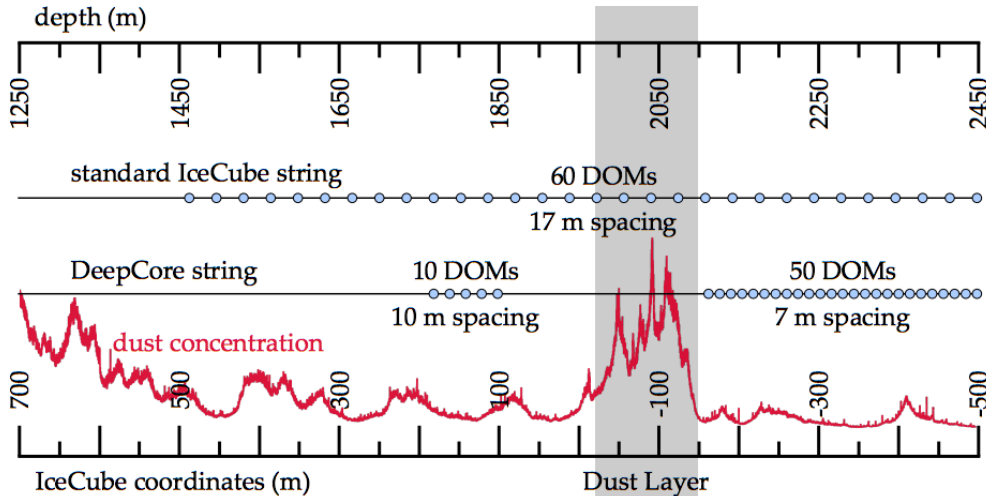


Figure 3.6 – A comparison of the standard IceCube string (right) to the DeepCore string (left). The IceCube string uses DOMs spaced 17 m apart while DeepCore divides the DOMs into a fiducial (bottom) and veto plug (top). The dust concentration is shown in red. The concentration of dust in the ice affects the scattering and absorption of the glacial ice.

Events at the TeV scales of the IceCube detector show well-defined topologies, as shown in Figure 3.7. The IceCube detector has performed many measurements, including searches for sterile neutrinos [67], anisotropy in the cosmic ray flux [74], measurements of the neutrino cross section at high energies [75], and the first discoveries of an astrophysical neutrino flux [76].

3.2.2 DeepCore: Extending the Reach to GeV Scales

The DeepCore detector was designed to be a smaller, denser detector optimized for the measurement of atmospheric neutrino oscillations. The denser spacing and clear ice of DeepCore lower the energy threshold to around 10 GeV [72], permitting the study of oscillations. DeepCore was installed at the bottom of the IceCube array near the center of the IceCube hexagonal grid, shown in Figure 3.8.

In DeepCore, the desire for lower energy events led to the introduction of a separate trigger, known as *SMT3*. This trigger, using only DOMs within the DeepCore fiducial volume, searches for at least three HLC launches occurring within 2.5 microseconds. This effectively lowers the triggering threshold from roughly 100 GeV with the larger IceCube array to approximately 10 GeV. The SMT3 rate, at 250 Hz [37, 72], is substantially smaller than the SMT8 rate due to both the increased overburden as well as the smaller number of PMTs included in the SMT3 DOMSet. By placing the detector inside of the larger IceCube array, DeepCore allows analyzers to use the IceCube detector as an active veto, reducing the background rate to 17 Hz.

DeepCore events do not show the clean topological separation of the higher energy IceCube events as seen in Figure 3.7. Events may be separated broadly into *cascade-like* and *track-like* statistically using information contained in the timing of hits in the detector. Such separation techniques are energy-dependent and do not perform well at very low energies.

DeepCore has observed atmospheric neutrino oscillations in the $\nu_\mu \rightarrow \nu_\tau$ in the disappearance channel [79, 80, 81], with the most recent measurement showing competitive precision to dedicated measurements performed with particle accelerators.

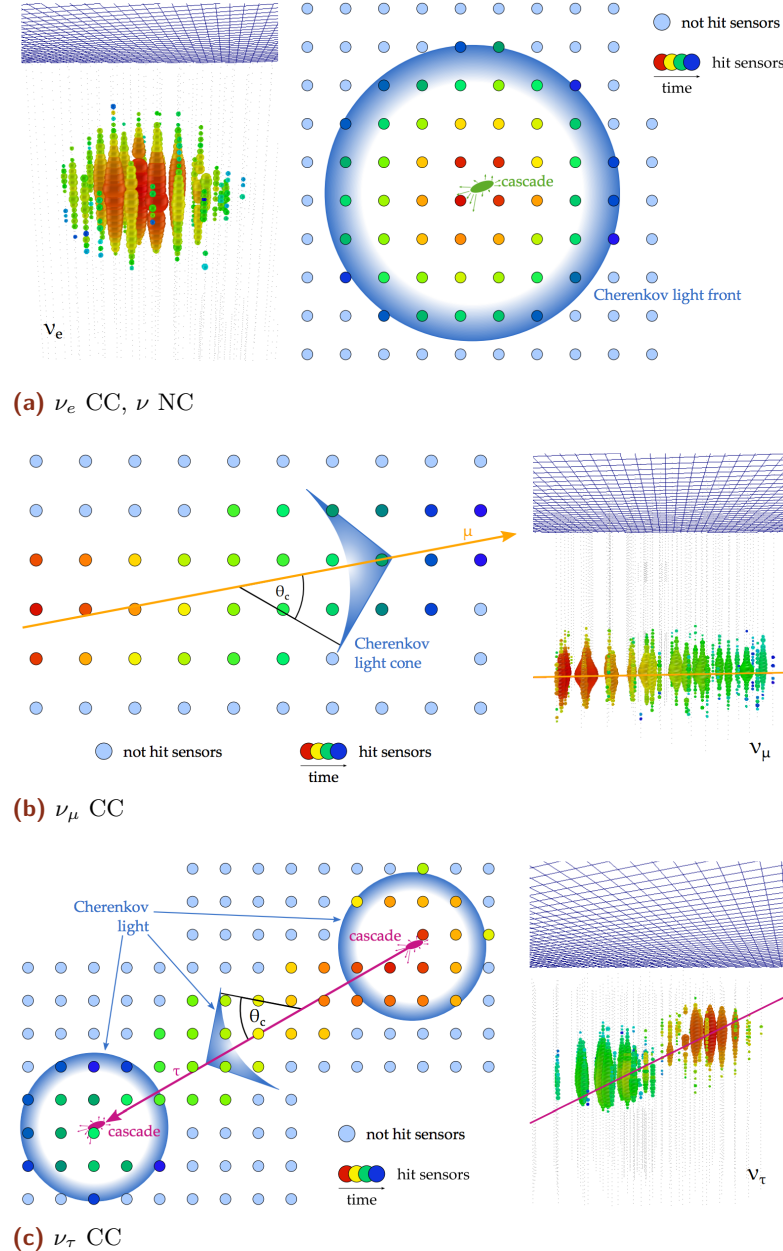


Figure 3.7 – Examples of event topologies above 1 TeV using the full IceCube array. Event views shown in (a) and (b) are from actual events discovered by the IceCube detector [77]. Images taken from [78]. (a) ν_e CC and ν NC show similar behavior from electromagnetic and hadronic interactions, which result in a shower of particles that quickly scatter in the ice. Cherenkov emission from these events appears roughly spherical in the detector. These events are known as "cascades". (b) ν_μ CC events begin with a hadronic interaction, then produce Cherenkov light from the outgoing muon. Above 1 TeV, the track of the outgoing muon becomes clearly visible. (c) Above 10 TeV, the tau lepton from a ν_τ CC may travel a significant distance before decaying. This results in two well-separated cascades in the detector, a tell-tale signature of ν_τ CC interactions.

lofsubfigure\newline(a)\newline(a) ν_e CC, ν NC\nlofsubfigure\newline(b)\newline(b) ν_μ \newline CC\nlofsubfigure\newline(c)\newline(c) ν_τ CC

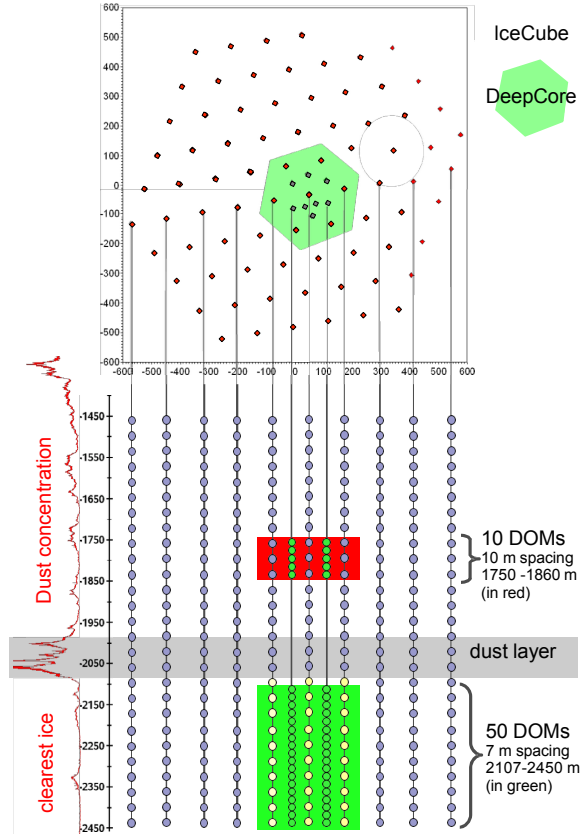


Figure 3.8 – The layout of the DeepCore detector. DeepCore is installed at the bottom of the IceCube detector in the clearest ice. A subset of DOMs were also deployed above DeepCore to improve muon identification of very-downgoing events.

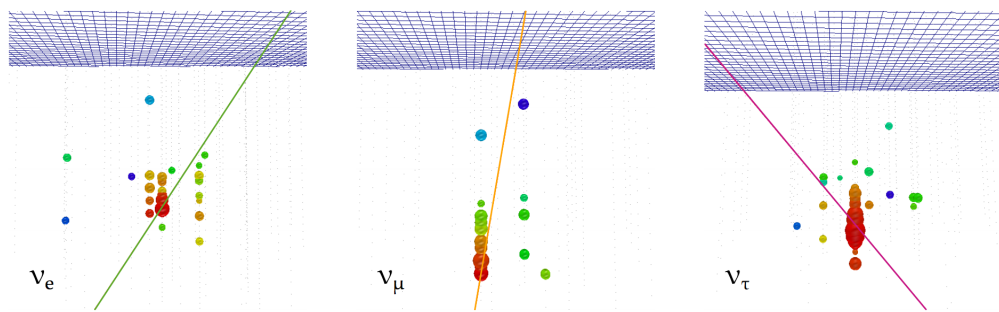


Figure 3.9 – A selection of 50 GeV simulated events in DeepCore taken from [78]. Unlike the event topologies at high energies, DeepCore events do not show distinct event types.

While DeepCore was designed for oscillation physics, the neutrinos may be used for other purposes as well. Recent work with DeepCore has shown sensitivity to studying dark matter interactions in the sun [82] and in the galaxy [83].

3.3 The Bulk Ice Model

The Antarctic glacier, with a thickness of 2.8 km at the geographic south pole [73], forms both the support structure and the interaction medium for IceCube. During deployment, measurements of the scattering properties of the ice were taken during deployment of the IceCube strings. The IceCube dust logger emitted laser light aimed into the undrilled ice and detected backscattered photons[84, 85]. The results are shown in Figure 3.10

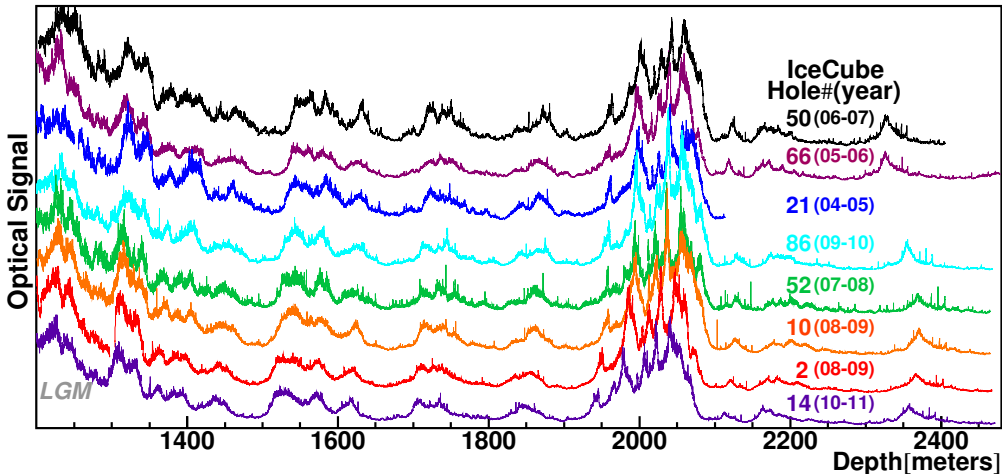


Figure 3.10 – The data from the dust loggers deployed in various drill holes in IceCube during deployment. Data from individual holes has been offset in the y direction for clarity. Larger relative values of the "Optical Signal" represent more scattering in the ice while smaller values indicate clearer ice. The "dust layer" is visible in all drill holes around 2000 m. Deepcore DOMs are deployed below this layer. Image taken from [86].

Peaks are present in the dust logger data due to volcanic events in the Earth's past [84]. The most significant peak, a set of features around a depth of 2000 m, form what is known as the *dust layer* of IceCube, a region with significantly higher scattering and absorption properties than the surrounding ice.

To improve the modeling of the glacier, dedicated measurements have been performed using light-emitting diodes (LEDs, also known as *flashers* in IceCube) onboard the DOMs [73, 37]. In specialized calibration runs, the LEDs are flashed at a few Hertz for a few minutes while nearby DOMs receive the emitted light. Monte Carlo simulations of the flashers are used with varying ice properties in order to identify the most likely properties of the ice. Each flashing and detecting DOM pair provides a set of known times, positions, and light output in the ice, allowing for the properties of the intervening medium to be determined.

The modern ice model used for this thesis consists of three main properties: the absorption, the scattering, and the anisotropy of the ice [87]. The measured properties of the absorption and scattering may be seen in Figure 3.11 while the effect of the anisotropy can be seen in Figure 3.12. Scattering photons change direction, losing information about the direction of the emission source. Absorbed photons are not visible to the detector, potentially modifying the observed number of photons and the reconstructed energy

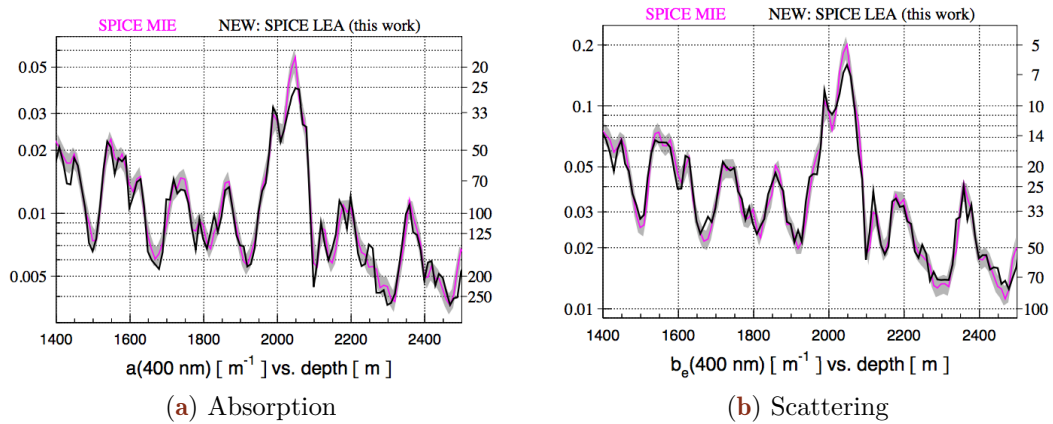


Figure 3.11 – The absorption and effective scattering properties of the ice as fit to flasher data. Two models are shown representing different generations of ice models used for simulation. The "Mie" model does not include anisotropy while the "Lea" model does. Figure from [87].

of an event. The anisotropy, consisting of a direction and magnitude, modifies the ice properties as a function of direction due to movement and compression of the glacier over time. The anisotropy affects both the scattering and absorption from each direction in the x-y plane and can affect the azimuthal directions of reconstructions in IceCube.

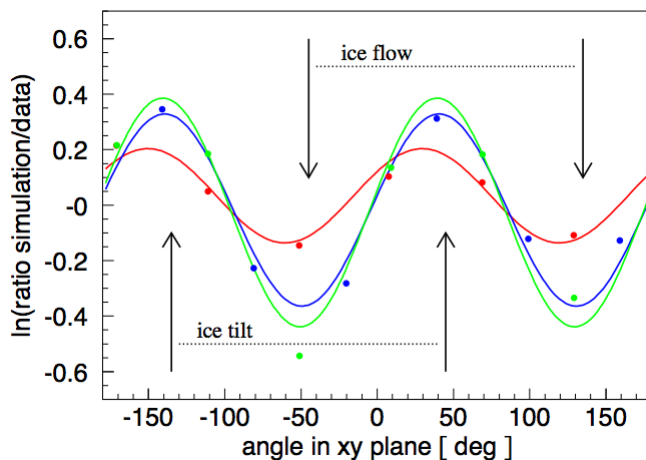


Figure 3.12 – The effect of the anisotropy on the light output from a flasher on string 63. Measurements (points) are shown for receiving DOMs at three distances: at 125 m (red), at 217 m (blue), and at 250 m (green). A line is included to show the expected effect of anisotropy at each distance. The y-axis shows the ratio of a simulation of the same flasher without including anisotropy to data. A modulation is observed as a function of direction in the x-y plane.

3.4 The Hole Ice

After the strings were deployed, each drill hole was allowed to refreeze. The refrozen column of ice around each string is referred to as the *hole ice*. Using a dedicated camera deployed at the bottom of string 80, the refreezing process of the hole ice has been observed over the course of several years [88, 37]. Images obtained from the camera show the refrozen ice divided into three distinct regions.

find good quality
swedish camera pics?

The outermost region, the *bulk ice*, is the original glacial ice and is unaffected by the deployment of the detector. The outer part of the drill hole shows improved clarity compared to the bulk ice. The central region of the drill hole, a central core of about 16 cm in diameter, shows significantly worse scattering properties than the bulk ice [37]. This central column, referred to as the *bubble column*, affects the photon acceptance of the PMT. Measurements to characterize the hole ice are ongoing.

Simulation of the IceCube-DeepCore Detector

In order to model both signal and background, *Monte Carlo simulations* of the detector are necessary. In the search for tau neutrinos, this is particularly important due to the low rates and high backgrounds expected, requiring multiple types of simulation for both signal and background.

Simulation in IceCube is broken into three broad stages, each of which will be discussed in turn. The generators used in the appearance analysis are discussed in Section 4. The propagation of the charged leptons and photons are then described in Section 4.2. Section 4.2.3 describes the simulation of the detector, including the PMT electronics and the detector noise.

4.1 Monte Carlo Generators

4.1.1 Background Generation

CORSIKA

The primary background for the observation of atmospheric neutrino events is the other particles present in the cosmic ray interactions in the atmosphere. These interactions produce many particles, most of which are stopped before reaching IceCube by the shielding provided by the Antarctic Glacier. In order to correctly account for the interactions and decays of these particles, the *CORSIKA* generator from Karlsruhe Institute of Technology is used[89]. The CORSIKA generator is a collection of code designed to simulate, interact, and propagate a cosmic ray air shower from the interaction point in the upper atmosphere to the surface. Originally designed for use with surface detectors such as Auger, HAWC, and IceTop, the code has been adapted for use in the IceCube collaboration by identifying the muon (and, sometimes, neutrino) components of the air shower.

CORSIKA has many modes of operation and options for configuration. The standard IceCube simulation of air showers uses the SIBYLL 2.1 hadronization mode [90] to follow the interactions through the shower.

IceCube simulation of air showers uses two possible modes of CORSIKA. The "Polygonato" mode, which generates cosmic rays following the model from [91]. The Polygonato flux parametrized the energy spectra of individual elements of the cosmic ray flux as power laws extrapolated to high energies. In typical IceCube simulation, CORSIKA simulation produced using the Polygonato model includes a mixture of muons from all seasons, effectively producing an averaged flux useful under the assumption of equal livetime throughout the year. The elemental ratios of the generated events follow the Polygonato flux directly, producing a "natural" flux of simulated events [89]. The natural spectrum of the Polygonato CORSIKA simulation has the benefit of allowing a direct physical interpretation of the resulting spectrum without the need for reweighting and simplifies the production of coincident showers, which require a natural spectrum.

The second model, the five-component mode, reduces the full spectrum of cosmic rays to five effective families: hydrogen, helium, nickel, aluminum, and iron. Each of these components is allowed to have different spectral properties. The five-component mode is

useful due to the ease with which the user can modify and reweight to different primary spectra, allowing the investigation of different cosmic ray compositions without the production of dedicated simulation. The simplicity associated with the reweighting of five-component simulation allows IceCube to produce unphysical spectra in order to optimize the production of simulated events necessary for the various analyses. The five-component simulation may be reweighted to match cosmic ray models, including both the Polygonato model and the newer H3a model, which models the cosmic ray flux using three distinct populations of sources [92]. While this slightly complicates the use of the simulation in analyses, the ability to test with various spectra has been an invaluable tool for high energy analyses, which can be sensitive to changes in the cosmic ray spectrum above the knee. Five-component CORSIKA simulation, due to the unphysical generation spectrum, cannot easily be used in the production of simulation involving timing coincidences between events and are currently supplemented by the Polygonato CORSIKA for this purpose.

In both cases, the particles from the air shower are only propagated to the surface of the ice. For analyses using the in-ice array, we take the muons reaching the surface from a CORSIKA simulation and propagate them through the ice, simulating the continuous and stochastic energy losses along the way. The muons are propagated to a surface in the ice consisting of a cylinder with radius 800 meters and length 1600 m centered on the IceCube detector. In order to reach the detector, a muon must result from a cosmic ray interaction of approximately 600 GeV due to the shielding of the glacier. Because of this, CORSIKA simulations typically have a lower energy cutoff of about this value to avoid simulating events that will not reach the detector.

In principle, neutrinos may also be produced using the CORSIKA generator. In practice, this tends to be extremely inefficient for most searches that are no explicitly looking for muons and neutrinos from the same air showers given the extremely low cross section of the neutrino relative to the muon. For this reason, the background generation with CORSIKA in IceCube typically refers to muon events only, with no accompanying neutrino.

MuonGun

CORSIKA simulations are computationally costly and offer few ways to directly control the spectrum of events at the detector. The characteristics of muons produced in an air shower are not known *a priori*. Targeted simulations in which particular muon samples are required cannot easily be generated with CORSIKA. In situations where the required muon simulation falls within a relatively narrow phase space, whether that be in energy, angle, or position inside of the detector, it can be beneficial to tailor simulation to the needs of specific analyses. Alternatively, there are situations in which the details of the cosmic ray interactions are an unnecessary complication to the final level IceCube analyses. In these situations, IceCube has developed a tool to bypass the full air shower simulation provided by CORSIKA, producing muons directly at a cylindrical surface inside the ice [93]. This tool, known as *MuonGun*, has the benefit of removing the computationally costly simulation of the full air shower, giving the user more control over the resulting simulated events at the cost of information about the initial cosmic ray interactions. This allows targeted, high statistics background simulation samples to be produced for analyses.

These features of MuonGun give the generator significant flexibility, allowing for a very focused simulation of muons that would not otherwise be possible with the current

implementation of the CORSIKA generator. The downside, as with all targeted generation, is of course that one must be aware of the limitations. For example, the settings described above will provide a good description of muons reaching and triggering the DeepCore array, but will not include the correct contributions of muons in the outer IceCube detector. This can result in disagreement between data and simulation if the limitations are not acknowledged and accounted for.

This abstraction disassociates the muon at the detector from the air shower, and therefore the cosmic ray, that produced it. In order to properly account for the dependence on the cosmic ray spectrum in the muon weights, dedicated simulations must be produced using the full CORSIKA generator. By following the interaction, showering, and propagation to the detector, IceCube is able to produce an effective parametrization of the association between a particular cosmic ray spectrum and the muons reaching the detector. This must only be done once, but requires a substantial number of simulated events in order to produce a clean parametrization in position, energy, zenith angle, and variables associated with shower multiplicities higher than one. The version of MuonGun at the time of writing provides the parametrizations for the Polygonato [91] and H4a [92] cosmic ray spectra. At the time of production for the analyses contained hereafter, all MuonGun simulation is produced assuming a multiplicity of 1, meaning that no bundles are yet produced with this generator. This is a limitation of simulation time: the multiplicity parametrizations vastly extend the parameter space and therefore require significantly more time and effort to handle correctly.

Noise-Only Events

While we only observe neutrinos and muons in the detector, we also observe a significant component of accidental triggers in the DeepCore array. These events, labeled *accidental triggers*, arise due to the low trigger threshold. In these events, no actual particle interactions due to muons or neutrinos are observed. Instead, detector noise alone satisfies the trigger conditions, producing an event.

Simulation of accidental triggers involves only the noise and electronics simulation. Because the events are relatively rare, the simulation requires a special mode, here called *long-frame* simulation, which produces continuous detector readout. Breaking the traditional concept of the "simulated event", these simulation sets instead produce a 100 ms long "event" of random detector noise. These hits are then run through the simulation of waveforms, coincidences, and triggering as a normal simulated event. After triggering, specialized code is used to divide the long-frame simulation into smaller events similar to neutrino and muon simulations as well as actual experimental readout.

Once the events are generated, weighting the events is relatively straightforward: the weight per event depends on the muon interaction rate and the total simulated time. The latter is straightforward to calculate, depending only on the number of long frame simulation events produced and the time window for each of these events. The former is important due to the definition of the accidental triggers. These events, by definition, may only occur when no muon or neutrino is interacting within the detector. The weight of the accidental triggers must account for this "deadtime" due to particle interactions. This rate, assumed to be approximately 2800 Hz, leads to a change in the effective livetime per event of roughly 15

Accidental triggers are computationally expensive to produce, given that they rely on a relatively rare property of random detector noise. In general, a few minutes of effective livetime can take up to two hours to create, with much of the processing time spent on

DOMs and hits that do not make it into final triggered events. This limits the total effective livetime that can be simulated in realistic timescales. Current simulations used in this thesis total approximately two months of effective livetime.

4.1.2 Signal Generation

GENIE

Background simulation is only part of the generation in IceCube. Studies searching for neutrino candidate events require simulated signal events to infer properties of the original events. At energies ranging from approximately 1 GeV to 1 TeV, IceCube has adopted the *GENIE* event generator [94]. This code, used widely throughout the oscillation community, includes information about the various interactions, cross sections, and uncertainties involved in neutrino physics from reactor energies upward.

Events in the GENIE generator are produced first by selecting events from a pure power law with a given spectral index, often chosen to be either E^{-1} or E^{-2} depending on the purpose. These events are then forced to interact with an electron or nucleon within a specified volume with a target with a density of ice assumed.

The type of interaction is determined using the cross section for the given flavor and energy. The cross section model, an updated version of GRV98 [95], includes resonant, elastic, quasielastic, and deep inelastic events. Particles produced in the interaction are propagated out of the nucleus, with final state interactions included. Hadrons with energies less than 30 GeV produced in GENIE simulation are propagated individually to obtain the light output using GEANT4 [96, 97]. Above 30 GeV, the lower event-to-event variability permits the use of parametrized light output for hadrons.

The GENIE code includes tools to reweight events based on uncertainties in eg. the axial masses, cross sections, and various aspects of the interactions themselves [94]. These features are used to model uncertainties in the tau neutrino analysis presented in this thesis.

The code is regularly updated, including both new features and retuning of parametrizations to match the latest data. The events produced in this work use GENIE version 2.8.6.

Neutrino-Generator

At energies higher than approximately 100 GeV, there are two changes to the simulation code. At these energies, the contribution to the cross section from deep inelastic interactions becomes dominant while the other interactions become negligible, as expected from Figure 1.7 [20]. This allows the simplification of the cross section calculations with no loss in generality. In addition, the cross section continues to rise linearly with the energy. This latter feature requires a detailed simulation of potential interactions far from the detector: namely, high energy neutrinos have a non-negligible chance of interacting while propagating through the Earth.

The *Neutrino-Generator* code (hereafter, *NuGen*) is designed to handle these higher energy interactions [98]. In this model, neutrinos are no longer produced and forced to interact in the ice directly. Instead, a neutrino is produced from a power law spectrum in the atmosphere surrounding the Earth. The event is then propagated through the planet, using the PREM model of the density layers in the Earth [47] to simulate potential interactions en route. Neutrinos which interact may be lost or may be regenerated following the decay of the daughter particles. Neutrinos arriving at the detector are then forced to interact in the detector fiducial volume, yielding a simulated event. Hadronic

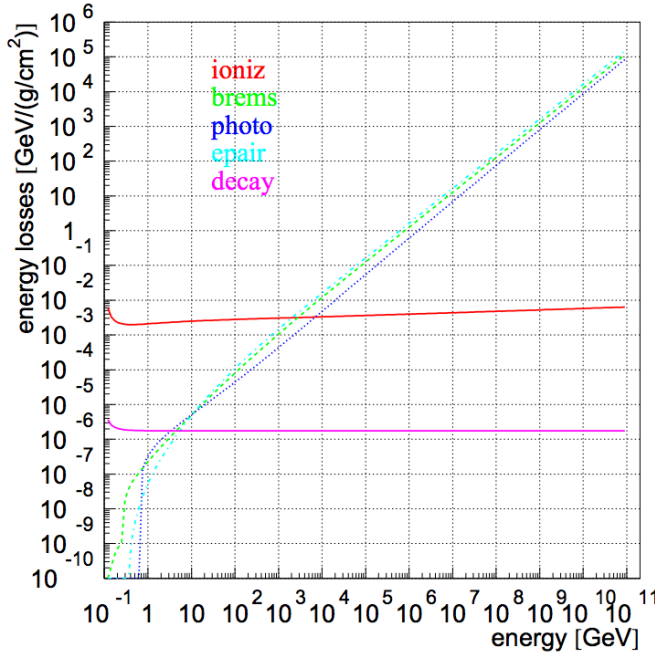


Figure 4.1 – Average energy losses ($\frac{-dE}{dx}$) for a muon in ice. At very low energies, ionization losses dominate. Above approximately 1 TeV, pair production and photonuclear effects become more important. Image taken from [21]

output is returned in the form of parametrized light output due to the large number of particles.

NuGen can be configured with various Earth models as well as different generation properties. For the studies contained herein, the NuGen files are produced with an E^{-2} spectrum and interact following the CSMS cross section.

4.2 Propagation of the Particles and Light

After generation, IceCube simulated events require two types of *propagation*. The first, the propagation of charged leptons, produces the energy losses in the detector due to continuous and stochastic emissions. These energy losses are then used to produce photons that may be propagated through the detector using models of the Antarctic glacier.

4.2.1 Lepton Propagation with PROPOSAL

The propagation of leptons in IceCube is performed using *PROPOSAL*, a software module which contains tools to simulate the propagation of leptons and hadrons with ionization, electron pair-production, bremsstrahlung, photonuclear interactions, and decay processes [99]. The Cherenkov light output from daughter particles in each case is handled by a parametrization of the associated energy deposition for a given true particle energy as shown in Figure 4.1.

PROPOSAL propagates the charged particles through the detector, producing a series of energy emissions associated with each propagated particle. The module takes into account the position of the particle and uses separate cross sections for glacial ice and the underlying bedrock 300 m below IceCube.

4.2.2 CLSim for Photon Propagation

Once the energy deposition at each position is calculated, the resulting photons must be produced and propagated. There exist two modules which can handle this: Photon Propagation Code *PPC* and OpenCL Simulation Code *CLSim*. The differences are largely of implementation details and both have been verified to give identical results. Only the latter, *CLSim*, will be discussed here.

CLSim is a code designed to propagate emitted photons using ray tracing algorithms [100]. The independence of the individual photons is leveraged to perform the propagation of all photons in parallelized calculations using the OpenCL programming language [101]. Photons are then propagated through the ice with the current best-fit knowledge about the scattering and absorption properties, continuing until either absorbed or until they reach a DOM. Photons which reach DOMs are stored.

The propagation of individual photons is efficient at low energies, where the scattering of individual photons is important. At energies above a few hundred GeV, the light yield is large enough that the propagation of individual photons is both excessively costly as well as unnecessary. In those cases, a feature known as *oversizing* is used by setting a *oversize factor*, N_{OS} . The oversize factor, often set to 5 for IceCube simulations above 1 TeV, allows for the production of "weighted photons" representing photon bundles with size proportional to N_{OS}^2 , significantly reducing the computational power necessary for large numbers of photons. In order to compensate for the bundling of photons, the effective radius of the DOM is also increased by N_{OS} .

Oversizing is efficient for the simulation of high energy events with large numbers of photon. This breaks down at GeV energies, where the photon flux from an event is low and scattering or absorption of individual photons matters. Because of the complications associated with oversizing at low energies, most simulations of DeepCore events are done with the oversizing features disabled.

4.2.3 Angular Acceptance and Hole Ice

When photons reach the surface of a DOM, the *angular acceptance* is applied in order to model the hole ice. This acceptance, calculated from a combination of lab and in-situ measurements, represents the PMT efficiency as a function of the photon arrival direction. The acceptance has a negligible efficiency for photons arriving from the back of the PMT and high efficiency for photons reaching the face of the PMT as shown in Figure 4.2. All other directions follow a curve between these two points. The angular acceptance model used in this thesis uses an empirical form fit to flasher data with two free parameters, as shown in Figure 4.2. The most forward direction in the PMT, shown with $\cos(\eta) = 1$, is most affected by the bubble column (see Section 3.3).

4.3 Simulating the Detector Electronics

4.3.1 Noise within IceCube-DeepCore

The noise simulation module used in IceCube, known as *Vuvuzela*, models the Poissonian and non-Poissonian detector noise using a set of five parameters, each representing distinct processes [71, 37].

The *thermal noise* and *radioactive decays* are Poisson processes simulated using rates fit during calibration. The thermal rate is correlated with the temperature and forms a large component of the noise in IceCube DOMs, with a typical rate of 200 Hz while the decay rate has a typical value of 50-100 Hz due to radioactive activity in the DOM glass.

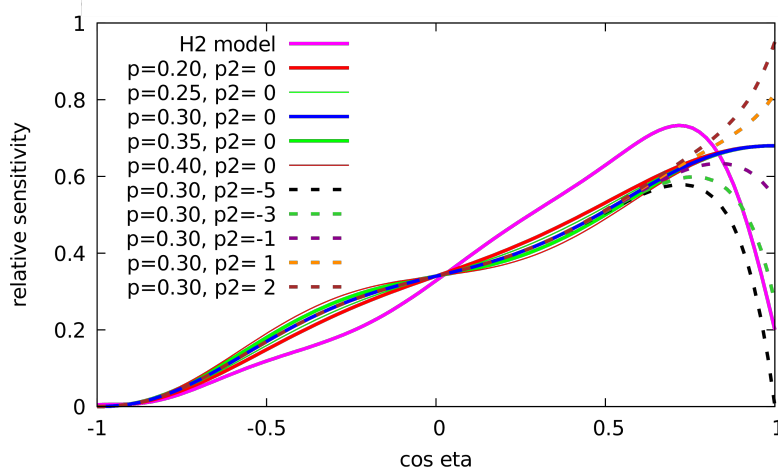


Figure 4.2 – Examples of the angular acceptance models used by IceCube. The relative sensitivity as a function of arrival direction is shown with $\cos(\eta)=-1$ indicating the back of the PMT and $\cos(\eta)=1$ the face. The variation of the acceptance model used for this search is shown using by varying two parameters in the model. The 'p' parameter primarily controls the acceptance at the side of the DOM while the 'p2' parameter controls the acceptance from the forward region. A second model, H2, is also shown.

In order to model this bursting behavior described in Section 3.1.4, an effective model used which represents the timing of consecutive hits using a log-normal distribution. This introduces three additional parameters to the noise model: the average number of hits in a "burst", giving the normalization; the mean time between hits within a burst; and the standard deviation of the timing within a burst. The non-Poissonian component to the noise model produces an additional 400 Hz of noise [71]. Noise hits in simulation are added as additional charge on each DOM at the face of the PMT.

The Vuvuzela model has previously been fit to each DOM in the detector, although with some limitations. Work completed during this thesis, discussed in Chapter 4.3.2, improved the calibration of the noise model.

4.3.2 PMTResponseSimulator and DOMLauncher

The IceCube detector does not directly measure photoelectrons emitted from the photocathode. Instead, IceCube events record the voltage response from the PMT via the output waveform. The production of simulated waveforms from incident photons is produced by a pair of modules.

The first module, *PMTResponseSimulator*, simulates the amplification process of the PMT, including the effects of pre-, late-, and afterpulsing. Each of these three effects is modeled using calibration measurements performed in the lab [69]. *PMTResponseSimulator* also calculates the amount of charge recorded by the DOM from each incident photon reaching the photocathode by sampling from the *single photoelectron* template (*SPE* template). The SPE template used in simulation generation is calculated from lab measurements of 118 DOMs prior to deployment [102]. The template, shown in Figure 4.3, is represented by the sum of an exponential and gaussian term and is applied identically to all DOMs. Prepulses, late pulses, and afterpulses are applied in a recursive process, which every incident hit having a probability of 0.3%, 3.5%, and 5.93% to produce each respectively. These probabilities were measured in the lab and are used for all DOMs.

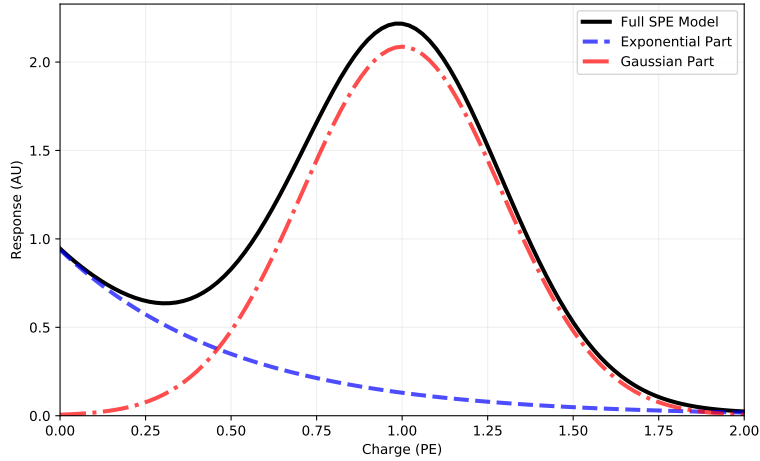


Figure 4.3 – The SPE template used in Monte Carlo simulation. The gaussian (red, dash-dot) and exponential (blue, dashed) parts of the full model (black) are shown. The SPE template is used as a sampling distribution for each incident photon in order to determine the observed charge. The SPE template is used for all DOMs.

The second module, *DOMLauncher*, handles the local coincidence circuits, simulation of the DOM clock, the discriminator, and digitization. The triggering system is then applied following the description of Section 3.1.5.

Updates to the Noise Simulation

5

The search for tau neutrinos is a search for rare particles near the detector threshold. Under these conditions, the search requires excellent understanding of threshold effects and detector behavior. In order to better model the detector, the noise simulation used in IceCube was updated with improved measurements after the discovery of disagreements in charge variables. This process is described in this chapter.

The chapter begins by describing the process used in previously to fit the Vuvuzela noise model for each DOM in Section 5. The limitations of the previous fitting process and the discovery of new disagreements is discussed in Sections 5.1 and 5.2 respectively. The new fitting procedure is then described in Section 5.3. New results of the fitting procedure are then discussed in Section 5.4.

5.1 A Summary of Previous Fits

Detector noise is a nuisance in most physics and astronomy experiments. PMT noise is assumed to be due to random emission from the photocathode and is affected by the gain of the PMT. Noise pulses from PMTs appear uniformly in time as a Poisson process.

The Poissonian noise model was used in the past in IceCube. With the introduction of the lower trigger threshold in DeepCore in 2010, however, it became clear that additional unsimulated sources of noise exist [71]. These additional hits appeared to occur in ‘bursts’ on a single PMT extending for up to a millisecond. Due to the time-correlations of these hits, the phenomenon was labeled *correlated noise*.

The Vuvuzela model, described briefly in Section 3.1.4, is now used to model both the Poissonian and non-Poissonian noise in IceCube. The empirical model consists of a Poisson process for electronic noise and radioactive decays and a correlated component modeled with a log-normal distribution. The model contains five free parameters per DOM. Ten minutes of untriggered data from the detector, dominated by noise hits, was used for calibration of the Vuvuzela parameters.

The Vuvuzela noise model is fit using the distributions of the time between subsequent hits, shown previously in Figure 3.4. Fits for each DOM were performed using the Pearson chi-squared test statistic between the data histogram, d , and the simulated histogram, m .

$$\chi^2 = \sum_i^{bins} \frac{(d_i - m_i)^2}{m_i} \quad (5.1)$$

The value of the χ^2 was minimized using a Metropolis-Hastings algorithm [17]. For each iteration of the algorithm, new parameters were selected and the response of the DOM was resimulated using PMTResponseSimulator and DOMLauncher. Each fit was computationally intensive, requiring between two and four CPU-weeks for each DOM. Due to the computationally requirements of the fits, the stopping condition was intentionally loosely defined, with a goodness-of-fit of 10% used.

Two examples from the original calibration work are shown in Figure 5.1. The Poissonian noise model used previously is shown for comparison. The Vuvuzela model more accurately reproduces the observed data across all timescales. Distributions of the number of hit

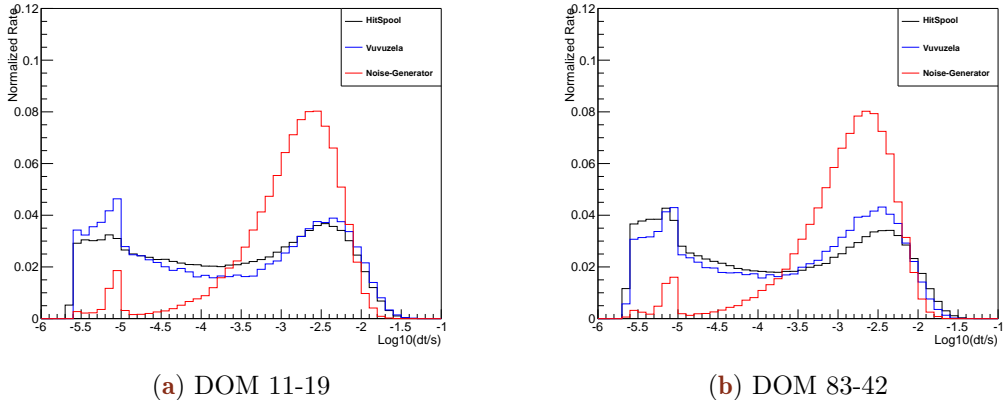


Figure 5.1 – Two examples of the original calibration work for the Vuvuzela model. The distribution of the time ("dt") between hits is shown. In black, untriggered detector data is shown. In red, a purely Poissonian noise model is shown. An afterpulsing peak is visible at 10^{-5} s. The Vuvuzela model is shown in blue. The Vuvuzela model shows improved agreement with data at all timescales.

DOMs and the number of accidental triggers due to detector noise, shown in Figure 5.2, improve significantly after inclusion of the updated noise model [71].

5.2 Limitations and Disagreement with Previous Fits

While accidental triggers with the Vuvuzela model better reproduced the rates observed in data, Figure 5.2 showed disagreement between data and simulation at very low numbers of hits. This region of the parameter space is dominated by accidental noise triggers in simulation.

An evaluation of the limitations of the previous calibration was performed in 2014, uncovering a number of possible improvements. The original fits were limited due to a number of factors. For example, the fits excluded the effect of atmospheric muons in the detector under the assumption that the hit rate per DOM due to atmospheric muons (approximately 5 Hz) is significantly smaller than the noise hit rate observed in previous calibration (about 600 Hz). Potential issues may arise from this assumption, which was not tested during original calibrations, including any potential time-correlated hits associated with muons.

Furthermore, some fits resulted in potentially-incomplete minimization. Due to the nature of the fit distributions, there existed significant degeneracy in the parameter space, leading to further difficulties.

During the fitting process, the strength of the afterpulsing peak at 9 microseconds was discovered to differ between DOMs. This effect was unsimulated, leading to convergence problems when fitting this region. In response, fits were artificially limited to timescales longer than 10 microseconds, allowing the minimizer to only observe part of the correlated noise distribution.

Because the noise hits are unlikely to satisfy the HLC conditions, timescales smaller than 6.4 microseconds were unavailable for investigation. No checks were performed for the Vuvuzela model below this limit.. The noise model itself was used down to 2 microseconds, however, resulting in uncertainty due to the extrapolation of the noise model to shorter times. The limit of 2 microseconds was implemented due to the inherent

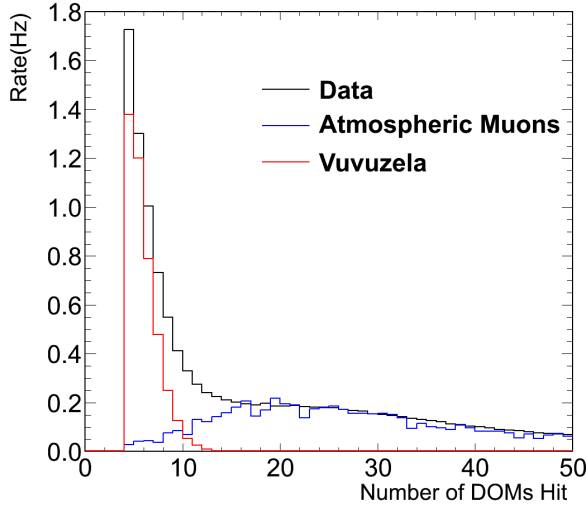


Figure 5.2 – The rates of events in DeepCore as a function of the number of hit DOMs in a cleaned hit series. The data, shown in black, consists of two components: the accidental triggers (red) and the atmospheric muons (blue). Accidental triggers produced using the Vuvuzela noise model reproduce most of the rate of events below 10 hit DOMs, although a rate disagreement remains. Image from [71].

difficulty in characterizing effects at these timescales due to artificial deadtime related to the HLC launch readout.

5.3 Low-dt Noise from Vuvuzela

In an attempt to address the imposed simulation limit at 2 microseconds, a new version of the Vuvuzela code, was created with this cutoff removed. The resulting noise, labeled *low-dt* noise for the short timescales (Δt), was used to produce a simulation of accidental noise triggers and CORSIKA muons for testing without further calibration.

The first tests, shown in Figure 5.3, used the number of hit DOMs in DeepCore events to evaluate the effect of the low-dt noise extension. The number of accidental triggers, dominant for events with fewer than 5 HLC hits, increased with the additional noise hits. The number of muons, which make up the majority of events with more than 10 HLC hits, decreased due to the use of the DeepCoreFilter, a veto described in further detail in Section ???. Both effects led to improved agreement between data and simulation.

Because the extended noise model adds hits occurring at timescales down to nanoseconds, multiple hits can occur within one waveform, leading to increased observed charge. When the noise distribution is extended below 2 microseconds, the tail of the distribution falls into the ATWD window of 322 nanoseconds, increasing the charge of noise hits in HLC DOMs. Furthermore, some fraction of the hits in a burst of correlated noise occur within the three bins recorded from the FADC for SLC hits. The result is that SLC hits due to noise no longer occur as single-photoelectron pulses, as is the case when noise hits are rare at the 10 nanosecond timescales, but as an integration of multiple single pulses. Such an effect would be most visible in the charge distribution of SLC DOMs, which are more likely to be due to noise hits than HLC DOMs.

The total charge of DOMs associated with HLC and SLC hits was evaluated to look for this effect due to the extended noise model. The result is shown in Figure 5.4. The change in the charge is observed clearly in the SLC charge distribution, where a systematic

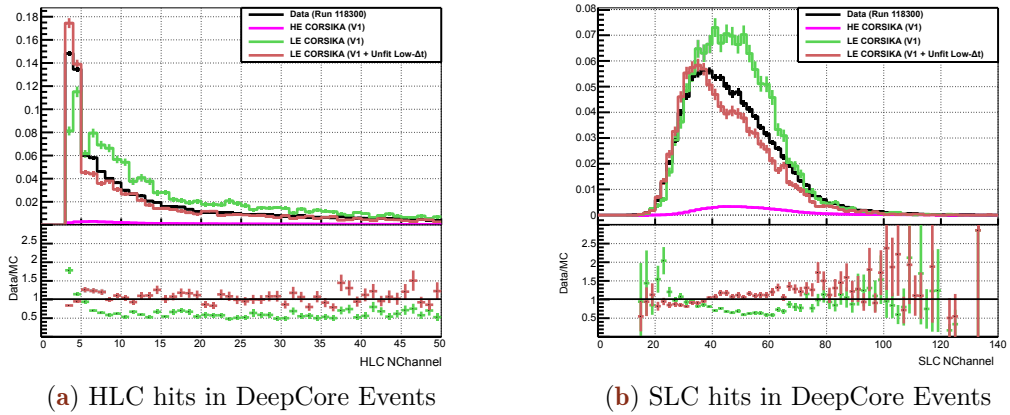


Figure 5.3 – The number of hit DOMs satisfying the (a) HLC and (b) SLC criteria described in Section 3.1.2. The distribution from 8 hours of data (black) is shown compared to a sample of CORSIKA muons at low-energy ($600 \text{ GeV} \leq E_{\text{primary}} \leq 100 \text{ TeV}$) and high energy ($100 \text{ TeV} \leq E_{\text{primary}} \leq 100 \text{ EeV}$). The addition of the low-dt extension to Vuvuzela improves the agreement between data and simulation in both HLC and SLC distributions.

shift is visible due to the low-dt extension. Both the original Vuvuzela model and the extended Vuvuzela model show significant disagreement with data in the SLC charge distribution. This demonstrated that the noise distribution at very short timescales was an important effect that deserved further attention.

The observed effect of the low-dt extension on the SLC charge distribution indicates that the distribution is sensitive to the region below 2 microseconds. The charge distribution of each DOM may therefore be used in the fitting procedure in order to characterize the low-dt end of the noise timing distribution. The effect, demonstrated in Figure 5.5, allows the investigation of a part of the distribution unavailable in previous fits.

5.4 Updating the Fitting Code

The effect of the low-dt extension on the charge distributions indicated the potential for improvement in the noise model distribution. New calibration fits for the updated noise model, referred to as *Vuvuzela V2* fits, were planned to include this extension for all DOMs.

With the opportunity to refit, a number of additional improvements were implemented. The afterpulsing peak at 9 microseconds was explicitly included in the fitting code. To account for the variability in the strength of the peak, a scale factor for the afterpulsing was included in the Vuvuzela V2 fits.

In order to include the effect of atmospheric muons, a set of Polygonato CORSIKA. The Polygonato model was selected due to the natural weighting scheme of the output files, allowing continuous simulation of the detector. Simulated files were divided into 10 microsecond long events (*long-frame* events), each containing multiple muons. The simulation was halted after photon propagation, giving a collection of muons without detector noise and effects applied.

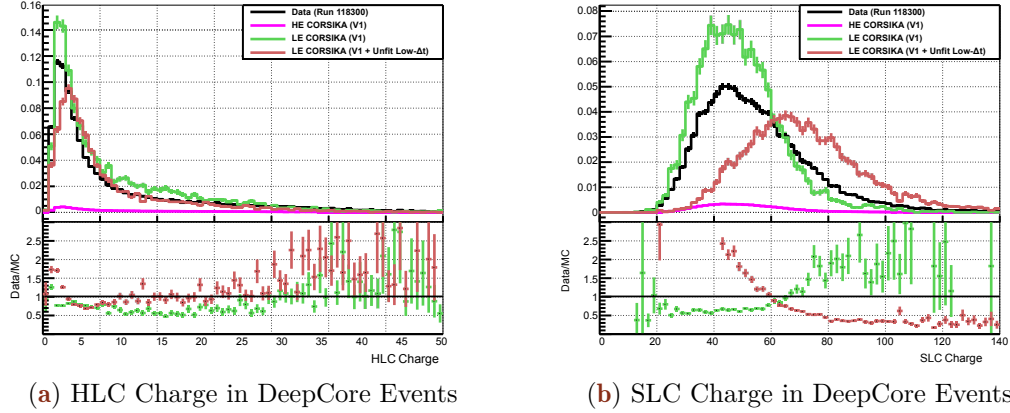


Figure 5.4 – The total amount of charge on DOMs satisfying the (a) HLC and (b) SLC criteria described in Section 3.1.2. The distribution from 8 hours of data (black) is shown compared to a sample of CORSIKA muons at low-energy ($600 \text{ GeV} \leq E_{\text{primary}} \leq 100 \text{ TeV}$) and high energy ($100 \text{ TeV} \leq E_{\text{primary}} \leq 100 \text{ EeV}$). Unlike in Figure 5.3, the charge distributions using the low-dt extension to Vuvuzela shows large disagreements with data. This is most visible in the SLC charge distribution.

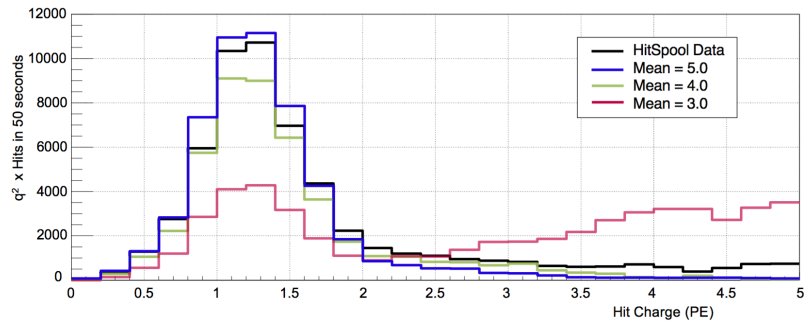


Figure 5.5 – The effect of changing the noise distribution parameters on the charge. Note the scale of the y-axis, which is scaled in order to emphasize the effect. Here, the gaussian mean is shifted from "5" (100 microseconds) to "3" (1 microsecond). All other parameters are held constant. By moving the correlated noise distribution to shorter timescales, more of distribution falls into one FADC bin, increasing the charge output for each launch.

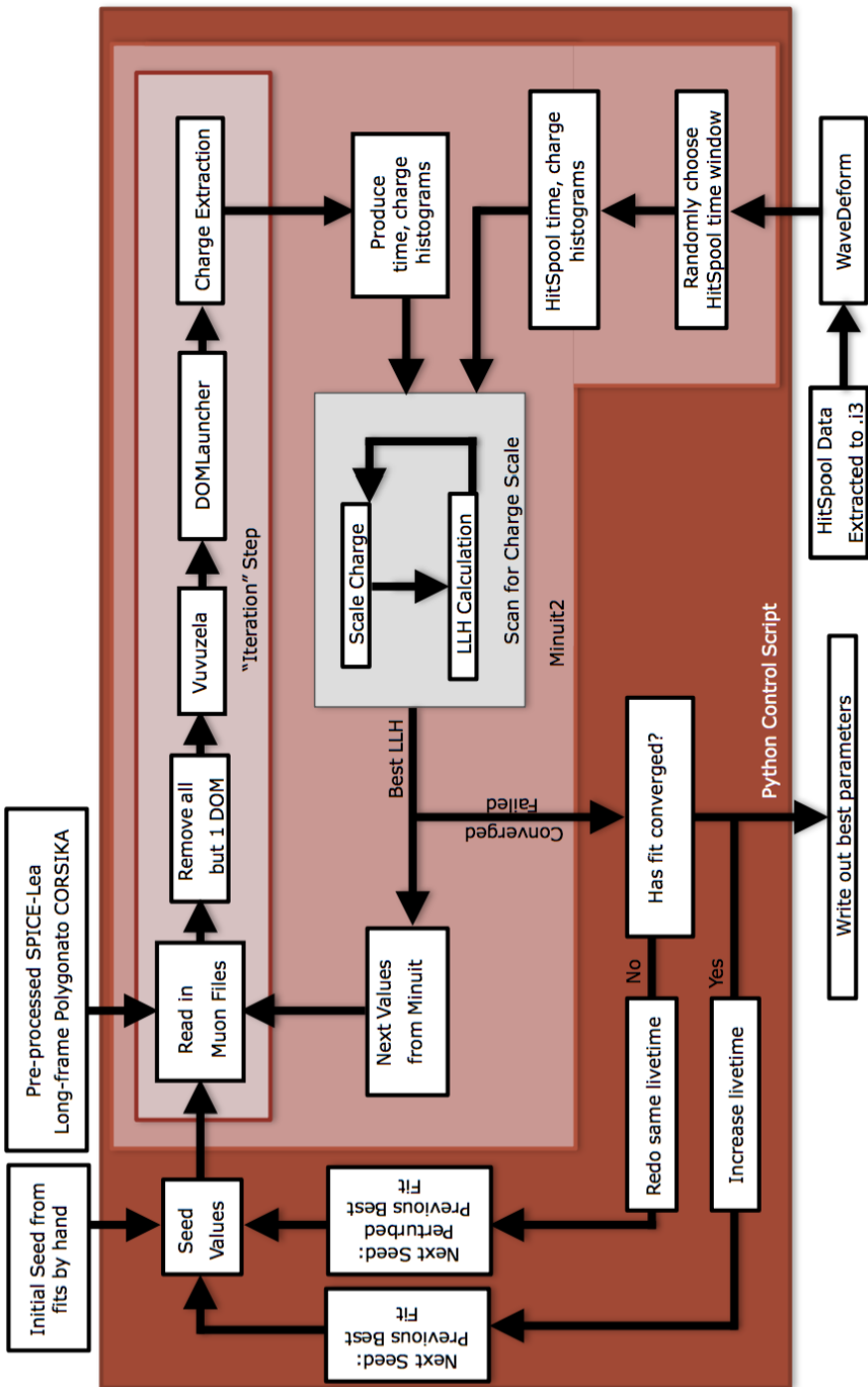


Figure 5.6 – A schematic diagram of the process used in the Vuvuzela V2 calibration fit.

The fitting process, described schematically in Figure 5.6, is divided into several parts. The code started with untriggered detector data as well as the produced long-frame CORSIKA events. The fit included a total of six explicit parameters: the five parameters from the original Vuvuzela model as well as a scale factor for the afterpulsing. Later investigations led to the introduction of a charge scale parameter to account for systematic differences between the data and simulated charge. Seeds for each parameter were taken from the Vuvuzela V1 calibration fits from 2012. Fits were performed for each DOM in parallel.

For each iteration, the long-frame CORSIKA files were filtered to remove information on all DOMs not currently being fit. The noise and detector simulation were applied using the current parameter set for the iteration. Charge extraction from the waveforms was performed using standard IceCube tools. After the simulation for a given set of parameters, histograms were produced for untriggered data and simulated hits. As in the previous fits, the time between subsequent hits is used as the primary observable of the noise behavior. In addition, the observed charge on the DOM is used as a second observable.

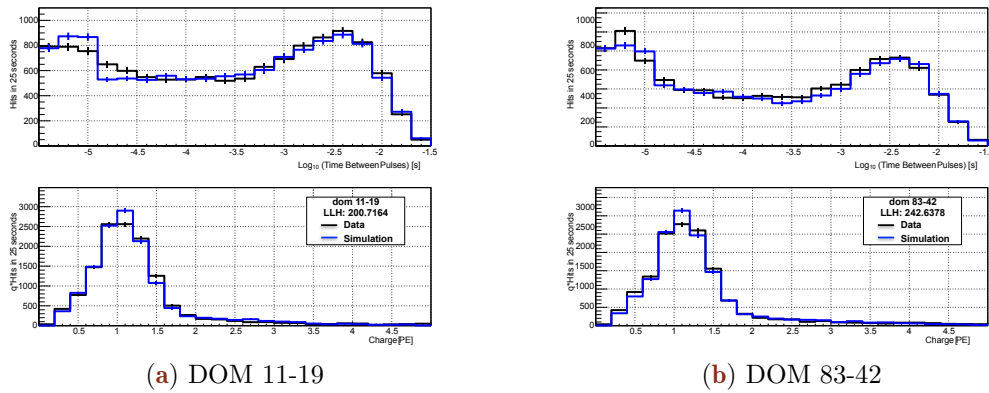


Figure 5.7 – Two examples of the new calibration fits for the Vuvuzela V2 model. The distribution of the time ("dt") between hits is shown on top. The distribution of charge is shown on the bottom. Note the y-axis of the charge distribution. In black, untriggered detector data is shown. The Vuvuzela V2 model is shown in blue. The new fits shown good agreement in both time and charge distributions.

The range of the histograms, from 6 microseconds until 1 second in the time and 0-5 photoelectrons in charge, provides sensitivity to the full range of the noise distribution. The distributions for DOMs 11-19 and 83-42 are shown in Figure 5.7.

Using the two distributions, a Poisson binned likelihood is formed. With the simulation in bin i of histogram j denoted by f_{ji} and the data hits in the same bin denoted by d_{ji} and ignoring normalization constants, the log-likelihood takes the form

$$LLH = \sum_j \sum_i^{nbins_j} d_{ji} \log(f_{ji}) + f_{ji} \quad (5.2)$$

The negative log-likelihood, $-LLH$ is minimized as a function of the fit parameters using iMinuit, a python wrapper for the minuit2 package [103, 104].

High charges from noise hits were rarely produced, limiting the effectiveness of the fitting strategy. To provide more weight to high charges, the histogram of the charges was

weighted by the value of the observed charge. This reduces the weight of very low charge launches, but increases the weight of higher charges.

Additional work showed that the charge distributions between data and simulation demonstrated disagreement in the charge distributions. This disagreement, due to miscalibration of the SPE peak in data, was accounted for by introducing a scale factor applied to the charge in simulation as a free parameter in the fit. The charge scaling applied to the simulated hits after detector simulation. To limit the computational complexity of the added parameter, the minimization over this charge scale factor is performed independently without resimulation. The form of this charge scale parameter assumes that the difference is a calibration issue in the data rather than a simulation problem. This has been shown to be the case, with an updated charge calibration now applied to data at final level.

The previous calibration attempts explicitly avoided fitting the behavior below 10 microseconds. In particular, it was noted that mismodeled afterpulsing behavior could lead to biased results in the noise parameters. The default value in simulation, assumed to be 5.93% for all PMTs, failed to take into account variations in the effects on each individual DOM. In the updated fit, the afterpulsing behavior has been investigated for each PMT by including an overall scale factor on the afterpulsing probability.

Late pulses, produced by electrons which backscatter to previous dynodes during the multiplication process, were also investigated for their effect on the goodness-of-fit in the noise distributions. These pulses occur at timescales of 50-200 nanoseconds and therefore are outside of both the SLC charge and timing distribution window. The late pulsing behavior was found to have a negligible impact due to both the rarity of late pulses as well as the lack of detailed information to constrain the distribution.

The effect of the afterpulsing parameter allowed some fits to fall into a poor local minimum. The degeneracy between parameters led to a local mimima from which the minimizer could not escape. In these cases, the probability of observing an afterpulse following a photoelectron would be moved from 5.6% to the unrealistically high value of 20%. This forced the gaussian mean of the Vuvuzela V2 model to move toward higher values and the gaussian sigma value to become unrealistically large. These fits were discovered by eye when looking at the best fit value of the afterpulsing probability, with a distinct population appearing due to this behavior. In order to constrain the fit to more realistic values, bounds were added to both the log-normal mean and afterpulsing probability for DOMs where fits showed abnormal behavior. DOMs with particularly strong afterpulsing peaks visible by eye in data were discovered. These DOMs were allowed to fit beyond the new boundary.

Due to the computational power required to produce large amounts of effective livetime at each iteration of the fitting process, a tiered approach was employed. Initial fits were seeded with the previous noise parameter fit values obtained in 2012. For these events, a coarse choice of binning both the timing and charge distributions and short effective livetime of just one minute were used. In addition, a weak tolerance value was used, allowing the minimizer to converge quickly to a reasonable minimum.

When the first tier completes the minimization process, the fit is restarted with a larger effective livetime, more bins, and a stronger tolerance using the best-fit parameters. The second tier used a 5 minute effective livetime, increasing the simulation time per iteration by a factor of 5.

The third and final tier increased the effective livetime to 10 minutes and again increased the number of bins. The final tier of minimization was the most computationally intensive and required between three and four weeks per DOM.

The fitting process for each tier continued until the minimization either converged or failed. Failure could occur due to electronics issues, such as computing cluster downtime, or due to a limit of 10000 iterations set in the minimizer to prevent issues with maximum processing time available on the computing cluster. In the case of a failure, the fitting tier was restarted with a new set of seed values. The new seed values were selected from a gaussian distribution centered on the previous seed with a width of 5%. The fit was then restarted. This process was continued until the third tier was complete for all DOMs.

5.5 Results of New Noise Fits

New calibration fits were completed over the course of two months for nearly all DOMs in the IceCube detector. String 25 and DOMs previously disabled due to malfunction are absent from the untriggered data, taken in 2014, used here and were therefore left unfit. The parameters for string 25 were selected using the average of all other fits.

The Vuvuzela V2 fits were checked after convergence in Figure 5.8 and Figure. One notable feature is the number of DOMs with afterpulsing at and beyond the fitter boundary. The likelihood values associated with these fits, however, appear to be consistent with other fits. Due to a planned overhaul of the afterpulsing simulation, the fit values of the afterpulsing probabilities have not been adopted for simulation. Therefore, no further investigation of the probabilities has been pursued.

The thermal rate is associated with the electronic noise, which should show increasing rate with increasing depth due to the rising temperature. This effect is only weakly apparent in Figure 5.9.

Other parameters should be independent of depth. As a test of the fits, each of the other parameters is plotted as a function of depth as well. No significant correlation is observed.

Finally, the likelihood values should be independent of depth. This final test, shown in Figure 5.10, shows surprising results in at least two ways: a 'band' structure appears in the plot. and there appears to be a depth-dependent decrease in the likelihood value, indicating that the lower part of the detector yields better fit results. This was initially unexpected, given that the noise is an internal property of the DOM and not of the surrounding medium.

This effect occurs due to a combination of factors. It is worth noting that the noise measurements of each DOM are not fully independent. The fits themselves use the long-frame CORSIKA to model the effects of muons in the untriggered data from the detector.

This leads to two subtle limitations in the fitting process. The long-frame CORSIKA is produced with a single flux model, in this case the Polygonato model used in CORSIKA [91]. Because the long-frame CORSIKA cannot be reweighted to other models, uncertainties or mismodeling in the muon flux can lead to disagreement in the fitting of noise parameters. The muon flux decreases with increasing depth, resulting in a lower muon contamination, and consequently smaller effects from mismodeling of the muon background, for deeper DOMs.

In addition, the long-frame CORSIKA implicitly assumes a single model of the ice for photon propagation. Mismodeling of the scattering and absorption of the ice therefore may also give rise to disagreement in the noise calibration. While large-scale properties of the ice are believed to be well-reproduced by the chosen ice model, SpiceLea [87], there will inevitably be remaining disagreements.

The net effect of these two assumptions in the muon simulation is effectively correlated with the convolution of the ice model and the muon flux. In particular, the best fits

occur where the DOM is either A) well-shielded from light due to muons by the large overburden or B) well-shielded due to large absorption in the ice. In both cases, the contamination from light due to muons in the fitted time and charge distributions will be small, leading to a more ‘pure’ noise distribution that is well-fit by the Vuvuzela V2 noise model.

The sensitivity of the noise calibration procedure to underlying assumptions of both the muon flux and the absorption properties in the detector imply that little further improvement is likely without additional work on one or both issues. Simulation of long-frame CORSIKA is, unfortunately, not possible with newer flux models at this time. As the primary uncertainty affecting the goodness-of-fit appears to be due to the visibility and flux of the muons themselves, merely updating to a newer model of the ice will be unlikely to significantly improve the current fit parameters.

The newly calibrated low-dt Vuvuzela was provided to the IceCube simulation group in January of 2015 and quickly integrated into the low-energy simulation chain. New neutrino, muon, and accidental noise trigger simulations were produced soon thereafter. The updated noise model shows significantly better agreement in both the total charge distribution and the number of hit DOMs for both HLC and SLC+HLC hits. The rate of accidental triggers improved relative to previous calibrations, with the remaining rate disagreement reduced from 50% to approximately 15%. Negligible effect was observed in the low-energy neutrino events at final level for existing samples.

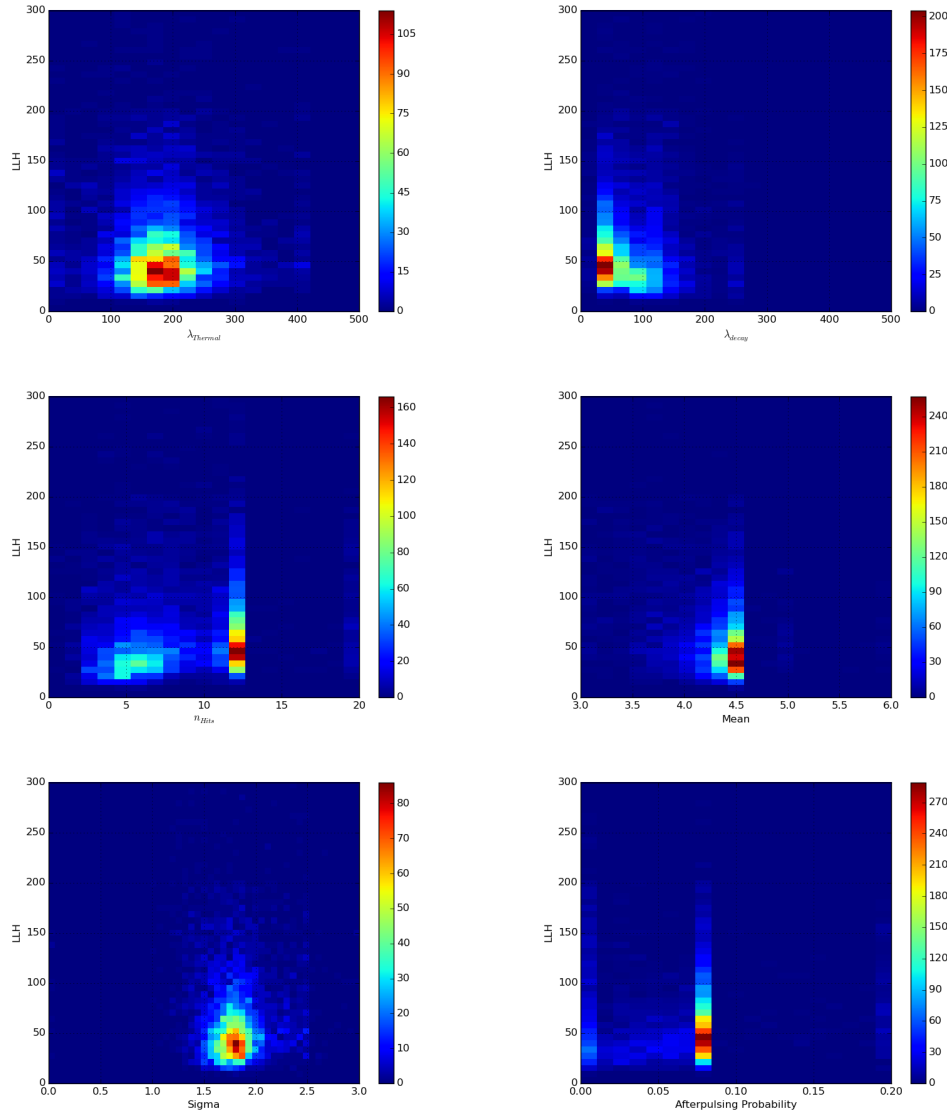


Figure 5.8 – The distributions of each new fit parameter in the Vuvuzela V2 model. The colorbar scale shows the number of DOMs in each bin. The effects of fit bounds are visible in most distributions except for the thermal noise rate and the width of the log-normal distribution describing the non-Poissonian noise.

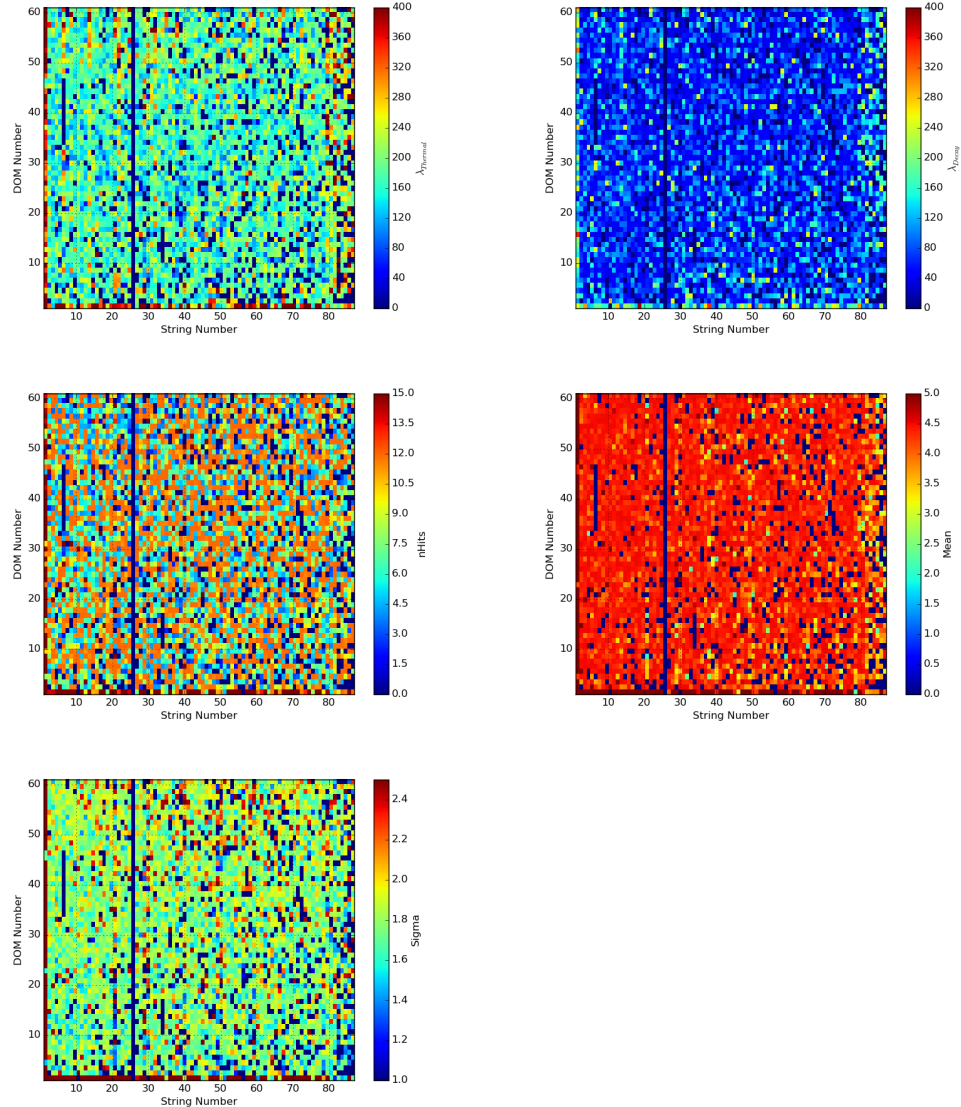


Figure 5.9 – The distributions of each new fit parameter in the Vuvuzela V2 model as a function of the string and DOM number. Note that the top of the detector is at the bottom of this plot. No parameter appears to be correlated with depth. DOMs on string 25 are missing from the dataset. In addition, DOMs which are disabled due to malfunction are also unavailable.

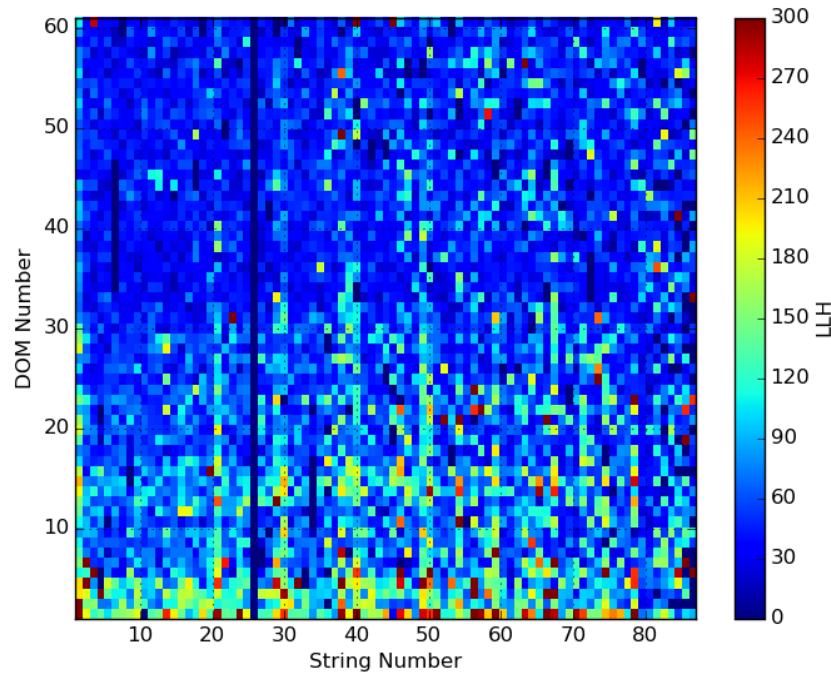


Figure 5.10 – The log-likelihood as a function of string and DOM number for the Vuvuzela V2 fits. Note that DOM 1 is at the top of the detector and DOM 60 at the bottom. The likelihood value was expected to be independent of depth, but shows some structure. These structures are correlated with both the ice model and the muon flux.

Low-Energy Muon Simulation

The updates of the noise simulation provide one reduction of background uncertainties in the appearance analysis. Another large uncertainty existing in the analysis is due to the limited simulation statistics of the atmospheric muon samples.

For low-energy oscillation analyses, the simulation of muons has proven difficult due to the computationally intensive simulation scheme. Large numbers of simulated events are produced for general IceCube analysis use, although the vast majority do not reach DeepCore. In response, previous analyses [79, 80, 81, 66] have developed methods to reuse data events which fail the selection as a model the background at final level. Severely limited simulated statistics from the CORSIKA generator precluded strong checks of these samples, but good fits were obtained with oscillation measurements consistent with other experiments.

For the search for tau neutrinos, new background generation techniques were used to more robustly model atmospheric muons. Two new generation schemes for low energy IceCube analyses are discussed here. The first, briefly discussed in Section 6.1, provided the final background sample used in the search for tau neutrinos. The second method, discussed in Section 6.2, is more experimental, but shows potential to further improve the background generation efficiency substantially for future analyses.

6.1 CORSIKA Generation In DeepCore

In IceCube, most simulation is produced centrally for use by the entire collaboration. This is especially true for background simulation produced with the CORSIKA generator. CORSIKA simulation, using the 5-component scheme discussed in Section 4.1.1, is the most common background simulation used in IceCube. These simulations are broken into two energy ranges based on the simulated primary particle energy in order to allow efficient generation of rare, high energy events. These are "low energy" CORSIKA, produced with primary energies $600\text{GeV} \leq E_{\text{prim}} < 10\text{TeV}$, and "high energy" CORSIKA, with energies $10\text{TeV} \leq E_{\text{prim}} < 100\text{EeV}$. These samples are produced in the upper atmosphere using the CORSIKA 5-component mode, then propagated to the detector, losing energy in transit.

Unlike MuonGun, CORSIKA generation does not currently possess a method to target specific sections of the detector. Instead, muons are pass through a upright cylinder of radius 800 m and length 1600 m around the center of IceCube. This allows uniform coverage useful for a wide range of analyses.

The centralized CORSIKA simulation in IceCube results in high statistics datasets used by all analyses in the collaboration. The production of these sets is computationally intensive, requiring hundreds of CPU-years and GPU-years worth of processing time in order to reach sufficient statistics. The number of unweighted simulation events and required computational resources required for centralized CORSIKA sets is shown in Table 6.1. Included is the 'simulation efficiency', the average number of events produced per computational year.

$$\epsilon = \frac{N_{\text{final}}}{t_{\text{CPU}} + t_{\text{GPU}}} \quad (6.1)$$

Generator	Sim. Req.	Number of Events			ϵ
	CPU	GPU	Generation	Final Level	
CORSIKA	188.9 Years	48.75 Years	8×10^{12}	284	1.20

Table 6.1 – The simulation requirements needed for the production of the standard CORSIKA sets in IceCube. The number of events reaching final level of the appearance search (Section 7.6.3) are shown. CORSIKA simulations are computationally intensive, but inadequate for low energy analyses in IceCube.

For analyses using DeepCore, the CORSIKA generation scheme results in many muons that are easily rejected. Events which interact solely outside of the DeepCore fiducial volume are removed early by a veto algorithm discussed in Section ??, reducing the background statistics from $O(10^{12})$ to $O(10^6)$. Additional cuts reduce this number further, with the GRECO selection described in Chapter 6.3 removing all but 284 events from an initial sample of 8×10^{12} . These events represent nearly 10% of the final level sample after weighting.

The final sample of muons in GRECO is too statistically limited to be of use in oscillation analyses. While previous analyses have used data-driven estimates of the background shape, verification of such techniques is itself limited by the simulated background statistics as well. In order to produce sufficient statistics for use in the appearance analysis, new background simulation techniques were necessary.

6.2 MuonGun for DeepCore

As described in Section 4.1.1, the MuonGun generation scheme provides a method to target specific parts of the detector. Doing so allows for *biased generation*, leaving some regions undersimulated while increasing the simulation statistics in the target volume. The limited size of the DeepCore fiducial volume provides an ideal use case for this biased generation.

In MuonGun, the muons are produced on a *generation cylinder* with a radius of 800 meters and length of 1600 meters, matching the final muon positions of the CORSIKA generator. The muons are pulled from a power law spectrum of the user's choice. An offset power law distribution is selected for this work in order to align with previous analyses [93].

$$f(E) = (E + E_0)^\gamma \quad (6.2)$$

where E is the energy of the muon at the generation cylinder, E_0 is an offset energy for generation, and γ is a configured spectral index. For this thesis, a power law is selected with a soft spectral index of -5, an offset of 700 GeV, parameters which correspond to the defaults assigned for example code. Note that the cosmic ray spectral index is approximately -2.7. The steep spectral index selected for generation leads to overgeneration of very low energy events. These events are expected to produce little light in the outer detector, making them difficult to identify from vetoing algorithms. Low energy muons are therefore expected to dominate the low energy background at final level of the GRECO sample.

CORSIKA events observed in the GRECO analysis at Level 5 (Section 7.4.3), the last cut level with significant CORSIKA statistics available, are used to select an energy range for MuonGun simulation. These events are shown in Figure ?? The lower energy limit, 160

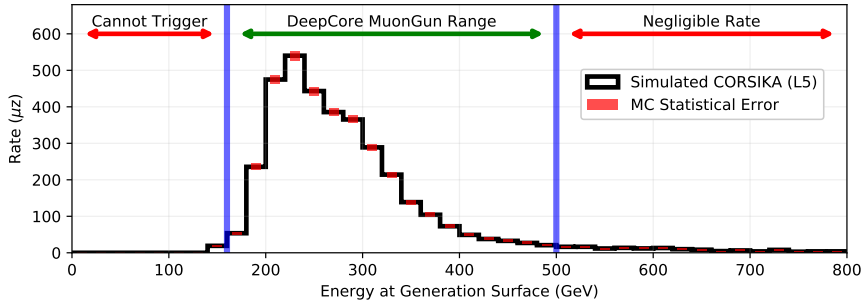


Figure 6.1 – The distribution of CORSIKA muon energies at the MuonGun generation surface using GRECO Level 5 muon events. Very few events trigger are seen below 160 GeV and less than 5% of events occur beyond 500 GeV. These two energies set the bounds for the MuonGun generation. MuonGun simulation has also been produced and tested above 500 GeV, but no simulated events survived to final level in GRECO.

Generator	Sim. Req.		Number of Events		ϵ
	CPU	GPU	Generation	Final Level	
CORSIKA	188.9 Years	48.75 Years	8×10^{12}	284	1.20
MuonGun	10.27 Years	12.11 Years	3×10^9	2486	111.08

Table 6.2 – The simulation requirements needed for the production of MuonGun simulation for DeepCore. The MuonGun simulation is nearly two orders of magnitude more efficient at producing statistics at final level in the appearance analysis.

GeV, is selected by using CORSIKA simulation to identify the minimum energy required for a muon at this surface to reach and trigger the DeepCore detector. A high energy limit on the MuonGun generation was set at 500 GeV, beyond which less than 5% of events remain. The energy range selected, shown in Figure 6.1, includes more than 95% of the distribution of CORSIKA events.

The angular spectrum of the MuonGun simulation is created by setting a *target cylinder* toward which the generated muon must intersect. For this work, the DeepCore fiducial volume is used as a target, encompassing a cylinder with radius 150 meters and length 500 meters centered on the geometric center of DeepCore at $x=(46.3, -34.9, -300)$.

A sample of muons was created using these settings of MuonGun and the resulting resource requirements are shown in Figure 6.2. The efficiency improvement from changing to MuonGun is substantial, increasing from 1.20 CORSIKA events/year to 111.08 MuonGun events/year, an increase of nearly two orders of magnitude. The MuonGun generation for DeepCore proved to be a far more efficient method of generation of low energy background events than the centralized CORSIKA simulation produced for the collaboration.

This simulation scheme has limitations. Because the target volume is small, events which do not enter DeepCore are not included in these sets. These events form a substantial background at early selection levels and cannot be ignored. For this reason, CORSIKA muons are required for the development of selections and will be used in the Chapter 6.3 until Level 5 (Section ??).

The generated statistics are useful for analyses at or near final level, where muons outside of DeepCore are no longer a dominant source of background. The newly produced MuonGun statistics are used to model the muon background after Level 6 (Section ??).

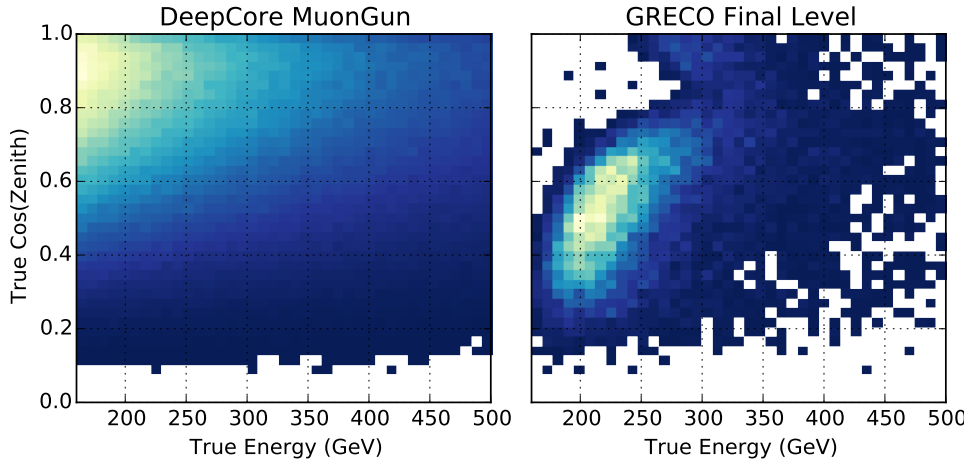


Figure 6.2 – The generated spectrum from MuonGun in energy and zenith angle compared to the events reaching the final level of the GRECO event selection. Both distributions have been normalized to 1. The majority of events produced by MuonGun are downgoing and low energy. These events do not reach final level.

6.3 Simulation Efficiency with KDE Prescales

After processing to the final level of the GRECO event selection (see Chapter 6.3), the background MuonGun simulation retains 2486 simulated events of the original sample of 3×10^9 generated events. The sample is sufficient for the search for appearance, but further improvements are possible.

While the previous section focused on improvements based on the simulation volume using MuonGun, inefficiencies still exist in the energy and zenith angle spectrum of the generated events. This inefficiency is shown in Figure 6.3. The majority of the events produced by MuonGun are very downgoing ($\cos(\text{zenith}) \approx 1$) and low energy. These events are noticeably absent from the final level sample.

In addition to the energy- and zenith-dependent effects, the GRECO selection exhibits strong azimuthal selection bias. This arises due to three effects. The first is the offset between the center of IceCube (and therefore the center of the generation volume) at $(x, y) = (0, 0)$ and DeepCore at $(x, y) = (46.3, -34.9)$. Due to this offset, the distance required to reach the DeepCore fiducial volume at an azimuthal angle around 150 degrees is longer than the corresponding distance at 0 degrees. This gives rise to an azimuthal effect appearing as a sinusoidal variation of the minimum generated energy of events at final level.

The second is the regular hexagonal structure of the IceCube volume, with long "corridors" through which muons may reach DeepCore without crossing any strings. Cuts designed to look for hits left in the veto region produce these azimuthal biases when muons close to strings are more likely to be identified and removed than those further from strings (see Section ??).

Finally, the DeepCore detector is not fully surrounded by an even layer of strings. This may be seen in Figure 3.8, where a layer of four strings is available for muon identification in the top left, but a layer of only three strings is available on the bottom right. Events entering the detector from this direction are more likely to reach DeepCore without being tagged, resulting in a larger acceptance of events around 300 degrees.

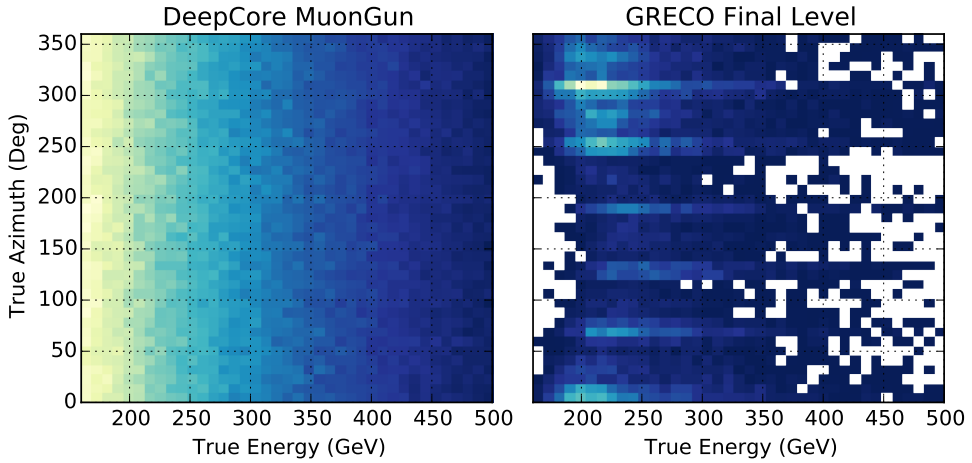


Figure 6.3 – The generated spectrum from MuonGun in energy and azimuthal angle compared to the events reaching the final level of the GRECO event selection. Both distributions have been normalized to 1. Events in the final level sample are strongly biased in azimuth due to the geometry of the detector.

In order to improve simulation statistics at final level, the existing MuonGun simulation scheme was modified to include an energy-, zenith-, and azimuthally-dependent prescale factor. This approach, here referred to as a *KDE prescale*, allows simulation to be produced with a known bias matching that of a given set of input files.

In this scheme, the *kernal density estimator (KDE)* from SciPy [105] is applied to all remaining events at final level of the GRECO event selection. The KDE uses a Gaussian kernal to represent each event in energy, zenith, and azimuth. The resulting KDE is normalized to produce an approximation of the final selection probability density function. In the new simulation scheme, an event is produced using standard settings for MuonGun generation described in the previous section. Immediately following generation, the probability of the new event reaching final level is calculated from the KDE, with typical values of approximately 10^{-4} for a likely event and 10^{-9} or lower for unlikely events. A prescale multiplicative factor of 10^5 is used to set the overall probability scale. The product, p of the prescale factor and KDE probability is used in order to accept or reject events. The value is interpreted as an acceptance probability and may not exceed 100%. Any values for which this may be the case are directly set to 100%.

Using a random number generator, this p factor is used to retain or reject the muon event. The simulation then proceeds as normal, with photon propagation, detector simulation, triggering, and filtering.

When events need to be weighted by a flux model, the p factor must be included as well. The weighting scheme utilizes the standard MuonGun weighting code to find the event weight. The total weight is then scaled by $\frac{1}{p}$ to correct the rates and uncertainties for the simulated events.

The results of this experimental method are shown in Table 6.3. By removing unlikely events early in the simulation chain, the required computational resources are further reduced compared to the general CORSIKA simulation sets used by the IceCube collaboration. While the number of events at final level is comparable to the MuonGun methods described in Section 6.1, the required time for simulation is reduced to less than 1 computation-year.

Generator	Sim. Req.		Number of Events			ϵ
	CPU	GPU	Generation	Final	Level	
CORSIKA	188.9 Years	48.75 Years	8×10^{12}	284		1.20
MuonGun	10.27 Years	12.11 Years	3×10^9	2486		111.08
MuonGun+KDE	75 Days	175 Days	9×10^8	3588		5241.92

Table 6.3 – The simulation requirements and number of events for each muon generation scheme. The use of the KDE prescale improves the simulation efficiency by a factor of 50x compared to the DeepCore MuonGun simulation method described in Section 6.1.

Further optimizations are possible at the expense of accuracy. For example, the oversizing methods described in Section 4.2.2 may be used to reduce the number of propagated photons. Using $N_{OS}=3$, the GPU simulation requirements are reduced by approximately 8x, leading to a total simulation efficiency of 13527.55. The oversizing is known to cause a small bias in the simulated photon arrival time, potentially leading to bias in particle reconstructions. Oversizing should be used with care in order to minimize or eliminate these biases.

The KDE prescale demonstrated here used only unweighted events due to limitations in the SciPy software. The KDE therefore encodes some bias towards the production of low energy muons due to the soft spectral index of the MuonGun DeepCore generation. Other implementations of multidimensional KDEs can accept event weights [106, 107]. The use of these algorithms would be beneficial and remove some dependence on the generation characteristics of the source events used for building the KDE.

The simulation using KDE prescales is limited by the events used to form the KDE. If too few events are used, the KDE may not adequately represent the shape of the underlying spectrum, leading to little gain in efficiency. Likewise, if a region is underrepresented in the sample, the KDE may not describe the distribution of events in this region. Care should be taken in order to check for unsimulated regions before using the KDE prescale to avoid these situations.

The use of the KDE prescale method shows substantial promise in improving simulation efficiency. Work is ongoing within the IceCube collaboration at the time of this writing to investigate use of the method for DeepCore analyses. If adopted, the improved simulation efficiency may allow future analyzers to significantly reduce the statistical uncertainty in the simulated background samples.

GRECO: An Event Selection at the Limits of DeepCore

The search for appearance in atmospheric neutrinos requires a selection of neutrino candidate events. The events passing the SMT3 trigger in DeepCore, however, are dominated by Muons, at 280 Hz [37] compared to a neutrino rate of about 4 mHz.

In order to remove the atmospheric muons, an *event selection* is necessary. The GeV Reconstructed Events with Containment for Oscillations (*GRECO*) event selection is presented here. This selection was developed for the appearance analysis and reduces the atmospheric muon rate to around 0.07 mHz while retaining around 0.7 mHz of atmospheric neutrino events.

The selection consists of multiple stages, or *cut levels*. Each will be presented sequentially.

7.1 Hit Cleaning

Following the triggering of the detector, the waveforms of each hit must be extracted to obtain information about the charge of events. Not all recorded pulses are the result of muon or neutrino interactions in the detector, however. To identify hits relevant for the study of muons or neutrinos, a number of *hit cleaning* algorithms are used.

7.1.1 Pulse Extraction

The extraction of charge and timing information from recorded waveforms is performed using the *wavedeform* module, which accepts and processes the information from the launches in each triggered event. Wavedeform attempts to reconstruct the original charge information from the digitized waveform information.

Wavedeform uses a parametrized version of the PMT pulse associated with a single photoelectron shown in Figure 4.3 extended to include a timing dimension describing the timing profile of the PMT amplification process. Beginning with a single pulse template, a least squares minimization is performed to find the best-fit time of a single pulse in the observed waveform. Additional copies of the pulse template are added and new minimizations are performed until the goodness-of-fit improvement from additional pulses is negligible. The resulting sets of pulses, including associated timing and normalization, are returned as *reconstructed pulses*, more commonly referred to as simply *pulses*. These pulses represent the best-fit recreation of the analog pulses in the PMT prior to the digitization process.

Both HLC and SLC waveforms are fit, although the limited information in SLC waveforms necessarily results in the loss of information. When available, information from the ATWD is provided a larger weight relative to the information from the FADC due to the finer binning in time, allowing for more detailed information on PMT behavior near the beginning of the launch of the DOM.

7.1.2 Hit Cleaning

In general, a set of pulses from a given event, referred to as a *pulse series*, contains a significant number of pulses due to random detector noise. These additional pulses are not useful for understanding the particle interactions and are therefore typically removed during processing. There exist multiple ways to identify pulses likely to be due to detector noise, three of which will be detailed in order from most strict to most accepting.

The most strict cleaning results from the exclusive use of local coincidence information. This type of cleaning is referred to as *HLC cleaning* and is shown in Figure 7.1. By selecting only pulses that result from DOMs satisfying the HLC criteria discussed in Section 3.1.2, the resulting pulse series can be cleaned of nearly all detector noise. No additional processing is necessary, although cleaning the pulse series based solely on local coincidence criteria comes at the expense of a potentially significant amount of information about the event, since all SLC hits are removed.

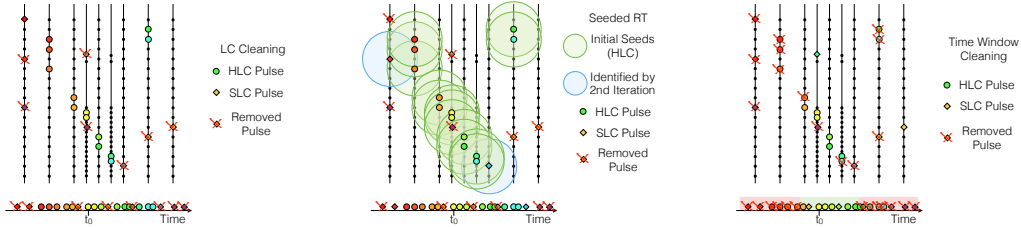


Figure 7.1 – An illustration of the LC, SeededRT, and time window cleaning methods. (Left) All SLC pulses are removed while all HLC pulses are retained. (Middle) Pulses are removed based on time and distance from nearby HLC DOMs, allowing some SLC pulses to be accepted. (Right) Pulses are removed using the time relative to either the trigger (STW) or the maximum pulse density in time (DTW).

SeededRT Cleaning

Instead of simply using HLC hits, additional processing may be used to identify potentially interesting SLC pulses as well. The *SeededRT (SRT)* algorithm is one such algorithm, requiring a seed, radius, and time in order to search for additional information in the event as shown in Figure 7.1. SeededRT begins with a subset of "interesting" pulses, often a selection of the HLC pulses, as a seed. Once a seed is selected, a sphere is drawn around each seeded DOM. Any nearby DOMs within the sphere and time window are added to the output pulse series. Once all seed DOMs have been checked, a new seed is created composed of the all current output pulse series. The process is repeated until no further pulses are discovered.

The most effective set of parameters is dependent on the detector geometry, since a given radius sphere will contain more DOMs in the DeepCore fiducial than the same sphere outside of DeepCore. Because of this, different settings are chosen for these two regions. In the less dense IceCube detector, a typical value for the radius is 150 m and for the time window is 1000 ns. In DeepCore, these values are typically halved, with a radius of 75 m and a time window of 500 ns.

The SeededRT algorithm is commonly used in IceCube, allowing for a pulse series with minimal noise contributions while finding most hits due to muon or neutrino interactions.

Time Window Cleaning

The most permissive pulse cleaning algorithm results in very little loss in pulses due to particle interactions, but allows nearly all noise pulses into the final hit series. This *Static Time Window* cleaning, often referred to using just the acronym *STW* cleaning, looks for pulses near the time of the trigger. For DeepCore processing, any pulses more than 4 microseconds before or more than 6 microseconds after the SMT3 time are removed.

There exists a second type of time window cleaning applied more rarely, but used in the GRECO selection. The *Dynamic Time Window* cleaning, hereafter *DTW* cleaning, is a time window cleaning algorithm that uses the maximum pulse density in time to find the most likely interaction time of a muon or neutrino. The timing window is placed around this time instead of around the trigger. DTW cleaning is generally chosen with a significantly tighter window, often consisting of only a few hundred nanoseconds compared to the multiple microseconds used in the *STW* cleaning.

Time window cleaning is typically used in combination with additional cleaning methods, resulting in little loss in useful signal due to the wide time window (in *STW* cleaning) or in a very pure set of hits likely to be due to unscattered light.

7.2 Level 1: The DeepCoreFilter

Triggers are generally designed to be as accepting of the proposed physics signal as possible, regardless of the background rates. Typically, limitations exist solely in the processing and storage capabilities in order to prevent the unintentional loss of valuable information. After triggering, various filters may be applied with the sole purpose of removing the collected background. For the purposes of this document, the only filter considered is the *DeepCoreFilter*.

The DeepCoreFilter proceeds by splitting the pulses identified by the SeededRT cleaning into "veto" and "fiducial" pulses, with each DOM given a designation based on its position in the detector as described in Section 3.1.6 [72, 71]. The average and standard deviation in time are first calculated for the fiducial pulses. All hit DOMs with the first pulse occurring more than one standard deviation away from the mean time are removed from the fiducial pulse series in order to further limit the contributions from noise pulses.

With the updated fiducial pulse series, a center of gravity, or *CoG*, of the remaining DOMs is calculated.

$$\vec{x}_{CoG} = \frac{\sum_i^{DOMs} \vec{x}_i}{N_{hits}} \quad (7.1)$$

The "corrected" average time of the fiducial pulses is then calculated by assuming that the pulse is due to light emission at the CoG, as would be the case for a point-like interaction of a cascade event.

$$t_{CoG} = \frac{\sum_i^{DOMs} t_i^0 - \frac{\vec{x}_i - \vec{x}_{CoG}}{c_{ice}}}{N_{hits}} \quad (7.2)$$

where t_i^0 denotes the time of the first observed pulse and \vec{x} the position of each DOM. All veto pulses are then compared to this CoG time and position by calculating an effective particle speed, v .

$$v = \frac{|\vec{x}_{CoG} - \vec{x}_{hit}|}{t_{CoG} - t_{hit}} \quad (7.3)$$

Muons passing through the detector will do so at the speed of light, 0.3 m/ns. Unscattered hits left behind in the detector show this peak clearly for muons. Low energy neutrino events, on the other hand, typically begin in DeepCore, with hits outside of the fiducial region following hits inside. These neutrino events show a peak at negative speeds.

The DeepCoreFilter is the first step in a low energy analysis in IceCube and is used in many analyses [71, 78, 79, 80, 81]. The algorithm reduces the atmospheric muon background from 280 Hz to approximately 17 Hz while retaining 99.4% of neutrino events which begin in DeepCore [72].

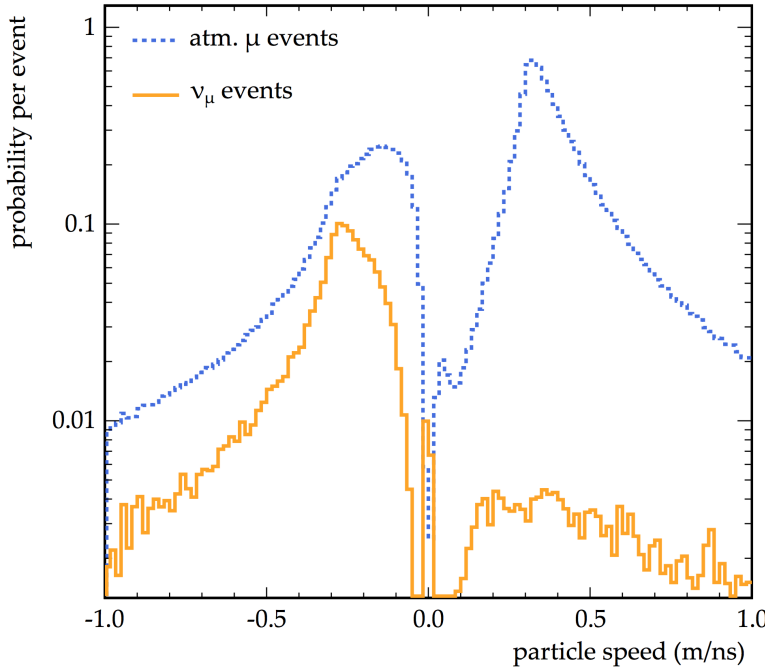


Figure 7.2 – The distribution of effective particle speeds used by the DeepCoreFilter to identify and reject muons. Because muons interact first outside of DeepCore, a large peak is visible at speeds around 0.3 m/ns, the speed of light. Figure from [72]

7.3 Low-En Level 3 Cuts

After the DeepCoreFilter is used to remove events, variations of hit cleaning algorithms and reconstructions are used. This processing stage, *Level 2*, does not remove events from the selection and will not be discussed here.

Following the Level 2 processing, the *Low energy Level 3* cuts are introduced. These cuts are standardized and used in all DeepCore oscillation analyses. The Level 3 processing stage introduces the structure of the remaining cut levels by using a set of *accidental event cuts* and *muon cuts*.

After the DeepCoreFilter, approximately half of the remaining rate consists of muons. The remainder is due to accidental triggers due to random detector noise due to the low trigger threshold used in DeepCore.

7.3.1 Accidental Rejection at L3

Three cuts are introduced at Level3 in order to reduce the observed number of accidental triggers. Events are required to have at least pulses and a total charge of at least 3 PE in a 250 ns DTW cleaned pulse series in the DeepCoreFiducial region. This removes events which have reached Level 3 processing via random detector noise in the fiducial region.

In addition, the *NoiseEngine* algorithm is used to identify accidental triggers [71]. NoiseEngine uses the relative direction between each pair of hits to search for directionality of the event. Events with fewer than three hit pairs pointing in the same direction fail the algorithm and are rejected. After the NoiseEngine algorithm, more than 96% of accidental triggers are removed from the analysis.

7.3.2 Muon Rejection at L3

The removal of muons relies on some understanding of the characteristics of these events at Level 3. Muons at this level are generally bright enough to be identified by hits in the outer part of the detector, known as the *veto region*. Because neutrino candidates of interest in this search are low energy, no light emission is expected in the veto region due to neutrinos. This may be used to identify muons using cuts described here.

First Hit Z Position

Because the muon tracks are primarily steeply inclined, most will leave hits in the upper part of the detector. Neutrinos of interest in the search for appearance will primarily emit light within the DeepCore fiducial volume, leading to little or no light emission in the top half of the detector. This difference between neutrino and muon emission in the upper part of the detector can be used to identify background muons. The position of the first hit in a STW+SRT cleaned pulse series consisting of DeepCore fiducial hits is used to look for muons using this principle. Any event with a first hit above $Z=-120$ m is removed.

NAbove200

The total charge of recorded hits occurring in the top of the detector is also used in the analysis. This variable, known as *NAbove200*, counts the amount of charge occurring before the SMT3 trigger above a depth of -200 meters. If more than 12 DOMs are hit above $Z=-200$ m, then the event is removed.

RTVeto

The SeededRT algorithm is useful for removing accidental noise hits in the detector. It may also be used to find clusters of hits due to muons in the outer part of the detector as well. This technique, known as *RTVeto*, uses the SeededRT algorithm to identify the largest cluster of pulses in the outer detector. The number of hits in this cluster is used to identify atmospheric muon events. The RTVeto algorithm uses a radius of 250 m and a time window of 1000 ns for both DeepCore and IceCube DOMs.

The cut is used in combination with the total amount of charge observed in the DeepCore fiducial region to define a few separate cut conditions. For the purposes of this search, only the lowest energy version is relevant. In this case, any event with a cluster of 4 or more hit DOMs in the outer detector is removed.

C2QR6

Atmospheric muon events at Level 3 tend to leave long tracks and take $O(3 \mu\text{s})$ to cross the detector. Oscillation neutrino events produce small light patterns small due to the low energies involved, with light being deposited quickly. The difference in the light emission profile of the two event types may also be exploited to reject atmospheric muons background events.

Type	IceCube Processing		
	Any Filter	DC Filter	Low-en L3
CORSIKA	990598	9178	969.818
MuonGun	60669	2982	442.493
Accidentals	35855	8117	283.559
ν_e	1.842	1.721	1.262
ν_μ	11.317	6.360	4.758
ν_τ	0.293	0.270	0.206
MC Total*	1026466	17303	1260
Data	1154426	19092	1092

Table 7.1 – The event rates after the Level 3 cuts in GRECO. The total simulated rate is calculated using CORSIKA events and ignoring MuonGun. The data rate is estimated from a burn sample of 10 runs at Level 3. Rates are given in mHz.

To test the deposition time for light in each event, the *charge ratio in 600 ns* (*QR6*) is calculated as the ratio of charge observed in the first 600 ns and the total amount of observed charge.

$$QR6 = \frac{\sum_i^{t_i < 600} \text{hits}}{q} \sum_i q_i \quad (7.4)$$

Here the time is measured relative to the first observed hit in a STW+SRT pulse series. Atmospheric muons will tend to deposit light over a longer timescale, resulting in a charge ratio near 0. Neutrinos will deposit light quickly, with a charge ratio near 1.

The algorithm relies sensitively on the first observed hit. The observation of noise hits before the particle interaction can lead to an erroneous definition of the time window. In order to reduce this possibility, the first two hits may be ignored for the calculation. This form, the *cleaned charge ratio in 600 ns* (*C2QR6*) is used in the Level 3 processing to remove atmospheric muon events.

7.3.3 Rates at Level 3

The rates after the Level 3 cuts are applied is shown in Table 7.1. The atmospheric muons are reduced by about an order of magnitude. The removal of accidental triggered events forms a large part of the reduction in rate at Level 3, with the rates decreased by more 96%.

7.4 GRECO Level 4 Cuts

The first GRECO-specific cut level is designated *level 4*, or *L4*, was first introduced in 2011 using very similar variables at the Level 3 cuts. This is performed for historical reasons, as the DeepCore Level 3 and GRECO Level 4 were produced in parallel.

As in the DeepCore Level 3 processing, the GRECO Level 4 is divided into two types of cuts: those that remove accidental triggers due to detector noise and those that remove atmospheric muons. The cuts for atmospheric muons are then fed into a *boosted decision tree* (*BDT*), a multivariate algorithm designed to better separate signal from background [108].

7.4.1 Accidental Rejection at L4

Similar to the cuts applied at Level 3, the GRECO Level 4 begins with a cut on the number of observed hits. In this case, static time window cleaning is applied with a range of $-3500\text{ns} \leq t \leq 4000\text{ns}$ for hits in the DeepCore fiducial volume. A dynamic time window cleaning is then applied with a window of 200 ns. Any events with fewer than three hits in this stricter pulse series is removed.

7.4.2 Muon Rejection at L4

Some cuts used to identify muons in the GRECO Level 4 are similar to those applied in the Level 3 processing. A stricter hit cleaning algorithm is used at this cut level to identify muons missed at Level 3.

FirstHit Z

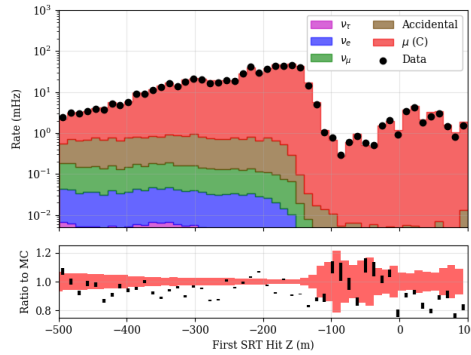


Figure 7.3 – The Z position of the first hit in a cleaned hit series. Note the shape difference between the atmospheric muons in red and the various neutrino flavors, particularly above -200 meters.

The Z position of the first hit DOM in the event is included for the GRECO Level4. The cut continues to show separation between neutrino events and atmospheric muons with the new hit cleaning.

NAbove200

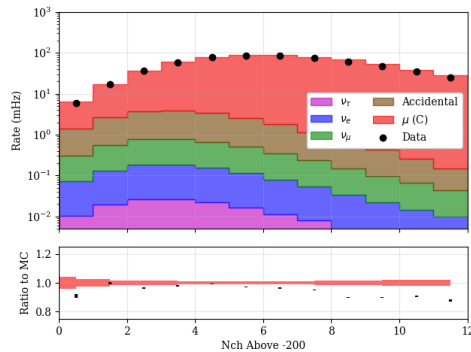


Figure 7.4 – The number of hits above Z=-200 meters

Similarly, the number of hit DOMs identified above Z=-200 m is again used with a new hit series. Once again, some separating power remains.

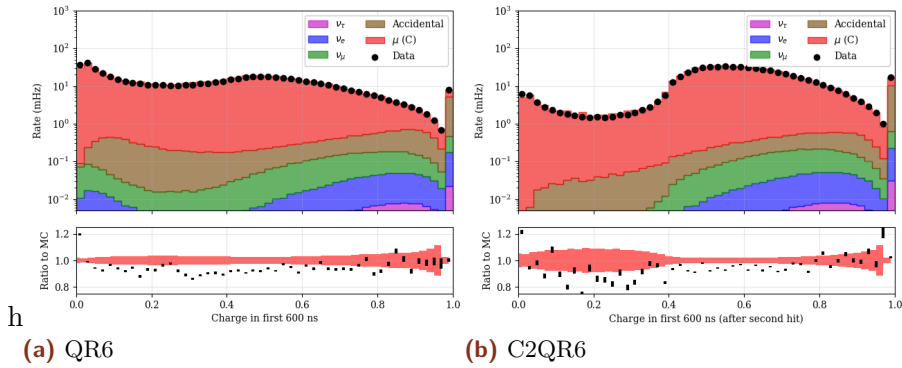


Figure 7.5 – The charge ratio variables used in the GRECO Level 4 cuts.
 lofsubfigure\newline(a)QR6lofsubfigure\newline(b)C2QR6

QR6/C2QR6

Both the QR6 and C2QR6 are used in the GRECO Level 4 processing. The two show some degeneracy, although the BDT training suffers if only one is available. Note that there exists some significant disagreement between data and simulation at low values of C2QR6. This region does not contain much signal and will be removed by the BDT.

Tensor of Inertia

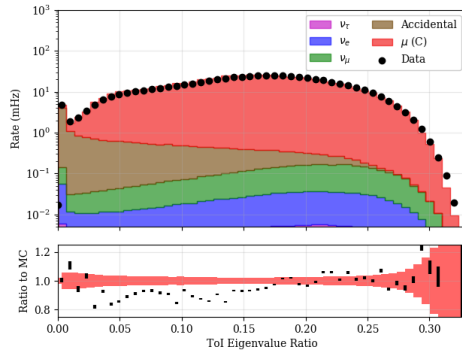


Figure 7.6 – The eigenvalue ratio from a ToI calculation. Larger values indicate more apparent elongation in the event.

At this early level, the shape difference in the observed hit pattern will be relatively clear. Many neutrinos with energies in the range of 1-100 GeV will appear to be rather small and compact in DeepCore forming a cascade-like event. Muons will have a longer visible track. These differences may be interpreted via use of the *Tensor of Inertia eigenvalue ratio* (more briefly, *ToI*). This variable is defined in analogously to the tensor of inertia from mechanics, with the measured charge taking the place of the mass.

$$\begin{aligned} I_X &= \sum_{i=0}^{nhits} (y_i^2 + z_i^2) q_i \\ I_Y &= \sum_{i=0}^{nhits} (x_i^2 + z_i^2) q_i \\ I_Z &= \sum_{i=0}^{nhits} (x_i^2 + y_i^2) q_i \end{aligned} \quad (7.5)$$

These three moments yield information about the shape of the event. The eigenvalue ratio is defined as

$$e = \frac{\max(I_j)}{I_x + I_y + I_z} \quad (7.6)$$

Events which are very track-like, and therefore muon-like, have eigenvalue ratios near 0 while more cascade-like events have eigenvalue ratios close to $\frac{1}{3}$.

Linefit Speed

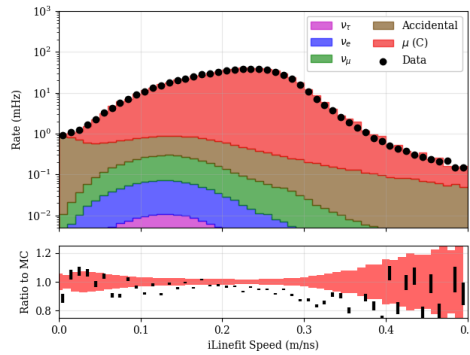


Figure 7.7 – The apparent speed, in units of meters per nanosecond, corresponding to the hits in the event. Faster speeds are associated with particle travel instead of light travel.

The *line fit* is a first-guess reconstruction used in IceCube. The algorithm assumes that the hit pattern in an event may be modeled as a plane wave passing through the detector at speed v_{LF} . The speed of the plane wave may be solved analytically [109].

$$\vec{v}_{LF} = \frac{\langle t_i \cdot \vec{x}_i \rangle - \langle \vec{x}_i \rangle \langle t_i \rangle}{\langle t^2 \rangle - \langle t_i \rangle^2} \quad (7.7)$$

where $\langle t_i \rangle$ denotes the average hit time. Cascade-like events have hits moving without a preferred direction while the atmospheric muons have a single preferred direction. Using the line fit speed, the neutrino sample is expected to have a speed closer to 0 while the atmospheric muons show a speed closer to the speed of light, 0.3 m/ns.

The L4 BDT

A Boosted Decision Tree (*BDT*) is trained at L4 to further reduce the atmospheric muon background by a factor of 10x. The variables described above were provided to a BDT training using the CORSIKA as the background training sample and GENIE simulation as the signal sample. The BDT uses a series of *trees*, collections of multidimensional cuts, to classify events as either signal-like or background-like [108]. After *boosting*, a process by which event weights are adjusted based on the success or failure of previous classification attempts. The BDT returns a *score* ranging from -1 (background-like) to +1 (signal-like) which may be used as a cut variable in an analysis.

The score returned by the GRECO Level 4 BDT is shown in Figure 7.8. The distribution ranges from -0.6 to +0.6, indicating that no signal or background events are perfectly identifiable. Separation is observed between the atmospheric muon events, which peak around a score of -0.25, and signal, peaking at +0.15.

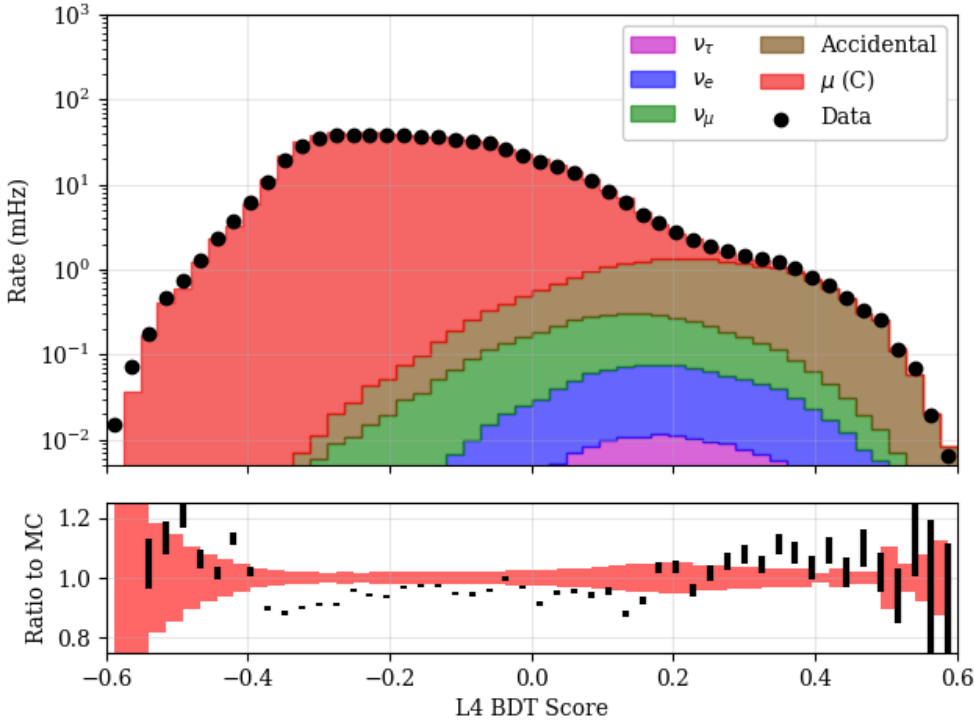


Figure 7.8 – The distribution of the boosted decision tree used at L4. A cut is applied at 0.04 to remove a significant fraction of atmospheric muon background events. Note the ratio, which shows disagreement in the very muon-like region. The region of disagreement is removed by the cut.

Comparisons to MC show mild disagreement, particularly in the most muon-like regions that get cut away. It's not obvious what causes the disagreement, although it is possible that the assumed cosmic ray flux model is simply an inaccurate model of some part of the spectrum that contributes. Alternatively, this may be an artifact of undiscovered mismodeling of the atmospheric muon events. Differences in the high energy muon events would likely have clear tracks visible in the detector, contributing to the region around -0.5. No investigation of the disagreement has been performed, as these events are removed from the GRECO selection.

A shoulder attributable to the accidental triggers is visible at high values of the BDT score, peaking around 0.25, indicating that these events appear more signal-like than the neutrino samples. While initially puzzling, investigation of the training of the BDT showed that the original training sample did not include these events. Instead, only CORSIKA and GENIE events were used to train the BDT. Because the training lacked any accidental triggers as a reference, the BDT picked the most obvious feature of the GENIE sets: that the signal events were primarily low energy with lower light deposition than the background. These are also key features of the noise triggers.

The GRECO Level 4 places a cut at 0.04 in the BDT score, removing a large fraction of the background sample. A large fraction of the neutrino sample is also removed in order to reduce the muon rates by a factor of 20x.

7.4.3 Rates at Level 4

The rates of the selection after the Level 4 cuts are applied is shown in Table 7.2. After the GRECO Level 4 BDT, the number of atmospheric muons is reduced to 50 Hz, a

Type	IceCube Processing			GRECO L4
	Any Filter	DC Filter	Low-en L3	
CORSIKA	990598	9178	969.818	50.511
MuonGun	60669	2982	442.493	33.562
Accidentals	35855	8117	283.559	11.963
ν_e	1.842	1.721	1.262	0.783
ν_μ	11.317	6.360	4.758	2.503
ν_τ	0.293	0.270	0.206	0.134
MC Total*	1026466	17303	1260	65.893
Data	1154426	19092	1092	68.592

Table 7.2 – The event rates after the Level 4 cuts in GRECO. The total simulated rate is calculated using CORSIKA events and ignoring MuonGun. The data rate is estimated from a burn sample of 30 runs at Level 4. Rates are given in mHz.

mere 25x the muon neutrino rate. The number of accidental triggers is also reduced in the analysis due to the dedicated cuts applied at this level. The number of accidental triggers is still larger than the number of neutrinos expected, however, indicating that further cuts are necessary.

7.5 GRECO Level 5 Cuts

The next stage of cuts, known as the *GRECO Level 5*, or more simply, *L5*, also uses a BDT.

7.5.1 Accidental Rejection at L5

Unlike the previous stages, however, there is no explicit cut introduced at L5 to remove accidental triggers. Instead, an implicit requirement on the number of hit DOMs arises due to the reconstruction used at Level 5. The STW+SRT pulse series containing DeepCore fiducial pulses is used to fit a total of 6 free parameters. The parameters are degenerate if fewer than five hits are used. In this case, the reconstruction fails to converge and the event is removed. Because of this degeneracy, the GRECO Level 5 implicitly requires at least 6 hit DOMs in this hit series.

7.5.2 Muon Rejection at L5

Time to 75% Charge

The first variable used to create the L5 BDT is the amount of time required to deposit 75% of the total charge, the t_{75} . Similar to the QR6 and C2QR6 variables, the t_{75} is a variable designed to look at the hit distribution in time. However, the variable is now produced in the reverse manner: where the QR6 variable refers to the amount of a charge in a given window, the t_{75} instead attempts to find the amount of time for a given charge level. This provides an on the total event length and timing distribution.

The neutrino events deposit energy quickly due to the low energies of the sample of interest in this thesis. The muon events take longer to reach 75% of the total charge due to the long travel time of the events through the detector.

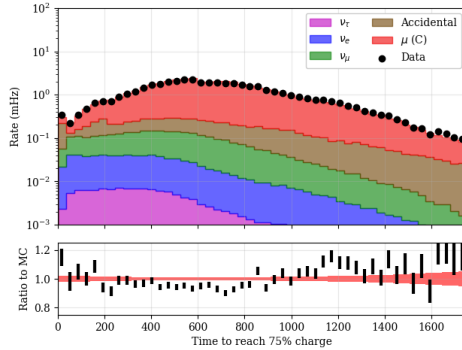


Figure 7.9 – The time to accumulate 75% of the total charge of the event. Atmospheric muons tend to produce light in the detector over a longer time than the low energy atmospheric neutrinos used in the search for tau neutrino appearance.

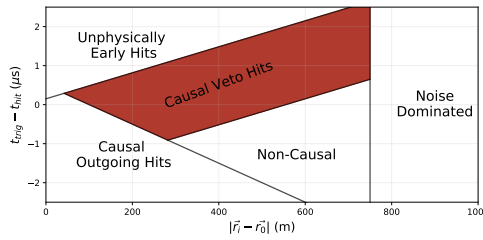


Figure 7.10 – A schematic diagram showing the regions of the VICH algorithm. VICH returns the number of hit DOMs in the shaded region, corresponding to the pulses that are both causally connected with the trigger and entering DeepCore.

Veto Identified Causal Hits

The *Veto Identified Causal Hits* (*VICH*) algorithm is also used in the GRECO Level 5. This algorithm uses an uncleaned hit series to search for hits that are causally connected to the trigger [78]. The first DOM to contribute to the DeepCore trigger is used to define the trigger time and position.

Five regions are defined based on various criteria shown in Figure 7.10. Hits which are not causally connected to the trigger are ignored. Hits which occur too far away from DeepCore are also ignored to reduce the effect of detector noise. A causal region which is consistent with light travel outgoing from the trigger position is also ignored.

The VICH algorithm returns the number of hits in the remaining "causal veto region".

First Hit ρ

The Z position of the first hit was used in the GRECO Level 4 cuts in order to identify atmospheric muons coming from above DeepCore. The X and Y position may also be used to identify muons. These are combined to define a *radial distance* (ρ_{36}) from the center of DeepCore, here defined to be the position of string 36 at $(x, y) = (46.3, -34.9)$.

$$\rho_{36} = \sqrt{(x - x_0)^2 + (y - y_0)^2} \quad (7.8)$$

The radial distance is a general parameter and can be used with any event vertex. For the GRECO Level 5, the first hit in the STW+SRT pulse series is used. Atmospheric muons entering DeepCore are more likely to be found at larger values of ρ_{36} while

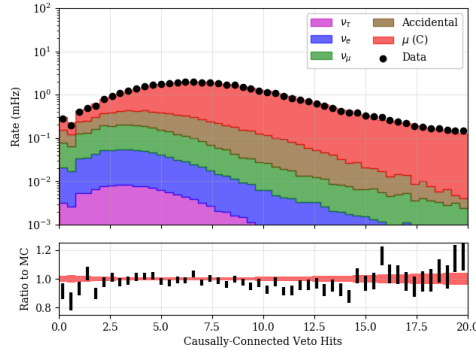


Figure 7.11 – The amount of causally-connected charge discovered in the veto region.

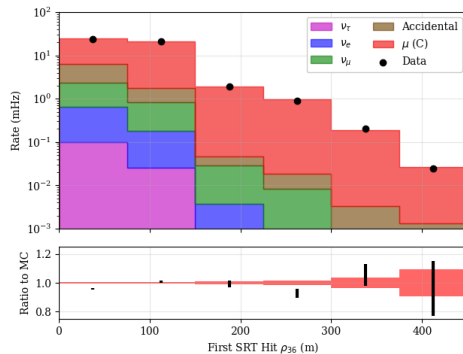


Figure 7.12 – The radial position of the earliest hit of a cleaned hit series. The radial position is measured relative to string 36, the center of DeepCore.

neutrinos are more likely to be found within the DeepCore fiducial volume, which stops at $\rho_{36} = 125$.

Quartiles CoG

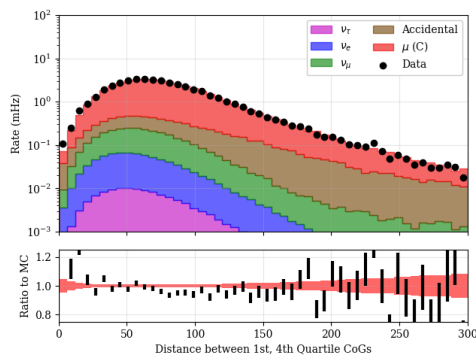


Figure 7.13 – The distance between the centers of gravity of the first and last quartile in time.

The distance traveled by muons may be exploited as well. In particular, a track-like event is expected to travel over a longer distance than a cascade-like event of a similar energy. In GRECO Level 5, the distance between the CoGs of the first and last quartiles in time are used to characterize the distance traveled by the interaction. For atmospheric muon events, this distance is expected to be larger than for low energy neutrino events.

Z-Travel

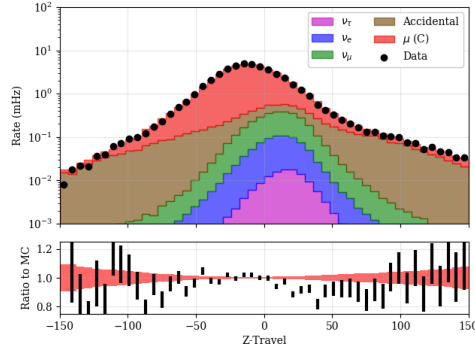


Figure 7.14 – The distance traveled in Z between the first and last quartile of hits in time.

The total distance traveled in the detector is only one useful measure that may be calculated using the quantiles in time. Another useful metric is the distance traveled only in the Z coordinate. The value, known as the *z-travel*, is a measure of the direction of the particle

$$\Delta Z = Z_{Last} - Z_{First} \quad (7.9)$$

The z-travel is typically used to identify atmospheric muons. Atmospheric muons traveling through the detector from above will have a negative z-travel distance and neutrinos may be positive or negative, but is likely to be small due to the small size of neutrino events. The accidental triggers also are well-separated from the simulated neutrinos. These events do not have a preferred direction and appear at all values of the z-travel and appear at all values. The accidental events dominate at the tails of the distribution.

SPE Zenith

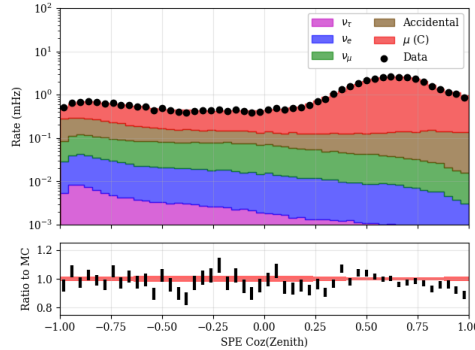


Figure 7.15 – The zenith angle distribution of events from an 11-iteration SPE fit. The fit assumes an infinite track hypothesis and uses only hit DOMs.

More advanced reconstructions are viable at this level, providing new potential for the identification of atmospheric muons from neutrino candidates. These reconstructions must account for the effects of scattering in order to produce meaningful results.

The time required for a Cherenkov photon to reach a DOM from a point-like emission is

$$t_{point} = t_{emission} + \frac{n}{c} |\vec{r}| \quad (7.10)$$

where $|\vec{r}|$ is the distance between the emission point and the DOM. The corresponding time from a muon track is

$$t_{track} = t_{emission} + \frac{\vec{r} \cdot \hat{n} + \rho \tan \theta_C}{c} \quad (7.11)$$

where \hat{n} is a unit vector pointing in the direction of the muon track, θ_C is the Cherenkov angle, and $\rho = |\vec{r} - (\vec{r} \cdot \hat{n}) \hat{n}|$ is the impact parameter of the track with respect to the DOM [93]. In the absence of scattering, all photons would arrive at the DOM according to these times. The addition of scattering delays photons, as they travel a greater distance before reaching the DOM. These delayed photons give a *time residual* distribution. There is no analytic form for the timing which includes the effects of scattering, although approximations exist. One such approximation, the Podel function [110], may be used to estimate the time residual distributions as a function of source-reciever distances [111]. The Podel functions may be used to construct a likelihood of the form

$$L(x_{vertex}, t_{vertex}, \hat{n}) = \prod_i^{pulses} \frac{dP_{Podel}(t_i - t_{point} | x_{vertex}, t_{vertex}, \hat{n})}{dt} \quad (7.12)$$

where P_{Podel} the Podel function used to model the distribution of time residuals. This likelihood may be maximized or, equivalently, the negative log-likelihood may be minimized in order to obtain the best-fit values for the position, time, and direction of the track. The likelihood construction assumes an infinite muon track without defined starting and stopping points. Because this construction implicitly assumes that only one photon is received per DOM, this is referred to as the *single photoelectron (SPE)* fit.

The SPE fit is minimized numerically using the simplex method [112]. A total of 11 seeds are used for the SPE fit performed in the GRECO Level 5, each of which differs from the others in direction. A minimization is performed with each seed and the best fit result is returned. The GRECO Level 5 SPE fit uses another SPE fit, performed with only 2 seeds produced during the general IceCube processing at Level 2.

The zenith angle returned by the SPE fit is used in the Level 5 processing. The atmospheric muons are primarily downgoing events. Therefore the direction of the reconstructed track is a useful tool for separating neutrino signal and atmospheric muon background.

The L5 BDT

The six variables described in the GRECO Level 5 are again used to train a BDT. At the time of training, updated versions of both the GENIE and CORSIKA simulations were provided as part of a ongoing upgrade of the IceCube simulation. The L5 BDT was trained using simulation files containing the then-newly available Vuvuzela V1 noise model and an updated version of the GENIE Monte Carlo generator.

A set of fifteen variables were tested. At each step of the training, the least important variable was removed to limit the possible effects of overtraining. The process continued until changes in the cut efficiency larger than 1% were observed, resulting in a boost decision tree containing the six most important variables tested as described above.

The distribution of BDT score is shown in ???. The data and simulation show good agreement in the muon-dominated region. In the signal region, the data statistics is low,

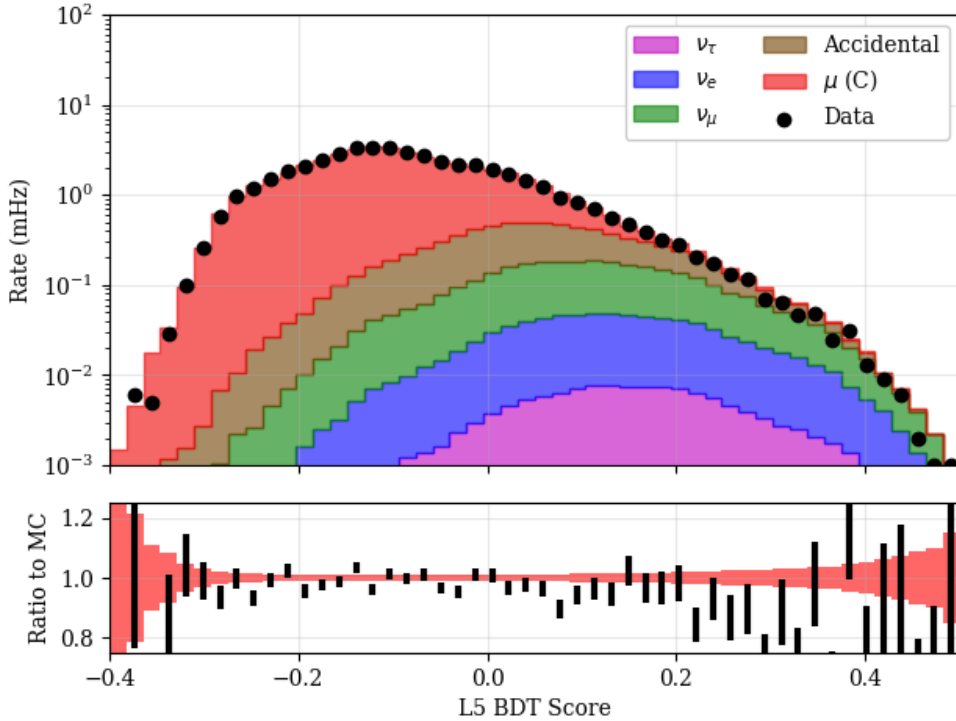


Figure 7.16 – The distribution of the boosted decision tree used at L5. A cut is again applied at 0.04 to remove a significant fraction of atmospheric muon background events.

but the rates are consistent between data and simulation. A cut is placed at a score of 0.04, which gives approximately 95% background rejection with a somewhat significant hit of 30% to all neutrino rates.

7.5.3 Rates at Level 5

After the GRECO Level 5 cuts, the event rates for the atmospheric muons are a factor of 3x larger than the neutrino flux. The rate from accidental triggers in the detector is comparable to the muon neutrino rate. The tau neutrino rate is more than an order of magnitude smaller than the muon rates, making up less than 2% of the total rate. Additional cuts are needed in order to lower both sets of background below the neutrino rate.

7.6 GRECO Level 6 Cuts

Unlike previous levels, the GRECO L6 does not rely on a trained boosted decision tree. The choice was made due to concerns about the significantly limited background simulation. Such a limitation could lead to overtraining, a situation difficult to test with few simulated events.

Two cuts are applied to the sample at GRECO Level 6 for the removal of the remaining accidental triggers. An additional three cuts are applied to reduce the muon background rate.

7.6.1 Accidental Rejection at L6

Type	IceCube Processing			GRECO	
	Any Filter	DC Filter	Low-en L3	L4	L5
CORSIKA	990598	9178	969.818	50.511	4.100
MuonGun	60669	2982	442.493	33.562	3.022
Accidentals	35855	8117	283.559	11.963	1.799
ν_e	1.842	1.721	1.262	0.783	0.544
ν_μ	11.317	6.360	4.758	2.503	1.629
ν_τ	0.293	0.270	0.206	0.134	0.103
MC Total*	1026466	17303	1260	65.893	8.176
Data	1154426	19092	1092	68.592	7.422

Table 7.3 – The event rates after the Level 5 cuts in GRECO. The total simulated rate is calculated using CORSIKA events and ignoring MuonGun. The data rate is estimated from a burn sample of 30 runs at Level 5. Rates are given in mHz.

Fill-Ratio at L6

After GRECO Level 5, the accidental trigger rate is significantly larger than the expected rate of neutrinos. While the rate of these accidental triggers is low at this stage relative to the rate at L3, they form an important background to the remaining set of neutrino events. In order to limit their effect, two cuts are introduced to separate signal neutrinos from the accidental background.

The first of these cuts, the *fill-ratio*, is a variable typically used in the search for high energy cascades [113, 114] by quantifying the topology and compactness of hits within an event.

Fill-Ratio begins with a reconstructed vertex and pulse series. In the case of the GRECO Level 6, the first hit position in DeepCore within a STW+SRT cleaned pulse series is used as an event vertex. Both the pulse series and the event vertex are used in the fill-ratio calculation.

A radius is computed using the provided information. Many options are available for the calculation of different radii, including calculations using the mean or variance of the distance between the pulses and the vertex, a parametrized radius calculation using the number of hit DOMs, and a calculation using a previously reconstructed energy. Each configuration was tested in GRECO Level 6 with the calculation using the mean distance from the vertex showing the most promise.

$$\bar{r}_{\text{Fill-Ratio}} = A \left| \frac{\sum_i^{npulses} (\vec{x}_i - \vec{x}_{\text{vertex}})}{npulses} \right| \quad (7.13)$$

where A is a configurable scale factor. The algorithm next identifies all DOMs contained within a sphere centered on the provided vertex with a radius of $\bar{r}_{\text{Fill-Ratio}}$. The fill-ratio value is then given by the ratio of contained DOMs observing a pulse to the total number of contained DOMs.

$$f = \frac{\sum_i^{ncont} (|\vec{r}_i| < \bar{r}_{\text{Fill-Ratio}} \& Q_i > 0)}{\sum_j^{ncont} (|\vec{r}_j| < \bar{r}_{\text{Fill-Ratio}})} \quad (7.14)$$

This results in a measure of the compactness of a hypothetical cascade, where we expect the resulting hit distribution to be approximately spherically symmetric. An approximately spherically symmetric cascade-like event will completely fill the fill-ratio

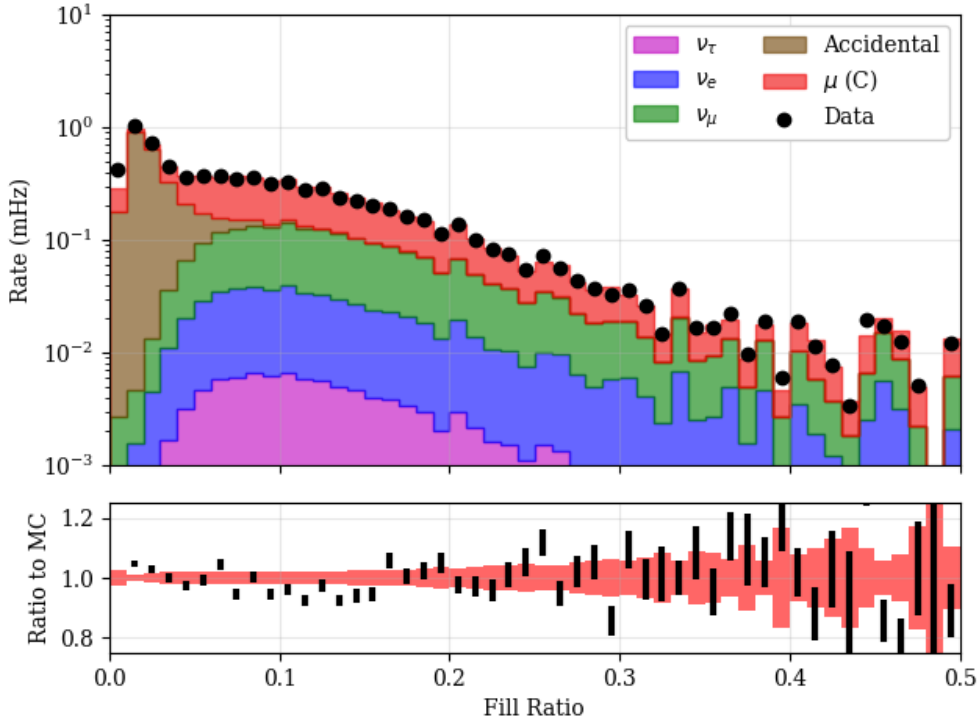


Figure 7.17 – The fill-ratio distribution. Note the excess of events at low values, a region dominated by the accidental triggers due to detector noise in simulation. A cut is applied at 0.05 to remove these accidental triggers.

sphere, resulting in a value near 1.0. An extended, track-like event will have hits that are, on average, further from the starting vertex, leading to a large value of $\bar{f}_{FillRatio}$, a large number of contained DOMs, and a small value of the fill-ratio.

In the context of high energy events, the fill-ratio provides good separation between cascade-like and track-like events. Fill-ratio has not previously been used in low energy analyses, however, due to the short muon tracks of muon neutrino interactions in the 20 GeV region important for atmospheric oscillations. At GRECO Level 6, fill-ratio has been tested to identify neutrino and atmospheric muon events with no significant separating power observed.

Significant separating power was observed between the neutrino events and accidental triggers, however. The accidental triggers include pulses throughout the detector with no clustering in the event, unlike events caused by muon or neutrino interactions, which typically have some type of clustering of pulses around the interaction position. These events receive a large radius due to this lack of clustering and a correspondingly small value of the fill-ratio. A choice of $A=1.6$ and the radius calculated using the mean distance between the first hit and all other cleaned pulses gives the separating power shown in Figure 7.17.

The observed separation at a value of 0.05 allows up to one order of magnitude of reduction in the rate of accidental triggers with a relatively small reduction in signal rate of approximately 10%. The use of fill-ratio reduces the number of accidental triggers expected below the neutrino rate.

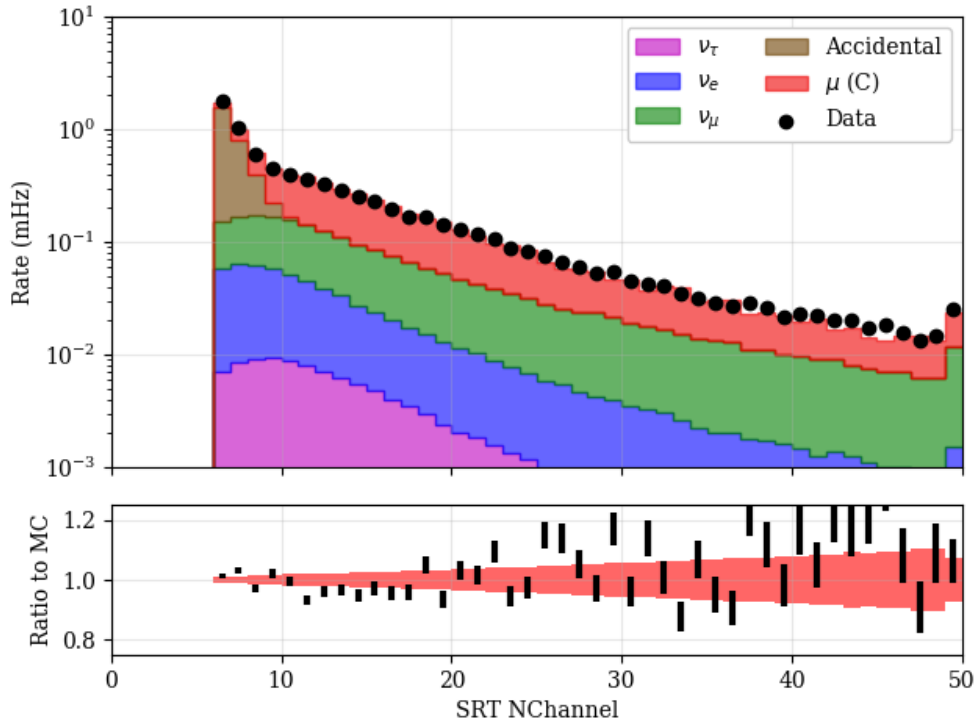


Figure 7.18 – The number of channels in the STW+SRT cleaned hit series at GRECO Level 6. At least 8 hits are required for the reconstruction performed at GRECO Level 7. Events with fewer than 8 hits are removed during Level 6, coincidentally reducing the number of accidental triggers expected.

The L6 NChannel Cut

At GRECO Level 5, the SPE reconstruction was used to calculate the position, time, and direction of an infinite muon track. The final reconstruction used in this analysis, Pegleg, is discussed in Section 7.7. Like the SPE reconstruction used at Level 5, the Pegleg reconstruction requires a minimum number of hits in order to converge. In order to prepare for the reconstruction performed at GRECO Level 7, events with fewer than 8 hits in the STW+SRT cleaned DeepCore pulse series are removed from the selection. This removal is performed in order to prepare for the Pegleg reconstruction, but it also removes a significant number of accidental triggers from the selection. These events, shown in Figure 7.18, The accidental triggers make up about 0.3% of events in the sample following the combination of this cut as and the fill-ratio cut.

7.6.2 Muon Rejection at L6

CorridorCut

The remaining atmospheric muon background after the GRECO Level 5 processing show strong selection bias, with few events remaining showing clear tracks in the veto region. In the past, minimum-ionizing muons were discovered to be leaking into the DeepCore fiducial volume along *corridors*, lines connecting the inner part of the detector to the outer edge without crossing any strings. These events pass between strings and leave little trace in the form of identifiable hits in the outer detector. Examples of these corridors are shown in Figure 7.20.

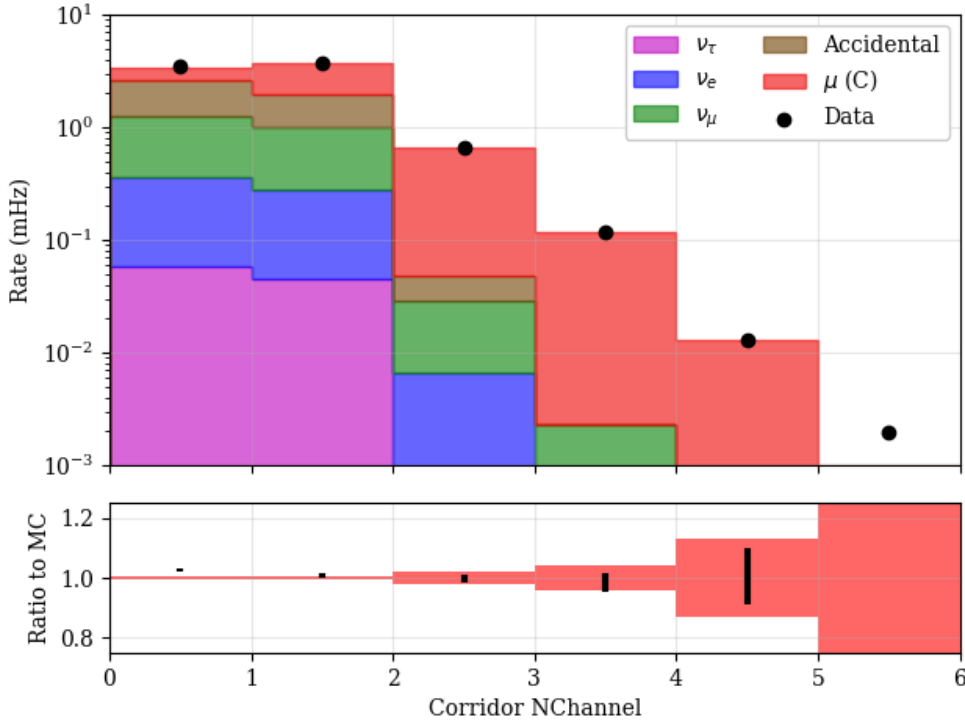


Figure 7.19 – The number of channels discovered along one of the various "corridors" in the detector. Events with at least two hits discovered along a corridor are removed.

In order to identify these muons, a cut was developed to look along pre-defined corridors for SLC hits correlated with pulses in DeepCore. A CoG of the event is calculated from the STW+SRT cleaned DeepCore pulse series. The string nearest the CoG is used to choose a set of 'corridor' strings to check for the event. The number of hit DOMs found on the corridor strings in an uncleaned pulse series is returned.

Due to the effects of random detector noise, a cut limiting the number of discovered corridor hits to 0 would result in a significant loss of signal events. Instead, one hit is allowed, with two or more discovered DOMs leading to the removal of the event from further processing. At this stage, there are few events due to atmospheric muons with detectable energy in the veto, resulting in the removal of few events. The events removed, however, are dominated by atmospheric muons, as seen in Figure 7.19.

FiniteReco Starting Containment

The SPE reconstruction used in L5 was created using an infinite muon hypothesis. In order to refine this reconstruction, the *FiniteReco* algorithm is employed.

FiniteReco is a module that accepts a previous reconstruction and a given set of pulses [78]. The start and end point of the muon track may be estimated by assuming light is emitted from the track at the Cherenkov angle. The direction of the muon track remains unchanged. In the GRECO Level 6 processing, the SPE reconstruction from the Level 5 processing is used in the FiniteReco reconstruction.

The starting position of the resulting reconstructed particle may be used to estimate the interaction point of the particle. Figure ?? shows the position of the reconstructed vertex in terms of depth and distance from string 36. If an event begins outside of the DeepCore fiducial volume, the event is likely to contain a muon and can be removed from

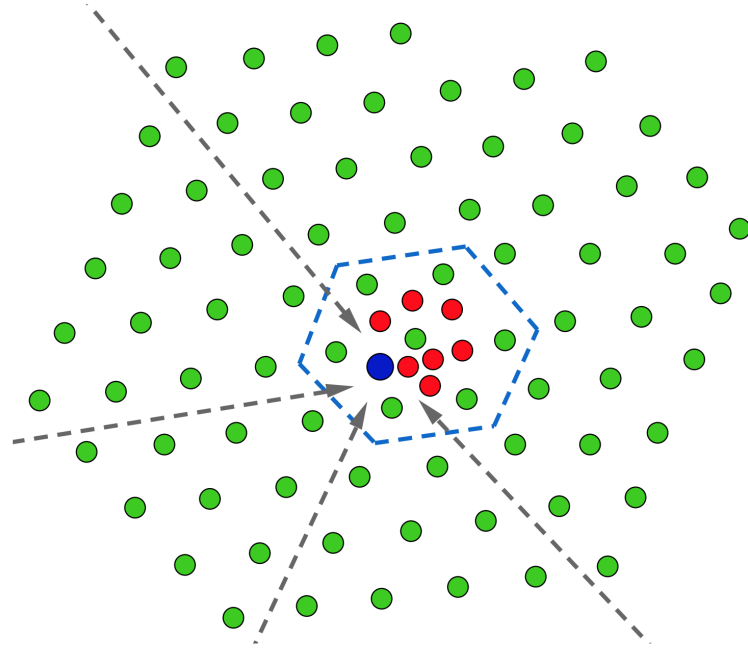


Figure 7.20 – An example of "corridors" into the DeepCore fiducial volume. Muons may pass into the fiducial volume, outlined in blue, undetected by following the paths indicated by the dashed lines. Image from [115]

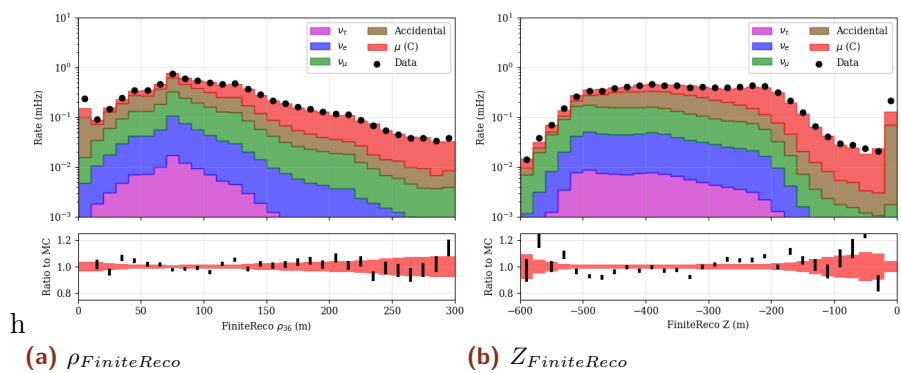


Figure 7.21 – The FiniteReco containment cuts. Note the excess of muons at the top and outer edge of the DeepCore fiducial volume.

lofsubfigure\newline(a)\rho_{FiniteReco}\newline(b)\newlineZ_{FiniteReco}

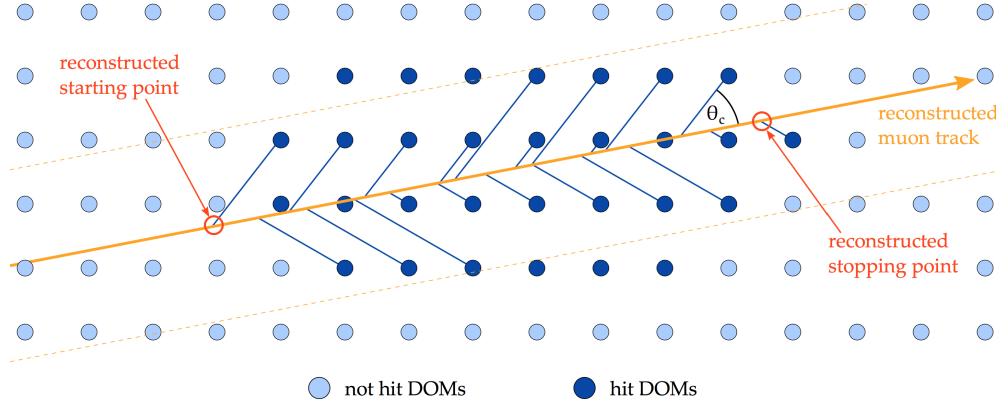


Figure 7.22 – The FiniteReco starting and endpoint reconstruction method. FiniteReco uses an existing muon track reconstruction and the collection of hit DOMs to estimate the starting and end point of the muon track. Diagram from [78].

Type	IceCube Processing			GRECO		
	Any Filter	DC Filter	Low-en L3	L4	L5	L6
CORSIKA	990598	9178	969.818	50.511	4.100	0.443
MuonGun	60669	2982	442.493	33.562	3.022	0.315
Accidentals	35855	8117	283.559	11.963	1.799	0.102
ν_e	1.842	1.721	1.262	0.783	0.544	0.362
ν_μ	11.317	6.360	4.758	2.503	1.629	1.011
ν_τ	0.293	0.270	0.206	0.134	0.103	0.074
MC Total*	1026466	17303	1260	65.893	8.176	1.991
Data	1154426	19092	1092	68.592	7.422	1.841

Table 7.4 – The event rates after the Level 6 cuts in GRECO. The total simulated rate is calculated using CORSIKA events and ignoring MuonGun. The data rate is estimated from a burn sample of 100 runs at Level 6. Rates are given in mHz.

the sample. Cuts are applied at the positions shown, resulting in a significant reduction in the number of muon events expected at final level.

find good quality
swedish camera pics?

7.6.3 Rates at Level 6

After the GRECO Level 6 cuts, the sample is dominated by neutrino events. The expected muon rate from CORSIKA simulation makes up 22% of the total sample. The rate from accidental events is also small, with only 5% of events due to random detector noise.

7.7 GRECO Level 7: Final Level

The final level of the GRECO event selection, *GRECO Level 7*, is the most computationally expensive stage of the selection. While previous stages have focused on speed, using cuts based on analytic variables or on fast reconstructions using approximations to the scattering of the ice, the GRECO Level 7 employs the Pegleg reconstruction. This reconstruction is expensive, requiring an average of 10 minutes per event.

The Pegleg reconstruction can be used to define new cuts to further reduce the atmospheric muon rates

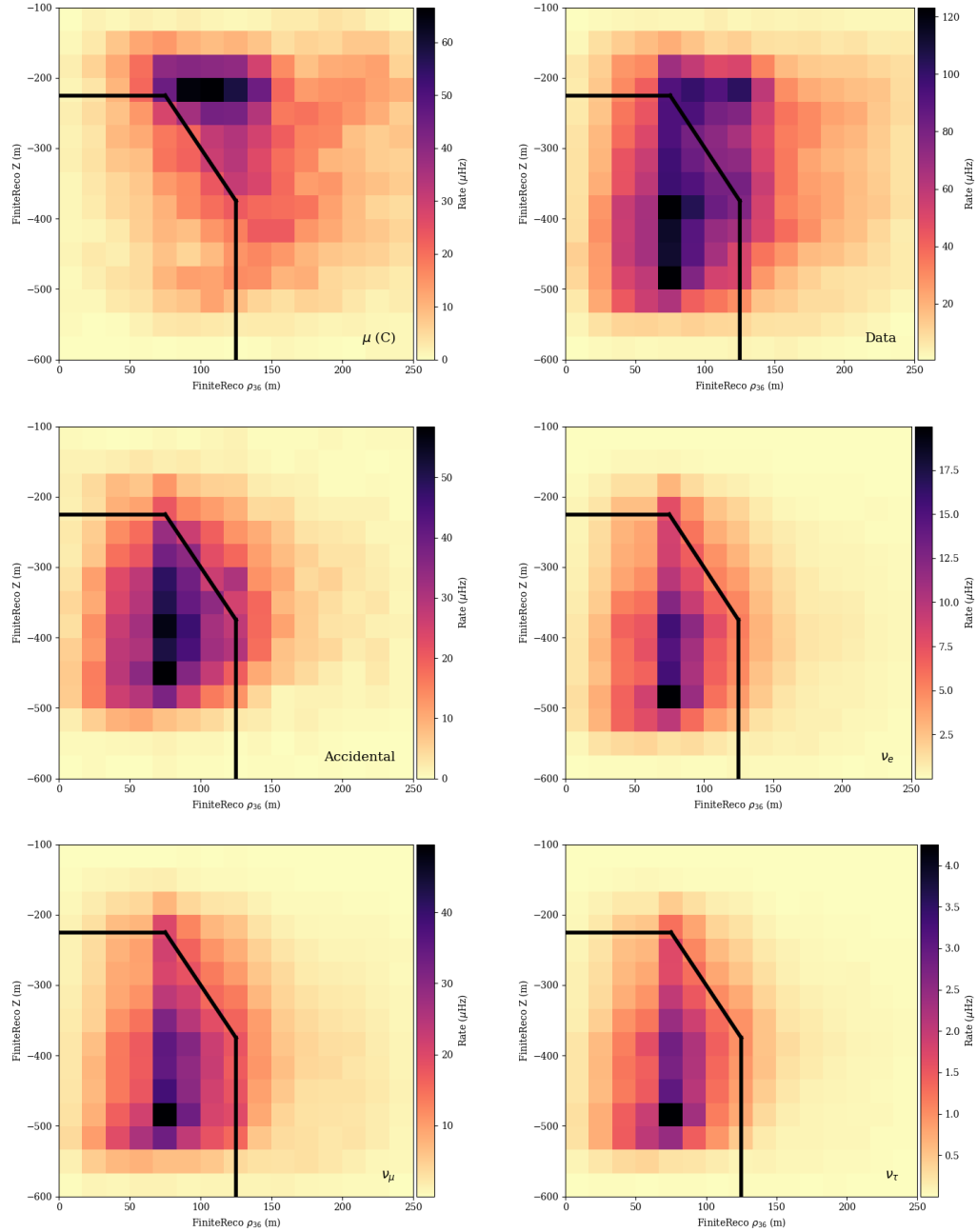


Figure 7.23 – The FiniteReco containment cut for each of the channels. The cut itself is shown with the black line. The atmospheric muons, modeled with the CORSIKA generator, are reconstructed at the top of the DeepCore volume.

7.7.1 Reconstruction using PegLeg

The existing reconstructions used in previous levels of the GRECO processing use either analytic or simplified likelihood reconstructions to estimate particle parameters. The position of the first hit and the finite muon reconstruction from FiniteReco provide separating power between atmospheric muons and neutrino events, but are designed to be computationally inexpensive instead of precise. At final level, these estimates are refined using a novel reconstruction method developed specifically for low-energy and oscillation searches with DeepCore.

The *PegLeg* reconstruction [106], a refinement of previous work [115], is a low-energy reconstruction that uses a hybrid cascade+muon hypothesis. The reconstruction returns a total of eight parameters: the position (x, y, z), time (t), direction (θ, ϕ), total energy ($E_{cascade}$) and track length (L). The total energy of the event is calculated by assuming the muon track is minimally ionizing with an energy loss of 220 MeV/m in ice [115].

$$E_{total} = E_{cascade} + (220\text{MeV}/\text{m}) L \quad (7.15)$$

The algorithm requires seeds for each of the particle parameters and a collection of hits over which to run. Pegleg also requires a set of splines describing the expected charge as a function of distance from the emission point. These splines are created using the CLSim module (see Section 4.2.2) to directly account for the scattering and absorption properties of the bulk ice model.

For each particle hypothesis, the event is broken into time steps in time based on the observed pulses in the event. At each time step, the expected charge at each DOM is calculated based on the energy and position of the particle hypothesis. The charge expectation is evaluated for all DOMs, regardless of whether a hit is observed or not. The total likelihood of the hypothesis is then the product of the likelihoods at each DOM.

The likelihood space itself typically possesses multiple local minima due to the small number of hits. The fit is performed using the MultiNest minimizer package [116] in order to handle the complex likelihood space. The MultiNest algorithm calculates the likelihood for a set of 100 hypotheses at each iteration. The likelihood at each point is used to estimate the underlying likelihood space and produces new hypotheses for testing using importance nested sampling [117].

Given the large dimensionality of the space, significant computational power is required for the fit. Simplifications are introduced to reduce the computational requirements of the Pegleg reconstruction. Track lengths are limited to integer multiples of the track length used to produce the ice model spline functions. While this requirement is lifted in newer versions of the software [106], that change has not yet propagated to the current GRECO events. In addition, only DOMs within 150 meters of the current particle position are evaluated to find the expected charge. All other DOMs are assumed to have an expected charge consistent with noise rates. This assumption allows the minimizer to avoid costly calculations of expected charge for distant DOMs at the expense of higher energy event resolutions.

In early versions of the PegLeg fit, the charge of individual pulses is used directly in the likelihood calculations [118]. Following the discoveries discussed in 7.8.1, however, the use of the charge was removed [106]. In the version of PegLeg used in the final version of this analysis, a deadtime window of 45 nanoseconds is introduced for each DOM directly following a pulse. During this window, the DOM may not contribute any further information to the fit. This changes the reconstruction likelihood from being on the observed charge to being sensitive only to the observation or absence of charge.

Using this modification, disagreements between the data and simulated pulses resulting from mismodeling may be minimized.

Each event takes approximately 10 minutes on average to converge in the reconstruction. There also exists a significant tail to the reconstruction time, sometimes extending to multiple hours for a single event. With a large expected sample of events, the reconstruction time is the most computationally intensive part of the event selection.

7.7.2 Containment with PegLeg

With a more refined reconstruction, additional constraints on the containment of the starting vertices are possible. Similar to the work done with FiniteReco at Level 6, the reconstructed Z and ρ_{36} receive cuts in two dimensions as shown in 7.24. Once again, events at the top of and near the edge of DeepCore are more likely to be muons. An additional cut is applied at the bottom of the detector in order to limit the effect of observed discrepancies between data and simulation. Removing these events results in a 75% reduction of the atmospheric muon background at a cost of approximately 10% of the overall neutrino rate.

7.7.3 Other Cuts at L7

Cuts are also applied to the average reconstructed energy per hit DOM and the scatter in the timing distribution of hits., shown together in Figure 7.25 The former is expected to yields high values for events dominated by flaring DOMs (Section 7.7.3) or events where a particle interaction occurs very close to the face of a DOM. The distribution also shows some disagreement at low values, although good agreement between data and simulation is found for large values.

The reason for this is likely related to the issues discovered in Section 7.8.1, although this disagreement has not been investigated further. A cut removing events with more than 3 GeV/DOM is applied only to events with fewer than 14 hits, limiting the impact on the neutrino signal events.

The scatter in the hit times shows very good agreement between data and simulation and is useful as a proxy for the overall scattering of the event. The cut, which removes events where the standard deviation of the hit times is larger than 800 nanoseconds, is also only applied for events with fewer than 14 hits. This limits the loss of neutrino events while removing a fraction of the remaining accidental triggers.

The cuts applied to the standard deviation in the hit times and the reconstructed energy per hit DOM are applied in two dimensions, as shown in Figure 7.25.

7.8 Calibration Discoveries with GRECO

Checks with the GRECO selection during the search for appearance uncovered disagreements between data and simulation. Five discoveries made with the selection are discussed here.

7.8.1 The Simulation SPE Templates

During the development of the GRECO selection, new calibration measurements showed that the SPE peak in data was misaligned. This SPE peak, a part of the SPE template described for simulation in Section 4.3.1, is used to convert between the pulses of the waveform, in units of millivolts, and the charge units in IceCube, in units of photoelectrons. The peak is intended to correspond to a value of 1 PE, indicating a single photon interacting at the photocathode of the PMT. While previous measurements had measured

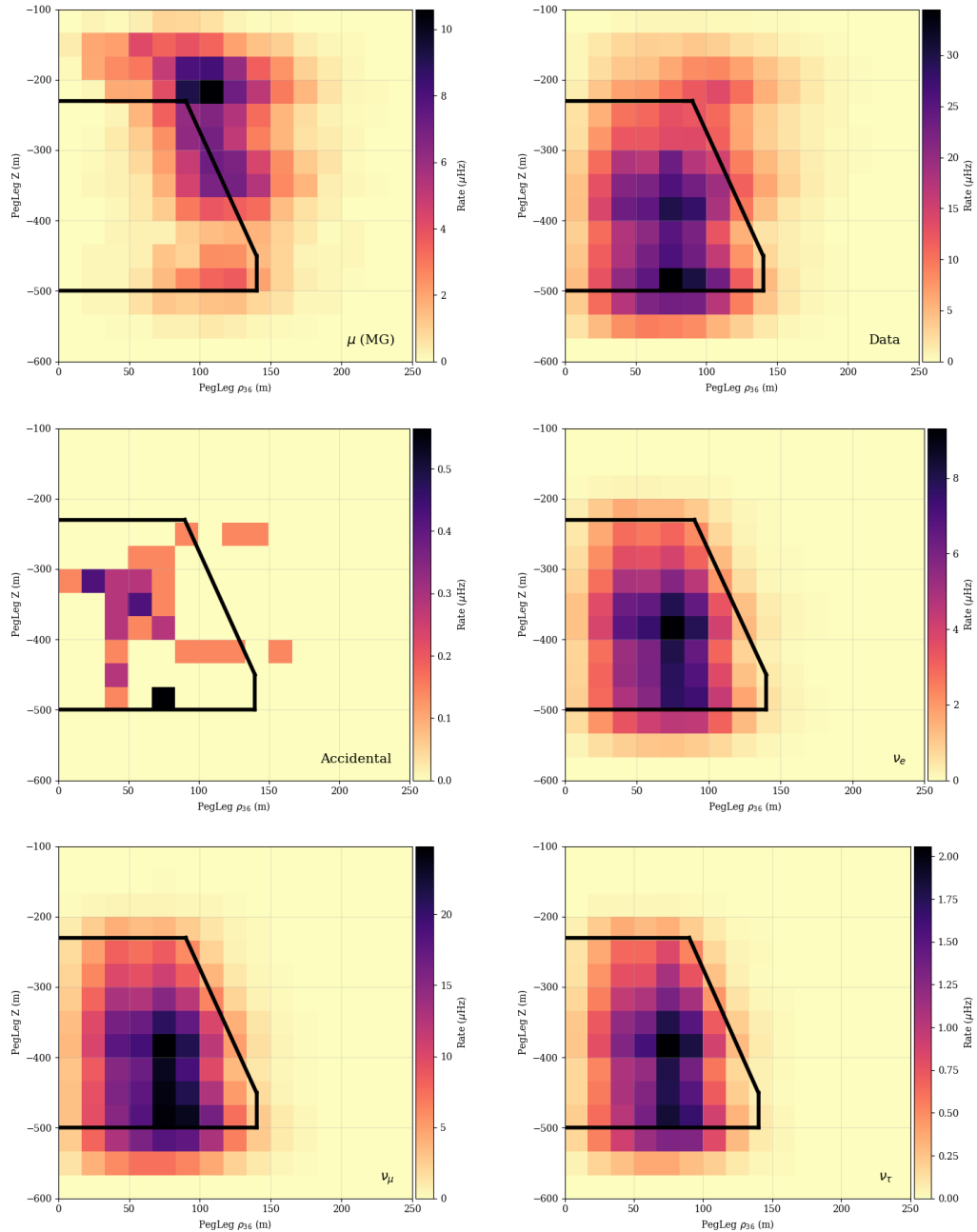


Figure 7.24 – The Pegeg L7 containment cut for each of the channels. The cut is shown with the black line. Note that the atmospheric muons are here represented by the higher-statistics MuonGun sample.

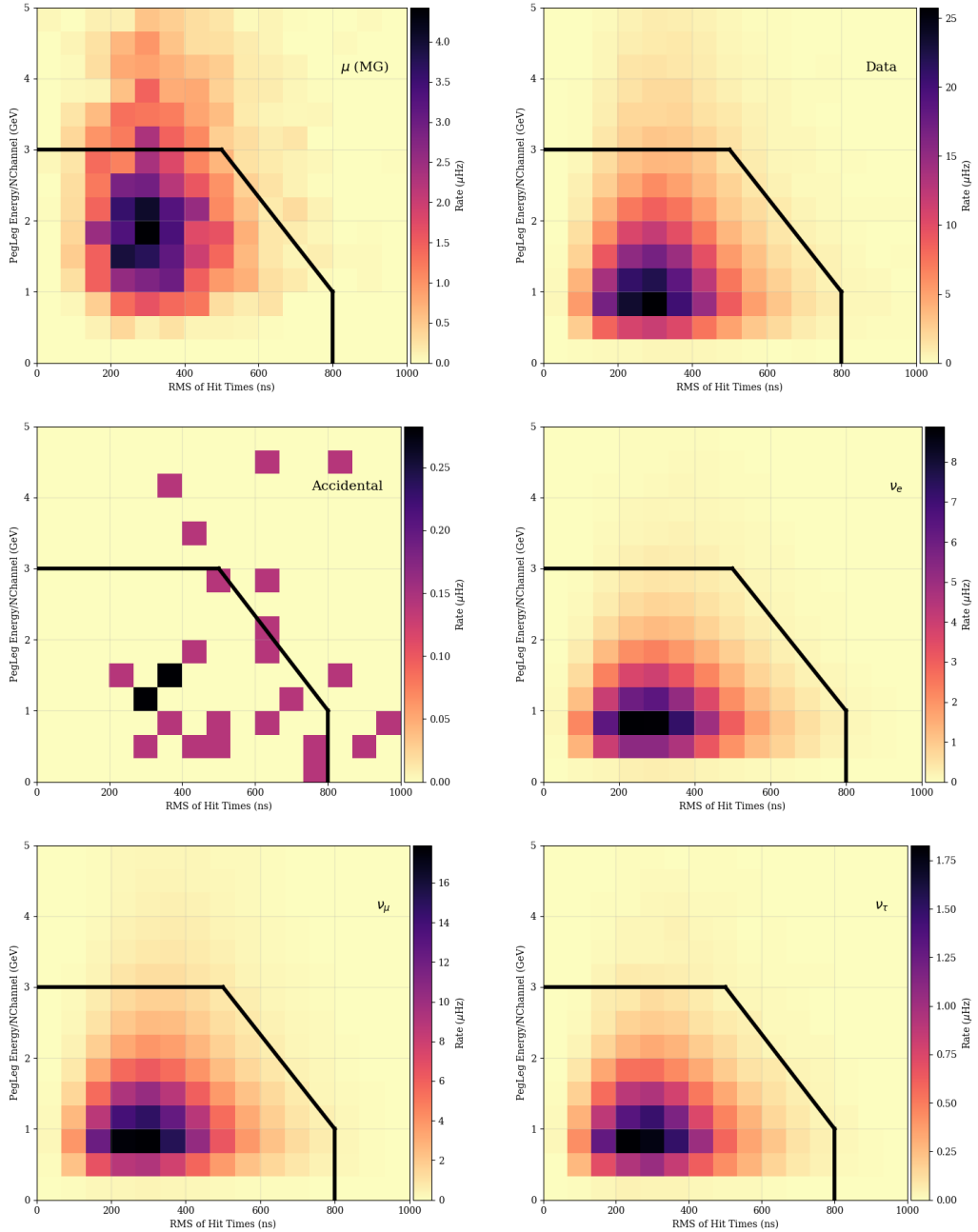


Figure 7.25 – The cuts applied to the reconstructed energy per hit DOM and the standard deviation in the hit times. The cuts are designed to remove atmospheric muons and highly scattered hits from the selection. The 2D cut shown here is applied only to hits events with fewer than 14 hit DOMs.

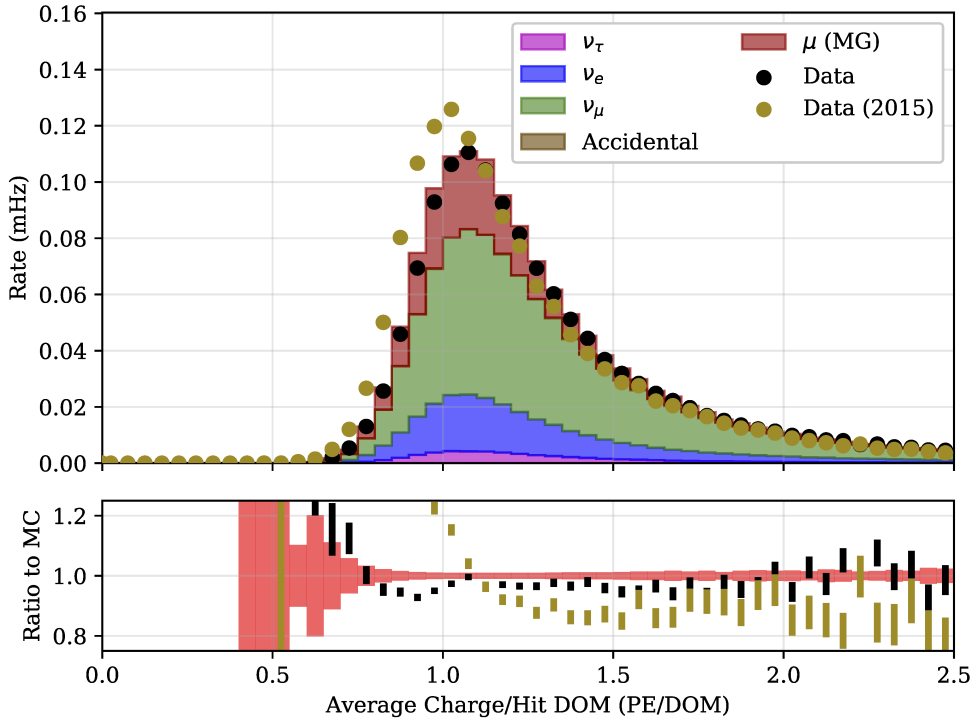


Figure 7.26 – The effects of the SPE correction applied to data in 2015. As expected, the peak of the distribution is closer to 1 PE in the corrected 2015 data (gold circles) than in previous years (black circles). The corrected data disagrees with the simulation.

an average SPE template for the detector data, the new calibrations were used to measure the templates for individual DOMs.

The updated calibration measurements showed that the SPE peak used in data was not at 1 PE, but was, on average, at 1.045 PE. The IceCube collaboration subsequently corrected the SPE templates for data beginning in the IC86-5 (2015-2016) season, shifting the location of the extracted SPE peak in data from 1.045 PE to 1 PE. The correction is believed to result in a more accurate extraction of the charge in data. The simulation SPE template, shown in Figure 4.3, peaked at 1 PE by definition and was not changed. This shift mirrors effects observed during the fitting of the Vuvuzela V2 model in which a charge scaling variable was introduced to improve agreement with data and simulation (see Section 5.3).

After the correction, analyses searching for high energy neutrinos in the IceCube detector showed improved data and simulation agreement. Previous analyses searching for oscillations in DeepCore had observed good agreement between data and Monte Carlo simulations prior to the correction to the SPE template in data [79, 80, 81]. In order to evaluate the effect of the correction, the IC86-5 data was processed using the standard GRECO processing scripts.

At low energies, most observed hits are due to single photons reaching the PMT. The average charge per DOM is therefore expected to approximately follow the SPE template. This variable was used to evaluate the effects of the correction at Level 7 of the GRECO selection.

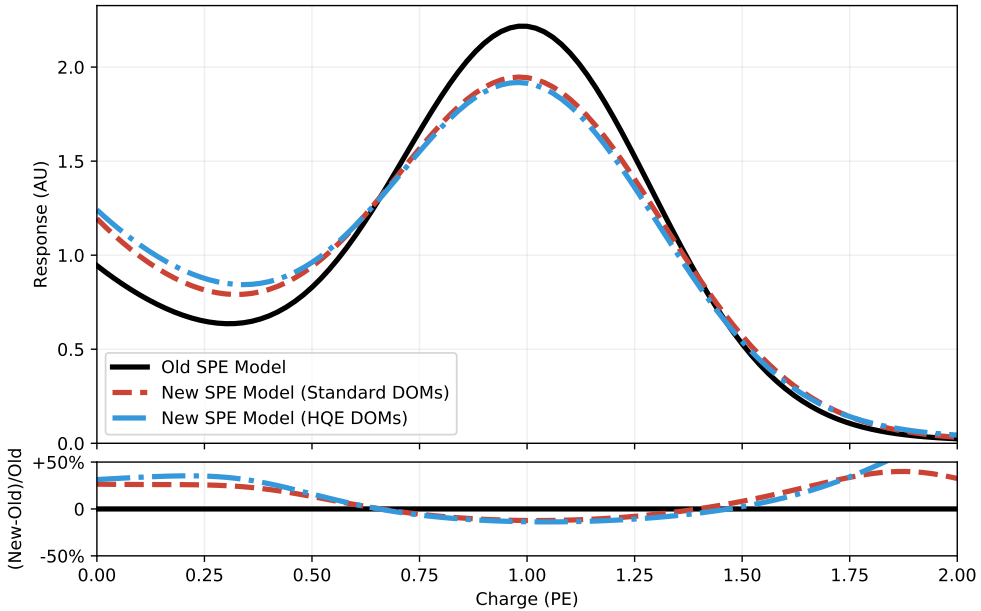


Figure 7.27 – A comparison of the old SPE template previously used in the simulation of events to the new average templates for the high quantum efficiency DOMs and the standard IceCube DOMs. The new models predict a higher number of pulses with low charge, consistent with the excess observed from the corrected 2015 data in Figure 7.26.

The result is shown in Figure 7.26. As expected, the 2015 data shows a shift downward, with a peak closer to 1 PE. Unexpectedly, however, the corrected dataset shows substantial disagreement with simulated events.

Investigations of the disagreement showed that the data and simulation disagreed at all cut levels, including low cut levels unrelated to the GRECO selection. The issue has been identified to be the SPE templates used in the simulation. The template used is calculated as the average of the templates 118 DOMs measured in the lab prior to deployment [102]. All DOMs are simulated using identical parameters.

New work has been performed to apply the SPE templates measured in the data calibrations to the Monte Carlo simulation used in IceCube. These results have produced new SPE templates for all DOMs in the detector. The new templates, shown in Figure 7.27, predict more hits with low charges, as observed in the 2015 data of Figure 7.26.

These new simulation SPE template are newly implemented in the iceCube simulation. Due to time constraints, the updated simulation has not been evaluated in the GRECO sample. In order to reduce the potential disagreement arising between data and simulation due to mismodeled low charges, both the data and simulation have been processed with a version of the Pegleg reconstruction designed to limit the dependence on charge information.

7.8.2 Disagreement in PMT Simulation

While investigating charge variables related to the SPE template, additional disagreements were discovered in the PMT simulation. The first suspected cause of charge disagreements was erroneous splitting of the waveform during charge extraction.

The SPE template is used to convert the digitized waveforms from the FADC and ATWD into reconstructed photoelectrons consisting of charge and timing information. While

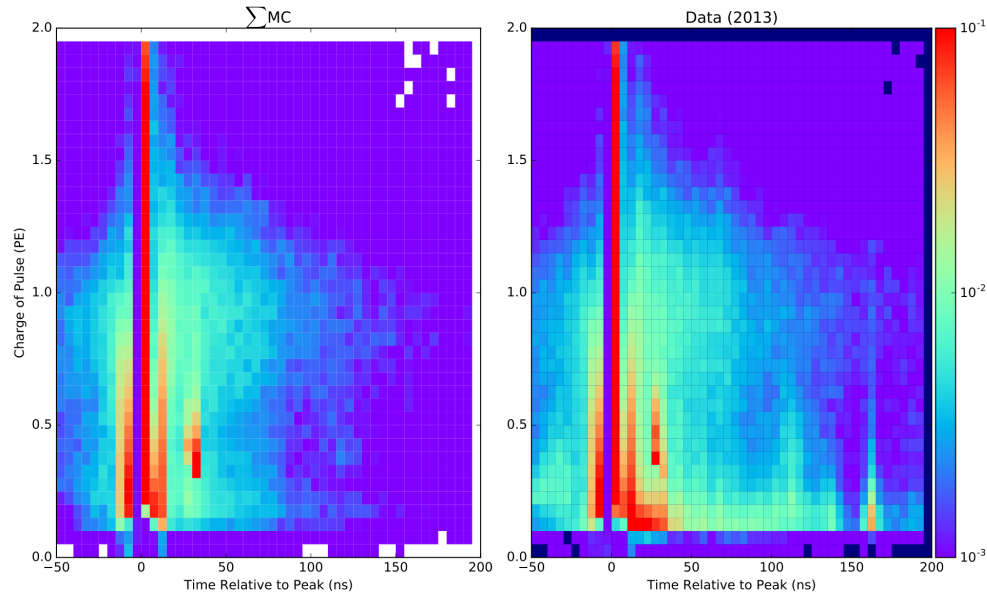


Figure 7.28 – A comparison of the charge extraction in data and simulation at GRECO L7. Both the time and charge are shown for individual pulses on all DOMs. The time is measured relative to the largest pulse observed on each DOM during an event. The data and simulation histograms are independently normalized to 1.0. While the two show broad agreement, notable differences occur at low charge.

the simulated response is known exactly when extracting pulses, the associated charge response of the DOM in data requires careful calibration. Using a mismodeled charge response to extract pulses in the data can result in single photoelectrons being erroneously split into multiple smaller reconstructed pulses.

Potential mismodeling effects of the charge extraction were checked in 7.28. In these figures, the charge of each individual pulse is shown as a function of the arrival time, which is normalized to the time of the largest extracted pulse in the DOM for each event.

Significant disagreements between the data and simulation are visible. The erroneously split pulses are visible in data as a low-charge tail from $t=0$ until $t=50$ nanoseconds. In addition to this effect, however, many other regions of disagreement are visible. In data, there appear to be a significant number of prepulses not visible in the simulation occurring between $t=-50$ and $t=-20$ nanoseconds. The structure of the late pulses, appearing with approximately 0.4 PE of charge and at time $t=30$ nanoseconds also appears notably different between the data and simulation. A final set of pulses, occurring at 160 nanoseconds, also appears to be unsimulated. This timing structure requires additional calibration resources to identify and better simulate, the scope of which is beyond this work. Regardless, the presence of unsimulated features indicates that at least some charge information in the simulation is unreliable.

The observed disagreements in the pulses and the SPE templates led to the removal of charge information from the Pegleg reconstruction. The disagreements remain unexplained, although updated calibration measurements may be performed using the GRECO sample. Using a procedure similar to that used for the fitting of the Vuvuzela V2 parameters (see Section 5.3), it may be possible to produce a more accurate model of the PMT effects in IceCube in the future.

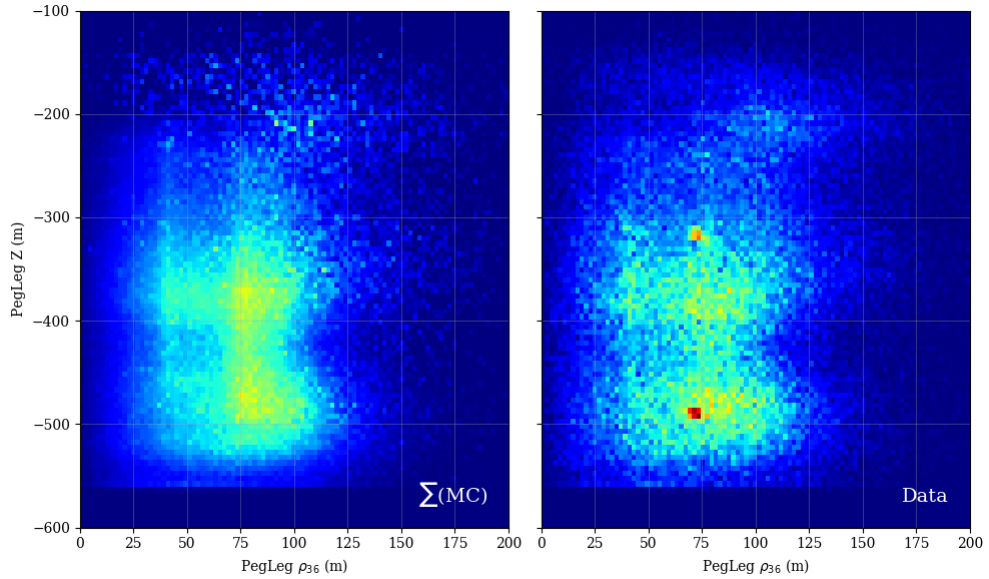


Figure 7.29 – The reconstructed Z position plotted against the reconstructed distance from string 36. The L7 cuts from GRECO have been removed for this plot. The colorbars in both plots have been normalized to be identical. The data and simulation show reasonable agreement except for two points in the data, near $\rho_{36} = 75$ at depths of -310 and -490.

7.8.3 Discovery of Flaring DOMs

Initial investigations into the poor agreement between data and Monte Carlo simulations led to comparisons of various reconstructed quantities believed to be independent of the expected signal. The decision was made to investigate these quantities using the simulation weights calculated with the baseline values.

Previous analyses have shown that the uncertainties in the ice model can lead to significant disagreements between data and simulation. The existing uncertainties on the bulk ice assume that the coefficients for all ice layers are fully correlated. However, it is possible that the ice model coefficients in parts of the detector are more poorly modeled than others. By looking at the event rate in data and simulation as a function of the depth and position in the detector, discrepancies in the ice model may be identified.

Two-dimensional histograms of the depth and radial distance also show systematic disagreement in some regions, as shown in 7.29. These excess events appear to occur on a single string, string 83, shown in 7.30, indicating an effect occurring due to the DOM hardware in the detector.

Follow-up work has shown that these DOMs, known here as *flaring DOMs*, appear to spontaneously emit light for unknown reasons. The light output is identifiable both based on the position of the hits and the amount of charge observed in nearby DOMs. These spurious events, first discovered in the GRECO selection, have since spawned dedicated searches to better understand spontaneous light emission from the DOMs. A small handful of DOMs have been identified by these searches with emission times as frequent as 1 Hz.

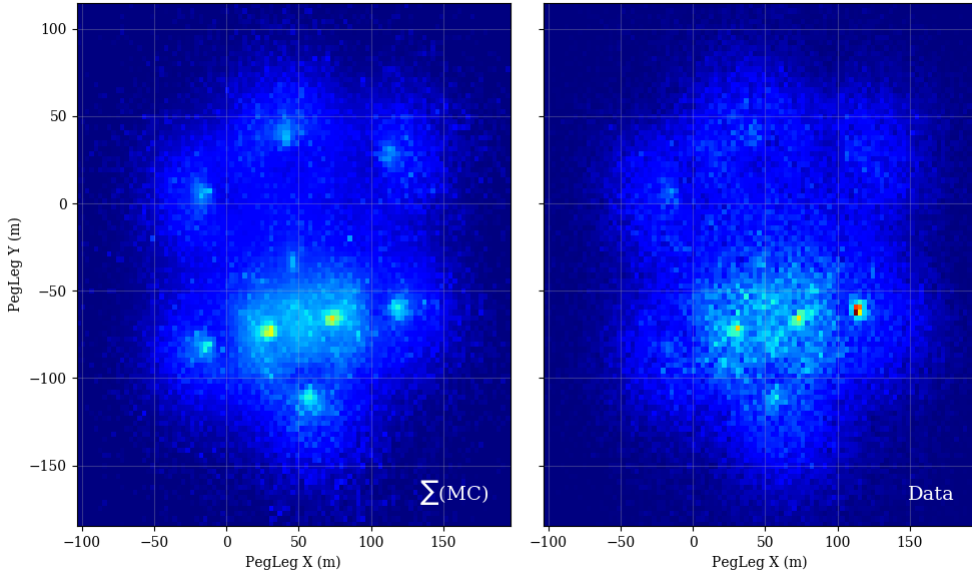


Figure 7.30 – The reconstructed X position and Y position of events in the detector. The L7 cuts from GRECO have been removed for this plot. The colorbars in both plots have been normalized to be identical. Once again, reasonable agreement is observed in most regions, although data events have a clear excess near $x=110$ m, $y=-60$ m. This position corresponds to string 83.

The affected events may be identified based on the charge profiles. DOMs directly adjacent to the emitting DOM observe a significant fraction of the total charge of the event. This may be characterized using the ‘charge RMS’ of the event

$$q_{RMS} = \frac{\sigma_q}{\sum_{hits} q_i} \quad (7.16)$$

This is shown in Figure 7.31. Events with a $q_{RMS} > 0.85$ are removed from the analysis, removing the most obvious spurious events. A total of 975 events are removed from the GRECO data, resulting in a total reduction of 1.3% of the event sample. The removal of these events in data and simulation does not significantly impact the sample due to the low event rates involved.

7.8.4 Simulation of Bedrock

Further investigations of the reconstructed Z position from Pegleg uncovered disagreements, shown in 7.32. A small deficit of events in data is observed at $Z \approx -450$. Checks performed with other samples have shown similar disagreements at these depths, indicating disagreement in the ice model. Previously unblinded oscillation samples showing this issue have not observed significant issues in the goodness-of-fit. New ice models are underway with dedicated work to fix this region is underway.

Near the bottom of the detector, a clear excess of events in data indicated a mismodeling in the simulation. Events which interact below the detector typically require higher energies than those inside the fiducial volume in order to trigger DeepCore.

In the GRECO selection, events with energies above 1 TeV are modeled using NuGen simulation in order to account for events not properly simulated in the GENIE generator. Previous investigations have shown that the two generators use similar models of the cross-section and return similar event rates at low levels. The events from the NuGen

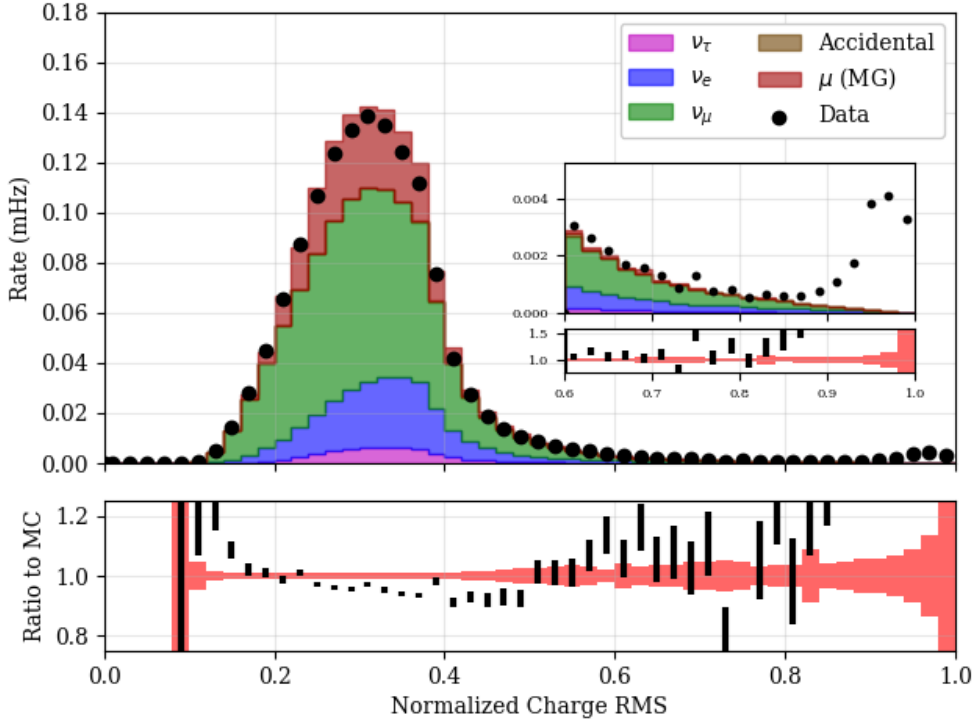


Figure 7.31 – The RMS of the charges within each event at final level. The value of the RMS is normalized using the total charge observed. The events with flaring DOMs cluster at high values of the charge RMS, visible in the inset.

generator were shown to make up a significant fraction of the high energy tail in the GRECO sample. These events were therefore checked for potential issues.

The NuGen and GENIE simulated event samples are merged in the GRECO analyses after removing NuGen events in overlapping energy ranges. The generated samples do include these overlapping regions, however. For the purposes of testing, the full sample of GENIE and NuGen events were compared in true and reconstructed energy and Z position. A comparison of the overlapping energy range of NuGen and GENIE events contained within the DeepCore fiducial volume showed some disagreement in the muon neutrino event sample. Figure 7.33 shows no disagreement in the neutral current and electron neutrino charged current events, indicating an effect specific to the muon neutrinos.

Limiting the energy range of both samples to the overlapping region 100-1000 GeV, other distributions may be checked. The cause of the discrepancy between the generators is shown in Figure 7.34. The two generators show broad agreement until a depth of approximately -830 meters, corresponding to the interface between the Antarctic glacier and the underlying bedrock. In the GRECO selection, only events with an outgoing muon have the range necessary to reach DeepCore from the bedrock.

Further checks discovered the issue in IceCube's implementation of the GENIE generator. When calculating the interaction probability for the neutrino interactions, the density of material is included. In the implementation of GENIE previously used by the IceCube collaboration, events were assumed to occur solely within or near the fiducial volume of DeepCore due to the low energies involved. The bedrock was therefore deemed unnecessary and not implemented in favor of assuming a uniform density of ice throughout the simulation volume. During initial implementation, the GENIE generator was planned

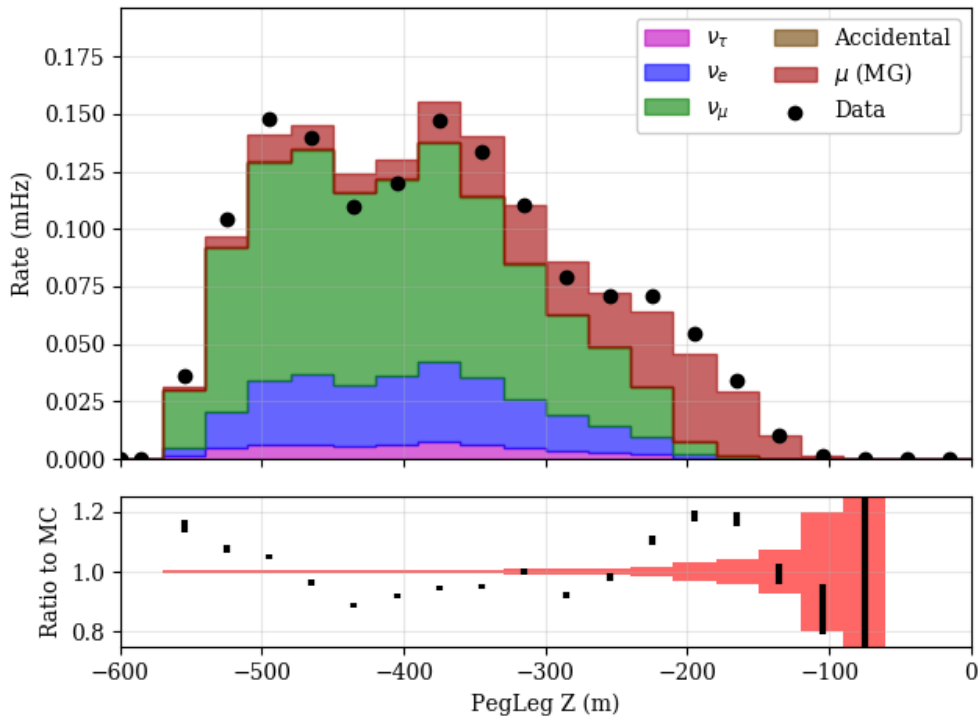


Figure 7.32 – The reconstructed Z position using PegLeg. The GRECO L7 cuts have not been applied in order to show discrepancies below the detector. Noticeable disagreement is seen below the detector at a depth of -500 m. Additional disagreements are also visible at the top of DeepCore, a region dominated by atmospheric muons.

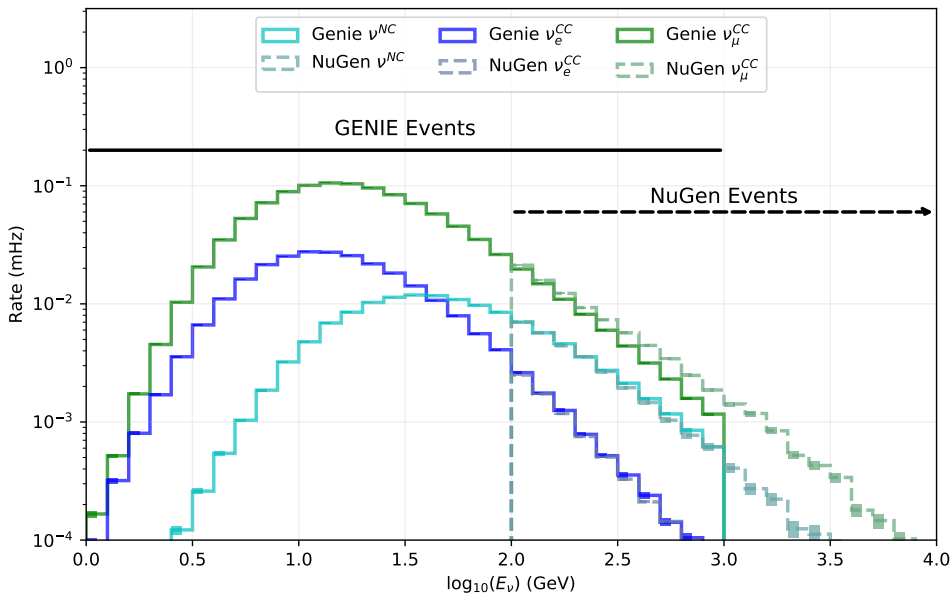


Figure 7.33 – The NuGen and GENIE true energy spectra at final level. The neutrinos are shown without oscillations applied. The overlapping energy range, 100-1000 GeV, show good agreement between the two generators for neutral current and electron neutrino charged current interactions. The muon neutrinos disagree in the overlapping energy range.

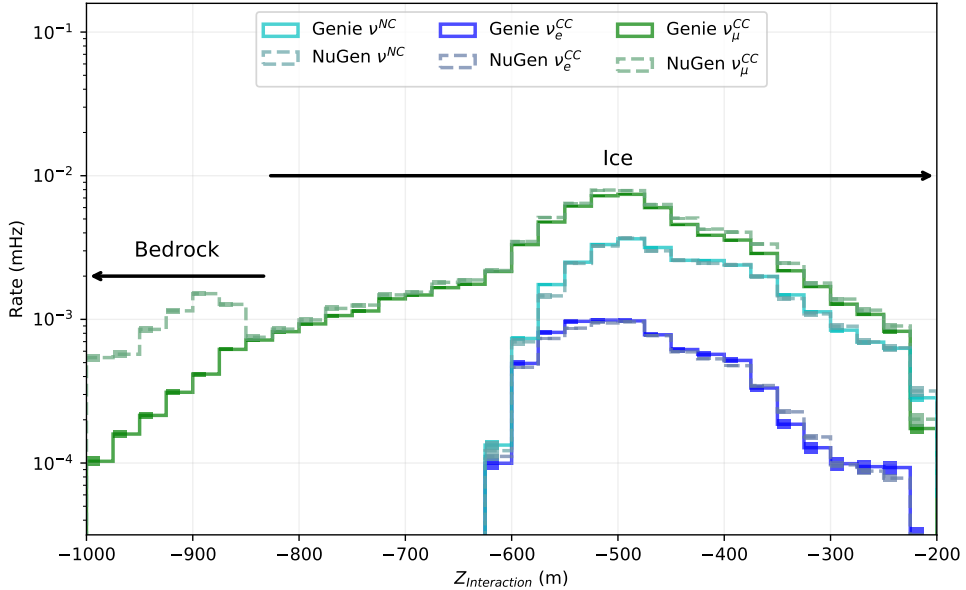


Figure 7.34 – The NuGen and GENIE interaction depths at final level. Only events from the overlapping region of 100 GeV to 1 TeV are included. NuGen and GENIE agree above -830 m . The implementation of the GENIE generator in IceCube does not correctly model the bedrock at $Z < -830\text{ m}$.

for use up to 100 GeV due to technical limitations. Later work expanded this range up to 1 TeV with future work ongoing to push toward 10 TeV. The problems with the bedrock were mistakenly overlooked during the upgrades of the generator, leading to the systematic disagreement shown in Figure 7.32.

The bedrock has been properly included in both the NuGen generator as well as the PROPOSAL module for propagating the charged leptons. GENIE events therefore suffer solely from an incorrect interaction probability due to the discovered bug.

In order to limit other potential issues from the bedrock, the analysis space was restricted, removing events below the bottom of the detector ($Z_{reco} \leq -500$). This cut significantly reduces the size of the sample by reducing the high energy events included at final level. The additional cut has some impact on the expected sensitivity, but was deemed necessary to minimize the potential impact of systematics issues associated with the bedrock events.

7.8.5 Anisotropy of DeepCore

The reconstructed zenith and energy are used in the search for appearance. The azimuthal direction is not used for oscillation searches, but was checked for agreement.

As described in Section 3.2.2, the anisotropy of the ice model can bias the propagation of light in the detector in the azimuthal direction. This can result in azimuthally biased reconstructions. The anisotropy is characterized using a direction and magnitude, both of which are used to model the effect throughout the detector. The IceCube simulation assumes that the anisotropy is independent of depth.

The reconstructed azimuthal directions from Pegleg in the GRECO sample is shown in Figure 7.35. Both data and the simulated events show sinusoidal variation as a function of azimuthal direction, a result of the anisotropy in the ice. The effect in data is stronger than in simulation, indicating that the average anisotropy of the DeepCore fiducial region is stronger than assumed for DeepCore.

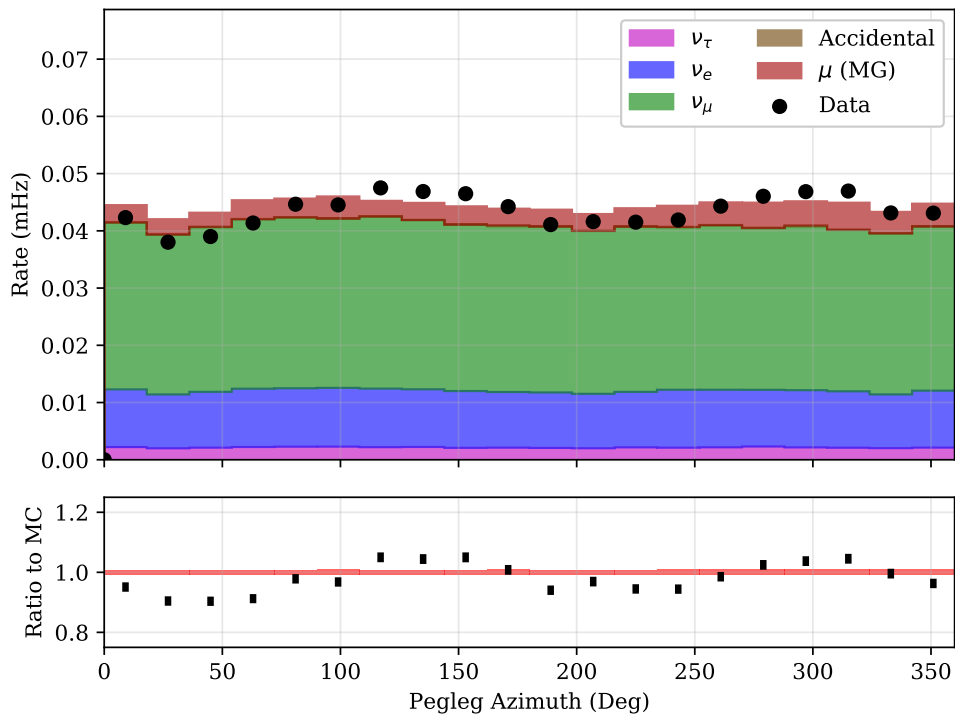


Figure 7.35 – The reconstructed azimuthal direction from the Pegleg reconstruction at GRECO Level 7. The data and simulation have been scaled to the same rate. A variation as a function of azimuthal angle is seen in both the simulated events and data, although the effect is stronger in data.

Type	IceCube Processing			GRECO				Analysis Binning
	Any Filter	DC Filter	Low-en L3	L4	L5	L6	L7	
CORSIKA	990598	9178	969.818	50.511	4.100	0.443	0.100	0.092
MuonGun	60669	2982	442.493	33.562	3.022	0.315	0.080	0.07
Accidentals	35855	8117	283.559	11.963	1.799	0.102	0.002	0.001
ν_e	1.842	1.721	1.262	0.783	0.544	0.362	0.325	0.194
ν_μ	11.317	6.360	4.758	2.503	1.629	1.011	0.676	0.552
ν_τ	0.293	0.270	0.206	0.134	0.103	0.074	0.051	0.045
MC Total*	1026466	17303	1260	65.893	8.176	1.991	1.153	0.884
Data	1154426	19092	1092	68.592	7.422	1.841	0.871	0.715

Table 7.5 – The event rates at each cut level in the GRECO selection. Note that the MuonGun events are included in this table, but do not contribute to the total Monte Carlo expectation to prevent double-counting of muon events from the CORSIKA sample. All rates are given in millihertz.

Figure 7.36 – The true neutrino energy and zenith of the GRECO sample at final level. The sample shows an asymmetry between upgoing ($\cos(\theta) < 0$) and downgoing ($\cos(\theta) > 0$) event rates in the neutrinos due to selection bias. The sample has a long tail of events at both high and low energies. Using the NuFit 2.2 oscillation parameters and the flux model from Honda, the ν_τ events are observed in the very upgoing region around $10^{1.4} = 25$ GeV.

The anisotropy effects of GRECO are the first hint that the anisotropy of the ice may not be uniform throughout the detector volume. New calibration measurements to incorporate these new properties into the simulation are underway. Because the anisotropy is not expected to directly impact the oscillation analysis, no additional cuts are introduced to the sample.

7.9 The Properties of the GRECO Event Selection

The completion of cuts yields the completed GRECO event selection. The rates of each sample of simulation and data are shown numerically in 7.5 or graphically in ???. Also included is the analysis binning as described in ?? for reference.

7.9.1 Energy and Zenith Reach

The GRECO sample covers a wide range of energies, with some final level events possessing energies as low as 2 GeV or as high as 1 TeV. The bulk of the neutrino sample, shown in ??, occurs at the expected oscillation minimum near 25 GeV. Most neutrino events originate at the horizon, as expected from the atmospheric neutrino flux, although there exists an asymmetry between the upward- and downward-going events. This asymmetry originates from the event selection, which selects against downward-going events in order to minimize the atmospheric muon background.

7.9.2 Reconstructed Variables

The true variables of the neutrino distributions are not observables in most GRECO analyses. Instead, all events are described using the reconstructed energies and zenith angles. The ν_τ sample reconstructs to slightly lower energies due to the loss in energy from the outgoing neutrino. The sample, when compared to data, shows reasonable

Figure 7.37 – The reconstructed energy and zenith of the GRECO sample at final level. Events in data reconstruct to both relatively high energies ($E_R > 100$ GeV) and very low energies ($E_R \approx 2$ GeV). Using the NuFit 2.2 oscillation parameters and the flux model from Honda, the ν_τ events are observed in the very upgoing region around $10^{1.4} = 25$ GeV.

shape agreement in both energy and zenith, although systematic disagreements occur above 100 GeV.

Something in here about resolution, you nitwit!

A Search for Tau Neutrinos from Oscillations

The GRECO event selection expects tau neutrinos with a rate of $45 \mu\text{Hz}$, corresponding to an expectation about 1400 events per year of data. These events may be used in the search for tau neutrino appearance with DeepCore. The details of the analysis using the GRECO dataset are described here.

8.1 Binning of the Appearance Analysis

The search for tau appearance with DeepCore uses a binned likelihood, described in 8.3.6, to fit the simulation to the data. In order to understand the potential for IceCube's measurement of appearance, a choice of binning must be decided upon. The analysis uses two variables to describe the oscillations: the reconstructed energy and zenith angle. These dimensions form an integral part of the standard oscillation analysis and are often used in measurements of atmospheric mixing parameters [115, 78, 79, 80, 81, 66, 67, 56].

The choice of binning for zenith angles is selected to be similar, but somewhat finer than previous work [79, 80, 81]. The appearance analysis uses events from the full sky. The upgoing events ($\cos(\phi) = -1$) pass through the full diameter of the Earth where we expect the strongest oscillation effects. The downgoing events ($\cos(\phi) = 1$) originate in showers above the Antarctic. The energy binning is selected to match previous work from DeepCore and consists of 8 bins logarithmically spaced from 5.6 GeV to 56 GeV, avoiding potential problems due to disagreements at high energies discussed in Section 7.8.3.

8.1.1 Particle ID Variables

In addition, recent work with DeepCore has shown that a third dimension separating the sample into cascade-like and track-like events may provide better sensitivity than using solely track-like events [80, 81, 66, 119]. A separation of this type, referred to as a *particle identification* variable (*PID*), allows the disappearance and appearance effects to be observed independently and provides a stronger limit on systematics effects. Two such variables are available in the GRECO sample, shown in Figure 8.1.

The first PID candidate variable, the reconstructed length of a muon track, provides separation between events with a clear muon track from those without one. This leads to reasonable separation between the ν_μ events undergoing disappearance and ν_τ events undergoing appearance. This may be seen in Figure 8.1a, where the cumulative distribution of the various simulation components are shown as a function of the reconstructed track length. The optimal separation between the ν_μ and ν_τ charged-current samples occurs between 30-50 meters. By separating the sample into cascade-like events (eg. $L < 50 \text{ m}$) and track-like events ($L \geq 50 \text{ m}$), the disappearance and appearance may be partially disentangled.

The second potential PID variable is the likelihood ratio between PegLeg's mixed cascade+track reconstruction and an analogous cascade-only reconstruction performed using the same tools. A higher likelihood (lower log-likelihood) in the cascade fit implies that the event is more likely intrinsically cascade-like while the reverse is true for intrinsically

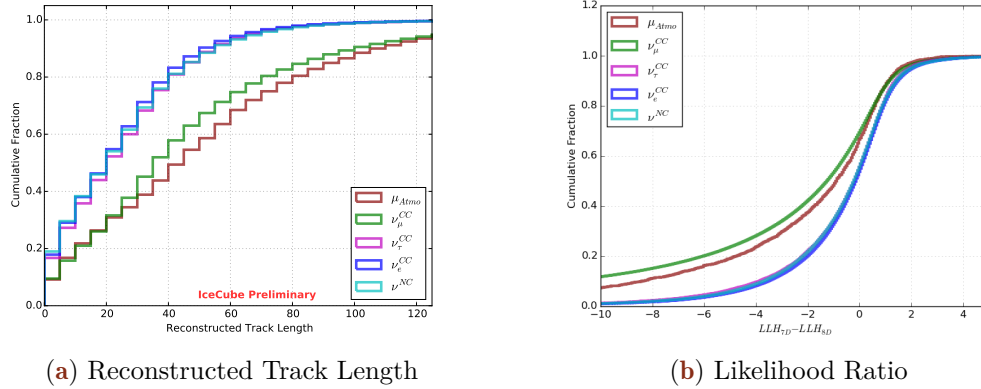


Figure 8.1 – The cumulative distributions of two possible variables to separate track-like events (muon neutrino charged current, atmospheric muons) from the cascade-like events (neutral current, electron neutrinos, and tau neutrinos). Larger separations between the muon neutrino charged current and the tau neutrino charged current events indicates better separating power.

track-like events. The information contained in the likelihoods of both fits may be combined to form a likelihood ratio, typically expressed in terms of the log-likelihoods.

$$\Delta LLH = \log_{10} R_L = \log_{10} (L_{\text{Cascade}}) - \log_{10} (L_{\text{Pegleg}}) \quad (8.1)$$

The cumulative plot of the likelihood ratio is shown in Figure 8.1b. There exists a broad choice of values with similar separation properties from approximately $-4 < \Delta LLH < -2$. Once again, separating events into two samples using the likelihood ratio may improve the ability of the analysis to disentangle the disappearance and appearance effects.

Both variables show separating power and likely have similar behavior: an event with a longer reconstructed muon track should be expected to prefer the PegLeg reconstruction over a cascade-only reconstruction. In order to choose between the parameters, the efficacy of separating each of the simulation samples from the tau neutrino charged current signal was evaluated. The results are shown in Figure 8.2, which give the fraction muon neutrino events rejected and the number of tau neutrino events accepted into the "cascade-like" sample for various choices of the PID values. Values further from a diagonal indicate better separation between the muon and tau neutrino events. The track length performs uniformly better than the likelihood ratio in separating the disappearing muon neutrino charged-current and appearing tau neutrino charged current events. The reconstructed track length is therefore selected as the PID variable for this analysis.

A choice of 50 meters of reconstructed track length is selected to separate the GRECO events into track-like ($L \geq 50$ m) and cascade-like ($L < 50$ m) event samples. Because the PegLeg reconstructed energy includes a contribution from the muon track, the division of the sample has an effect on the minimum energy of track-like events. Using Equation 7.15, the minimum energy of track-like events with no cascade energy and $L \geq 50$ m is 11 GeV. Track-like events are kinematically limited from reconstructing with energies below this threshold. Both track- and cascade-like events may reconstruct with higher energies than 10 GeV.

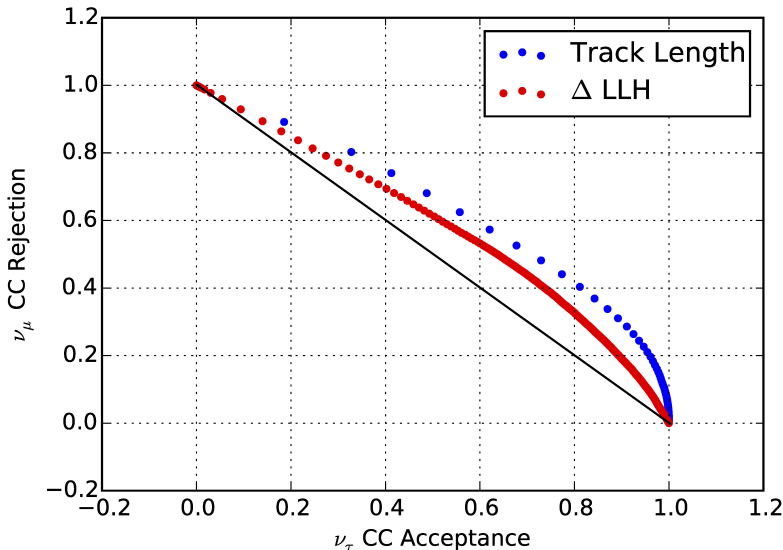


Figure 8.2 – A comparison of the separating power between the reconstructed track length and the likelihood ratio. Each point represents one possible choice of separation value from Figure 8.1. Points further from the 1-1 line, shown in black, indicate stronger separating power between the muon neutrino and tau neutrino charge current events.

8.1.2 The MC Fit Templates

The binned expectations used in the fit for tau neutrino appearance are shown in Figures 8.3 and 8.4. The neutrino histograms assume the oscillation parameters given by the Nu-Fit global fits described in Section 2.2.2 [58]. The disappearance of muon neutrino events is visible in both the muon neutrino charged current and the data histograms. The tau neutrino events appear primarily in the cascade-like histogram, separated from the disappearance. The signal ν_τ events occur in the very upgoing cascade channel and make up, at most, approximately 10% of the events in those bins.

Figure 8.4 includes histograms of both the simulated muons, produced using the DeepCore MuonGun generation scheme developed in Section 6.1, and the accidental triggers, produced using the Vuvuzela V2 model described in Chapter 4.3.2. Both samples are limited by the available simulation statistics. In the case of the accidental triggers, the severely limited statistics available at the final level of the analysis precludes the direct use of the remaining events. Instead, the accidental trigger simulation is modeled assuming a uniform distribution with a total event rate equal to the expected rate from the remaining simulation sample. The rate of accidental triggers is expected to be low, so no bias in the fit for appearance is expected.

The muon background histogram contains approximately 2400 simulated events spread over 140 bins. The atmospheric muon background events tend to reconstruct as downgoing events, primarily visible in the track-like channel. Significant statistical uncertainties in the region of expected appearance limit the potential reach of the analysis. While additional simulated statistics would be beneficial, potentially following the scheme introduced in Section 6.2, the production of new sets has not been completed due to time constraints.

8.2 Parametrizing the Tau Neutrino Appearance

In order to measure the appearance of ν_τ events, a choice of "appearance parameter" must be selected. Previous analyses have characterized the appearance using a normalization term [120, 119, 121]. This normalization is used in this analysis for consistency with previous analyses.

8.2.1 CC vs CC+NC

As described in 1.4.1, neutrinos may interact via the charged-current and neutral-current interactions. These interactions provide separate windows into the measurement tau neutrino appearance. Tau neutrino events may interact in either of these channels depending on the neutrino energy.

With a mass of 1776.82 ± 0.16 MeV and a lifetime of 290.3 ± 0.5 femtoseconds [17], tau leptons produced during neutrino oscillations in DeepCore tend to travel short distances O(1 mm) before decaying. The charged-current interactions of the tau result in a variety of signatures due to the unique decay behavior of the tau lepton.

$$\tau^- \rightarrow \begin{cases} \mu^- \bar{\nu}_\mu \nu_\tau & 17.41 \pm 0.04\% \\ e^- \bar{\nu}_e \nu_\tau & 17.83 \pm 0.04\% \\ \text{Hadrons} & \text{Otherwise} \end{cases} \quad (8.2)$$

In either the muonic or the electronic decay modes, a fraction of the energy is lost to outgoing neutrinos, resulting in a smaller observed charge than would be associated with a corresponding interaction of another neutrino type. Furthermore, the muonic decay mode may lead to a visible muon track for the tau neutrino interaction. These muon tracks associated with the appearance of tau neutrino would appear at lower energies than the tracks corresponding to the muon neutrino disappearance, allowing both effects to be observed simultaneously.

Unlike the varied results of the charged current interactions, neutral current interactions of neutrinos are assumed to have identical coupling and behavior, regardless of flavor and, therefore, undergo no observable change due to unitary oscillations. Because of this, studies of the standard unitary PMNS matrix tend to treat neutral current events as effectively non-oscillating [120, 119, 121, 81]. In contrast, searches for new physics and sterile neutrinos result can result in a change in the apparent number of neutral current interactions in the detector [62].

For this analysis, both channels are used to measure the appearance of tau neutrinos. A fit using charged-current events as the signal is used to provide limits on the modifications to a 3x3 mixing matrix without the introduction of neutral-current altering behavior. A second fit, including both neutral current and charged current tau neutrino events as signal, provides more insight into possible extra flavors of neutrinos.

8.2.2 The ν_τ Normalization

In the atmospheric neutrino flux, tau neutrinos are only produced directly above energies of a few TeV. Because effectively all tau neutrino events observable in DeepCore are the result of neutrino oscillations, the total number of observed tau neutrino interactions is a direct measure of the appearance. The number of tau neutrino events interacting in DeepCore is, however, affected by systematics. These systematics will be discussed further in Section 8.2.3. A parametrization of the appearance must account for these systematics variations to provide a useful result.

Following the definition of analyses performed by other experiments [120, 119, 121, 81], the tau neutrino normalization, N_τ , is adopted as the physics parameter for this analysis. The normalization is a fit parameter, defined to be a scaling of the number of expected tau neutrino events after all systematics effects are applied. The parameter modifies the number of events expected in each bin

$$f'_{ijk} = \left(\sum_{m \neq \nu_\tau} f_{ijk}^m(\theta_{23}, \Delta m_{32}^2, \dots) \right) + N_{\nu_\tau} f_{ijk}^{\nu_\tau}(\theta_{23}, \Delta m_{32}^2, \dots) \quad (8.3)$$

where f_{ijk}^m is the contribution to the total rate in bin ijk from a particle type

$$m = (\nu_e^{CC}, \nu_\mu^{CC}, \nu_\tau^{CC}, \nu^{NC}, \mu_{Atm}, Accidental). \quad (8.4)$$

A value of $N_{\nu_\tau} = 1.0$ indicates that the number of events is consistent with the number expected assuming unitary oscillations and the cross section model adopted by the GENIE generator. If the value differs significantly from 1.0, it may be indicative of either mismodeled cross-sections [122, 119] or of novel physics[123]. Due to the large existing uncertainties in the PMNS matrix described in 2.3.2, either situation is likely to yield valuable information.

8.2.3 Limits on the Tau Neutrino Normalization

This analysis is not the first to search for tau neutrino appearance. Two other experiments, OPERA and Super-Kamiokande, have reported previous measurements parametrized in the same way.

The OPERA Limit

The *Oscillation Project with Emulsion-tRacking Apparatus*, better known by the acronym *OPERA*, is an experiment designed to search for tau neutrino appearance [22]. Unlike IceCube’s use of atmospheric neutrinos, OPERA uses muon neutrinos produced in the CERN Neutrinos to Gran Sasso (CNGS) beamline. OPERA uses bricks of emulsion cloud chambers in order to accurately track and reconstruct neutrino interactions in the fiducial volume. This technique allows analyzers to identify not only the initial neutrino interaction vertex, but also the decay products along the path of the charged lepton produced in charged current interactions. An example of one tau neutrino event observed is shown in Figure 8.5. In OPERA, the muon and tau lepton produce different signals due to the short lifetime and unique decay properties of the tau lepton. The ability to identify the particle dynamics is balanced by the small fiducial volume of the experiment, yielding only 5408 useful events for analysis from five years of data-taking [121].

In 2015, OPERA Collaboration released the final result in their search for tau neutrino appearance using charged current interactions. Five candidate events were identified in the data sample with a signal expectation of 2.64 ± 0.53 and a background expectation of 0.25 ± 0.05 . The data unambiguously rules out the no-appearance hypothesis, with a rejection at 5.1σ .

OPERA reported a final value of $N_\tau^{CC} = 1.8_{-1.1}^{+1.8}$ at the 90% level. This value is consistant with the standard unitary oscillation scheme, but with large errors.

The Super-Kamiokande Limit

Super-Kamiokande, described in Section 2.2.1, also has reported results in searches for tau neutrino appearance. The Super-Kamiokande collaboration developed a new event

Interaction Mode	Non-tau-like	tau-like	All
CC nue	3071.0	1399.2	4470.2
CC numu	4231.9	783.4	5015.3
CC nutau	49.1	136.1	185.2
NC	291.8	548.3	840.1

Table 8.1 – The rates expected for each of the neutrino types in the Super-Kamiokande search for tau neutrino appearance. Reproduced from [119].

selection in the search for tau neutrino events, including the implementation of a neural net trained to identify tau-like and non-tau-like events [120, 119]. The neural net includes information about the energy of the event and is trained against a background sample of simulated events. Events are analyzed in terms of the zenith angle and the neural net output variable.

The background and signal events, shown in Figure 8.6 are fit to 5326 days of atmospheric neutrino data with an unbinned likelihood with 28 systematic effects included in the analysis.

The expected rates of the Super-Kamiokande analysis are shown in Figure 8.1. The Super-Kamiokande measurement yields an expectation of 185.2 tau neutrino events in 5326 days or approximately 12.7 events per year. After fitting, the final rejection of the no-appearance hypothesis, $N_\tau^{CC}=0$, is found to be 4.6σ . Like OPERA, Super-Kamiokande finds more tau neutrino candidate events than expected, with a best-fit normalization of $N_\tau^{CC} = 1.47 \pm 0.32$ at the 68% level.

8.3 Systematics Considerations

The tau neutrino component of the GRECO selection makes up only 5% of the expected event rate. The measurement is sensitive to a number of *systematics* parameters, including uncertainties related to the oscillation parameters, the neutrino and muon flux parameters, neutrino cross sections, and various detector systematics. Each of these systematics effects will be described.

8.3.1 Oscillation Parameters

The GRECO selection is primarily sensitive to atmospheric neutrinos around 20 GeV. These neutrinos travel distances from approximately 20 km (directly downgoing) to 12700 km (directly upgoing). At these energies and distances, little effect is expected from the solar and reactor parameters. This has been tested with the GRECO sample by changing each parameter by the 1σ range given in [58]. The total value of the χ^2 , defined as in 8.4, was used to select the most important parameters for this fit.

The results are shown in 8.2. The atmospheric mixing parameters have significantly larger impacts on the analysis histogram than the other parameters. For the purposes of GRECO analyses, only these parameters are therefore considered.

The atmospheric mixing parameters, θ_{23} and Δm_{31}^2 are allowed to vary in the fit for appearance. The effect of each is shown in Figures 8.7 and 8.8. Of the two, the mass splitting term has strong correlations expected with tau neutrino normalization N_τ , changing both the location as well as the strength of the observed appearance.

Parameter	Baseline	Tested Shift	$\sum_{bins} \chi^2$
Δm_{31}^2	2.2526×10^{-3}	$+0.10 \times 10^{-3}$	2.776
Δm_{21}^2	7.49×10^{-5}	$+0.19 \times 10^{-5}$	5.392×10^{-4}
θ_{23}	0.72431	+0.02094	1.262
θ_{13}	0.14765	+0.00262	1.802×10^{-3}
θ_{12}	0.58853	+0.01379	2.978×10^{-4}
δ_{CP}	0.0	$+\frac{\pi}{2}$	2.407×10^{-2}

Table 8.2 – Total χ^2 impact of each of the oscillation parameters. a $\sum \chi^2 \approx 1$ corresponds to a 1σ effect in the histogram. The atmospheric mixing parameters, Δm_{31}^2 and θ_{23} are the most important oscillation parameters for the GRECO selection. Of the remaining parameters, the CP-violating phase is the next most important.

8.3.2 Neutrino Flux Uncertainties

The underlying flux models of the atmospheric neutrinos and background muons provide significant uncertainties for this analysis. The implementation of the flux used in IceCube is produced using a computationally expensive Monte Carlo simulation of the Earth [18]. Four implemented systematic uncertainties used in this analysis modify the shape of this flux for the neutrinos. A fifth systematic uncertainty scales the total neutrino flux to account for uncertainties in the total event rate. This neutrino normalization is allowed to float freely with a constraint that the value be larger than 0.

Neutrino Spectral Index

The spectral index of the neutrino flux is related to the cosmic ray spectrum. The change in the neutrino flux, $\delta\gamma_\nu$ is implemented by modifying the neutrino event weight, w_i based on the energy of the event.

$$w'_i = \left(\frac{E_i}{1 \text{ GeV}} \right)^{\delta\gamma_\nu} w_i \quad (8.5)$$

For IceCube, an gaussian prior of 0 ± 0.1 is assumed for the uncertainty in the spectral index. The effect is shown in Figure 8.9.

ν_e/ν_μ Ratio

The number of electron and muon neutrinos produced during air showers depends on the dynamics of the shower and the hadronization model used in the prediction. For IceCube, the ratio of the electron and muon fluxes is used as a systematic by scaling the relative contributions of each in the flux model. The scaling factor, N_{ν_e} is applied to the electron neutrino flux as a flat scale factor with a conservative prior of 1.0 ± 0.05 derived from [124]. The effect on the histogram is shown in Figure 8.10.

$\nu/\bar{\nu}$ and Upward/Horizontal Ratios

The shape of the neutrino spectrum is derived from Monte Carlo simulations that modify the elements of the neutrino flux prediction [124, 125]. In order to utilize these uncertainties in the appearance analysis, parametrizations of the effects, shown in Figure 8.11, are included in the analysis [80, 81]. The effects of the $\nu/\bar{\nu}$ uncertainty and the upward/horizontal uncertainty are shown in Figures 8.12 and 8.13 respectively.

8.3.3 Atmospheric Muon Flux

The appearance analysis includes two systematics on the atmospheric muon flux. The first is a normalization factor that scales the total number muons in the detector. This normalization is constrained to be positive, but otherwise includes a flat prior.

The second is an uncertainty on the cosmic ray spectral index, $\gamma_\mu^p .71 \pm 0.01$ for hydrogen nuclei and $\gamma_\mu^{He} .60 \pm 0.01$ for helium nuclei, derived from [125]. The uncertainty was evaluated by reweighting events based on the cosmic ray primary energies of CORSIKA simulation processed to GRECO Level 5. The resulting uncertainties were parametrized in terms of the energy at the MuonGun generation cylinder (see Section 6.1) and the direction of the muon [126].

The change in the analysis histograms due to the uncertainty in the spectral index of the cosmic ray spectrum is shown in Figure 8.14. The effect is small, resulting less than a 0.1% shift in most bins. Despite the small effect, the parameter is included in the fit in order to account for uncertainties in the cosmic ray muons.

8.3.4 Propagation Uncertainties

The propagation of simulated muon events from the air shower to the detector is performed using the PROPOSAL software discussed briefly in Section 4.2.1. The parametrizations of the stochastic emissions each possess uncertainties on the order of 10% [99]. The effect of these uncertainties was evaluated using a toy model parametrizing the energy losses used in PROPOSAL. While effects on the atmospheric muon events were observed, the effect was small in the analysis histogram. The observed effects are within the statistical errors from the limited background simulation samples.

The production of the more accurate simulation has not been performed due to time limitations, although such uncertainties may be included in future analyses with the production scheme introduced in Section 6.2.

8.3.5 Cross-section Uncertainties

Uncertainties on the neutrino cross section can affect the rates of events in the final sample. Parametrizations of the QE, RES, and DIS interaction cross section uncertainties were tested for inclusion in this analysis.

Axial Masses

The axial mass terms, described briefly in Section 1.4, control the cross section for the resonant and quasielastic interactions. Uncertainties are defined conservatively, following the default uncertainties available in the GENIE generator [94].

The GENIE generator provides tools to recalculate event weights for changes in the axial masses. The axial mass uncertainties from GENIE are $m_a^{QE} = 0.99_{-0.15}^{+0.25}$ GeV and $m_a^{RES} = (1.12 \pm 0.22)$ GeV. For each QE and RES event, the GENIE functions are used to find weights for 5 points ($-2\sigma, -1\sigma, 0, +1\sigma, +2\sigma$). These weights are fit to a second order polynomial for each event to produce a smooth parametrization for the weight as a function of axial mass value.

The QE and RES events occur at low energies, as expected from Figure 1.7. The uncertainties reflect this, with the largest impact occurring at low reconstructed energy, as shown in Figures 8.15 and 8.16.

DIS Cross-sections

Unlike the QE and RES, the uncertainty of the deep inelastic cross section cannot be modeled using an axial mass term. Work by IceCube collaborators [127] have instead parametrized the uncertainty in the DIS events using comparisons between GENIE events and data from the NuTeV experiment [128]. The parametrization uses the Bjorken scaling factor,

$$x = \frac{Q^2}{2M\nu}, \quad (8.6)$$

where $Q^2 = -q^2$ is the 4-momentum transfer, M is the nucleon mass, and $\nu = E_{had}$ is the energy of the hadronic system [20]. The GENIE event rate can be corrected to match the NuTeV data using a empirical power law [127]:

$$w'_i = \begin{cases} (1 - 1.65125a)x^{-a}w_i & \nu \\ (1 - 1.8073a)x^{-a}w_i & \bar{\nu} \end{cases} \quad (8.7)$$

where a is 0 ± 0.0757 for neutrinos and 0 ± 0.1008 for antineutrinos. This method has been tested with the GRECO Level 7 dataset. The resulting uncertainties, shown in Figures 8.17 and 8.18, are small and have large degeneracies with other parameters. Because of the small size and degeneracy, these systematic uncertainties are not used in the fit.

IceCube is sensitive to both neutral current and charged current interactions. The uncertainty in the interaction cross section for the charged current is handled with the QE, RES, DIS uncertainties. To handle the uncertainty in the neutral current cross section, the normalization of neutral current interactions is fit in the tau appearance analysis. This normalization is measured relative to the charged current rates.

$$f'_{NC} = N_{NC} \cdot \frac{\sigma_{NC}}{\sigma_{CC}} \quad (8.8)$$

As in previous IceCube analyses, the neutral current normalization is fit with a prior of 1.0 ± 0.2 [80, 81]. The effects are shown in Figure 8.19.

8.3.6 Detector Systematics

While the previous systematics have been concerned with global physics parameters, the remainder are dedicated to understanding the uncertainties associated with the IceCube detector itself, such as the properties of the PMTs and the ice. These parameters, collectively referred to as the *detector systematics*, do not have analytic forms, but may affect the rate of events, the reconstruction properties of a given event, or both. The effect of these uncertainties must be evaluated using dedicated Monte Carlo simulations. The GRECO event selection uses a number of simulation sets, shown in 8.3 for signal and 8.4 for background, to characterize the effects of these detector systematics. Each set contains at least one simulation parameter changed from the baseline set and are run through the full GRECO processing.

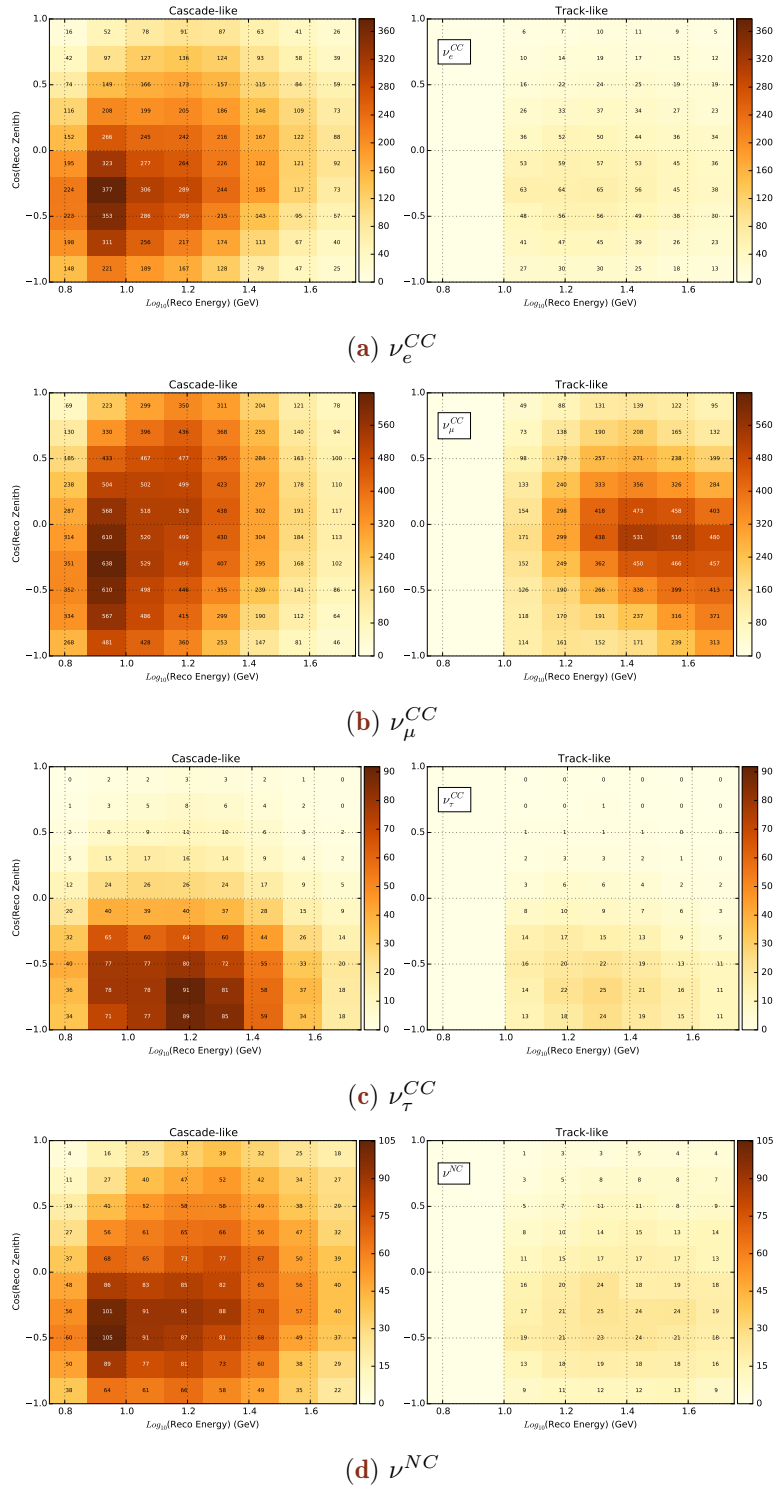


Figure 8.3 – The neutrino histograms used in the fit for appearance. The colorbar shows the expected rate from the 3 year sample used in this thesis. The disappearance in the muon neutrino events is visible in the upgoing ($\cos(\theta)=-1$) track-like histogram around an energy of $10^{1.3}=20$ GeV. The appearance of tau neutrinos is primarily concentrated in the cascade-like histogram.

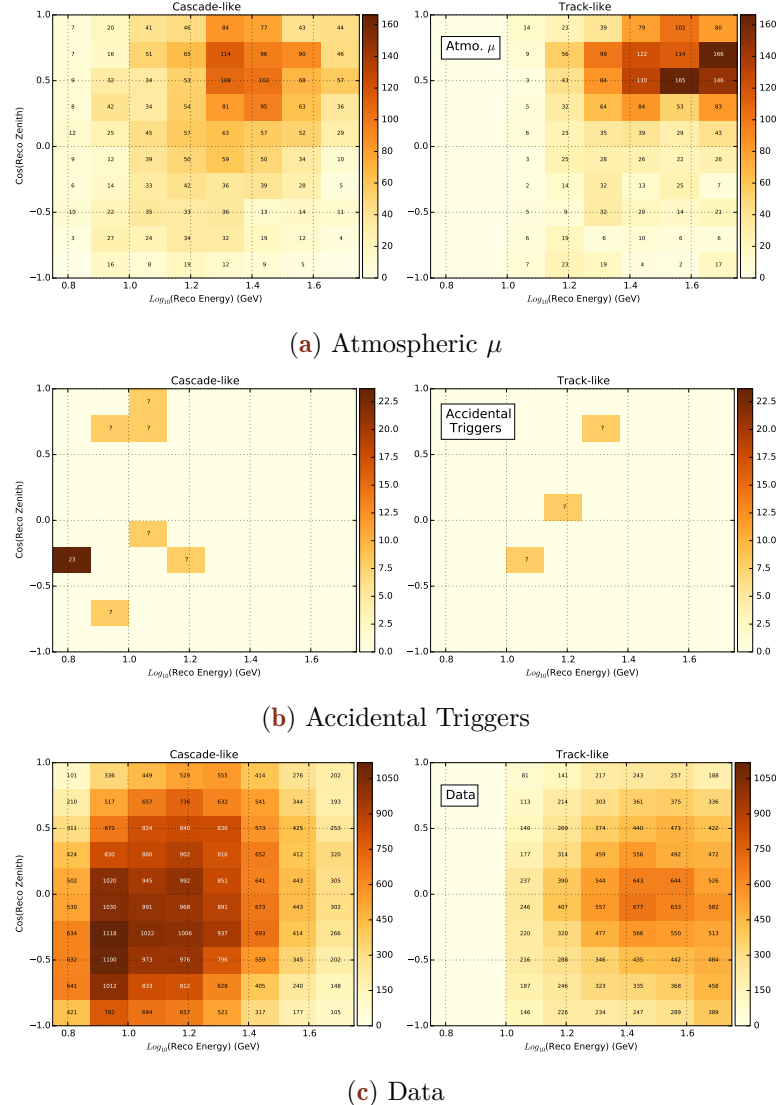


Figure 8.4 – The background (a, b) and data (c) histograms used in the fit for appearance. The colorbar shows the expected rate from the 3 year sample used in this thesis. The disappearance of muon neutrinos is visible in data histogram in the upgoing ($\cos(\theta)=-1$) track-like histogram around an energy of $10^{1.3}=20$ GeV. Both the muon and accidental trigger histograms are limited by the simulations statistics.

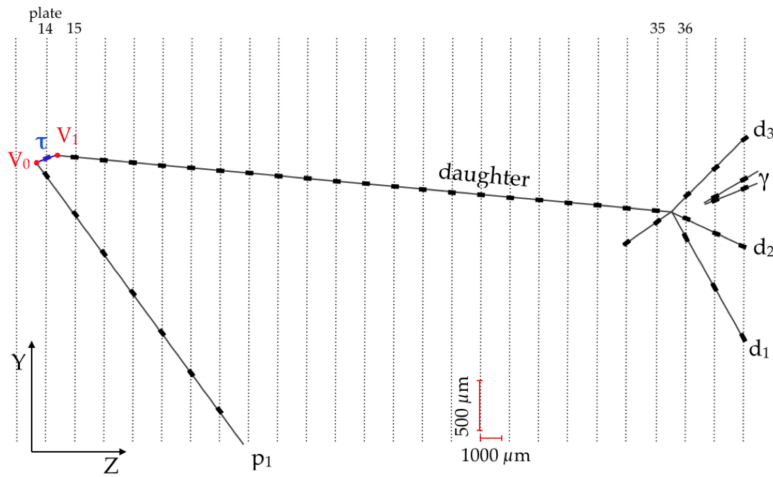


Figure 8.5 – An event display of the reconstructed interaction of a tau neutrino interaction in the OPERA detect. The initial interaction vertex, V_0 , produces a tau lepton, shown in blue. The OPERA detector’s small resolution enables the identification of individual tau neutrino interactions. Figure from [121].

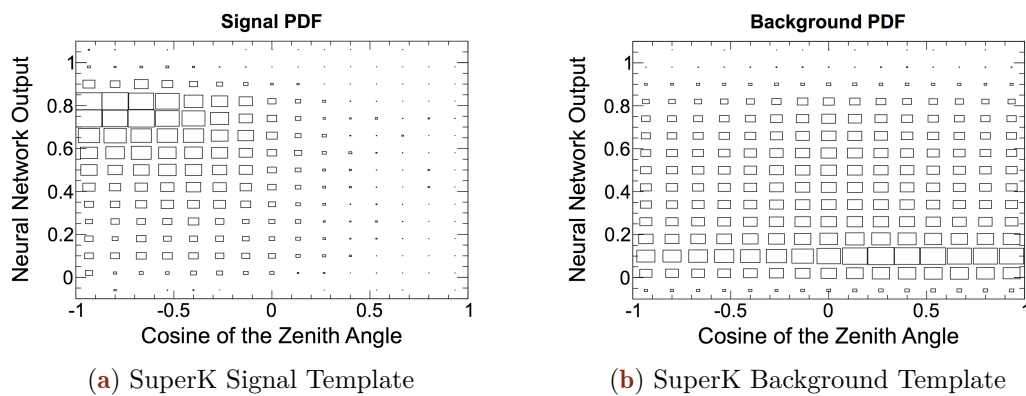


Figure 8.6 – The signal (a) and background (b) histograms used in the Super-Kamiokande search for tau neutrino appearance. The data is binned to show the location of events, although the fit is performed using an unbinned likelihood. The signal tau neutrino events appear in the upgoing region. Image from [119].

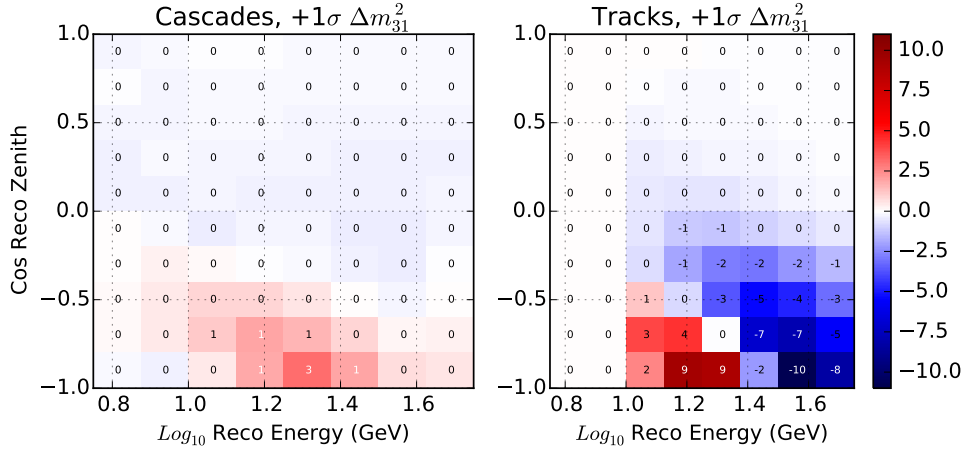


Figure 8.7 – The effect of Δm_{31}^2 in the analysis histogram. The colorbar shows the percent change in rate per bin for a shift of 10% in the mass splitting from the baseline value, $2.526 \cdot 10^{-3} \text{ eV}^2$, to $2.779 \cdot 10^{-3} \text{ eV}^2$. A strong disappearance effect is observed in the track-like events while the number of events in the appearance signal region of the cascade-like histogram is increased. The mass splitting shows the strongest correlation with the value of N_τ .

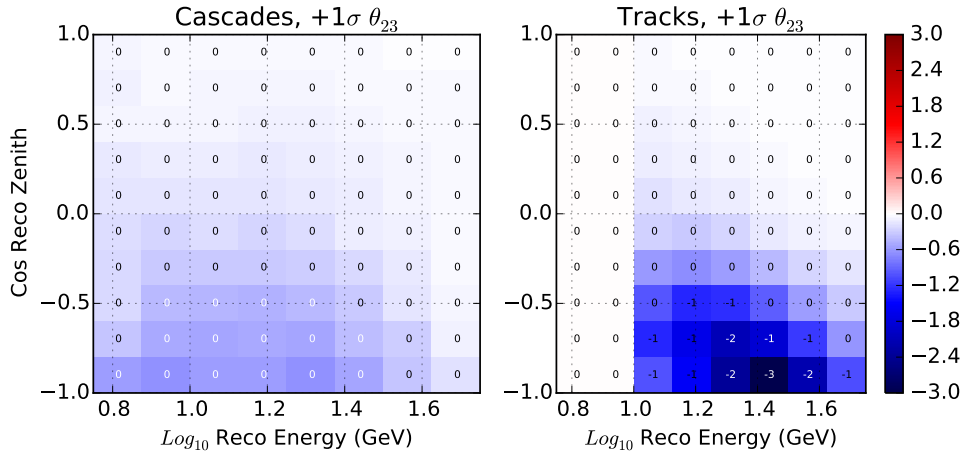


Figure 8.8 – The effect of θ_{23} in the analysis histogram. The colorbar shows the percent change in rate per bin for a shift of 10% from the baseline value, $\sin^2 \theta_{23} = 0.440$, to $\sin^2 \theta_{23} = 0.50$. As expected, the appearance modulates the strength of the disappearance. Because both the cascade-like and track-like sample are dominated by muon neutrino charged current events, this change results in a net disappearance in both histograms.

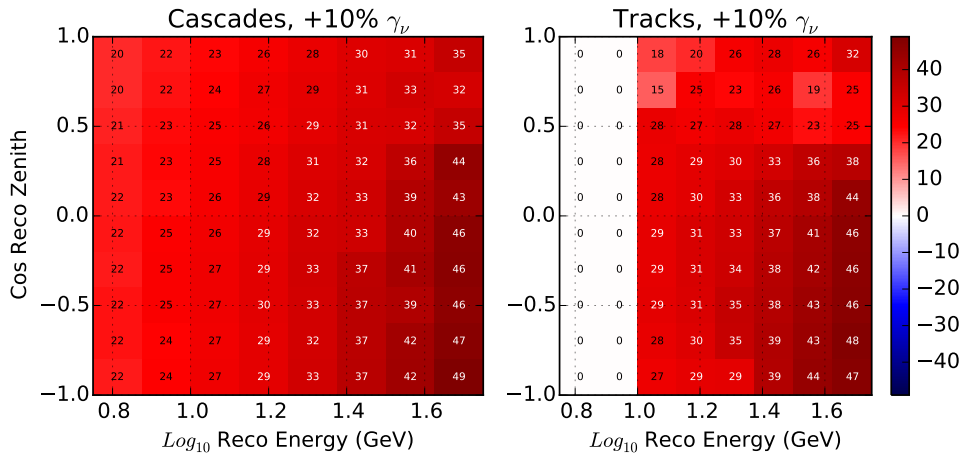


Figure 8.9 – The effect of $\delta\gamma_\nu$ in the analysis histogram. The colorbar shows the percent change in rate per bin for a shift of 10% from the baseline value. The spectral index has a strong effect on both histograms as a function of energy.

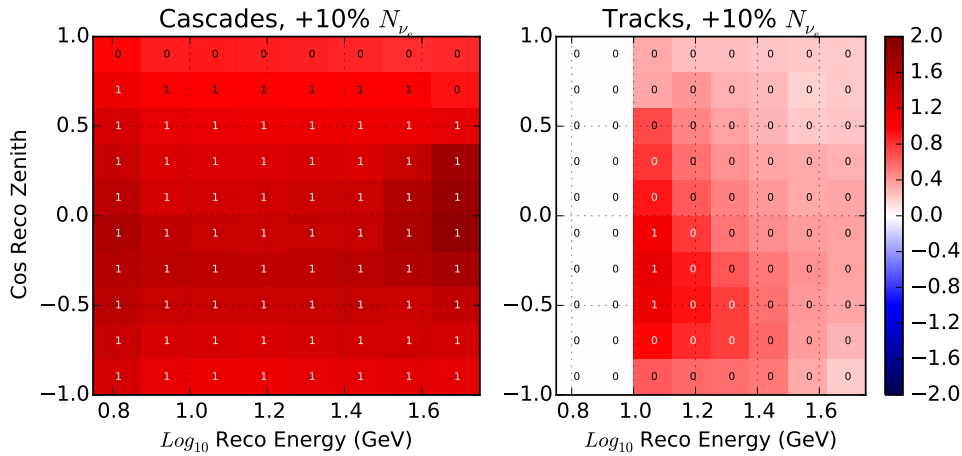


Figure 8.10 – The effect of N_{ν_e} in the analysis histogram. The colorbar shows the percent change in rate per bin for a shift of 5% from the baseline value. The spectral index has a strong effect on both histograms as a function of energy. The strongest impact occurs in the cascade-like events near the horizon.

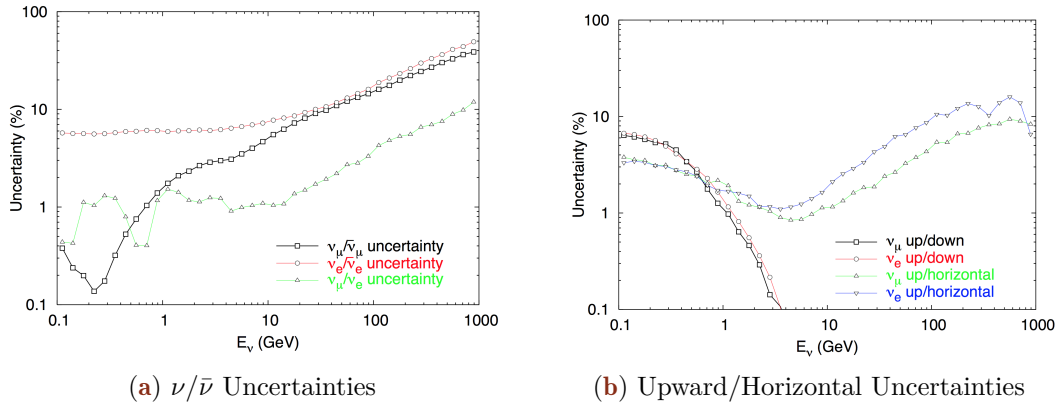


Figure 8.11 – The neutrino flux uncertainties calculated in [124]. (a) The ratio of the muon to electron neutrino fluxes is shown in green. The effect is applied as an energy-independent scale factor with a conservative prior of 5% assumed in this analysis. The uncertainty of the neutrino to antineutrino flux, shown in black and red for muon neutrinos and electron neutrinos respectively, is parametrized as a function of energy and zenith for inclusion in the appearance analysis. (b) The ratio of the upward flux to the horizontal flux in the atmospheric neutrinos. The ratio changes due to uncertainties in the pion and kaon decays in cosmic ray air showers. The shape of the uncertainty is parametrized in energy and zenith for inclusion in this analysis.

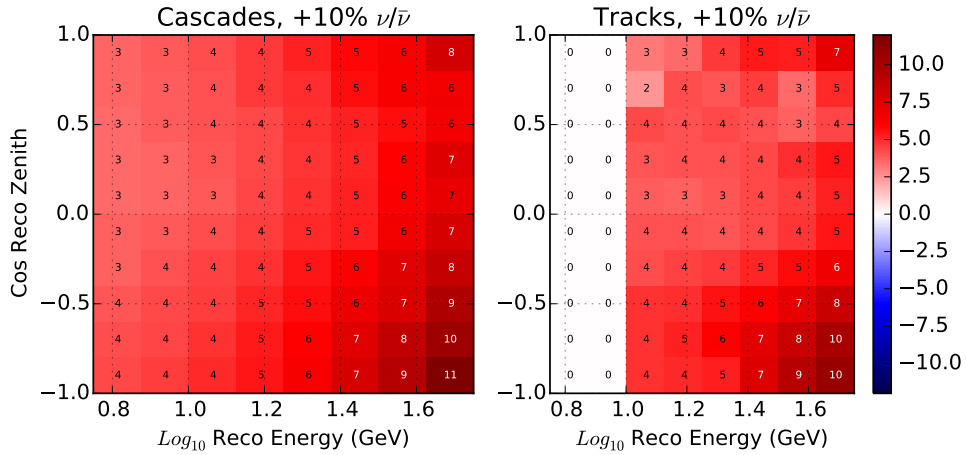


Figure 8.12 – The effect of the $\nu/\bar{\nu}$ uncertainty in the analysis histogram. The colorbar shows the percent change in rate per bin for a shift of 1σ from the baseline value where 1σ corresponds to the uncertainties of Figure 8.11a. Changing the ratio affects both histograms with the strongest effect occurring at the highest energies as expected

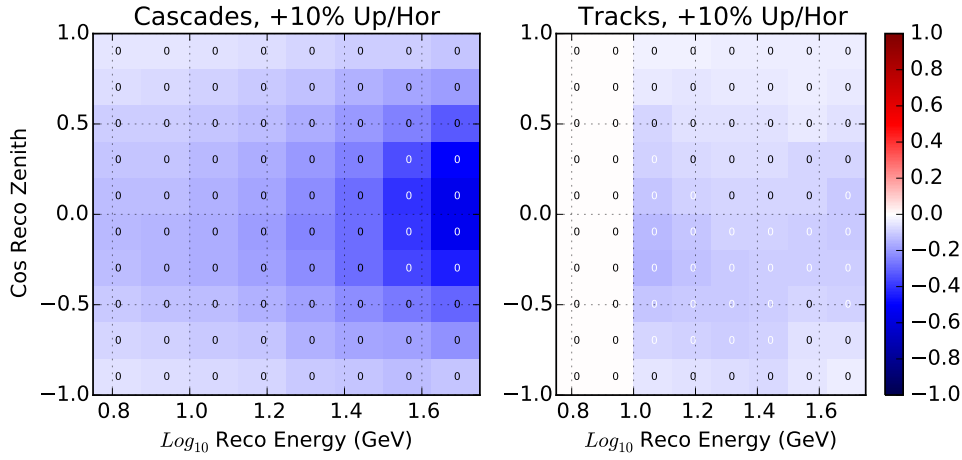


Figure 8.13 – The effect of the upward/horizontal uncertainty in the analysis histogram. The colorbar shows the percent change in rate per bin for a shift of 1σ from the baseline value where 1σ corresponds to the uncertainties of Figure 8.11b. The uncertainty of the up/horizontal ratio has a small impact in the analysis space.

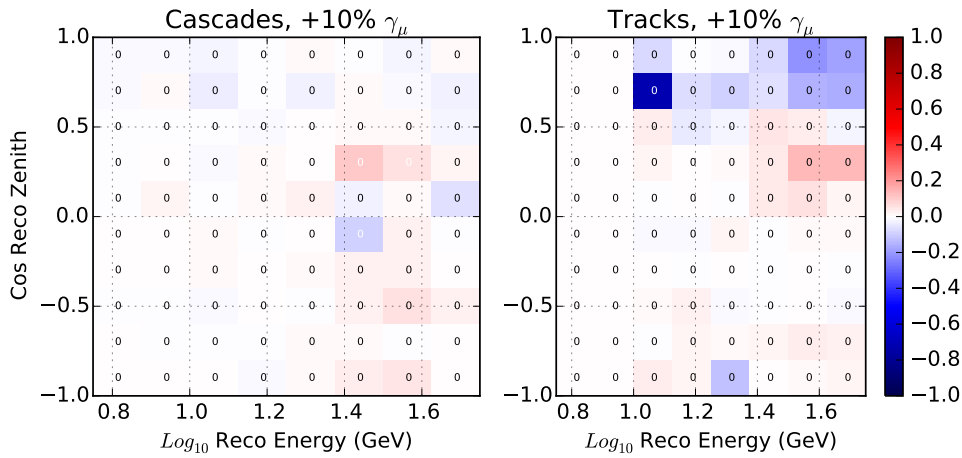


Figure 8.14 – The effect of the $\delta\gamma_{CR}$ uncertainty in the analysis histogram. The colorbar shows the percent change in rate per bin for a shift of 1σ from the baseline value where 1σ corresponds to the uncertainties of [126].

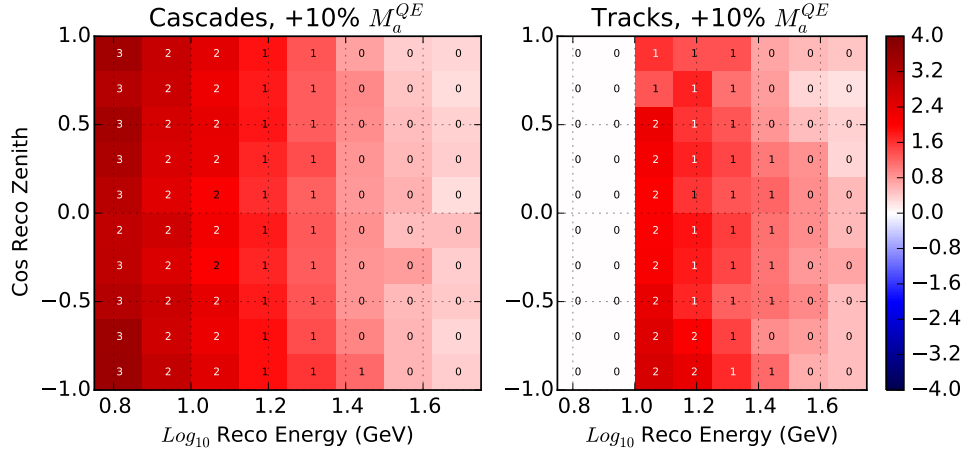


Figure 8.15 – The effect of the axial mass m_a^{QE} uncertainty in the analysis histogram. The colorbar shows the percent change in rate per bin for a shift of 1σ from the baseline value using the GENIE reweighting code.

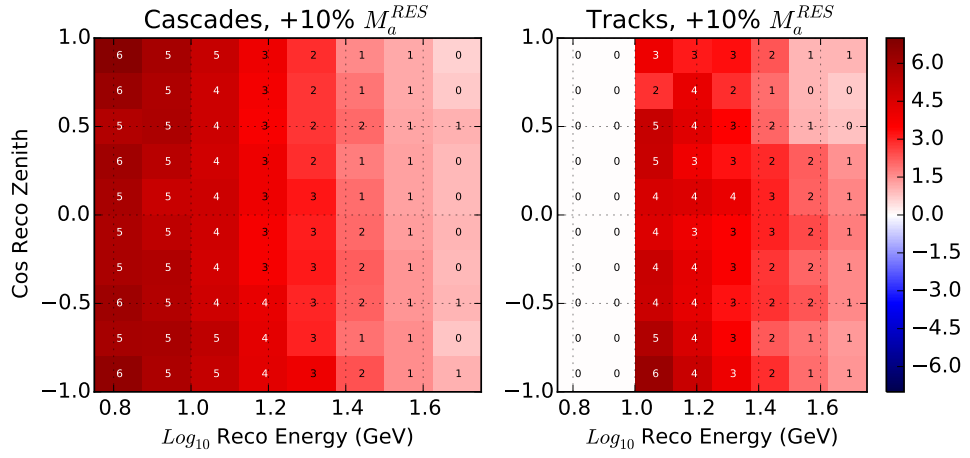


Figure 8.16 – The effect of the axial mass m_a^{RES} uncertainty in the analysis histogram. The colorbar shows the percent change in rate per bin for a shift of 1σ from the baseline value using the GENIE reweighting code.

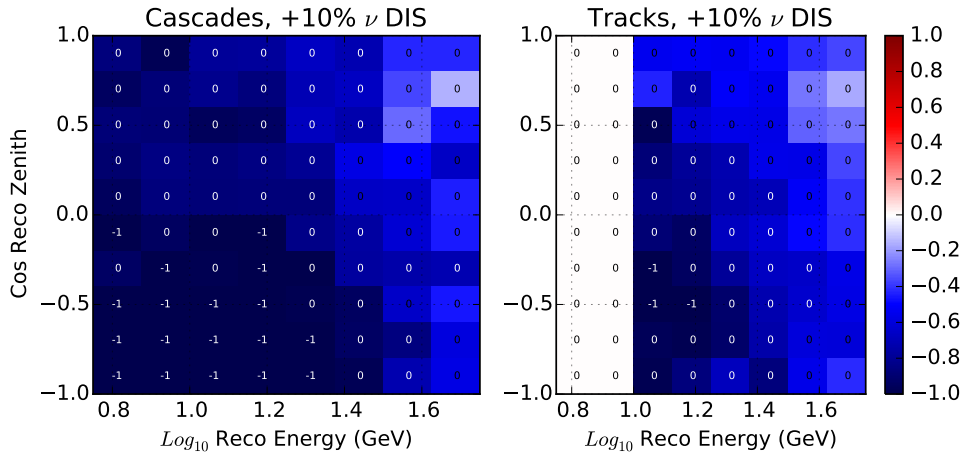


Figure 8.17 – The effect of the DIS uncertainty for neutrinos in the analysis histogram. The colorbar shows the percent change in rate per bin for a shift of 1σ . The effect is small and largely degenerate with other parameters.

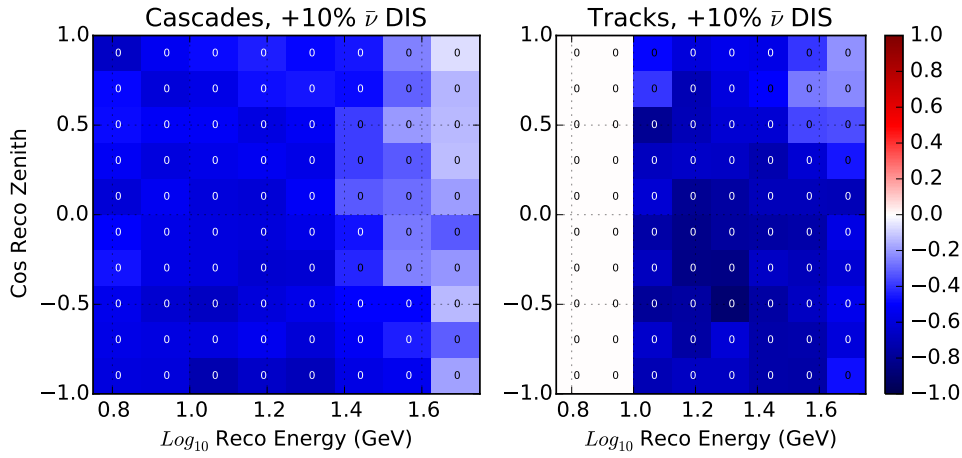


Figure 8.18 – The effect of the DIS uncertainty for neutrinos in the analysis histogram. The colorbar shows the percent change in rate per bin for a shift of 1σ . The effect is small and largely degenerate with other parameters.

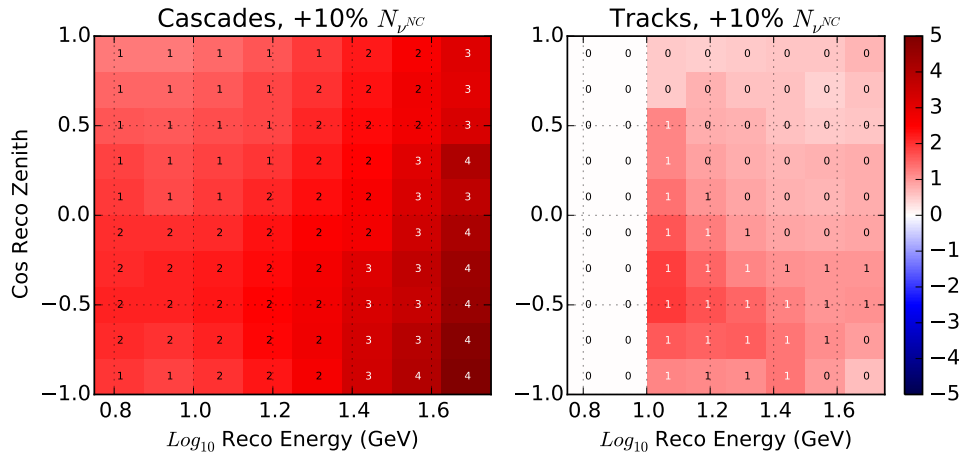


Figure 8.19 – The effect of the neutral current normalization in the analysis histogram. The colorbar shows the percent change in rate per bin for a shift of 20%. The effect appears most strongly in the cascade-like sample.

Set Number	Coincident Fraction	DOM Eff	Hole Ice	Forward Coeff	Absorption	Scattering	Livetime
Baseline	0%	100%	25	0	100%	100%	30 years
640C	100%	100%	25	0	100%	100%	30 years
641	0%	88%	25	0	100%	100%	30 years
643		94%					
644		97%					
645		103%					
646		106%					
648		112%					
660	0%	100%	15	0	100%	100%	10 years
661			20				
662			30				
663			35				
670	0%	100%	25	2.0	100%	100%	10 years
671				-5.0			
672				-3.0			
673				1.0			
674				-1.0			
681	0%	100%	25	0.0	92.9%	92.9%	30 years
682					110%	100%	
683					100%	110%	

Table 8.3 – Systematics sets used for the characterization of the signal neutrino events. While all listed sets have up to 30 years of effective livetime available, not all events are processed in each set.

Set Number	Oversizing	DOM Eff	Hole Ice	Forward Coeff	Absorption	Scattering	Comments
Baseline	1.0	99%	25	0	100%	100%	1 year DeepCore MuonGun
A	1.0	69.3% 79.2%	30	0	100%	100%	
B							
C	1.0	99%	15	0	100%	100%	
D			30				
E	1.0	99%	30	-2	100%	100%	
F				-4			
G	3.0	99%	25	0	100%	100%	1 year KDE Prescale
H					110%		
I					80%		
J					100%	80%	
K						110%	
L						120%	
M						92.9%	
N						114.2%	114.2%

Table 8.4 – Systematics sets used for the characterization of the atmospheric muon background. Note that the bulk ice systematics sets use the KDE prescale simulation scheme introduced in Section 6.2.

Parametrizing with Hyperplanes

For each of the simulation sets and each particle type, histograms are produced using the reconstructed energy, zenith, and track length. These systematic histograms give information about the expected change of the final histogram as a function of the changing systematics parameters, but the information is encoded in discretized points with statistical fluctuations due to the finite simulation statistics. In order to produce continuous systematics for analysis, the discrete detector systematics must be parametrized.

For this work, a *hyperplane*, is fit to the detector systematics sets for each particle type and for each bin in the analysis histogram. The hyperplane used in the search for appearance is a parametrization method in which each bin receives a reweighting factor of the form

$$f'_{ijk} = \left(\sum_m^{detsys} (h_m(x_m)) + b^{ijk} \right) f_{ijk} \quad (8.9)$$

where $h_m(x_m)$ is an 1D function describing the effect of systematic m as a function of the systematic value x_m and b^{ijk} is a constant term.

For neutrinos, a simple linear model is assumed for each detector systematic, with one free coefficient associated with each systematic as well as one free constant term independent of the systematics. The form of the hyperplane for each neutrino type in the bin ijk is given by 8.10.

$$f'_{ijk} = \left(\sum_m^{detsys} (a_m^{ijk}(x_m - x_m^0)) + b^{ijk} \right) f_{ijk} \quad (8.10)$$

For atmospheric muons, the form is slightly modified due to the strong effects observed from both the DOM efficiency and absorption uncertainties. In these two cases, an exponential model is selected to better describe the observed effects in simulation.

$$f'_{ijk} = \left(\sum_{m \neq DE, Abs}^{detsys} (a_m^{ijk}(x_m - x_m^0)) + \sum_m^{DE, Abs} (a_m^{ijk} e^{b^{ijk}(x_m - x_m^0)}) + c^{ijk} \right) f_{ijk} \quad (8.11)$$

The hyperplane coefficients are fit for each bin the analysis histogram, producing continuous parametrizations to describe the detector effects. During minimization, the rates in each bin may be calculated by using the systematics values \vec{x}_m in the hyperplane.

There are limitations in the approach used here. Features in the systematics histograms are encoded when the hyperplane coefficients are fit. These features, which include the oscillation disappearance minimum, will not change during minimization. Tests performed with hyperplanes calculated with different oscillation parameters found negligible effect in the final fit values in the appearance analysis.

Coincident Fraction

The GENIE simulation sets are produced with exactly one neutrino interaction per event. In the actual detector, a fraction of triggered events will consist of a temporally coincident muon and neutrino pair which may be from the same air shower or from independent showers. These events are known as *coincident events*. In order to account for this possibility, a sample of such events were simulated with independent neutrino and muon

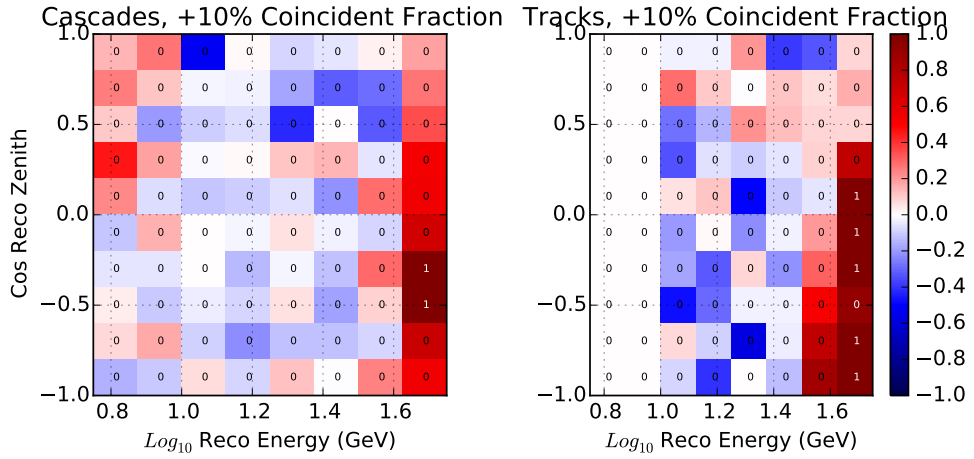


Figure 8.20 – The effect of the coincident event rate in the analysis histogram. The colorbar shows the percent change in rate per bin for a shift of 10%. The parameter is implemented to be independently rate-preserving for each type of neutrino. The coincident event rate induces a small change in the rate of events at high energies.

generation. Every produced event contains at least one atmospheric muon in addition to exactly one neutrino interaction. By interpolating between this "100% coincident" sample and the standard "0% coincident" sets, the effect of the coincidences may be included in the final analysis.

The GRECO event selection actively selects against atmospheric muon-like events. The lowest order effect of this choice is that increasing the coincident event fraction leads to a correspondingly lower total event rate, as events with muons are removed from the selection. In order to distinguish the effect of the coincident events from a global normalization factor, the coincident event fraction is implemented to preserve the total number of events of each neutrino type. The effect of this systematic in the final analysis is shown in Figure 8.20.

In most analyses in IceCube, a coincident event fraction of approximately 10% is assumed. This is derived from a combination of the atmospheric neutrino and muon fluxes assuming independent poissonian rates. At final level, the true fraction of coincident events is unknown, but previous oscillation analyses have found no clear issues using the standard simulation sets assuming no coincident events. A prior is therefore implemented with a one-sided Gaussian distribution centered at 0% with a 10% width.

DOM Efficiency

As with all PMTs, the light detection probability of the IceCube DOMs is not perfect. The total efficiency of detecting incident photons is about 25% at 390 nm for the PMT used in standard IceCube DOMs [37, 69]. Before and during deployment, the quantum efficiency of 16 DOMs were tested. The efficiency of the DOMs was again measured in-situ in order to better account for local effects like cable shadowing and the glass-ice interface [129]. Dedicated measurements post-deployment have used minimum ionizing muons in data and simulation and derived a modification of the assumed efficiency, hereafter referred to as the *DOM efficiency*, of $99\% \pm 5\%$. In this analysis, a more conservative estimate of the uncertainty for the DOM efficiency, $99\% \pm 10\%$, is used for consistency

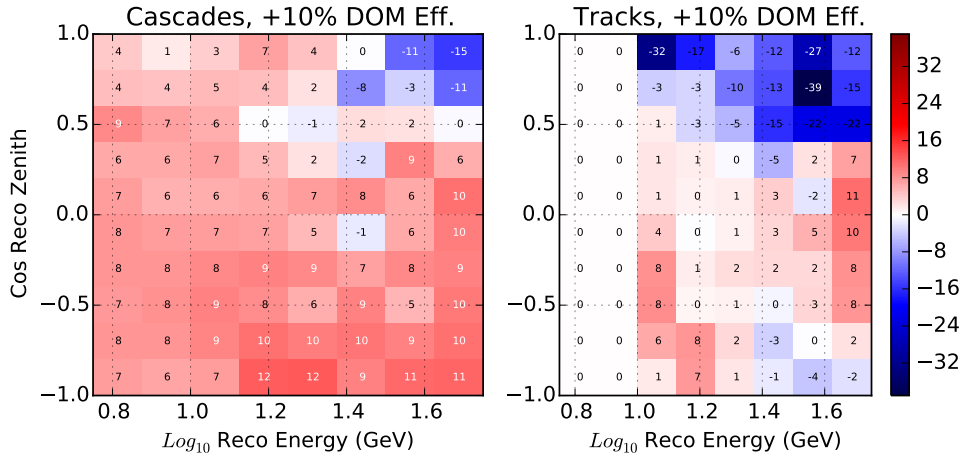


Figure 8.21 – The effect of the DOM efficiency in the analysis histogram. The colorbar shows the percent change in rate per bin for a shift of 10%. The DOM efficiency increases the number of photons observed, improving both the reconstruction resolution and veto efficiency.

with previous oscillation measurements. The difference between the two uncertainties has been tested and no impact on the final fit was discovered.

The DOM efficiency scales the probability of observing photons incident at the face of the DOM. A higher DOM efficiency leads to more information about individual particle interactions, leading to better reconstructions. The improved reconstructions lead to higher neutrino event rates at final level as well as more well-defined oscillation features in the reconstructed space. In addition, higher DOM efficiency increases the number of hits observed along atmospheric muon tracks, yielding improved veto efficiency. The net effect of changing the DOM efficiency by 10% is shown in Figure 8.21.

Bulk Absorption and Scattering

As described in Section 3.2.2, the bulk ice model used in IceCube is fit in-situ using data from the deployment and detector operation in a process similar to the one described in 5.3. The model consists of scattering and absorption coefficients fit as a function of depth within the detector. Uncertainties for these scattering and absorption coefficients, shown in Figure 3.11, provide a significant source of uncertainty for physics measurements in IceCube. To handle these effects at the analysis level, global scale factors are used to modify all scattering or absorption coefficients in the bulk ice model simultaneously. Using the most recent published uncertainties on our ice model, a total uncertainty of 10% is assumed for these global scale factors [87]. Three sets of scale factors are typically used, corresponding to sets with 10% larger absorption coefficients, 10% larger scattering coefficients, and a 7.1% reduction to both sets of coefficients.

The bulk ice uncertainties have not been tested in previous oscillation analyses [79, 80, 81], but have been tested in the appearance analysis presented here. Both parameters have significant impacts in the appearance analysis.

The scattering and absorption exhibit different behaviors at final level in the GRECO sample. In general, the absorption behaves in a similar manner to the DOM efficiency, as both parameters modify the number of observed photons at the face of the PMT. In the signal samples, the effects of absorption uncertainties is relatively small. The

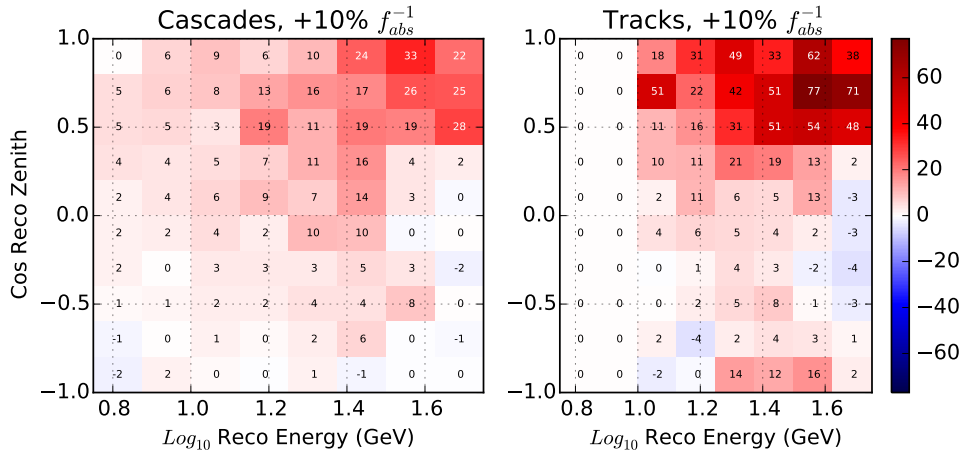


Figure 8.22 – The effect of the absorption in the analysis histogram. The colorbar shows the percent change in rate per bin for a shift of 10%. The absorption stops photons before they reach DOMs and has similar effects as the DOM efficiency.

most notable feature is an overall rate decrease (increase) for larger (smaller) absorption coefficients. As in the DOM efficiency, the depth of the oscillation minimum is also affected by the absorption coefficients due to a change in the reconstruction resolution. The absorption, shown in Figure 8.22, affects the atmospheric muons much more strongly than the neutrinos. Once again, this is due to the event selection: with weaker absorption (smaller coefficients), more photons from the muon track may be detected. The observation of additional photons from the muon track improves the veto efficiency, leading to a significant decrease in the number of muons at final level.

The effect of the scattering is shown in Figure 8.23. A few bins in the downgoing track-like histogram show strong effects inconsistent with nearby bins. These bins arise due to statistical uncertainty in the parametrizations of the low statistics atmospheric muons sets. Other than these bins, the scattering does not appear to strongly affect the atmospheric muons.

In the neutrinos, the effects of the scattering are more important. In particular, stronger scattering (larger coefficients) lead to a reconstruction bias, with more events reconstructing as downgoing. This is a known effect of the reconstruction, where we use a version of the ice model which interprets off-time hits as being due to backscattered photons in a downgoing event.

Hole Ice and Forward Scattering

While the bulk ice refers to the scattering and absorption properties of the entire interaction volume, additional care must be taken for the hole ice described in Sections 3.3 and 4.2.3.

The uncertainties associated with the hole ice are some of the most important systematics in previous IceCube analyses [81]. The simulation of the hole ice model used here, discussed briefly in 4.2.3, requires two free parameters which will be referred to as the *hole ice* (p_1 in Figure 4.2) and *forward scattering* (p_2 in Figure 4.2) parameters.

The models of the angular acceptance were shown previously in Figure 4.2). The hole ice parameter, shown in Figure 8.24, modifies the efficiency of accepting photons incident

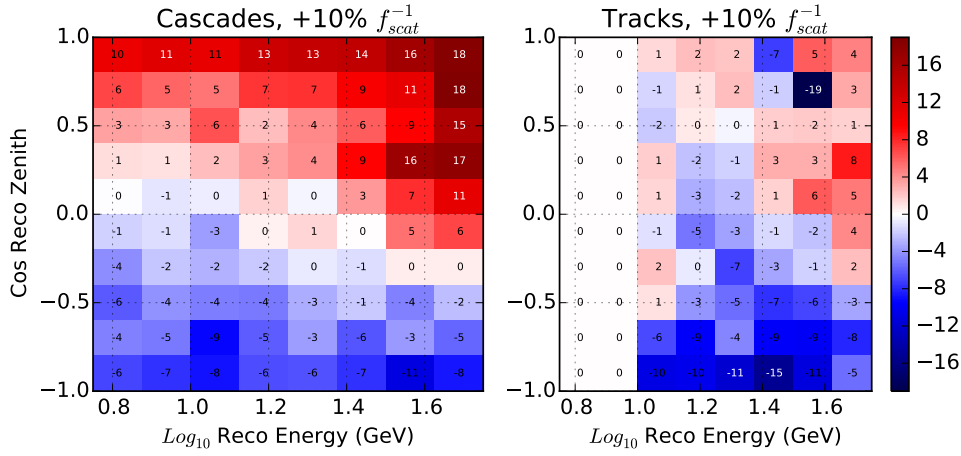


Figure 8.23 – The effect of the scattering in the analysis histogram. The colorbar shows the percent change in rate per bin for a shift of 10%. The scattering changes the directions of photons as they propagate through the ice. Photons which scatter lose information about the source direction, leading to worse reconstructions.

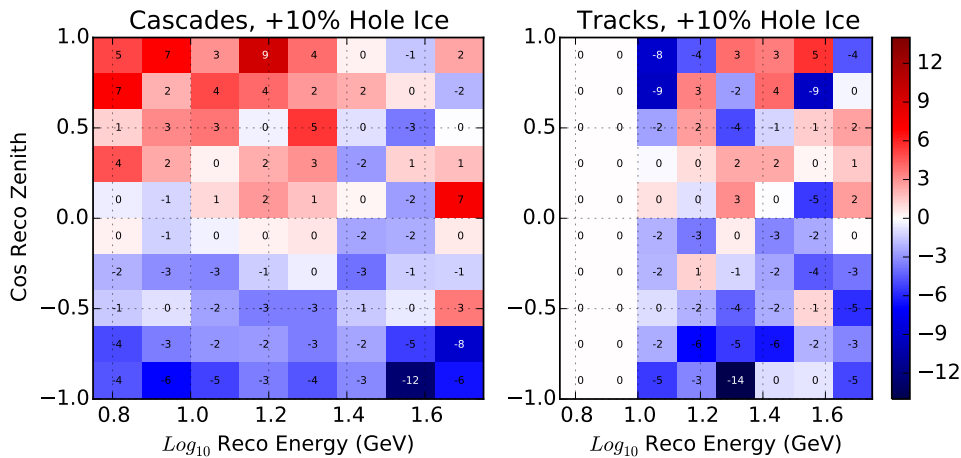


Figure 8.24 – The effect of the hole ice parameter in the analysis histogram. The colorbar shows the percent change in rate per bin for a shift of 10%. The hole ice parameter affects the efficiency of detecting photons at the side of the DOM. This parameter changes the angular distribution of photons at the DOM, leading to differences in the resolution of events.

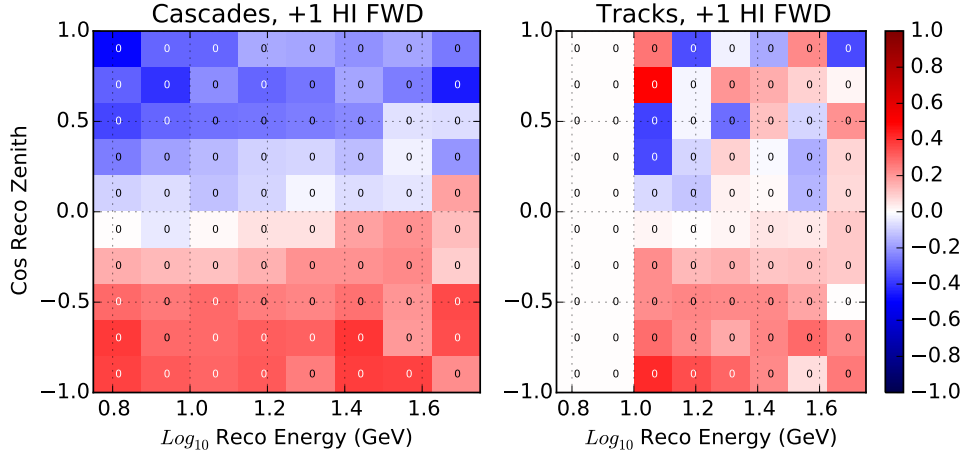


Figure 8.25 – The effect of the forward scattering parameter in the analysis histogram. The colorbar shows the percent change in rate per bin for a shift of 10%. The forward scattering value affects the efficiency of detecting photons at the front of the DOM. This parameter changes the angular distribution of photons at the DOM, leading to differences in the resolution of events.

from the horizon at each DOM while the forward scattering, shown in Figure 8.25, modifies only the acceptance of the very-forward region.

The effects of the two hole ice parameters show similar behavior to that of the scattering uncertainty in the bulk ice, as all three coefficients are modeling the scattering properties of different locations in the ice. Tests performed using the GRECO sample have shown that the three parameters are sufficiently distinct to include all three.

8.4 The Test Statistic for the Analysis

The measurement of tau appearance includes many systematics parameters. To obtain the best fit set of values, a minimization is performed using a χ^2 test statistic. The form of the χ^2 , which includes terms related to the limited simulation statistics available, is described here.

8.4.1 The χ^2 Fit

The χ^2 is a test statistic used to describe the agreement between two binned histograms. In defining the χ^2 , the observed number of events in each bin of the histogram is assumed to be independently gaussian distributed with mean $\mu = \sum_j^{Evt} w_j$ equal to the expected number of events in simulation.

$$P(x|\mu) = Ne^{\frac{(x-\sum_j^{Evt} w_j)^2}{\sigma^2}} \quad (8.12)$$

where N is a normalization constant. The variance within the bin is described by the Poisson uncertainty in the bin

$$\sigma^2 = \mu = \sum_j^{Evt} w_j \quad (8.13)$$

The χ^2 may be defined using by calculating the log-likelihood of the gaussian distribution.

$$\log(L(\mu|x)) = \log(N) + \frac{(x - \sum_j^{Evts} w_j)^2}{\sigma^2} \quad (8.14)$$

The first term is a constant and typically ignored. The remainder gives the definition of the standard χ^2 test statistic used for minimization. This is typically summed over all bins to obtain a single value describing the agreement between the data and expectation. The standard χ^2 calculation is then

$$\chi^2 = \sum_i^{bins} \frac{(x_i - \sum_j^{Evts} w_{ij})^2}{\sum_j^{Evts} w_{ij}}. \quad (8.15)$$

8.4.2 Finite Statistics

The χ^2 distribution implicitly assumes that the dominant source of uncertainty at the best-fit point comes from the statistical fluctuations of the data around the true distribution represented by the Monte Carlo simulation. The statistical properties of the background simulation sets cannot be ignored for the appearance analysis, however.

The statistical fluctuations of the simulation are often negligible when the simulated livetime provides at least an order of magnitude larger simulation statistics than expected from the data itself. Additional simulated statistics may be produced to reduce fluctuations in the Monte Carlo histograms. In the situation where this is infeasible, modifications to the likelihood space itself may be used to account for the additional uncertainties. For this analysis, the statistical uncertainties of the underlying simulation sets are added to the weighted uncertainties in quadrature. This results in a modification of Equation 8.13.

$$\sigma^2 = \sum_j^{Evts} w_j + w_j^2 \quad (8.16)$$

This changes the definition of the χ^2 .

$$\chi_1^2 = \sum_i^{bins} \frac{(x_i - \sum_j^{Evts} w_{ij})^2}{\sum_j^{Evts} w_j + \sum_j^{Evts} w_{ij}^2} \quad (8.17)$$

Due to the large uncertainties associated with the atmospheric muon sample, further considerations are necessary. In particular, the uncertainties associated with atmospheric muon simulation statistics may be used by the fitter in order to reduce the χ_{FS}^2 value. This situation proceeds with the minimization process until a runaway effect is observed by increasing the statistical uncertainties at the expense of data/simulation agreement. In this case, the numerator becomes

$$\lim_{N_\mu \rightarrow \infty} \left(x_i - \sum_j^{Evts} w_{ij} \right)^2 = \left(\sum_j^{Evts} w_{ij} \right)^2 \quad (8.18)$$

The resulting limit in each bin as the event weights become large is therefore

$$\lim_{N_\mu \rightarrow \infty} \chi_1^2 = \sum_i^{bins} \frac{\left(\sum_j^{Evts} w_{ij}\right)^2}{\left(\sum_j^{Evts} w_{ij}\right)^2 + \sum_j^{Evts} w_{ij}^2} \quad (8.19)$$

$$\lim_{N_\mu \rightarrow \infty} \chi_1^2 = 1. \quad (8.20)$$

While this is a particular concern for all simulation types, the dominant contribution to the $\sum_j^{Evts} w_{ij}^2$ term is the atmospheric muons. In addition, the atmospheric muons have the strongest impacts from non-normalization systematic uncertainties. This is particularly true in the case of the DOM efficiency and absorption uncertainties, which both strongly affect the total number of muons observed. Modifying either the or the normalization systematics in the fit may lead to this runaway behavior, an effect not observed from the neutrino simulation.

In order to prevent this situation, a further modification of the χ^2 is necessary. For this analysis, the total scale of the statistical uncertainty due to atmospheric muons is fixed the seed values of the fit.

$$N_i^\mu = \frac{\left(\sum_j^{Evts} w_{ij}^2\right)_{Seed}}{\sum_j^{Evts} w_{ij}^2} \quad (8.21)$$

With this modification, the χ^2 is now defined to be

$$\chi_{FS}^2 = \sum_i^{bins} \frac{\left(x_i - \sum_j^{Evts} w_{ij}\right)^2}{\sum_j^{Evts} w_j + \left(\sum_j^{Evts} w_{ij}^2\right)_\nu + N_i^\mu \left(\sum_j^{Evts} w_{ij}^2\right)_\mu} \quad (8.22)$$

Taking the limit of this χ^2 as the event weights become large now gives

$$\lim_{N_\mu \rightarrow \infty} \chi_{FS}^2 = \sum_i^{bins} \frac{\left(x_i - \sum_j^{Evts} w_{ij}\right)^2}{\sum_j^{Evts} w_j + \left(\sum_j^{Evts} w_{ij}^2\right)_\nu + N_i^\mu \left(\sum_j^{Evts} w_{ij}^2\right)_\mu} \quad (8.23)$$

$$\lim_{N_\mu \rightarrow \infty} \chi_{FS}^2 = \sum_i^{bins} \sum_j^{Evts} w_{ij} \quad (8.24)$$

in agreement with the limit obtained from the standard χ^2 .

8.4.3 Fit Priors

In many cases, the systematics listed in 8.2.3 have known constraints from external measurements. This information can be useful in the analysis and should be included to bias the minimization toward the most likely systematics values. These constraints are included in the form of *priors* in the analysis. Priors are additional terms included multiplicatively (additively) in the likelihood (log-likelihood) calculation. These often take the form of a Gaussian distribution with mean μ and variance σ^2 given by external measurements. In the search for appearance, most priors are handled assuming a standard gaussian form. For a systematic m with value x_m , these additional terms take the form

$$\chi_m^2 = \frac{(x_m - \mu)^2}{\sigma^2} \quad (8.25)$$

These additional terms are added to 8.22 in order to calculate the final χ^2_{FS} used in the minimization for this analysis.

$$\chi^2_{Total} = \sum_i^{bins} (\chi^2_{FS})_i + \sum_m^{syst} \chi_m^2 \quad (8.26)$$

A list of priors is shown in 8.5. The systematics are divided into two "types": parameters calculated from the hyperplane and "analytic" parameters which do not require additional simulation. Note that the coincident event fraction is effectively a one-sided Gaussian due to physical constraints on the value.

	Systematic	Unit	Type	Baseline/Seed Value	Prior	Allowed Range	Reference
Physics Parameter	N_{ν_τ}	-	Analytic	1.0	-	0.0 - 2.0	-
Oscillations	Δm_{3j}^2 $\sin^2 \theta_{23}$	10^{-3} eV^2 -	Analytic Analytic	2.526 0.440 (NO), 0.66 (IO)	- -	2.0 - 3.0 0.0 - 1.0	[58] [58]
Total Rates	$N_n u, N_m u$	Years	Analytic	2.25	-	0.0 - 10.0	-
Cross-section	Axial Mass (QE) Axial Mass (RES) $N_{\nu_{NC}}$	σ σ -	Analytic Analytic Analytic	0.0 0.0 1.0	0.0 ± 1.0 0.0 ± 1.0 1.0 ± 0.2	-5.0 - 5.0 -5.0 - 5.0 0.0 - 2.0	[94] [94] [81]
Flux	γ_ν γ_μ Up/Horizontal Ratio $\nu/\bar{\nu}$ Ratio Φ_{ν_e} Coincident Fraction	- σ σ σ - -	Analytic Analytic Analytic Analytic Analytic Hyperplane	0.0 0.0 0.0 0.0 1.0 0.0	0.0 ± 0.10 0.0 ± 1.0 0.0 ± 1.0 0.0 ± 1.0 1.0 ± 0.05 $0.0 + 0.10$	-0.50 - 0.50 -5.0 - 5.0 -5.0 - 5.0 -5.0 - 5.0 0.8 - 1.2 0.0 - 1.0	[18] [125] [124] [124] [124] -
Detector	DOM Efficiency Hole Ice Forward Scattering Absorption Scattering	- - - - -	Hyperplane Hyperplane Hyperlane Hyperplane Hyperplane	1.0 0.25 0.0 1.0 1.0	1.0 ± 0.1 0.25 ± 0.10 - 1.0 ± 0.1 1.0 ± 0.1	0.7 - 1.3 0.0 - 0.5 -5.0 - 5.0 0.5 - 1.5 0.5 - 1.5	[73, 129] [81] [81] [73] [73]

Table 8.5 – Priors and allowed ranges for each systematic included in this analysis.

8.4.4 Fitting Code

Checks in this analysis are first performed using solely simulation files. In order to understand the expected sensitivity of this analysis, a software fitting package previously used to fit the ν_μ disappearance is used [79, 80, 81].

The code, known as *OscFit*, works in multiple stages. After separating the simulation into separate channels consisting of ν_e^{CC} , ν_μ^{CC} , ν_τ^{CC} , ν^{NC} , μ_{atm} , and accidental triggers, the analytic systematics are applied. These systematics solely rely on information about the particle interaction in order to calculate correction factors to the event weights and are not sensitive to the order of application. The oscillation calculations are performed as analytic systematics based on the Prob3++ code [46] to calculate the full three-flavor unitary oscillations including matter effects within the Earth using a reference model of the Earth [47].

When including the neutral current interactions from tau neutrino events in the signal definition, the neutral current events are reweighted for oscillations at this stage. The *OscFit* code assumes the neutral current interaction rate is unaffected by oscillations. The tau neutrino neutral current events are not directly included in favor of the significantly higher simulation statistics from the other sets. Because no charged leptons are produced in the neutral current interactions, no differences in event topology are expected based on flavor of neutrino interaction. For the purposes of this analysis, the neutral current interactions from electron neutrino and muon neutrino events are instead used to model the effect of the tau neutrino neutral current events. The Prob3++ code calculates oscillation probabilities for these events to oscillate to tau neutrinos.

$$R_{\nu_\tau^{NC}} = R_{\nu_e^{NC}} P_{\nu_e \rightarrow \nu_\tau}(\theta_{23}, \Delta m_{3i}^2) + R_{\nu_\mu^{NC}} P_{\nu_\mu \rightarrow \nu_\tau}(\theta_{23}, \Delta m_{3i}^2) \quad (8.27)$$

The modification to the total neutral current rate given the tau neutrino normalization, N_{ν_τ} , is then given by

$$R'_{\nu^{NC}} = R_{\nu^{NC}} + R_{\nu_\tau^{NC}} (N_{\nu_\tau} - 1). \quad (8.28)$$

The modified weights are then used to histogram the simulated event samples into one histogram per simulation channel.

After histogramming, the detector systematics are applied to the each of the binned templates bin-by-bin using hyperplanes calculated as described in Section 8.3.6.

Once all systematics have been applied, the normalization terms representing the overall scale factors for the neutrino rate, N_ν , the muon rate, N_μ , and the accidental rate, N_{noise} , are multiplied to the respective histograms. The final histograms are summed together to form the final simulation expectation to be compared to the data using the χ^2_{FS} described in Equation 8.22.

The value of the χ^2_{FS} is minimized as a function of the various systematics using the iMinuit2 package [104, 103]. The minimization continues until the requested tolerance, 10^{-16} , is reached by the minimizer, after which the best fit histogram and systematics values are returned to the user.

8.5 Expected Sensitivity to Appearance

With the full set of systematics included, the *sensitivity* of the analysis may be calculated. The sensitivity is a measure of the expected result and can be performed with simulated events prior to the final fit to data.

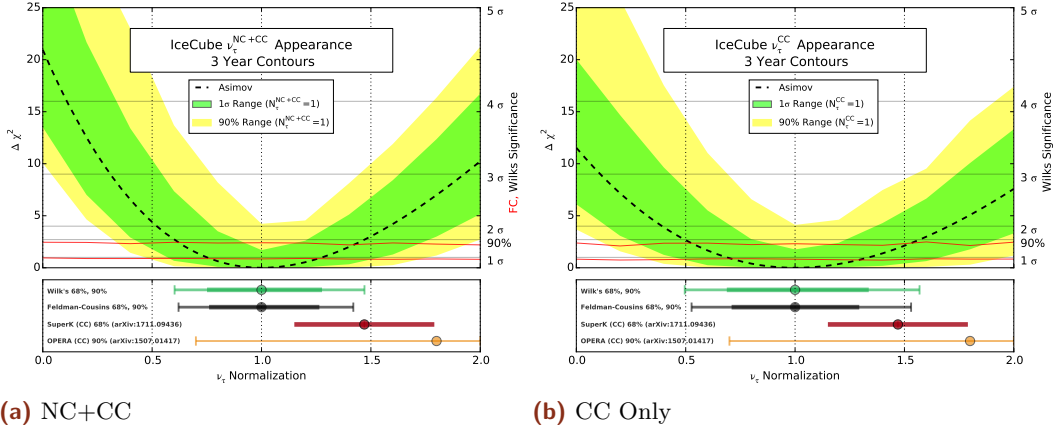


Figure 8.26 – The sensitivity of this analysis in the (a) NC+CC and (b) CC-only channel. The top plot shows the Asimov expectation (black dotted line) and the Brazilian flag (green, yellow bands). The significances assuming Wilk’s theorem (gray horizontal lines) and Feldman-Cousins (red horizontal lines) are also shown. The bottom plot shows the expected 1σ and 90% ranges for Wilks theorem and Feldman-Cousins compared to the most recent results from the OPERA and Super-Kamiokande analyses.

lofsubfigure\|numberline(a)NC+CClofsubfigure\|numberline(b)CC Only

To evaluate the expected sensitivity of this analysis, the OscFit code is used to find the best-fit value of the χ^2_{FS} . Multiple methods are used to evaluate both the average expected sensitivity and range of variation of the sensitivity due to both the data and simulation statistics. A summary of the results using all methods is shown in Figure 8.26. Each component will be described in turn.

8.5.1 The Asimov Dataset

The first method, known as the *Asimov* expectation [130], begins by creating the expected histogram using baseline values of the systematics and oscillations. The produced histogram, representing an exact PDF of the expected events, is then used as an estimate of the data. A scan is performed over values of N_{ν_τ} , minimizing the χ^2_{FS} at each point to produce a contour. A final minimization is performed allowing the minimizer to identify the global best-fit value of N_{ν_τ} .

The final expected sensitivity in the Asimov approach is given by calculating the likelihood ratio, $\Delta\chi^2$, between the values of the χ^2_{FS} at each point and the global best fit.

$$\Delta\chi^2(N_{\nu_\tau}) = \chi^2_{FS}(N_{\nu_\tau}) - \chi^2_{FS}(N_{\nu_\tau}^{Global}) \quad (8.29)$$

The value of $\Delta\chi^2_{FS}$ as a function of N_{ν_τ} is shown by the dotted black line in Figure 8.26. These values may be converted into expected significance levels using the procedure described in Section 8.5.2.

8.5.2 The Brazilian Flag

The second method, producing what is known as a *Brazilian flag* plot due to the color scheme, provides an estimate of the statistical uncertainty on the Asimov sensitivity. The production of a Brazilian flag begins with the production of a pseudo-data histogram from the Asimov histogram. Because the simulation sets used here have significant

uncertainties due to limited simulation statistics, the first step is to vary the event rate in each bin within the statistical uncertainties of the Monte Carlo.

A new realization of the simulation histogram is produced by sampling new rates in each bin using a gaussian distribution with mean $\mu_i = \sum_j^{Evt} w_{ij}$ and variance σ_i^{MC} given by

$$\sigma_i^2 = \sqrt{\sum_j^{Evt} w_{ij}^2}. \quad (8.30)$$

The new histograms are then summed together and a final rate in each bin is sampled from a Poisson distribution with mean equal to the new expectation, creating a representation of one possible realization of the data in the analysis. The OscFit minimization then proceeds as described in the Asimov case for each of 500 realizations of pseudo-data, with the calculation of the $\Delta\chi^2$ as described in 8.29. The Brazilian flag shows the 1σ and 90% range of $\Delta\chi^2$ values at each value of N_{ν_τ} . This provides a graphical representation, shown in the colored bands of Figure 8.26, of the expected range of variation of the sensitivity given solely statistical uncertainties.

8.6 Feldman-Cousins vs Wilk's Theorem

Estimates of the sensitivity of the analysis were performed using a theorem by Samuel S. Wilks [131]. The theorem describes the distribution of the likelihood ratio when fits form a "nested model". The nested model indicates that the fit parameters used in one fit hypothesis, H_0 , form a complete subset of those used in another fit hypothesis, H . if the two likelihoods used in the likelihood ratio differ by N parameters, Wilk's theorem states that the distribution of the test statistic $-2\ln\left(\frac{L}{L_0}\right) = \Delta\chi^2$ will asymptotically approach a chi-squared distribution with N degrees of freedom.

Wilk's theorem is a powerful tool used to estimate the significances of results and is widely used. In the case of the measurement of tau neutrino appearance, fits are performed twice in order to obtain the likelihood ratio: once with the value of N_τ fixed to various points and once with N_τ freely floating. The likelihood ratio is then calculated at each fit point relative to the overall best-fit likelihood using Equation 8.29. These two fits form a nested model with $N=1$, allowing the application of Wilk's theorem to estimate significances.

Wilk's theorem gives a useful estimate of the significance and requires negligible additional computational power. However, the theorem states only an asymptotic limit. Evaluation of the applicability of Wilk's theorem requires a more robust analysis using Monte Carlo trials.

A more robust procedure, introduced by Gary Feldman and Robert Cousins [132], may be applied instead. Instead of assuming a number of degrees of freedom, the Feldman-Cousins procedure requires directly using the distribution of the $\Delta\chi^2_{FS}$ test statistic in order to evaluate the significance. For public IceCube oscillation results, a method similar to the procedure by Feldman and Cousins is used [81].

To begin, a value of N_τ^{True} is selected. Monte Carlo trials are produced with this true value and the likelihood ratio between the best-fit value of N_τ and N_τ^{True} for each trial is calculated. The distribution of the likelihood ratios is used to identify the value of $(\Delta\chi^2_{FS})$ below which $P_{i=1\sigma}(\Delta\chi^2_{FS}) \approx 68.27\%$ of trials lie. This value is interpreted as the 1σ level for the chosen value of N_τ^{True} . The procedure may be repeated for each required value of N_τ^{True} and different significance levels i .

Examples of the likelihood ratio distribution for various values of N_τ^{True} are shown in Figure 8.27. A χ^2 distribution with 1 degree of freedom is overlaid, showing the expected

distribution assuming Wilk's theorem. The difference in location of the 90% level from Wilks (green) and Feldman-Cousins (red) is also shown. In general, the distributions show a preference for a slightly narrower distribution than expected from Wilk's theorem. The difference indicates that the Wilk's theorem approximation may be inaccurate and that the Feldman-Cousins procedure is necessary to correctly characterize the final result.

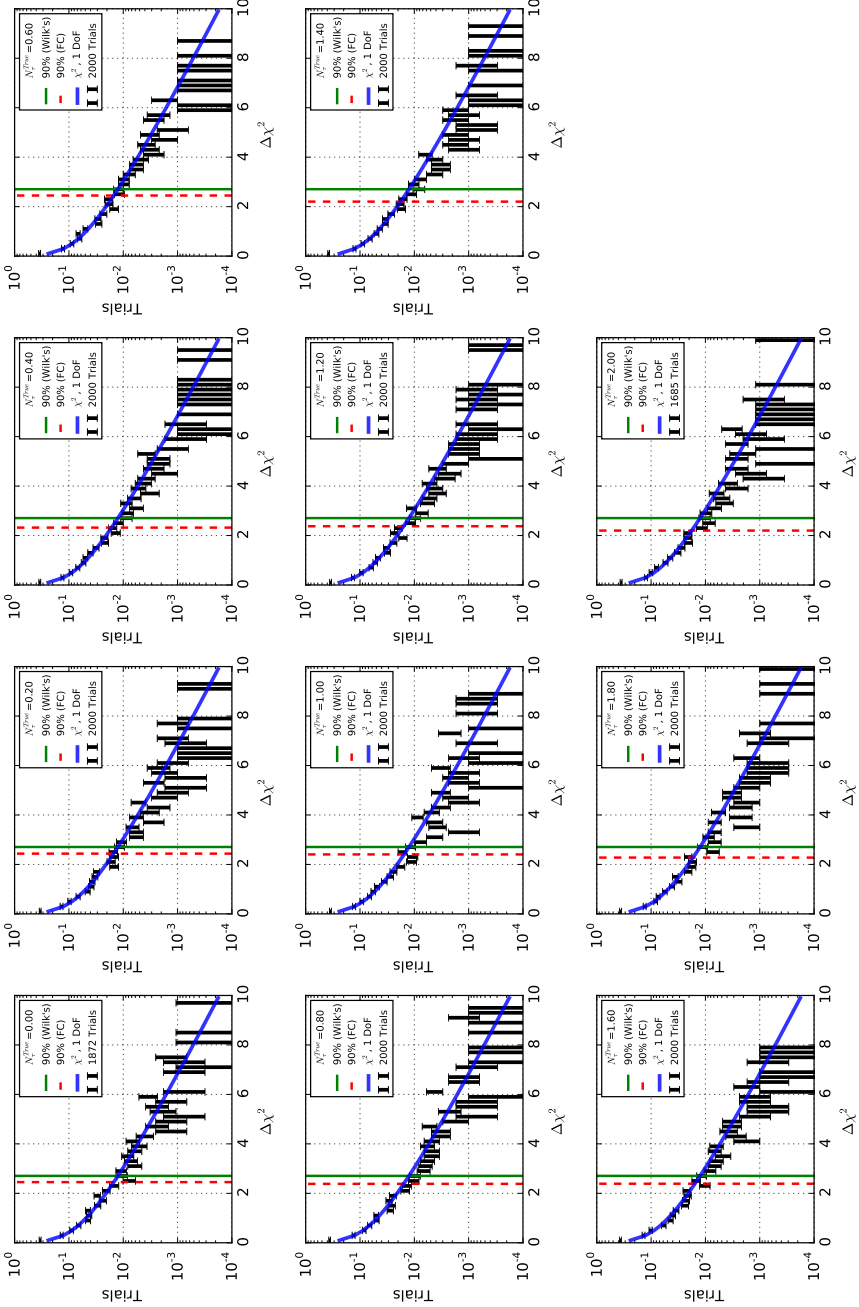


Figure 8.27 – The test statistic distributions for 11 points in N_{τ}^{True} in the NC+CC fit. The assumption of 1 degree of freedom from Wilk's theorem is tested by looking at the location of $(\Delta\chi_{FS}^2)_{90\%}$ for each point. The distribution calculated from Monte Carlo trials is narrower than that predicted by Wilk's theorem, indicating that a more complete treatment with the Feldman-Cousins procedure is necessary.

The Feldman-Cousins procedure yields the values of $\Delta\chi^2_{FS}$ corresponding to the 1σ and 90% confidence levels. The final confidence intervals at level i are obtained by finding the values of N_τ with $\Delta\chi^2_{FS} = (\Delta\chi^2_{FS})_{FC}^i$.

The evaluated $(\Delta\chi^2_{FS})_i$ are limited to the discrete values chosen in N_τ^{True} . In order to obtain a continuous model, the values of $(\Delta\chi^2_{FS})_i$ and the contour from data are splined using the UnivariateSpline from Scipy [105]. The crossing points of the two splines may then be calculated to obtain the best estimate for the final result.

The procedure does not rely on assumptions about the test statistic distribution and works even in cases where the likelihood ratio distribution is not chi-squared distributed. The number of trials required to reduce the effect of statistical fluctuations in the evaluation, however, can make such evaluations prohibitively expensive.

A total of 1000 trials at each point are evaluated for the fits to both N_τ^{CC} and N_τ^{NC+CC} . All trials were produced assuming the baseline values of each systematic and with $N_\tau = 1$. The resulting values of $(\Delta\chi^2_{FS})_{FC}^i$ are shown in the red lines in Figure 8.26.

8.7 Impact of Systematics

There are various ways to measure the impact of the included systematics in this analysis. Described here are methods to evaluate, in order of increasing importance, the total systematics impact, the impact of each systematic individually, the correlation between systematics, and the effect of non-baseline values. Each of these test different aspects of the sensitivity and all are included for completeness.

Total Systematics Impact

The total impact of the systematics on the sensitivity may be measured by comparing the total Asimov sensitivity to an Asimov sensitivity calculated using no systematics. This is shown at the bottom of Figure 8.28. It is clear from the comparison that the analysis is very sensitive to the included systematics set.

N+1 Tests: Sensitivity of Analysis to Systematic

A different test is also possible: Instead of calculating likelihoods with no systematics included, a single systematic may be used at a time. This test, called an N+1 test for the addition of one systematic at a time, yields useful information on a sample's sensitivity to single systematics. The results of the N+1 tests are shown in Figure 8.28.

A small change in sensitivity between the no-systematics case above and an N+1 Asimov sensitivity may have two possible explanations. The first that the current analysis is unaffected by changes in the systematic, implying that the systematic may be investigated for removal in the analysis. The second possibility is that the systematic may interact with other parameters in order to produce an effect. The second case is more difficult to diagnose, but further tests may be possible.

N-1 Tests: Redundancy Between Systematics

In contrast to the N+1 tests, N-1 tests start with the full suite of systematics included. One systematic is fixed to the baseline value and removed before minimization. The change in the expected result, shown in Figure 8.29, allows the investigation of redundancy between systematics. If, for example, two systematics have similar effects in the final histogram, then the N-1 test will show no change in sensitivity due to the removal.

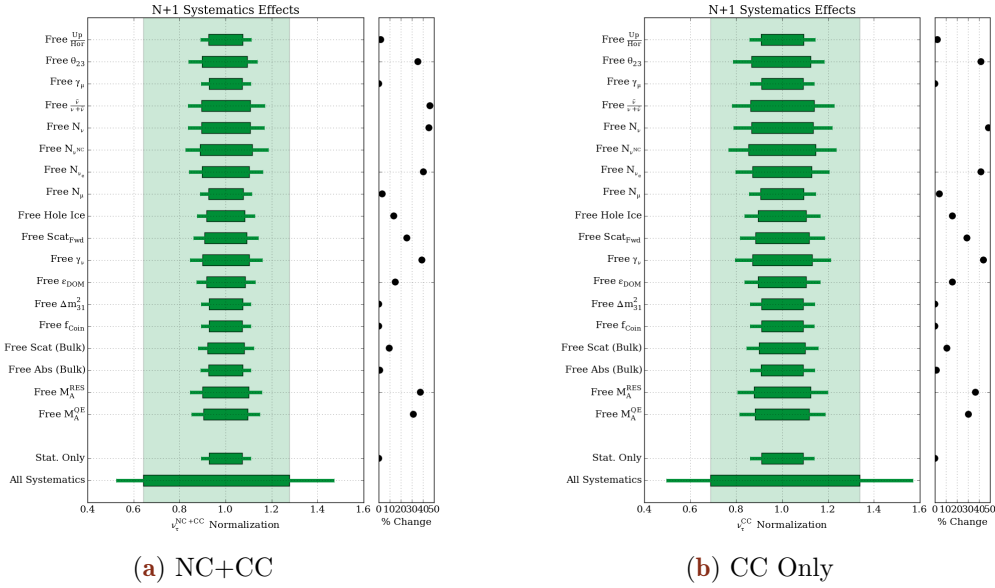


Figure 8.28 – The N+1 parameter tests for the NC+CC fit (a) and the CC-only fit (b). Only one parameter is allowed to move at a time. The change in the 1σ and 90% expected confidence intervals give an indication of the strength of each systematic in isolation.

The redundancy tests show that the analysis is most strongly affected by the mass splitting, Δm_{31}^2 , the $\nu/\bar{\nu}$ ratio, and the forward scattering in the hole ice model. The up/horizontal ratio, electron neutrino flux normalization, and muon spectral index all have negligible impact in the analysis according to the redundancy tests.

It is also possible that the analysis is strongly sensitive to the value of the systematic and is unlikely to move from the baseline value. These tests can be useful in identifying redundant parameters for removal, although with the caveat that combinations of parameters are not tested. After removal of multiple redundant parameters, the updated Asimov sensitivity should be tested once again to verify that the combination of removed parameters remains irrelevant for the fit. This procedure was used to remove the effects of the DIS and propagation uncertainties discussed in Sections 8.3.4 and 8.3.3 respectively. No further parameters have been removed from the appearance fit.

"Hidden Potential" Tests: Non-Baseline Values

Both the N+1 and N-1 test suffer from a particular flaw. Both fail to test the analysis for exceptionally strong sensitivity to particular systematics. In order to identify these parameters, the "hidden potential" test has been proposed. In this test, the Asimov sensitivity of the full analysis containing all proposed systematics is used as a baseline. Each systematic is then fixed, one at a time, off of the baseline value before rerunning the minimization. The parameters with priors tend to be fixed to one standard deviation from the prior mean. The change in the sensitivity gives an indirect measure of the strength of the systematic effect in the analysis. If no change is observed, the parameter is likely to be redundant and may be investigated for removal from the analysis.

hidden potential martin
n-1 tests *RUNNING*

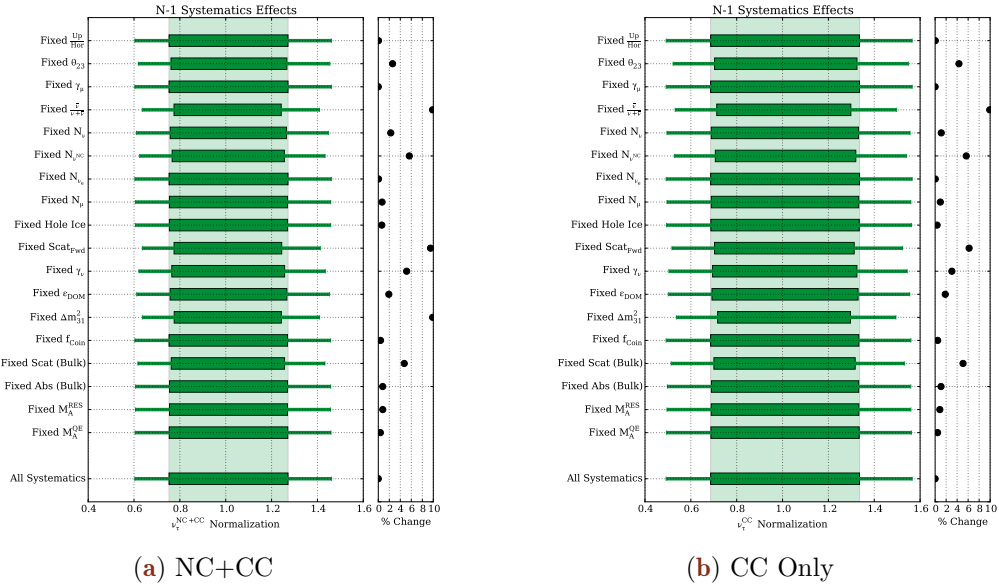


Figure 8.29 – The N-1 redundancy tests for the NC+CC fit (a) and the CC-only fit (b). Each parameter is held fixed at the baseline value and the change in the 1σ and 90% expected confidence intervals are tested to identify the most important parameters.

8.8 Fitting Data

Icecube analyses are developed *blindly* in order to minimize bias. A blind analysis limits potential bias in a measurement by either obfuscating the final measurement parameters or limiting the sensitivity of tests including data. Oscillation analyses using DeepCore use a staged blind analysis approach.

The initial stage, testing with a small sample of the data to detect software issues, is referred to as a *burn sample* test. The burn sample used in the search for appearance consisted of 1% of all data runs in three years. The results of the burn sample test were unremarkable and will not be discussed here.

The remaining stages in an IceCube oscillation analysis consist of *blind fits*, where the full dataset is fit while physics parameters are blinded, and the final *unblinding*, in which the best fit parameters are revealed. These stages will be discussed in turn.

8.8.1 Blind Fits: Checking the Goodness-of-Fit

Once the burn sample tests are complete, the next stage is to perform what is known as a *blind fit*. The concept, developed for oscillation analyses in IceCube, exists as an intermediate stage between the low-sensitivity burn sample tests and the final fit.

Unlike the burn sample fits, the blind fits is used the full data sample for testing. All systematics are included in the fit as normal. The final physics parameters, in this case the oscillation parameters, Δm_{31}^2 and θ_{23} , and the value of N_τ , are allowed to fit freely, but the final results are obfuscated. The goodness-of-fit and systematics values are free for investigation.

The blind fit exists in order to identify systematic disagreements between data and simulation. Investigations of poor agreement are performed blindly without knowledge of the impact on the physics parameters.

Analyzers are free to move onto a request for full unblinding if the goodness-of-fit exceeds 5%. If the goodness-of-fit is significantly lower than this limit, the sample and fit must be investigated further to identify any potential issues or oversights.

The goodness-of-fit, known more informally as the *p-value* associated with the fit, may be calculated via two closely-related methods. In the first, an ensemble of Monte Carlo trials is fit and the resulting χ^2_{FS} values extracted. The fraction of trials with χ^2_{FS} larger than that observed in data gives the first p-value.

The second method uses SciPy to fit a χ^2 distribution. The p-value may then be calculated from the continuous distribution by finding the total probability of observing a fit with a χ^2_{FS} value equally or worse than the data fit, $P_2(\chi^2_{FS} \geq (\chi^2_{FS})_{Data})$.

scipy

The first method generally will yield more accurate results, particularly if the resulting distribution is poorly modeled by a χ^2 distribution. If the fit is particularly poor, a large number of trials may be necessary in order to calculate an accurate p-value. In these cases, the second method may be used to provide an estimate of the p-value of the fit.

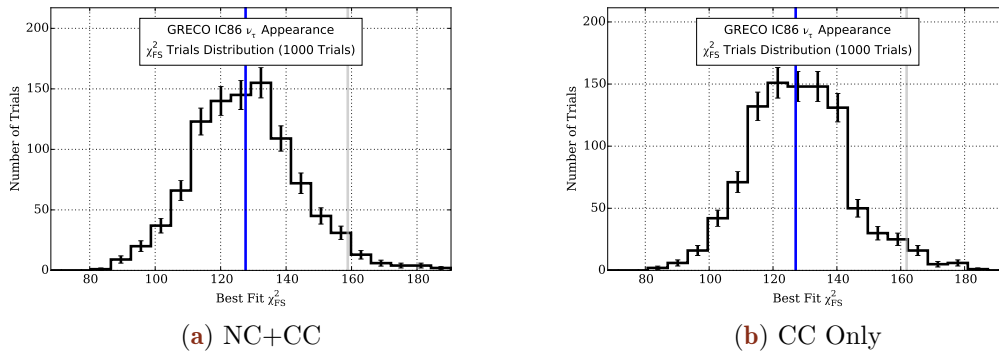


Figure 8.30 – Goodness of fit in the appearance search. The trials distribution, shown in black, is used to calculate the pvalue. The grey line shows the location corresponding to a 5% p-value. The blue line shows the value of χ^2_{FS} found from data. Both fits show good agreement with data and simulation.

During the first work with blind fits, this analysis used a wide range of reconstructed energies, including events up to 800 GeV in order to better constrain systematics terms in the non-oscillating higher energy regions. Blind fits in the GRECO analysis initially showed significant disagreement between the data and simulation, with a goodness-of-fit of 10^{-7} . Investigations yielded new discoveries, discussed in Section 7.7.3, about both the calibration of the Monte Carlo simulation and previously-unknown erroneous events in the data.

After the removal of the flaring DOM events, the correction of bedrock events, and the elimination of the charge in the PegLeg fit, a new blind fit was performed and the goodness-of-fit was again tested. The resulting χ^2_{FS} for the charged-current only and neutral-current + charged-current fits were 127.095 and 127.623 respectively. One thousand trials were run for each fit using the updated sample, yielding estimates of the test statistic distributions. The p-values, shown in Figure 8.30, were $p=52.8\%$ and $p=49.8\%$ calculated from trials respectively.

The full map of the χ^2_{FS} values is shown in Figures 8.31 and 8.32. No single region of disagreement is visible, indicating that there are no significant remaining unmodeled systematic uncertainties.

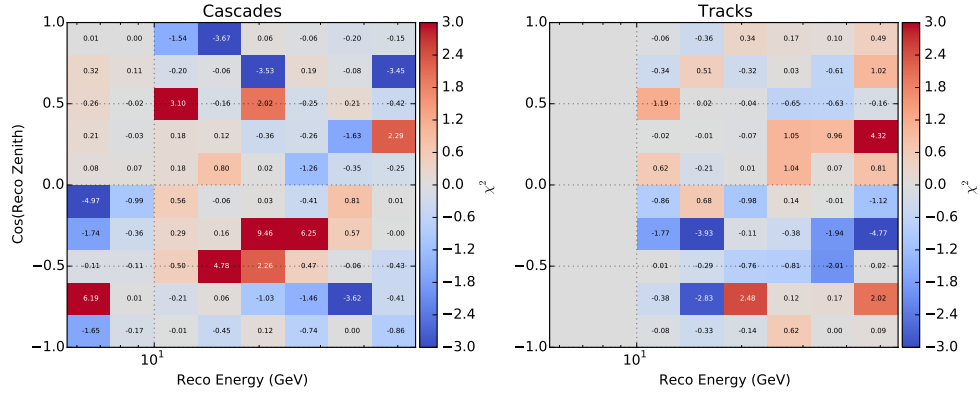


Figure 8.31 – A map of the "signed" χ_{FS}^2 values for the CC-only fit. There is no single region of disagreement.

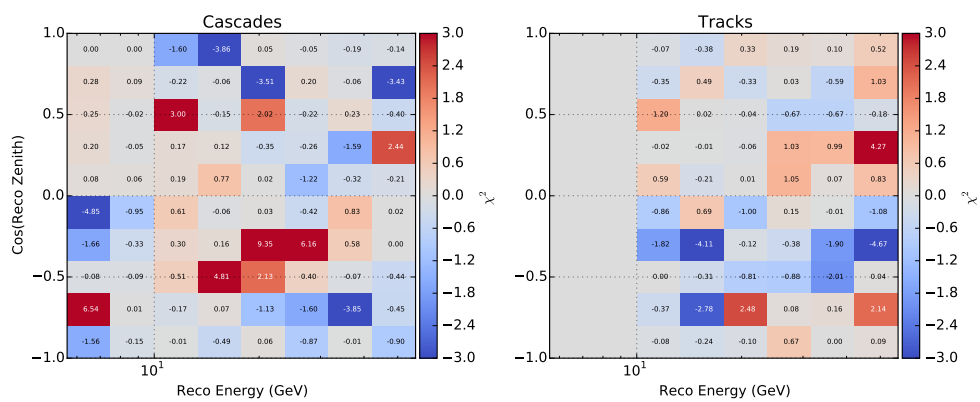


Figure 8.32 – A map of the "signed" χ_{FS}^2 values for the NC+CC fit. There is no single region of disagreement.

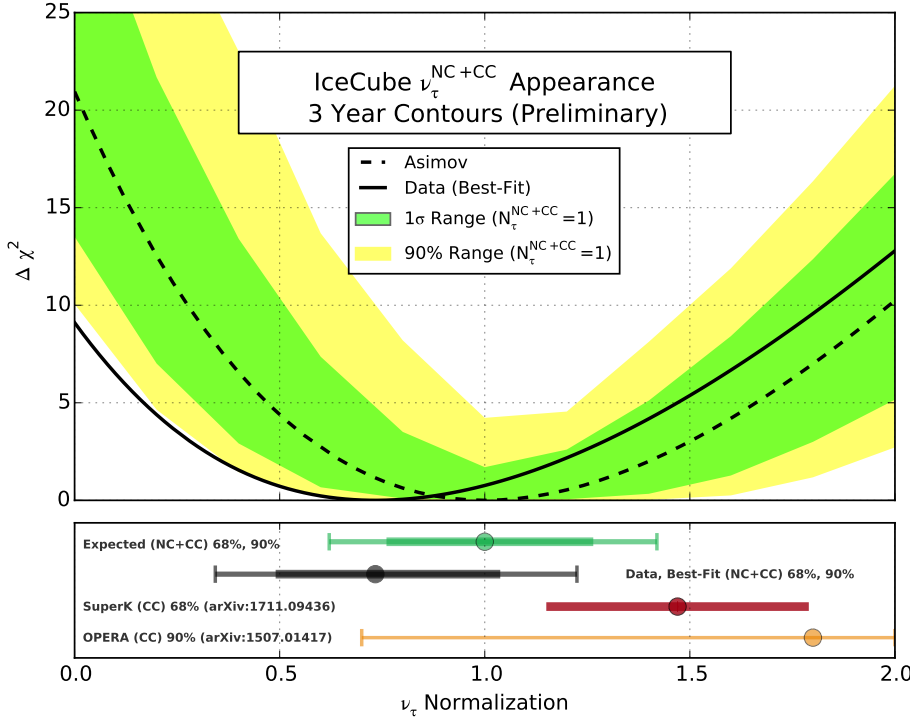


Figure 8.33 – The final result of the CC-only fit. The best fit is lower than 1.0, at $N_\tau^{CC} = 0.566^{+0.356}_{-0.303}$ (syst+stat).

8.9 Results from the Search for Appearance

With good agreement between data and simulation in both fits, the appearance measurement with GRECO was granted unblinding approval. For the fit using only charged-current tau neutrino events, the best fit value was found to be $N_\tau^{CC} = 0.566^{+0.356}_{-0.303}$ (syst+stat). For the fit including both neutral and charged tau neutrinos, the best fit was $N_\tau^{NC+CC} = 0.733^{+0.305}_{-0.243}$ (syst+stat). Both intervals are given at the 1σ level and include the effects of the Feldman-Cousins procedure. Both results, shown in Figure 8.9 and Figure 8.34, fit lower than expected from unitary 3-flavor oscillations, although both are consistent with such a model.

The final value of the systematics, shown numerically in Table 8.6 and graphically in Figure 8.35, are within 1σ of the expectation at the best-fit points. Many systematics were expected to be determined primarily from the data instead of from priors. Figures 8.36 and 8.37 show the expected values of each systematic for 1000 trials. The shaded band shows the assumed 1σ prior range for each of the parameters, if present. Not only are all systematics within the relevant priors, but most systematics fit within the expected posteriors as well.

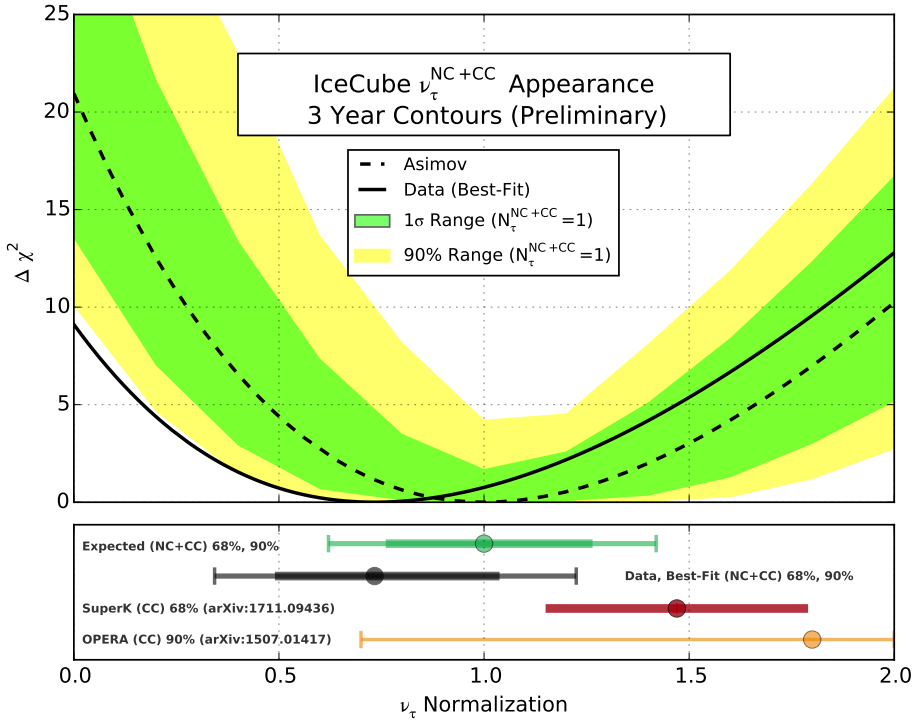


Figure 8.34 – The final result of the NC+CC fit. The best fit is lower than 1.0, at $N_\tau^{NC+CC} = 0.733^{+0.305}_{-0.243}$ (syst+stat).

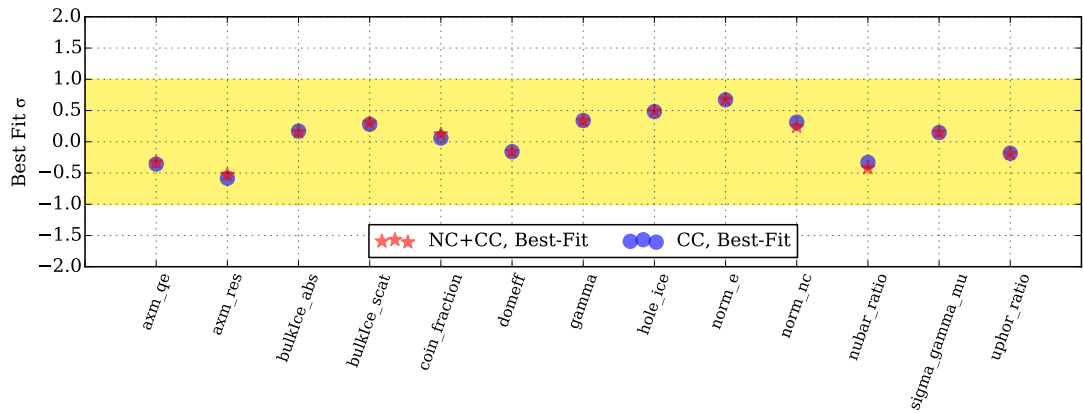


Figure 8.35 – The value of each systematic with priors. The best-fit values are shown for each while the priors are shown by the yellow band. The CC and NC+CC fits are highly correlated, as expected, with very little difference in the systematics best-fit values. All values fit well within the expected 1σ ranges.

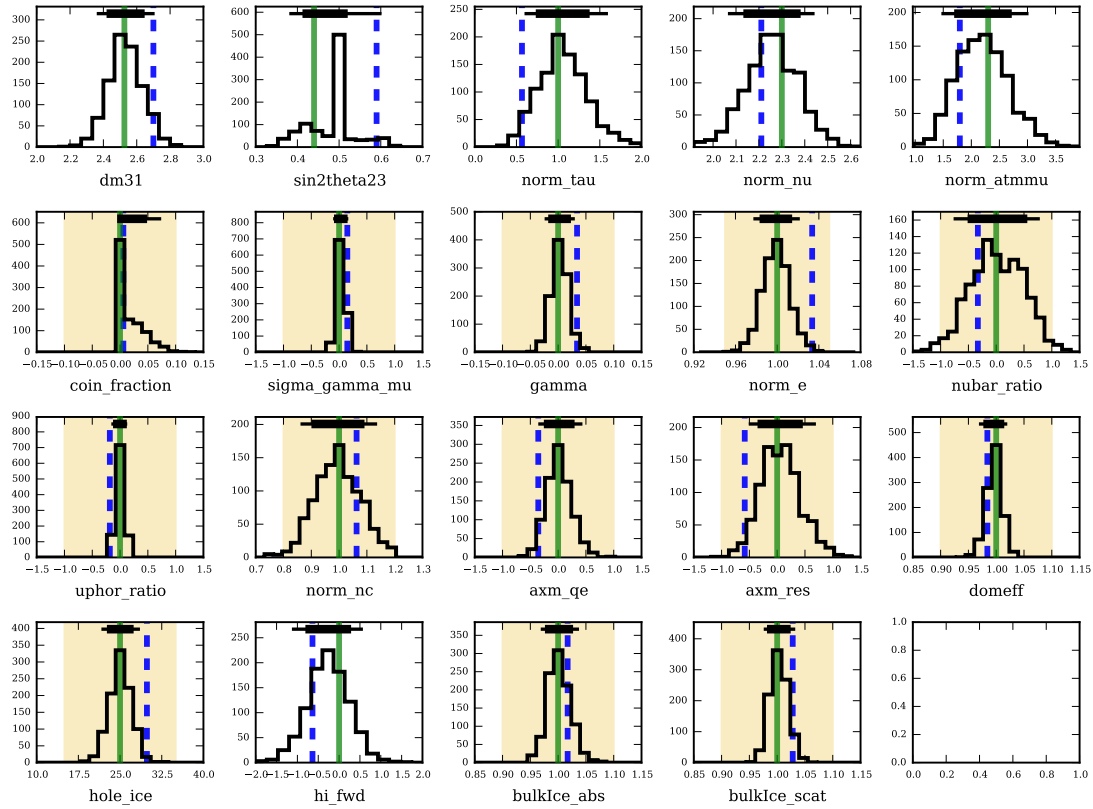


Figure 8.36 – A comparison of the posterior expected from trials to the final data fit value for each parameter for the CC-only fit. The trials used to build the posterior distribution in each parameter assume baseline values for systematics, $N_\tau^{CC} = 1$, and Nu-Fit 2.2 values [57]. The green vertical line shows the true injected value. The blue dotted line shows the best-fit value from data. The black bar shows the 1σ and 90% ranges calculated from the posterior distribution.

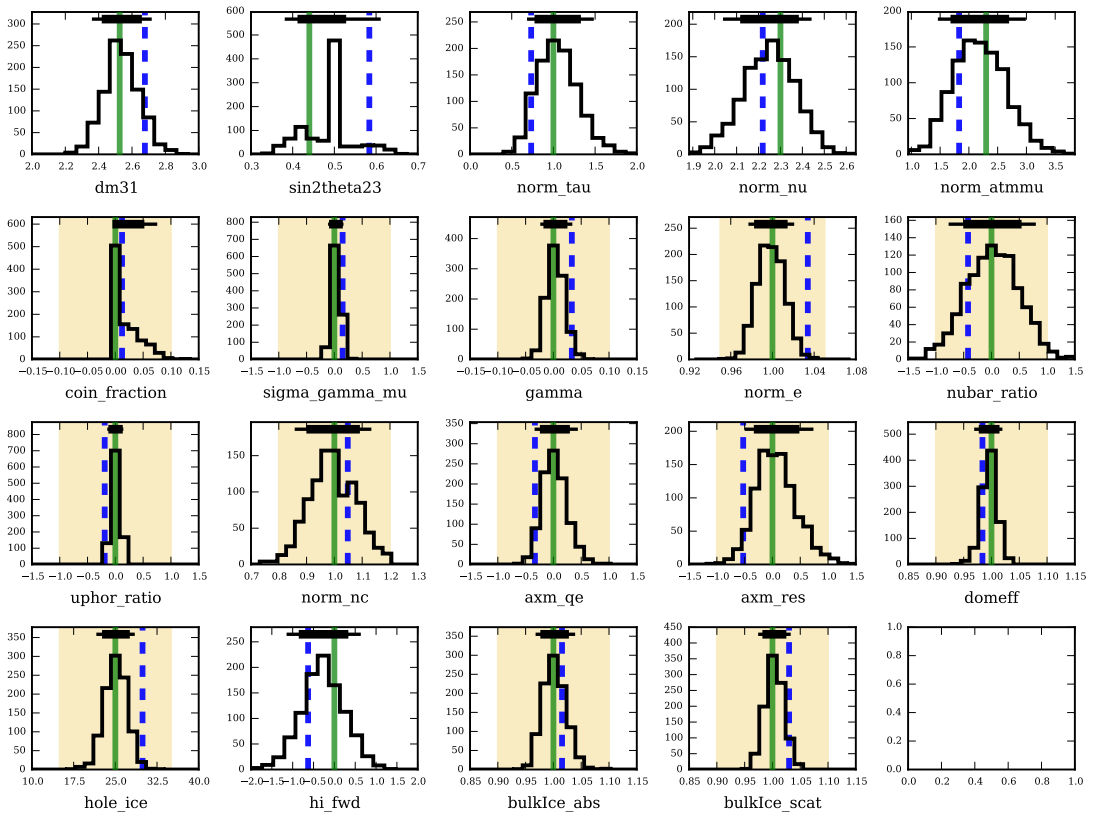


Figure 8.37 – A comparison of the posterior expected from trials to the final data fit value for each parameter for the NC+CC fit. The trials used to build the posterior distribution in each parameter assume baseline values for systematics, $N_{\tau}^{NC+CC} = 1$, and Nu-Fit 2.2 values [57]

Parameter Type	Fit Parameter	Units	Prior	Disappearance	Appearance	
					CC-Only	NC+CC
Oscillations	Δm_{32}^2	10^{-3} eV^2	-	2.548	2.625	2.602
	$\sin^2(\theta_{23})$	-	-	0.576	0.590	0.584
	N_τ	-	-	1.0 (Fixed)	0.566	0.733
Cross-section	Axial Mass (QE)	σ	0 ± 1.0	-0.250	-0.357	-0.332
	Axial Mass (RES)	σ	0 ± 1.0	-0.3737	-0.583	-0.526
	N_{NC}	-	1 ± 0.2	1.016	1.063	1.048
Neutrino Flux	ν_μ Norm	Years	-	2.151	2.210	2.219
	ν_e/ν_μ	-	1 ± 0.05	1.031	1.034	1.033
	γ_ν	-	0 ± 0.10	0.045	0.034	0.033
	$\nu/\bar{\nu}$	σ	0 ± 1.0	-0.700	-0.330	-0.422
	Up/Hor	σ	0 ± 1.0	-0.207	-0.184	-0.191
	$f_{Coincident}$	%	$0 + 0.1$	0.027	0.006	0.012
	μ Norm	Years	-	1.845	1.795	1.830
Muon Flux	γ_{CR}	σ	0 ± 1.0	0.113	0.148	0.148
	DOM Efficiency	-	1.0 ± 0.1	0.980	0.984	0.984
	Hole Ice	-	25 ± 10	30.526	29.833	29.894
	Forward Scattering	-	-	-0.839	-0.638	-0.630
	Absorption	%	1.0 ± 0.1	1.014	1.017	1.016
	Scattering	%	1.0 ± 0.1	1.033	1.028	1.030

Table 8.6 – The best-fit systematics values for each systematic parameter in the fit. The corresponding parameters for $N_\tau = 1$ (ie, the muon neutrino disappearance fit) are included for reference. The CC-only and NC+CC fits are highly correlated, as expected.

The DeepCore results are the first to fit a value lower than expected, with both OPERA and Super-Kamiokande experiments returning results larger than $N_{\tau}^{CC} = 1$. The results are consistent with unitary oscillations.

8.10 Complementary Measurements from This Analysis

8.10.1 Oscillation Parameters

Thanks to significant contributions from others [106, 133], dedicated measurements of the atmospheric mixing parameters have also been performed using the GRECO selection. In these measurements, the value of $N_{\nu_{\tau}}$ remains fixed to unity. The derived results are therefore directly comparable to results from other oscillation experiments.

ν_{μ} Disappearance Results

Using similar tools as the appearance analysis, a complementary search for ν_{μ} disappearance was performed [133]. The measurement of the disappearance parameters, Δm_{3j}^2 and θ_{23} , used an identical choice of binning and systematics set as the appearance search described above. The χ^2_{FS} statistic was found by minimization with the iMinuit package [103, 104] across a grid of values arranged linearly in Δm_{3j}^2 and $\sin^2 \theta_{23}$ covering both octants. At each point, the disappearance parameters were fixed during minimization. Both the normal and inverted ordering were tested separately.

The result is shown in Figure 8.38 compared to previous atmospheric oscillation measurements by IceCube [81], Super-Kamiokande [134] and the MINOS experiment [135]. Results from accelerator measurements are shown from the NO ν A [136] and T2K [137] experiments. All results show the 90% contour around the best-fit point. The GRECO result mildly prefers the normal ordering and the second octant, although maximal mixing ($\sin^2 \theta_{23} = 0.5$) is well within the best-fit contours.

The GRECO result and previous IceCube results are statistically consistent with one another, although the GRECO result prefers a larger mass splitting. Global fits, which prefer a value of the mass splitting of $2.494^{+0.033}_{-0.031}$ as of the time of this writing [58], favor the new GRECO result over the previous IceCube result.

Mass Ordering

In order to quantify the preference for the mass ordering, a dedicated measurement using the GRECO sample was performed [106]. This measurement included differences relative to the appearance and disappearance measurements. Only upgoing reconstructed GRECO events were included, although the energy range was extended to 3-100 GeV. All simulation templates were smoothed during the analysis using a dedicated implementation of the kernel density estimation technique implemented in the C++ programming language [107]. This code, unlike the SciPy KDE implementation used in 6.2, includes functionality for weighted event samples and variable bandwidth estimation.

The systematics set used in the mass ordering analysis was identical to that of the disappearance measurement, with the value of $N_{\nu_{\tau}}$ fixed to unity. Systematics included in the mass ordering measurement were applied using a parallel branch of the OscFit code used in the appearance measurement.

Statistical uncertainties arising from the simulation statistics were estimated using a bootstrapping technique included in the KDE implementation. The test statistic used in

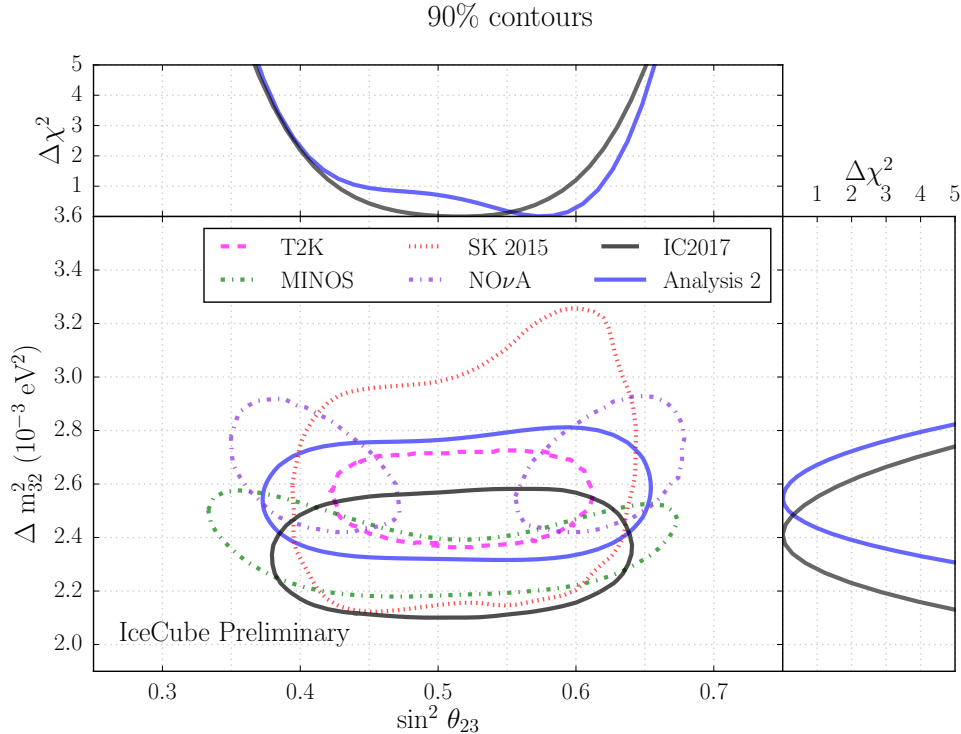


Figure 8.38 – The results of a muon neutrino disappearance measurement with the GRECO event selection. The new result, shown in blue, fits a larger value of the mass splitting than the most recent published IceCube results [81], shown in blue. The GRECO dataset also prefers a value away from maximal mixing, $\sin^2 \theta_{23} = 0.5$, a first for a DeepCore measurement. The GRECO results are competitive with dedication oscillation measurements from other experiments.

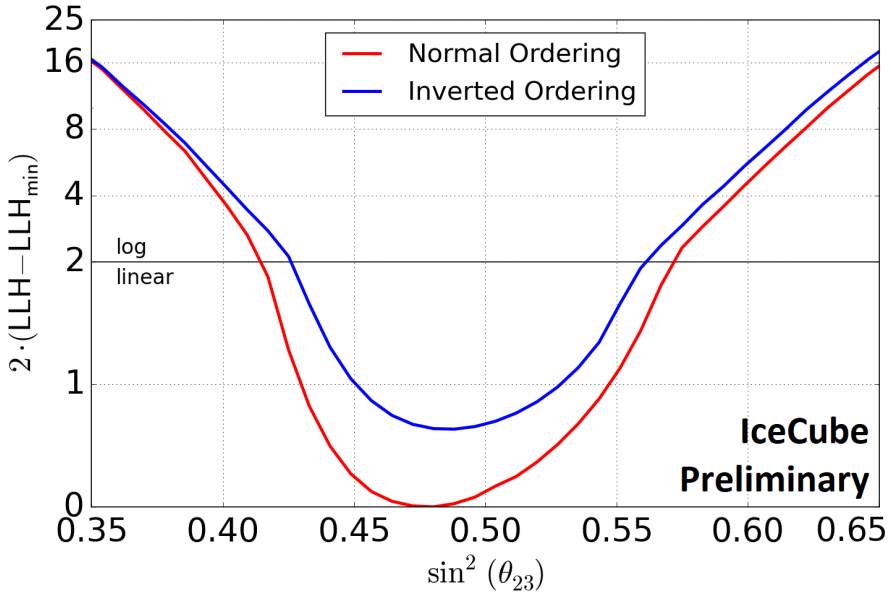


Figure 8.39 – The measurement of the neutrino mass ordering with the GRECO event selection. The fit is performed only on upgoing events, but includes contributions from a wider energy range than the measurement of tau neutrino appearance. A weak preference for normal ordering is observed.

the mass ordering measurement was the numerical convolution between the Poissonian uncertainty due to the expected event count and a Gaussian model of the bootstrapped Monte Carlo statistical uncertainty.

Unlike the appearance and disappearance measurements, the neutrino mass ordering is not a continuous parameter. The calculation of a final significance proceeds following the method described in [126], a full description of which is beyond the scope of this work. Using GRECO events, a good fit is obtained at the best-fit point with a p-value of approximately 80%. A weak preference for the normal mass ordering is found at approximately 0.3σ [106].

8.10.2 Implications and Future Work

There exist various ways to interpret the value of N_τ . The value of the tau neutrino normalizations in the CC-only and NC+CC channels are both consistent with the expected value of 1.0. The standard 3-flavor oscillation model is not strongly disfavored from the GRECO oscillation result. The current result does, however, provide some tension with the most recent exclusive result from Super-Kamiokande [119], which reported 1.47 ± 0.32 . The GRECO and Super-Kamiokande inclusive results differ by approximately 1.8σ , assuming the total uncertainties are added in quadrature. In practice, various systematics, including the atmospheric mixing angle and mass splitting, are likely correlated between the analyses, implying approximately 2σ of tension between the two results.

Assuming Gaussian uncertainties for the two results, the simple weighted average can be calculated in order to estimate the expectation from a combined fit. This value, 1.06 ± 0.22 , shows remarkable agreement with the expected value of 1.0, favoring the standard 3-flavor mixing matrix with large uncertainties. The OPERA value [121] strongly excludes the no-appearance hypothesis but has a negligible effect on this average. This analysis, like previous oscillation analyses produced by IceCube, has known limitations. The GRECO selection includes only three years of detector data. The runs of data from those three years are selected using strict criteria that explicitly excludes non-standard runs, including those that are ended prematurely. These short runs are often otherwise unremarkable, but make up a significant fraction of the uptime of the detector in these years and are potentially useful for analysis. The addition of these runs may increase the total number of events in the GRECO sample by up to 15%. The addition of these events presents a simple way to improve the existing result on relatively short timescales.

The three years of data may also be extended in other ways. The data was originally collected between April 2012 and May 2015. Since the beginning of this work, additional years of detector data have been collected and are ready for analysis. These additional years of data were not included due to calibration changes in the IC86-5 season, discussed in Section 7.8, which may lead to disagreement between years. These updated calibrations have since been applied to the earlier years of detector data as well, leading to a self-consistent dataset of approximately 7 years.

The analysis of these events requires a number of upgrades to the simulation which are ongoing at the time of this work. New efforts are underway updating the simulated SPE templates to better describe the charge profile observed in the detector. These new templates are fit to detector data for each DOM and are updated for each year, although the year-to-year variations have proven to be small. New signal and background simulation is therefore necessary to incorporate these upgrades. The new simulations are underway, with completion and verification expected within the coming year. If the

new sets show good agreement with data, charge information may be reintroduced to the reconstruction, potentially leading to improvements in the reconstructed resolution of events.

The current GRECO selection was the first oscillation selection in IceCube to successfully use simulated atmospheric muon background events at analysis level. The simulated livetime is too limited, at 10 months, to allow for precision measurements using the additional years of data. While the GRECO selection is efficient at rejecting these simulated muons, additional simulation efforts require vast computational resources. Future analyses will require significantly larger muon datasets in order to adequately describe backgrounds.

The production of additional events for these analyses will require nearly a factor of 9 more events to reach parity between the expected number of muon events in 7 years of data and the raw Monte Carlo statistics. If only the standard simulation methods are used, this will require about 1.5 years worth of production time. While the new sets would include muon bundles, a feature not present during production of this work, the sets may still be limited outside of the DeepCore fiducial volume.

To remedy this situation, work is ongoing to further develop and standardize the work described in Section 6.2. That effort has been shown to yield significant improvements to the production time of MuonGun simulation for the GRECO selection when using no DOM oversizing. This can improve to factors of 8x if using a DOM oversizing factor of 3. This may be a viable option for the production of various systematics sets in order to speed the production of background events. Additional improvements to the simulation efficiency are possible and will undoubtedly be investigated in the near future. Even using the improvements described here, however, large muon sets are, for the first time, viable as background models in IceCube oscillation analyses.

Improvements are not only possible in the background simulation, however. Investigations described in Section 7.7.3 have spawned discussions of the limitations of the current GENIE generator production scheme. While GENIE was originally planned to be used solely for very low energy oscillation analyses, the dawn of new event selections such as GRECO spanning wider energy ranges can lead to notable disagreement due to the generation scheme. To better describe the detector, GENIE generation must be examined to identify unsimulated phase space necessary for further analyses. The simulation of events below the detector, in both the GENIE generator as well as in future MuonGun background simulations, must be given priority in order to explain the events occurring at the bottom or below the IceCube detector.

Future measurements of the tau neutrino appearance are already underway. Software updates to the GRECO selection are continuing, with new analyses planned for appearance, disappearance, and other searches for low energy neutrinos.

Future measurements may incorporate an planned detector upgrade. The measurements and techniques for simulated backgrounds presented here will form an integral part of upgrade efforts. The GRECO selection may also provide a template for selections using the upgraded detector, significantly improving the sensitivity to future oscillation measurements.

Bibliography

- [1] H. Becquerel. “Sur les radiations émises par phosphorescence”. In: *Comptes Rendus* 122 (1896) (cit. on p. 15).
- [2] J Chadwick. “Intensitätsverteilung im magnetischen Spectrum der β -Strahlen von radium B + C”. In: *Verhandl. Dtsc. Phys. Ges.* 16 (1914), p. 383 (cit. on p. 15).
- [3] W. Pauli. *Offener Brief an die Gruppe der Radioaktiviten bei der Gauvereins-Tagung zu Tübingen*. ETH Zürich, 1930 (cit. on p. 15).
- [4] C. L. Cowan Jr., F. Reines, F. B. Harrison, H. W. Kruse, and A. D. McGuire. “Detection of the Free Neutrino: A Confirmation”. In: *Science* 124 (July 1956), pp. 103–104 (cit. on p. 15).
- [5] Nobel Foundation. *Nobel Prize in Physics*. 1995 (cit. on p. 16).
- [6] G. Danby, J-M. Gaillard, K. Goulian, et al. “Observation of High-Energy Neutrino Reactions and the Existence of Two Kinds of Neutrinos”. In: *Phys. Rev. Lett.* 9 (1 1962), pp. 36–44 (cit. on p. 16).
- [7] DONUT Collaboration, K. Kodama, N. Ushida, et al. “Observation of tau neutrino interactions”. In: *Physics Letters B* 504 (Apr. 2001), pp. 218–224. eprint: [hep-ex/0012035](#) (cit. on pp. 16, 24, 38).
- [8] K. Kodama, N. Ushida, C. Andreopoulos, et al. “Final tau-neutrino results from the DONuT experiment”. In: *Phys. Rev. D* 78.5, 052002 (Sept. 2008), p. 052002. arXiv: [0711.0728 \[hep-ex\]](#) (cit. on p. 16).
- [9] The ALEPH Collaboration, the DELPHI Collaboration, the L3 Collaboration, et al. “Precision Electroweak Measurements on the Z Resonance”. In: *ArXiv High Energy Physics - Experiment e-prints* (Sept. 2005). eprint: [hep-ex/0509008](#) (cit. on pp. 16, 32).
- [10] A. De Angelis. “Domenico Pacini, uncredited pioneer of the discovery of cosmic rays”. In: *ArXiv e-prints* (Mar. 2011). arXiv: [1103.4392](#) (cit. on p. 17).
- [11] J. R. Hoerandel. “Early cosmic-ray work published in German”. In: *American Institute of Physics Conference Series*. Ed. by J. F. Ormes. Vol. 1516. American Institute of Physics Conference Series. Feb. 2013, pp. 52–60. arXiv: [1212.0706](#) (cit. on p. 17).
- [12] Arthur H. Compton. “A Geographic Study of Cosmic Rays”. In: *Phys. Rev.* 43 (6 1933), pp. 387–403 (cit. on p. 17).
- [13] Nobel Foundation. *Nobel Prize in Physics*. 1936 (cit. on p. 17).
- [14] M Blau and H Wambacher. “Disintegration Processes by Cosmic Rays with the Simultaneous Emission of Several Heavy Particles”. In: 140 (Jan. 1937), pp. 585–585 (cit. on p. 17).

- [15] W. Bothe and W. Kolhoerster. “Das Wesen der Hoehenstrahlung”. In: *Zeitschrift fur Physik* 56 (Nov. 1929), pp. 751–777 (cit. on p. 17).
- [16] G. W. Clark, J. Earl, W. L. Kraushaar, et al. “Cosmic-Ray Air Showers at Sea Level”. In: *Phys. Rev.* 122 (2 1961), pp. 637–654 (cit. on p. 17).
- [17] K. A. Olive et al. “Review of Particle Physics”. In: *Chin. Phys. C*38 (2014), p. 090001 (cit. on pp. 17, 18, 23, 24, 28, 57, 117).
- [18] M. Honda, M. S. Athar, T. Kajita, K. Kasahara, and S. Midorikawa. “Atmospheric neutrino flux calculation using the NRLMSISE-00 atmospheric model”. In: *Phys. Rev. D* 92.2, 023004 (July 2015), p. 023004. arXiv: 1502.03916 [astro-ph.HE] (cit. on pp. 17, 19, 120, 144).
- [19] Wikimedia Commons. *File:Standard Model of Elementary Particles.svg* — *Wikimedia Commons, the free media repository*. [Online; accessed 23-February-2018]. 2017 (cit. on p. 20).
- [20] J. A. Formaggio and G. P. Zeller. “From eV to EeV: Neutrino cross sections across energy scales”. In: *Reviews of Modern Physics* 84 (July 2012), pp. 1307–1341. arXiv: 1305.7513 [hep-ex] (cit. on pp. 21, 22, 52, 122).
- [21] D. Chirkin and W. Rhode. “Propagating leptons through matter with Muon Monte Carlo (MMC)”. In: *ArXiv High Energy Physics - Phenomenology e-prints* (July 2004). eprint: hep-ph/0407075 (cit. on pp. 23, 53).
- [22] H. Pessard. “The Opera Experiment”. In: *High Energy Physics, ICHEP 2004*. Ed. by H. Chen, D. Du, W. Li, and C. Lu. Apr. 2005, pp. 299–303. eprint: hep-ex/0504033 (cit. on pp. 24, 38, 118).
- [23] Minos Collaboration, D. G. Michael, P. Adamson, et al. “The magnetized steel and scintillator calorimeters of the MINOS experiment”. In: *Nuclear Instruments and Methods in Physics Research A* 596 (Nov. 2008), pp. 190–228. arXiv: 0805.3170 [physics.ins-det] (cit. on p. 24).
- [24] S. Mufson, B. Baugh, C. Bower, et al. “Liquid scintillator production for the NOvA experiment”. In: *Nuclear Instruments and Methods in Physics Research A* 799 (Nov. 2015), pp. 1–9. arXiv: 1504.04035 [physics.ins-det] (cit. on p. 24).
- [25] L. Aliaga and et al. “Design, calibration, and performance of the MINERvA detector”. In: *Nuclear Instruments and Methods in Physics Research A* 743 (Apr. 2014), pp. 130–159. arXiv: 1305.5199 [physics.ins-det] (cit. on p. 24).
- [26] Y. Kudenko and T2K Collaboration. “The near neutrino detector for the T2K experiment”. In: *Nuclear Instruments and Methods in Physics Research A* 598 (Jan. 2009), pp. 289–295. arXiv: 0805.0411 [physics.ins-det] (cit. on p. 24).
- [27] M. Antonello, B. Baibussinov, V. Bellini, et al. “ICARUS at FNAL”. In: *ArXiv e-prints* (Dec. 2013). arXiv: 1312.7252 [physics.ins-det] (cit. on p. 24).
- [28] P. A. Čerenkov. “Visible Radiation Produced by Electrons Moving in a Medium with Velocities Exceeding that of Light”. In: *Physical Review* 52 (Aug. 1937), pp. 378–379 (cit. on p. 24).
- [29] P. A. Cherenkov. “Visible luminescence of pure liquids under the influence of - radiation”. In: *Dokl. Akad. Nauk SSSR* 2.8 (1934). [Usp. Fiz. Nauk93,no.2,385(1967)], pp. 451–454 (cit. on p. 24).

- [30] I. M. Frank and I. E. Tamm. “Coherent visible radiation of fast electrons passing through matter”. In: *Compt. Rend. Acad. Sci. URSS* 14.3 (1937). [Usp. Fiz. Nauk93,no.2,388(1967)], pp. 109–114 (cit. on pp. 24, 25).
- [31] D.J. Griffiths. *Introduction to Electrodynamics*. Ed. by Pearson Education Limited. Fourth. 2013 (cit. on p. 24).
- [32] S. Tavernier. *Experimental Techniques in Nuclear and Particle Physics*. Ed. by Springer-Verlag. 2010 (cit. on p. 25).
- [33] K.A. Olive and Particle Data Group. “Review of Particle Physics”. In: *Chinese Physics C* 38.9 (2014), p. 090001 (cit. on p. 25).
- [34] B. Aharmim, S. N. Ahmed, A. E. Anthony, et al. “Combined analysis of all three phases of solar neutrino data from the Sudbury Neutrino Observatory”. In: *Phys. Rev. C* 88.2, 025501 (Aug. 2013), p. 025501. arXiv: 1109.0763 [nucl-ex] (cit. on pp. 25, 30).
- [35] C. W. Walter. “The Super-Kamiokande Experiment”. In: *Neutrino Oscillations: Present Status and Future Plans*. Ed. by J. A. Thomas and P. L. Vahle. World Scientific Publishing Co, 2008, pp. 19–43 (cit. on p. 25).
- [36] F. Montanet. “Design and expected performance of the ANTARES neutrino telescope”. In: *Nuclear Physics B Proceedings Supplements* 87 (June 2000), pp. 436–438. eprint: astro-ph/0001380 (cit. on p. 25).
- [37] M. G. Aartsen, M. Ackermann, J. Adams, et al. “The IceCube Neutrino Observatory: instrumentation and online systems”. In: *Journal of Instrumentation* 12 (Mar. 2017), P03012. arXiv: 1612.05093 [astro-ph.IM] (cit. on pp. 25, 38, 40–43, 46–48, 54, 76, 136).
- [38] B. Pontecorvo. “Neutrino Experiments and the Problem of Conservation of Leptonic Charge”. In: *Sov. Phys. JETP* 26 (1968). [Zh. Eksp. Teor. Fiz.53,1717(1967)], pp. 984–988 (cit. on p. 26).
- [39] Z. Maki, M. Nakagawa, and S. Sakata. “Remarks on the Unified Model of Elementary Particles”. In: *Progress of Theoretical Physics* 28 (Nov. 1962), pp. 870–880 (cit. on p. 26).
- [40] C. Giganti, S. Lavignac, and M. Zito. “Neutrino oscillations: The rise of the PMNS paradigm”. In: *Progress in Particle and Nuclear Physics* 98 (Jan. 2018), pp. 1–54. arXiv: 1710.00715 [hep-ex] (cit. on pp. 27, 29, 32).
- [41] S. T. Petcov. “The Nature of Massive Neutrinos”. In: *Adv. High Energy Phys.* 2013 (2013), p. 852987. arXiv: 1303.5819 [hep-ph] (cit. on p. 27).
- [42] E. K. Akhmedov and A. Y. Smirnov. “Paradoxes of neutrino oscillations”. In: *Physics of Atomic Nuclei* 72 (Aug. 2009), pp. 1363–1381. arXiv: 0905.1903 [hep-ph] (cit. on p. 27).
- [43] A. Y. Smirnov. “The MSW Effect and Matter Effects in Neutrino Oscillations”. In: *Physica Scripta Volume T* 121 (Jan. 2005), pp. 57–64. eprint: hep-ph/0412391 (cit. on p. 29).
- [44] S. M. Bilenky. “Neutrino oscillations: brief history and present status”. In: *ArXiv e-prints* (Aug. 2014). arXiv: 1408.2864 [hep-ph] (cit. on p. 29).
- [45] V. Barger, K. Whisnant, S. Pakvasa, and R. J. N. Phillips. “Matter effects on three-neutrino oscillations”. In: *Phys. Rev. D* 22 (11 1980), pp. 2718–2726 (cit. on p. 29).

- [46] Super-Kamiokande Collaboration. *Prob3++*. 2012 (cit. on pp. 29, 145).
- [47] Adam M. Dziewonski and Don L. Anderson. “Preliminary reference Earth model”. In: *Physics of the Earth and Planetary Interiors* 25.4 (1981), pp. 297–356 (cit. on pp. 29, 52, 145).
- [48] John N. Bahcall. “Solar Neutrinos. I. Theoretical”. In: *Phys. Rev. Lett.* 12 (11 1964), pp. 300–302 (cit. on p. 29).
- [49] Raymond Davis. “Solar Neutrinos. II. Experimental”. In: *Phys. Rev. Lett.* 12 (11 1964), pp. 303–305 (cit. on p. 29).
- [50] Bruce T. Cleveland, Timothy Daily, Jr. Raymond Davis, et al. “Measurement of the Solar Electron Neutrino Flux with the Homestake Chlorine Detector”. In: *The Astrophysical Journal* 496.1 (1998), p. 505 (cit. on p. 29).
- [51] J. N. Abdurashitov, V. N. Gavrin, V. V. Gorbachev, et al. “Measurement of the solar neutrino capture rate with gallium metal. III. Results for the 2002-2007 data-taking period”. In: *Phys. Rev. C* 80.1, 015807 (July 2009), p. 015807. arXiv: 0901.2200 [nucl-ex] (cit. on p. 30).
- [52] W. Hampel, J. Handt, G. Heusser, et al. “GALLEX solar neutrino observations: results for GALLEX IV”. In: *Physics Letters B* 447.1 (1999), pp. 127–133 (cit. on p. 30).
- [53] M. Altmann, M. Balata, P. Belli, et al. “Complete results for five years of GNO solar neutrino observations”. In: *Physics Letters B* 616.3 (2005), pp. 174–190 (cit. on p. 30).
- [54] Herbert H. Chen. “Direct Approach to Resolve the Solar-Neutrino Problem”. In: *Phys. Rev. Lett.* 55 (14 1985), pp. 1534–1536 (cit. on p. 30).
- [55] Nobel Foundation. *Nobel Prize in Physics*. 2015 (cit. on pp. 30, 31).
- [56] Y. Fukuda, T. Hayakawa, E. Ichihara, et al. “Evidence for Oscillation of Atmospheric Neutrinos”. In: *Phys. Rev. Lett.* 81 (8 1998), pp. 1562–1567 (cit. on pp. 31, 114).
- [57] J. Bergström, M. C. Gonzalez-Garcia, M. Maltoni, and T. Schwetz. “Bayesian global analysis of neutrino oscillation data”. In: *Journal of High Energy Physics* 9, 200 (Sept. 2015), p. 200. arXiv: 1507.04366 [hep-ph] (cit. on pp. 32, 157, 158).
- [58] I. Esteban, M. C. Gonzalez-Garcia, M. Maltoni, I. Martinez-Soler, and T. Schwetz (cit. on pp. 32, 116, 119, 144, 160).
- [59] S. Gariazzo, C. Giunti, M. Laveder, Y. F. Li, and E. M. Zavanin. “Light sterile neutrinos”. In: *Journal of Physics G Nuclear Physics* 43.3, 033001 (Mar. 2015), p. 033001. arXiv: 1507.08204 [hep-ph] (cit. on pp. 32, 34).
- [60] J. M. Conrad, C. M. Ignarra, G. Karagiorgi, M. H. Shaevitz, and J. Spitz. “Sterile Neutrino Fits to Short Baseline Neutrino Oscillation Measurements”. In: *ArXiv e-prints* (July 2012). arXiv: 1207.4765 [hep-ex] (cit. on p. 32).
- [61] S. Gariazzo, C. Giunti, M. Laveder, and Y. F. Li. “Updated global 3+1 analysis of short-baseline neutrino oscillations”. In: *Journal of High Energy Physics* 6, 135 (June 2017), p. 135. arXiv: 1703.00860 [hep-ph] (cit. on pp. 32, 34).
- [62] P. Adamson, D. J. Auty, D. S. Ayres, et al. “Active to Sterile Neutrino Mixing Limits from Neutral-Current Interactions in MINOS”. In: *Physical Review Letters* 107.1, 011802 (July 2011), p. 011802. arXiv: 1104.3922 [hep-ex] (cit. on pp. 33, 117).

- [63] P. Adamson, I. Anghel, A. Aurisano, et al. “Search for Sterile Neutrinos Mixing with Muon Neutrinos in MINOS”. In: *Physical Review Letters* 117.15, 151803 (Oct. 2016), p. 151803. arXiv: 1607.01176 [hep-ex] (cit. on p. 33).
- [64] P. Adamson, L. Aliaga, D. Ambrose, et al. “Search for active-sterile neutrino mixing using neutral-current interactions in NOvA”. In: *Phys. Rev. D* 96.7, 072006 (Oct. 2017), p. 072006. arXiv: 1706.04592 [hep-ex] (cit. on p. 33).
- [65] K. Abe, Y. Haga, Y. Hayato, et al. “Limits on sterile neutrino mixing using atmospheric neutrinos in Super-Kamiokande”. In: *Phys. Rev. D* 91 (5 2015), p. 052019 (cit. on p. 33).
- [66] IceCube Collaboration, M. G. Aartsen, M. Ackermann, et al. “Search for sterile neutrino mixing using three years of IceCube DeepCore data”. In: *ArXiv e-prints* (Feb. 2017). arXiv: 1702.05160 [hep-ex] (cit. on pp. 33, 70, 114).
- [67] M. G. Aartsen, K. Abraham, M. Ackermann, et al. “Searches for Sterile Neutrinos with the IceCube Detector”. In: *Physical Review Letters* 117.7, 071801 (Aug. 2016), p. 071801. arXiv: 1605.01990 [hep-ex] (cit. on pp. 33, 43, 114).
- [68] Stephen Parke and Mark Ross-Lonergan. “Unitarity and the three flavor neutrino mixing matrix”. In: *Phys. Rev. D* 93 (11 2016), p. 113009 (cit. on pp. 35, 36).
- [69] M. G. Aartsen, M. Ackermann, J. Adams, et al. “Calibration and characterization of the IceCube photomultiplier tube”. In: *Nuclear Instruments and Methods in Physics Research Section A: Accelerators, Spectrometers, Detectors and Associated Equipment* 618.1 (2010), pp. 139 –152 (cit. on pp. 38, 39, 42, 55, 136).
- [70] Hamamatsu Photonics. *PHOTOMULTIPLIER TUBE DATA SHEET R7081-02 for ICECUBE Experiment*. 2003 (cit. on p. 38).
- [71] M. J. Larson. “Simulation and identification of non-Poissonian noise triggers in the IceCube neutrino detector”. M.Sc. Alabama U., 2013 (cit. on pp. 40, 41, 54, 55, 57–59, 78, 79).
- [72] R. Abbasi, Y. Abdou, T. Abu-Zayyad, et al. “The design and performance of IceCube DeepCore”. In: *Astroparticle Physics* 35 (May 2012), pp. 615–624. arXiv: 1109.6096 [astro-ph.IM] (cit. on pp. 42, 43, 78, 79).
- [73] M. G. Aartsen, R. Abbasi, Y. Abdou, et al. “Measurement of South Pole ice transparency with the IceCube LED calibration system”. In: *Nuclear Instruments and Methods in Physics Research A* 711 (May 2013), pp. 73–89. arXiv: 1301.5361 [astro-ph.IM] (cit. on pp. 42, 46, 144).
- [74] The HAWC Collaboration and The IceCube Collaboration. “Combined Analysis of Cosmic-Ray Anisotropy with IceCube and HAWC”. In: *ArXiv e-prints* (Aug. 2017). arXiv: 1708.03005 [astro-ph.HE] (cit. on p. 43).
- [75] M. G. Aartsen, G. C. Hill, A. Kyriacou, et al. “Measurement of the multi-TeV neutrino interaction cross-section with IceCube using Earth absorption”. In: *Nature* 551 (Nov. 2017), pp. 596–600. arXiv: 1711.08119 [hep-ex] (cit. on p. 43).
- [76] M. G. Aartsen, K. Abraham, M. Ackermann, et al. “Observation and Characterization of a Cosmic Muon Neutrino Flux from the Northern Hemisphere Using Six Years of IceCube Data”. In: *Ap.J.* 833, 3 (Dec. 2016), p. 3. arXiv: 1607.08006 [astro-ph.HE] (cit. on p. 43).

- [77] IceCube Collaboration. “Evidence for High-Energy Extraterrestrial Neutrinos at the IceCube Detector”. In: *Science* 342, 1242856 (Nov. 2013), p. 1242856. arXiv: 1311.5238 [astro-ph.HE] (cit. on p. 44).
- [78] S. Euler. “Observations of Oscillations of Atmospheric Neutrinos with the IceCube Neutrino Observatory”. Ph.D. Rheinisch-Westfälische Technische Hochschule (RWTH), 2013 (cit. on pp. 44, 45, 78, 87, 95, 97, 114).
- [79] M. G. Aartsen, R. Abbasi, Y. Abdou, et al. “Measurement of Atmospheric Neutrino Oscillations with IceCube”. In: *Physical Review Letters* 111.8, 081801 (Aug. 2013), p. 081801. arXiv: 1305.3909 [hep-ex] (cit. on pp. 43, 70, 78, 103, 114, 137, 145).
- [80] IceCube Collaboration, M. G. Aartsen, M. Ackermann, et al. “Determining neutrino oscillation parameters from atmospheric muon neutrino disappearance with three years of IceCube DeepCore data”. In: *ArXiv e-prints* (Oct. 2014). arXiv: 1410.7227 [hep-ex] (cit. on pp. 43, 70, 78, 103, 114, 120, 122, 137, 145).
- [81] IceCube Collaboration, M. G. Aartsen, M. Ackermann, et al. “Measurement of Atmospheric Neutrino Oscillations at 6–56 GeV with IceCube DeepCore”. In: *ArXiv e-prints* (July 2017). arXiv: 1707.07081 [hep-ex] (cit. on pp. 43, 70, 78, 103, 114, 117, 118, 120, 122, 137, 138, 144, 145, 147, 160, 161).
- [82] M. G. Aartsen, M. Ackermann, J. Adams, et al. “Search for annihilating dark matter in the Sun with 3 years of IceCube data”. In: *European Physical Journal C* 77, 146 (Mar. 2017), p. 146. arXiv: 1612.05949 [astro-ph.HE] (cit. on p. 46).
- [83] M. G. Aartsen, K. Abraham, M. Ackermann, et al. “All-flavour search for neutrinos from dark matter annihilations in the Milky Way with IceCube/DeepCore”. In: *European Physical Journal C* 76, 531 (Oct. 2016), p. 531. arXiv: 1606.00209 [astro-ph.HE] (cit. on p. 46).
- [84] N. E. Bramall, R. C. Bay, K. Woschnagg, R. A. Rohde, and P. B. Price. “A deep high-resolution optical log of dust, ash, and stratigraphy in South Pole glacial ice”. In: *Geophys. Res. Lett.* 32, L21815 (Nov. 2005), p. L21815 (cit. on p. 46).
- [85] M. Ackermann, J. Ahrens, X. Bai, et al. “Optical properties of deep glacial ice at the South Pole”. In: *Journal of Geophysical Research (Atmospheres)* 111, D13203 (July 2006), p. D13203 (cit. on p. 46).
- [86] IceCube Collaboration. *IceCube Dust Map*. 2011. URL: <http://icecube.berkeley.edu/~bay/dustmap/> (cit. on p. 46).
- [87] IceCube Collaboration, M. G. Aartsen, R. Abbasi, et al. “The IceCube Neutrino Observatory Part VI: Ice Properties, Reconstruction and Future Developments”. In: *ArXiv e-prints* (Sept. 2013). arXiv: 1309.7010 [astro-ph.HE] (cit. on pp. 46, 47, 65, 137).
- [88] M. Rongen. “Measuring the optical properties of IceCube drill holes”. In: *European Physical Journal Web of Conferences*. Vol. 116. European Physical Journal Web of Conferences. Apr. 2016, p. 06011 (cit. on p. 47).
- [89] D. Heck, G. Schatz, T. Thouw, J. Knapp, and J. N. Capdevielle. “CORSIKA: A Monte Carlo code to simulate extensive air showers”. In: (1998) (cit. on p. 49).
- [90] E.-J. Ahn, R. Engel, T. K. Gaisser, P. Lipari, and T. Stanev. “Cosmic ray interaction event generator SIBYLL 2.1”. In: *Phys. Rev. D* 80.9, 094003 (Nov. 2009), p. 094003. arXiv: 0906.4113 [hep-ph] (cit. on p. 49).

- [91] Joerg R. Hoerandel. “On the knee in the energy spectrum of cosmic rays”. In: *Astropart. Phys.* 19 (2003), pp. 193–220. arXiv: astro-ph/0210453 [astro-ph] (cit. on pp. 49, 51, 65).
- [92] T. K. Gaisser, T. Stanev, and S. Tilav. “Cosmic ray energy spectrum from measurements of air showers”. In: *Frontiers of Physics* 8 (Dec. 2013), pp. 748–758. arXiv: 1303.3565 [astro-ph.HE] (cit. on pp. 50, 51).
- [93] J. van Santen. “Neutrino Interactions in IceCube above 1 TeV: Constraints on Atmospheric Charmed-Meson Production and Investigation of the Astrophysical Neutrino Flux with 2 Years of IceCube Data taken 2010–2012”. PhD thesis. U. Wisconsin, Madison (main), 2014 (cit. on pp. 50, 71, 90).
- [94] C. Andreopoulos, C. Barry, S. Dytman, et al. “The GENIE Neutrino Monte Carlo Generator: Physics and User Manual”. In: *ArXiv e-prints* (Oct. 2015). arXiv: 1510.05494 [hep-ph] (cit. on pp. 52, 121, 144).
- [95] M. Gluck, E. Reya, and A. Vogt. “Dynamical parton distributions revisited”. In: *European Physical Journal C* 5 (Sept. 1998), pp. 461–470. eprint: hep-ph/9806404 (cit. on p. 52).
- [96] S. Agostinelli et al. “GEANT4: A Simulation toolkit”. In: *Nucl. Instrum. Meth.* A506 (2003), pp. 250–303 (cit. on p. 52).
- [97] Makoto Asai, Andrea Dotti, Marc Verderi, and Dennis H. Wright. “Recent developments in Geant4”. In: *Annals Nucl. Energy* 82 (2015), pp. 19–28 (cit. on p. 52).
- [98] A. Gazizov and M. Kowalski. “ANIS: High energy neutrino generator for neutrino telescopes”. In: *Computer Physics Communications* 172 (Nov. 2005), pp. 203–213. eprint: astro-ph/0406439 (cit. on p. 52).
- [99] J. H. Koehne, K. Frantzen, M. Schmitz, et al. “PROPOSAL: A tool for propagation of charged leptons”. In: *Comput. Phys. Commun.* 184 (2013), pp. 2070–2090 (cit. on pp. 53, 121).
- [100] Dmitry Chirkin. “Photon tracking with GPUs in IceCube”. In: *Nucl. Instrum. Meth.* A725 (2013), pp. 141–143 (cit. on p. 54).
- [101] John E. Stone, David Gohara, and Guochun Shi. “OpenCL: A Parallel Programming Standard for Heterogeneous Computing Systems”. In: *IEEE Des. Test* 12.3 (May 2010), pp. 66–73 (cit. on p. 54).
- [102] Y. Hasegawa. *Analysis of Charge Response functions of the IceCube PMTs*. Chiba University. 2007. URL: <http://www.ppl.phys.chiba-u.jp/research/IceCube/pmt/SPE/CRAanalysis.html> (cit. on pp. 55, 104).
- [103] iminuit team. *iminuit – A Python interface to Minuit* (cit. on pp. 63, 145, 160).
- [104] F. James and M. Roos. “Minuit – a system for function minimization and analysis of the parameter errors and correlations”. In: *Computer Physics Communications* 10 (Dec. 1975), pp. 343–367 (cit. on pp. 63, 145, 160).
- [105] Eric Jones, Travis Oliphant, Pearu Peterson, et al. *SciPy: Open source scientific tools for Python*. [Online; accessed <today>]. 2001– (cit. on pp. 74, 150).
- [106] M. Leuermann. “Testing the Neutrino Mass Ordering with Three Years of IceCube/DeepCore Data”. Pending. Ph.D. URheinisch-Westfälische Technische Hochschule (RWTH), 2018 (cit. on pp. 75, 99, 160, 162).

- [107] S. Schoenen. “Discovery and characterization of a diffuse astrophysical muon neutrino flux with the iceCube neutrino observatory”. Ph.D. Rheinisch-Westfälische Technische Hochschule (RWTH), 2017 (cit. on pp. 75, 160).
- [108] Andreas Hocker et al. “TMVA - Toolkit for Multivariate Data Analysis”. In: *PoS ACAT* (2007), p. 040. arXiv: [physics/0703039 \[PHYSICS\]](#) (cit. on pp. 81, 84).
- [109] AMANDA Collaboration. “Muon track reconstruction and data selection techniques in AMANDA”. In: *Nuclear Instruments and Methods in Physics Research Section A: Accelerators, Spectrometers, Detectors and Associated Equipment* 524.1 (2004), pp. 169 –194 (cit. on p. 84).
- [110] D. Pandel. “Bestimmung von Wasser- und Detektorparametern und Rekonstruktion von Myonen bis 100 TeV mit dem Baikal Neutrino Teleskop NT-72”. PhD thesis. Humboldt-Universität, 1996 (cit. on p. 90).
- [111] AMANDA Collaboration. “Muon track reconstruction and data selection techniques in AMANDA”. In: *Nuclear Instruments and Methods in Physics Research A* 524 (May 2004), pp. 169–194. eprint: [astro-ph/0407044](#) (cit. on p. 90).
- [112] J. A. Nelder and R. Mead. “A Simplex Method for Function Minimization”. In: *The Computer Journal* 7.4 (1965), pp. 308–313. eprint: [/oup/backfile/content_public/journal/comjnl/7/4/10.1093/comjnl/7.4.308/2/7-4-308.pdf](#) (cit. on p. 90).
- [113] IceCube Collaboration, M. G. Aartsen, R. Abbasi, et al. “The IceCube Neutrino Observatory Part II: Atmospheric and Diffuse UHE Neutrino Searches of All Flavors”. In: *ArXiv e-prints* (Sept. 2013). arXiv: [1309.7003 \[astro-ph.HE\]](#) (cit. on p. 92).
- [114] J. Kiryluk and for the IceCube Collaboration. “First search for extraterrestrial neutrino-induced cascades with IceCube”. In: *ArXiv e-prints* (Sept. 2009). arXiv: [0909.0989 \[astro-ph.HE\]](#) (cit. on p. 92).
- [115] M. Dunkman. “Measurement of Atmospheric Muon Neutrino Disappearance with IceCube-DeepCore”. Ph.D. The Pennsylvania State University, 2015 (cit. on pp. 96, 99, 114).
- [116] F. Feroz, M. P. Hobson, and M. Bridges. “MultiNest: an efficient and robust Bayesian inference tool for cosmology and particle physics”. In: *Monthly Notices of the Royal Astronomical Society* 398.4 (2009), pp. 1601–1614. eprint: [/oup/backfile/content_public/journal/mnras/398/4/10.1111/j.1365-2966.2009.14548.x/2/mnras0398-1601.pdf](#) (cit. on p. 99).
- [117] F. Feroz, M. P. Hobson, E. Cameron, and A. N. Pettitt. “Importance Nested Sampling and the MultiNest Algorithm”. In: *ArXiv e-prints* (June 2013). arXiv: [1306.2144 \[astro-ph.IM\]](#) (cit. on p. 99).
- [118] M. G. Aartsen, R. Abbasi, M. Ackermann, et al. “Energy reconstruction methods in the IceCube neutrino telescope”. In: *Journal of Instrumentation* 9, P03009 (Mar. 2014), P03009. arXiv: [1311.4767 \[physics.ins-det\]](#) (cit. on p. 99).
- [119] Super-Kamiokande Collaboration, : Z. Li, et al. “A Measurement of the Tau Neutrino Cross Section in Atmospheric Neutrino Oscillations with Super-Kamiokande”. In: *ArXiv e-prints* (Nov. 2017). arXiv: [1711.09436 \[hep-ex\]](#) (cit. on pp. 114, 117–119, 125, 162).

- [120] K. Abe, Y. Hayato, T. Iida, et al. “Evidence for the Appearance of Atmospheric Tau Neutrinos in Super-Kamiokande”. In: *Physical Review Letters* 110.18, 181802 (May 2013), p. 181802. arXiv: 1206.0328 [hep-ex] (cit. on pp. 117–119).
- [121] N. Agafonova, A. Aleksandrov, A. Anokhina, et al. “Discovery of τ Neutrino Appearance in the CNGS Neutrino Beam with the OPERA Experiment”. In: *Physical Review Letters* 115.12, 121802 (Sept. 2015), p. 121802. arXiv: 1507.01417 [hep-ex] (cit. on pp. 117, 118, 125, 162).
- [122] S. Aoki, A. Ariga, T. Ariga, et al. “Study of tau-neutrino production at the CERN SPS”. In: *ArXiv e-prints* (Aug. 2017). arXiv: 1708.08700 [hep-ex] (cit. on p. 118).
- [123] G. Pagliaroli, N. Di Marco, and M. Mannarelli. “Enhanced tau neutrino appearance through invisible decay”. In: *Phys. Rev. D* 93.11, 113011 (June 2016), p. 113011. arXiv: 1603.08696 [hep-ph] (cit. on p. 118).
- [124] G. D. Barr, S. Robbins, T. K. Gaisser, and T. Stanev. “Uncertainties in atmospheric neutrino fluxes”. In: *Phys. Rev. D* 74.9, 094009 (Nov. 2006), p. 094009. eprint: astro-ph/0611266 (cit. on pp. 120, 128, 144).
- [125] J. Evans, D. Garcia Gamez, S. D. Porzio, S. Söldner-Rembold, and S. Wren. “Uncertainties in atmospheric muon-neutrino fluxes arising from cosmic-ray primaries”. In: *Phys. Rev. D* 95.2, 023012 (Jan. 2017), p. 023012. arXiv: 1612.03219 [astro-ph.HE] (cit. on pp. 120, 121, 144).
- [126] S. Wren. “Neutrino Mass Ordering Studies with IceCube-DeepCore”. Ph.D. The University of Manchester, 2017 (cit. on pp. 121, 129, 162).
- [127] S. Mandalia. *Update on the differential DIS cross-section error*. Internal Presentation. 2016 (cit. on p. 122).
- [128] M. Tzanov, D. Naples, S. Boyd, et al. “Precise measurement of neutrino and antineutrino differential cross sections”. In: *Phys. Rev. D* 74.1, 012008 (July 2006), p. 012008. eprint: hep-ex/0509010 (cit. on p. 122).
- [129] J. Feintzeig. “Searches for Point-like Sources of Astrophysical Neutrinos with the IceCube Neutrino Observatory”. Ph.D. University of Wisconsin, 2014 (cit. on pp. 136, 144).
- [130] G. Cowan, K. Cranmer, E. Gross, and O. Vitells. “Asymptotic formulae for likelihood-based tests of new physics”. In: *European Physical Journal C* 71, 1554 (Feb. 2011), p. 1554. arXiv: 1007.1727 [physics.data-an] (cit. on p. 146).
- [131] S. S. Wilks. “The Large-Sample Distribution of the Likelihood Ratio for Testing Composite Hypotheses”. In: *Ann. Math. Statist.* 9.1 (Mar. 1938), pp. 60–62 (cit. on p. 147).
- [132] G. J. Feldman and R. D. Cousins. “Unified approach to the classical statistical analysis of small signals”. In: *Phys. Rev. D* 57 (Apr. 1998), pp. 3873–3889. eprint: physics/9711021 (cit. on p. 147).
- [133] E. Cheung. “Measurements of Atmospheric Neutrino Oscillation Parameters Using Three Years of IceCube Data”. Pending. Ph.D. University of Maryland, 2018 (cit. on p. 160).
- [134] R. Wendell. “Atmospheric results from Super-Kamiokande”. In: *American Institute of Physics Conference Series*. Vol. 1666. American Institute of Physics Conference Series. July 2015, p. 100001. arXiv: 1412.5234 [hep-ex] (cit. on p. 160).

- [135] P. Adamson, I. Anghel, C. Backhouse, et al. “Measurement of Neutrino and Antineutrino Oscillations Using Beam and Atmospheric Data in MINOS”. In: *Physical Review Letters* 110.25, 251801 (June 2013), p. 251801. arXiv: 1304.6335 [hep-ex] (cit. on p. 160).
- [136] The NOvA Collaboration, P. Adamson, L. Aliaga, et al. “Measurement of the neutrino mixing angle θ_{23} in NOvA”. In: *ArXiv e-prints* (Jan. 2017). arXiv: 1701.05891 [hep-ex] (cit. on p. 160).
- [137] T2K Collaboration, K. Abe, J. Amey, et al. “First combined analysis of neutrino and antineutrino oscillations at T2K”. In: *ArXiv e-prints* (Jan. 2017). arXiv: 1701.00432 [hep-ex] (cit. on p. 160).

Notes

■ Add a plot of the oscillation probabilities here	31
■ find good quality swedish camera pics?	47
■ Something in here about resolution, you nitwit!	113
■ hidden potential martin n-1 tests *RUNNING*	151
■ scipy	153